Rupture Characteristics of California Earthquakes

Thesis by

David Jay Wald

In Partial Fulfillment of the Requirements

for the Degree of

Doctor of Philosophy

California Institute of Technology

Pasadena, California

1993

(Submitted July 8, 1992)

Acknowledgements

This work would not have been possible without the friendship, support and love of my wife, Lisa. Of course, her proof reading should not go unmentioned.

Don Helmberger, my advisor, provided more than ample guidance, insight and encouragement during my tenure at the Seismo Lab. He always allowed me the flexibility and opportunity to pursue many of my own interests and ideas; for that, I am grateful.

Steve Hartzell was my mentor in my initial ground-motion source inversions; I owe a great deal to his tutelage and generosity. I have learned more (and have had more fun) in Tom Heaton's spontaneous coffee-hour classes than most in formal classes; his intuitive approach to seismology and ability to pinpoint the important issues have been exemplary. Hiroo Kanamori provided insight into the workings of many a geophysical problem, doing so with the admirable attitude that seismology is an adventure, not a job. I will miss his daily joviality and enthusiasm.

Most of the figures in this thesis were made with the MPLOT software written primarily by Shawn Larson, and I owe him many thanks. Neil Humphreys wrote the digitizing software I used to recover the historical 1906 seismograms. I thank the many reviewers of the papers that comprise this thesis, including several anonymous

individuals, as well as Greg Beroza, Art Frankel, Steve Hartzell, Tom Heaton, Paul Somerville, Paul Spudich, and Jamie Steidl.

Hong Kie Thio allowed me to keep a reasonable view of Caltech life at times when I might have lost all perspective. His friendship, insight, positive attitude, and strong coffee made the office atmosphere less trying and more enjoyable.

Many thanks go to the students of Seismo-lab with whom I interacted most: Andrea, Brad, Craig, Doug, Kuo-Fong, Linda, Lorraine, Monica, Richard, Shawn, Sharon, and special thanks go to my office-mates: Huw, Joanne, Alison, Bruce, Hong Kie and Blair. My interactions with everyone at Woodward-Clyde Consultants were extremely helpful. Paul Somerville, in particular, provided many ideas and reviews. I still miss Cindy—she is fixed in my memory.

I also thank those regulars at Coffee Hour - they know who they are, but to list a few, CRA, DLA, THH, HK and HKT. This institution (but not the coffee) will be missed. It is amazing how much one can learn while seemingly wasting time.

To *My Parents*

Abstract

David Jay Wald, Ph.D.

California Institute of Technology 1992

The rupture characteristics of the 1987 Superstition Hills ($M_S = 6.6$), the 1989 Loma Prieta ($M_S = 7.1$), and the 1991 Sierra Madre ($M_L = 5.8$) earthquakes were determined using a constrained, damped, least-squares inversion of strong motion and teleseismic waveforms. Extension of the modeling procedure to employ teleseismic, empirical Green's functions allowed determination of faulting details of a fourth earthquake, the great 1906 San Francisco event.

The 1987 Superstition Hills earthquake was the second and larger of two significant earthquakes that occurred on conjugate faults in the western Imperial Valley. The first event ($M_S = 6.2$), located on the Elmore Ranch Fault, had a geometry and mechanism favorable for triggering the larger event on the Superstition Hills Fault some 12 hours later. The Superstition Hills event was modeled as three independent subevents, each nucleating from a common location near the intersection of the two faults. This required rerupturing of one fault region on the time scale of several seconds. Slip was quite heterogeneous along strike, but fairly systematic as a function of depth. Substantial differences between the source process as observed from strong

motion data and from teleseismic data were observed.

The 1989 Loma Prieta Earthquake began with a small (magnitude 4.5 to 5.0) precursor, which preceded the main part of the rupture by about 2 sec. Rupture was bilateral, with the overall radiation greater from the northwest portion of the fault. Separate inversions of the teleseismic data (periods 3-30 sec) and strong motion data (periods 1-5 sec) resulted in similar models, indicating a close correspondence of long- and short-period radiation. Forward predictions of the local strong motions from the teleseismic rupture model matched the distribution, duration and overall frequency content of the recordings, suggesting that constraints on strong motions can be made with teleseismic broadband recordings.

Short period and broadband teleseismic waveform data and three-component strong-motion records were analyzed to obtain the source rupture history of the 1991 Sierra Madre earthquake. The near-field, shear-wave displacement pulse from this event had a relatively short duration (about 1 sec) for the magnitude of the event, requiring a particularly high-average stress drop (175 bars). The ground-motion variations in the Los Angeles region were controlled predominantly by source directivity. Rupture was updip and southwestward, resulting in strong motions and heavier damage in regions to the southwest of the epicenter and near the updip fault projection.

The rupture process of the 1906 San Francisco earthquake was analyzed, using all high-quality, teleseismic recordings archived in the 1908 Carnegie Report of the State Earthquake Investigation Commission. The recordings are relatively simple considering the great rupture length in 1906, requiring that substantial portions of

the fault, while having large slips, radiated little 5-25 sec energy. Two regions of the fault, one near the epicenter south of San Francisco, and one between Point Reyes and Fort Ross were responsible for generating the greater part of the energy observed on the teleseismic recordings. By comparison of our model for 1906 with modern, well-studied, large strike-slip events, we found similarities in rupture style with the relatively simple 1990 Philippines earthquake ($M_S = 7.8$), but contrasts with the complexity of the 1976 Guatemala earthquake ($M_S = 7.5$).

The rupture characteristics of these events when analyzed with previous finite-fault studies over the past decade indicate several common features. Variations in slip are more pronounced along strike than downdip. Vertical strike-slip faults show a systematic slip variation with depth, consistent with both shallow and deep zones with velocity-strengthening frictional resistance; nucleation is usually at the base of the seismogenic zone. Oblique and dip-slip events show much more depth variation in slip, indicative of thicker, more complex seismogenic zones associated with tectonic regimes involving crustal thickening or extension. The Superstition Hills, Loma Prieta and Sierra Madre strong-motion data sets all require short rise times, so only a small portion of the fault is slipping at a particular time, in agreement with the "self-healing" model described by Heaton [1990] and in conflict with long slip durations required by many crack-like models of dynamic rupture. With the exception of the Superstition Hills earthquake, seismic moments and slip distributions determined from the strong-motion data concur with moments and slips derived from geodetic and longer-period waveforms. This indicates that the higher-frequency data are sufficient for estimating the total slip, and therefore, the rupture durations

inferred represent the entire coseismic slip duration. The agreement between long- and short-period source models makes it possible to estimate ground motions for important historical events from source models determined using longer-period (5-15 sec), teleseismic body waves.

Table of Contents

List of Tables

List of Figures

Chapter 1

General Introduction

1.1 Objective and Motivation

Over the past decade, strong-motion, finite-fault rupture models, or slip-distribution models, have provided insight into the spatial and temporal details of the earthquake rupture process. With each additional well-recorded, moderate-to-large-sized crustal earthquake, we can not only determine the rupture characteristics unique to that event, but can now compare and contrast new results with those from other well-studied events in our growing database. In this dissertation, we present the analysis and results of four source studies for significant California earthquakes and add these results to our current catalogue of well-studied earthquakes. The methodology employed is a constrained, damped, least-squares inversion of waveform data for retrieval of the faulting history [Hartzell and Heaton, 1983].

The motivation for the type of finite-fault source study contained in the subsequent chapters is twofold. First, analysis of this recently enlarged set of source models provides an understanding of the consistencies and variations of rupture kinematics and dynamics from event to event. Only with an abundant data set can we make generalizations and draw robust conclusions about the physical source processes which

we are analyzing. Second, the ability to predict strong motions accurately enough for the purposes of hazard assessments and ground-motion site evaluation requires a sufficiently detailed characterization of both spatial and temporal fault-slip variations. These studies supply the basic source information necessary for such deterministic ground-motion estimates.

Finite-fault source studies have provided information beneficial to a wide range of seismological investigations and earthquake engineering applications. For example, from the analysis of seven finite-fault earthquake models, Heaton [1990] found that the slip duration at any given point on the fault, the dislocation rise time, is short relative to the total rupture duration. As pointed out by Heaton [1990], the requirement that only a small portion of the fault is slipping at one time, or "self-healing," has important implications for the underlying source dynamics. Mendoza and Hartzell [1988b] summarized several slip-distribution models and noted that large gaps in aftershock patterns often signify the regions that provide most of the energy release during the mainshock. They attributed the aftershock patterns to a secondary redistribution of stress following primary failure on the fault.

Quin [1990] used Archuleta's [1984] forward-rupture model for the 1979 Imperial Valley earthquake to convert the distribution of kinematic-slip parameters into estimates of the dynamic rupture processes using a Monte Carlo technique. Similarly, Miyatake [1992] also used Archuleta's [1984] slip model to reconstruct the dynamic rupture process using a propagating crack model. Miyatake [1992] obtained the stress distribution from the slip distribution, and by making the assumption that the static stress drop is nearly equal to dynamic stress drop, he retrieved the strength excess at each point on the fault. Recent work by Spudich [1992] suggests that it may also be possible to retrieve absolute stress values from those finite-fault models that indicate significant slip vector rotations at a given point on the fault.

In addition, the variations in slip as a function of depth in the Imperial Valley

provided constraints for Marone *et al.* [1991] for their proposed model of earthquake afterslip. They attributed afterslip to the interaction of a shallow region having velocity-strengthening, frictional behavior with a deeper, seismogenic region in which velocity-weakening was dominant. They found their model to be consistent with the slip distribution obtained for the 1987 Superstition Hills earthquake (Chapter 2).

A further use of slip-distribution models comes from the work of Michael and Eberhart-Phillips [1991], in which earthquake slip amplitudes are related to the static fault properties, particularly the compressional-wave velocity. They found that regions of high slip as determined from finite-fault rupture models appear to correlate with high seismic velocities and that rupture initiation or termination is associated with lower seismic velocities.

Source models have also provided improvements in the ability to characterize and predict damaging ground motions near large earthquakes. Well-determined slip-distribution models that have shown satisfactory fits to the observed strong motions can be used to estimate ground motions for hypothetical events by varying the deterministic source parameters. This is especially useful for earthquake scenarios not yet covered by empirical data sets (including sites near large earthquakes and regions that have no strong-motion observations). The deterministic parameters may include fault geometry, overall dimensions and amount of slip, as well as the geographic and geologic setting of the event. As an example, in Chapter 3 of this thesis, the slip-distribution model of the relatively deep, oblique-slip Loma Prieta rupture was transferred to a shallower, vertical strike-slip rupture consistent with an expected rupture along the San Andreas Fault. In this way, ground-motion variations attributable to source depth and faulting mechanism were examined.

Similarly, Saikia [1992], using the model of slip determined for the 1989 Loma Prieta earthquake (Chapter 3), simulated ground motions in Los Angeles that were due to a large hypothesized earthquake on the Elysian thrust fault zone, comparable

in size to the Loma Prieta event (M_s = 7.1). Using a semi-empirical simulation approach, Saikia produced attenuation relations for peak ground accelerations for the region, which lacks the sufficient recorded data in this magnitude range to constrain empirically the attenuation with distance.

1.2 Overview of the Thesis

The main body of the thesis is divided into five chapters. In Chapters 2 through 5, we discuss the results of analysis of four California earthquakes. The events are addressed in chronological order, with the exception of the 1906 San Francisco earthquake, which is presented last. The earthquakes are the 1987 Superstition Hills earthquake (Chapter 2), the 1989 Loma Prieta earthquake (Chapter 3), the 1991 Sierra Madre earthquake (Chapter 4) and lastly, the 1906 San Francisco earthquake (Chapter 5). The methodology employed is a constrained, damped, least-squares inversion of waveform data for retrieval of the faulting history [Hartzell and Heaton, 1983]. The historic data set from the 1906 San Francisco earthquake requires a different approach (empirical Green's function summation), which will be discussed in Chapter 5. In each of these chapters, the features of each waveform data set that drive the solution or control the final faulting model will be fully described.

While discussing these different events, emphasis will be placed on two basic questions. First, can we quantify the variations in complexity of the ruptures, and what are the implications of rupture complexity and heterogeneous slip for models of rupture dynamics and earthquake occurrence? Second, what is the connection between long (3-30 sec) and short periods (5 sec-10 Hz)? In particular, does the rupture process as viewed from (longer-period) teleseismic data contain information about the radiation at high frequencies in the near-field, which are responsible for most damaging ground motions?

Considering that there is much more long-period teleseismic data available for large earthquakes than strong-motion data, it is useful to know the extent and limitations of extracting source information from longer-period data in order to constrain the nature of higher-frequency fault radiation. As an example, for the 1906 San Francisco earthquake, one of the most important earthquakes for assessing damage potential in northern California, the only respectable waveform data are long-period teleseismic data, and we need to know whether we can extract source information relevant to estimating higher-frequency (damaging), strong ground motions that occurred and that will occur in the future.

After discussing the source modeling of these four earthquakes, the overall features and commonalities will be summarized in Chapter 6, and more general conclusions will be drawn in an effort to address the two questions above. These conclusions are based on the results of the above studies described herein, combined with other finite-fault source models contained in the recent geophysical literature.

Each of Chapters 2 through 5 has been published, or has been submitted for publication as a separate research paper. As such, each chapter is intended to be self-contained, complete with an abstract, methodology, results and conclusions. Although admittedly, this results in slight redundancy in some aspects, it obviates the need to cross-reference different chapters for each earthquake studied. For reference, Chapter 2 was published as "Rupture process of the 1987 Superstitions Hills earthquake from the inversion of strong motion data," in *Bull. Seism. Soc. Am.*, **80**, 1079-1098, 1990. An interesting exchange of views concerning the extent of the coseismic rupture during the Superstition Hills earthquake followed that publication, and exists as a "Comment" by A. Frankel and a "Reply" by Wald *et al.* in the *Bull. Seism. Soc. Am.*, **82**, 1511-1533, 1992. Chapter 3 can be found in an abbreviated form as "Rupture model of the 1989 Loma Prieta earthquake from the inversion of strong motion and broadband teleseismic data," in *Bull. Seism. Soc. Am.*, **81**,

1540-1572, 1991, and will appear in its entirety as "Strong-motion and broadband teleseismic analysis of the 1989 Loma Prieta earthquake for rupture process and hazards assessment" in the *Main Shock Characteristics* chapter of the upcoming *U.S.G.S. Professional Paper* devoted solely to the Loma Prieta earthquake. Chapter 4 will appear as "Strong-motion and broadband teleseismic analysis of the 1991 Sierra Madre, California, earthquake," in *J. Geophys. Res.*, **97**, 11,033-11,046, 1992. Chapter 5 has been submitted for publication and is in review.

Chapter 2

The 1987 Superstition Hills Earthquake

2.1 Abstract

A pair of significant earthquakes occurred on conjugate faults in the western Imperial Valley involving the through-going Superstition Hills fault and the Elmore Ranch cross fault. The first event was located on the Elmore Ranch fault, $M_S = 6.2$, and the larger event on the Superstition Hills fault, $M_S = 6.6$. The latter event is seen as a doublet teleseismically with the amplitudes in the ratio of 1:2 and delayed by about 8 sec. This 8-sec delay is also seen in about a dozen strong-motion records. These strong-motion records are used in a constrained, least-squares inversion scheme to determine the distribution of slip on a two-dimensional fault. Upon closer examination, the first of the doublets was found to be itself complex, requiring two episodes of slip. Thus, the rupture model was allowed to have three separate subevents, treated as separate ruptures, with independent locations and start times. The best fits were obtained when all three events initiated at the northwestern end of the fault near the intersection of the cross fault. Their respective delays are 2.1 and 8.6 sec relative to the first subevent, and their moments are 0.4, 0.8 and 4.0 x 10^{25} dyne-cm, about half of that seen teleseismically. This slip distribution suggests

multirupturing of a single asperity with stress drops of 60, 200 and 15 bars, respectively. The first two subevents were confined to a small area around the epicenter, while the third propagated 18 km southwestward, compatible with the teleseismic and afterslip observations.

2.2 Introduction

The Superstition Hills earthquake sequence of November 24, 1987 occurred on the west side of the Imperial Valley of southern California; see Figure 2.1. These events took place on a fault system consisting of the northwest-trending Superstition Hills fault and the conjugate, northeast-trending Elmore Ranch fault. The first mainshock, the Elmore Ranch earthquake ($M_S = 6.2$, 0154 GMT), along with its aftershocks and a wide distribution of predominantly left-lateral surface faulting, defines a northeast trend that was associated with left-lateral faulting at depth. Twelve hours later a second mainshock, the Superstition Hills earthquake ($M_S = 6.6$, 1315 GMT), initiated at the intersection of the northeast and southwest trends and was accompanied by right-lateral surface rupture of the Superstition Hills fault. This larger event is at least a doublet as observed teleseismically, and it is the rupture properties of this event that we address in this study.

Permanent, strong-motion accelerographs in the epicentral region (Figure 2.1) augmented by the timely placement of two portable stations by Doug Given of the U.S.G.S. provide a valuable data set for investigating the rupture process. The complexity of the Superstition Hills earthquake rupture is revealed in the strong-motion records; see Figure 2.2. In general, the acceleration recordings exhibit unusually long durations and relatively large amplitudes compared to other events of this magnitude. Three distinct subevents are recognized on most of the station recordings as indicated by arrows. In this study we seek to explain the complexity of these

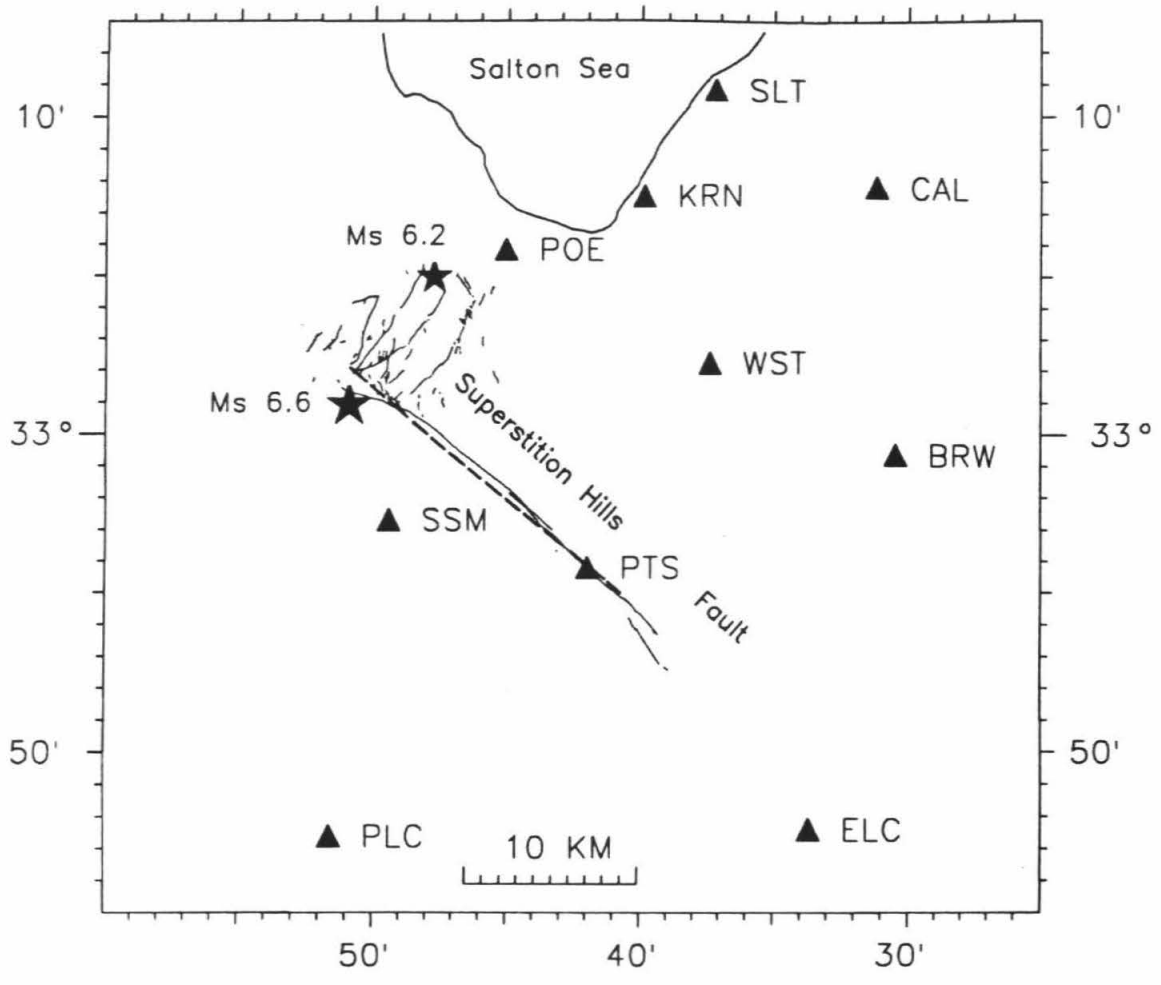

Figure 2.1: Location map showing strong ground-motion stations. Light lines show the extent of surface slip for both the Elmore Ranch and Superstition Hills earthquakes (epicenters are shown by asterisks). Temporary stations POE and KRN were put in place after the Elmore Ranch earthquake. The dashed line represents the fault segment used in the strong-motion inversion.

strong-motion observations by determining the fault rupture history and slip distribution. We employ the finite-fault waveform inversion procedure of Hartzell and Heaton [1983]. This analysis allows us to describe both the temporal and spatial distribution of slip on the fault and to attribute peak ground-motion arrivals to specific regions of concentrated dislocation.

In an earlier study of the strong-motion records, Frankel and Wennerberg [1989] presented a rupture model for this earthquake derived from a tomographic source inversion of the strong-motion velocity recordings. An advantage of their tomographic inversion is that it requires no *a priori* assumption about each subevent location, rupture time and rupture velocity. Their results present estimates of the timing, location, spatial extent, and rupture velocity for the three principal subevents for this earthquake, thus providing a useful starting point for this study. In their methodology, however, in order to invert the velocity seismograms for the slip acceleration as a function of time and yet limit the number of unknowns, a 1-D model fault model was used. Further, Green's functions were represented by a delta function with amplitudes approximated by the effects of propagation, radiation pattern and geometric spreading. In the present study, we represent faulting on a 2-D planar surface and employ Green's functions complete up to the frequency of 3 Hz, which includes the frequency band usually found adequately stable for this type of inversion [Hartzell and Heaton, 1983]. Although the linear inversion employed in this study does require an *a priori* estimate of the average rupture velocity, source-nucleation point and subevent-delay time, these values can be varied in subsequent runs over a reasonable range to recover the model parameters that are most consistent with the observations. This aspect of the inversion procedure will be discussed further.

An important question we address is the inconsistency between local and teleseismic models of this earthquake. Results of Frankel and Wennerberg [1989] suggest that high-frequency radiation is limited in spatial extent to the northern section of

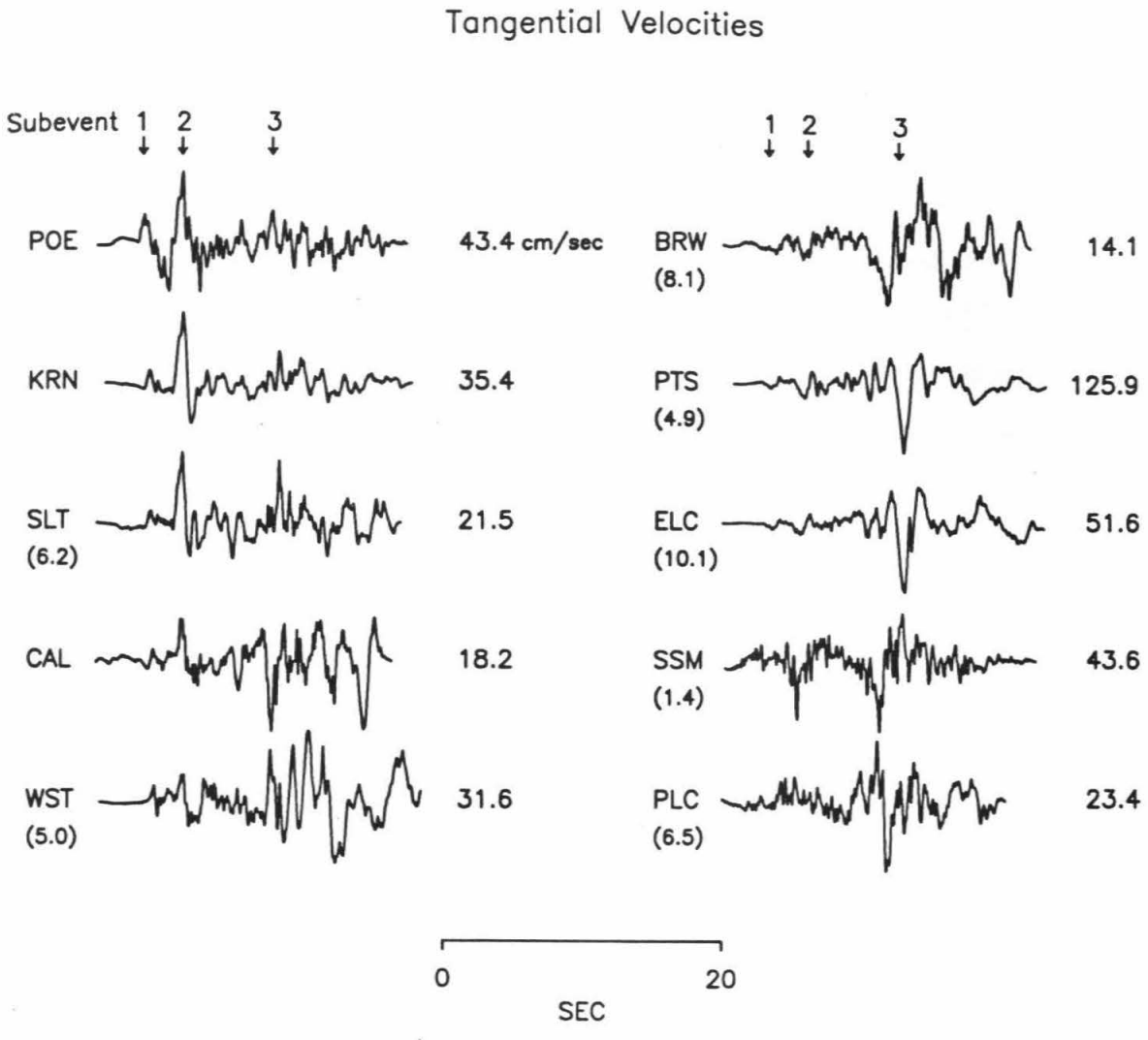

Figure 2.2: Tangential velocity recordings of the Superstition Hills earthquake obtained by rotating horizontal components to the back azimuth of the epicenter. Arrows indicate the approximate times of the three subevents. All traces are normalized to their peak value and are aligned vertically by the peak arrival of subevent 2. The time in seconds of the beginning of each trace after the origin time (1315:56.5 GMT) is given in parentheses below each record for which absolute time is available.

the Superstition Hills fault. This region is northwest of the fault stepover seen in Figure 2.1, 5 km northwest of station PTS. However, teleseismic studies that address the spatial distribution of the longer-period energy release [Bent *et al.*, 1989; Hwang *et al.*, 1990] require greater than 10 to 15 km of separation between the earlier subevents (subevents 1 and 2 as observed on the strong ground motions) and the later subevent (subevent 3 at local stations). These long-period and short-period results are mutually exclusive because subevent 3 of Frankel and Wennerberg [1989] is temporally correlated with the later teleseismic arrivals. That is, for both the local and teleseismic models to be correct, there would have to be rupture occurring simultaneously at two separate portions of the fault, one generating only short-period energy (northern portion of the fault), and the other only long-period energy (southern section of the fault). We attempt to resolve this issue.

The methodology we employ has been previously shown to provide valuable insight into the rupture history of other California earthquakes [Heaton, 1982; Hartzell and Heaton, 1983; Hartzell and Heaton, 1986; Mendoza and Hartzell, 1988a], as have other finite fault approaches [Olson and Apsel, 1982; Archuleta, 1984]. In addition to providing information on the details of each rupture, these studies provide information about the characteristics common to these events. Mendoza and Hartzell [1988b] summarized these slip-distribution models to note that large gaps in aftershock patterns often signify the regions that provide most of the energy release. From the distribution of slip, we can also place constraints on the location and depth extent of significant energy release and can characterize the local stress drop of individual subevents. In this investigation we add to the collection of earthquakes that were sufficiently well recorded to retrieve this type of source information. Our results provide an estimate of the spatial and temporal distribution of slip that will enhance such studies as cross-fault interaction [Hudnut *et al.*, 1989] and fault segmentation [Rymer, 1989] of the Superstition Hills earthquake sequence.

ID	Station	Components	Latitude	Longitude
POE	Poe Road	270,360	33.097	115.751
SLT	Salton Sea Wildlife Refuge	315	33.18	115.62
SSM	Superstition Mtn.	45,135	32.955	115.823
WST	Westmoreland Fire Station	90,180	33.037	115.623
ELC	El Centro Imperial Valley County Center	0,90	32.793	115.562
PTS	Parachute Test Site	225	32.93	115.70
KRN	Kornbloom Road	270,360	33.125	115.665
BRW	Brawley Airport	315	32.988	115.50
CAL	Calipatria Fire	315	33.13	115.52
PLC	Plaster City		32.79	115.86

Table 2.1: Strong-motion stations.

2.3 Data and Initial Analysis

The locations of the strong-motion stations used in this study are displayed in Figure 2.1 as discussed earlier. The strong-motion station abbreviations used in Figure 2.1, the station locations, and the components used in the inversion are given in Table 2.1. Also depicted in Figure 2.1 is the extent of surface faulting associated with these two events [Sharp *et al.*, 1989]. Accelerograms were hand-digitized from copies of the U.S.G.S. records [Porcella *et al.*, 1988] and were provided in digitized form by the C.D.M.G. [Huang et al, 1987] for stations Westmorland (WST) and El Centro (ELC). We concentrate primarily on the horizontal strong-motion records of the Superstition Hills earthquake for the following reasons. The strong velocity increase with depth in the Imperial Valley results in arrivals predominantly at near vertical incidence, thus isolating P waves on the vertical and S waves on the horizontal components. Consequently, the vertical components of motion are, in general, higher in frequency and smaller in amplitude and are therefore more difficult to hand digitize accurately as well as model (given our limited knowledge of the local velocity structure and constraints on computer time). Further, because of the difficulty in modeling high frequencies, velocity records rather than acceleration records are used in the inversion. The velocity records, obtained by integrating the acceleration recordings, are shown in a profile in Figure 2.2. For display purposes the records in Figure 2.2 have been aligned in time on the peak motion of subevent 2, the easiest arrival to recognize at all stations, and have been rotated to the back azimuth of the epicenter to obtain "tangential" components. While this rotation is correct for the energy originating near the epicenter, it is only approximate for source regions farther southeast along the fault.

Three subevents can be traced from station to station. A very good detailed analysis of these subevents has been provided by Frankel and Wennerberg [1989], and here we review some of the features they discuss and bring out additional observations

critical to our study. It can be seen that the time separation between the first two subevents shows little variation. The consistency of the 2-sec time separation at stations covering a wide range of azimuths requires a common source region with a limited extent and separate ruptures for these two subevents. The third subevent shows more variation with azimuth, suggesting a more extended rupture zone. As this subevent is delayed at least 6 sec from the seconds and yet begins rupturing near the other two subevents [Frankel and Wennerberg, 1989], it too requires a separate rupture initiation.

A most interesting feature of the observed velocity recordings is the apparent variation of directivity effects from subevents 2 and 3, most pronounced at stations directly towards the northeast (POE, KRN and SLT) and southeast (PTS, ELC). This observation is examined in the tangential records shown in Figure 2.3. On the left-hand side of this figure, the records are normalized to their peak values, while the waveforms on the right are all scaled to the peak amplitude of station PTS. With the exception of those stations directly towards the northeast, subevent 3 produces the dominant arrival at each station and provides the peak-velocity amplitude. This is consistent with teleseismic modeling results [Bent *et al.*, 1989; Hwang *et al.*, 1990] which show that on average, the seismic moment computed for the third subevent is roughly twice that of the combined first and second subevents. In sharp contrast, the northeastward stations are dominated by arrivals produced by subevent 2 and show less prominent arrivals because of the third subevent. However, from the right side of the figure, it can be seen that the absolute amplitude of the second subevent is comparable in both directions if one compares stations at similar distances, that is PTS is between POE and KRN in terms of distance from subevent 2. These observations can be explained by a spatially compact subevent 2, which produces no significant directivity and a large southeastward rupture for the third subevent, producing strong directivity effects in that direction. This is further substantiated

by the uniformity of the pulse width of subevent two at all stations, which is approximately 2 sec, and the variation of the total duration of subevent 3, which is from 3 sec at PTS to over 8 sec at stations towards the northeast.

The location of the initial rupture plays an important role in the inversion scheme. This poses a difficulty in that there is a discrepancy between the reported hypocentral depth (2 km) determined from the regional network data [Magistrale *et al.*, 1989] and the greater depths determined for the first subevents from waveform modeling (9 km from Frankel and Wennerberg, 1989; 10 km, Bent *et al.* 1989; 5 km, Hwang *et al.*, 1990]. Careful inspection of the strong-motion accelerograms for the closest stations shows a clear shear-wave arrival approximately 1.0 to 1.5 sec before the onset of subevent 1. This suggests that the shallow 2 km network, hypocentral depth may represent an earlier, small preshock, as suggested by Bent *et al.* 1989. The simplicity of the shear-wave arrivals for the first two subevents allowed Frankel and Wennerberg [1989] to estimate their common location near the epicenter, but closer to the intersection of the two fault zones (Figure 2.1). Although the depth determination for these subevents is not well constrained, synthetic seismograms computed for depths shallower than about 6 km show much more complexity than the subevent 1 and 2 observed waveforms. Furthermore, Bent *et al.* [1989] found that a shallow rupture was inconsistent with the surface waves observed at the Pasadena station (PAS, about 250 km northwest of the epicenter). We therefore adopt the depth of 9 km as chosen by Frankel and Wennerberg [1989], for our rupture initiation, although we later test deviations from this value. The initiation of subevent 3 is not impulsive at most stations and therefore could not be located from arrival times alone. The nucleation point of the third subevent was assumed to be at the same location of subevent 1 and 2, again based on Frankel and Wennerberg [1989], and it, too, was allowed to vary in subsequent forward models.

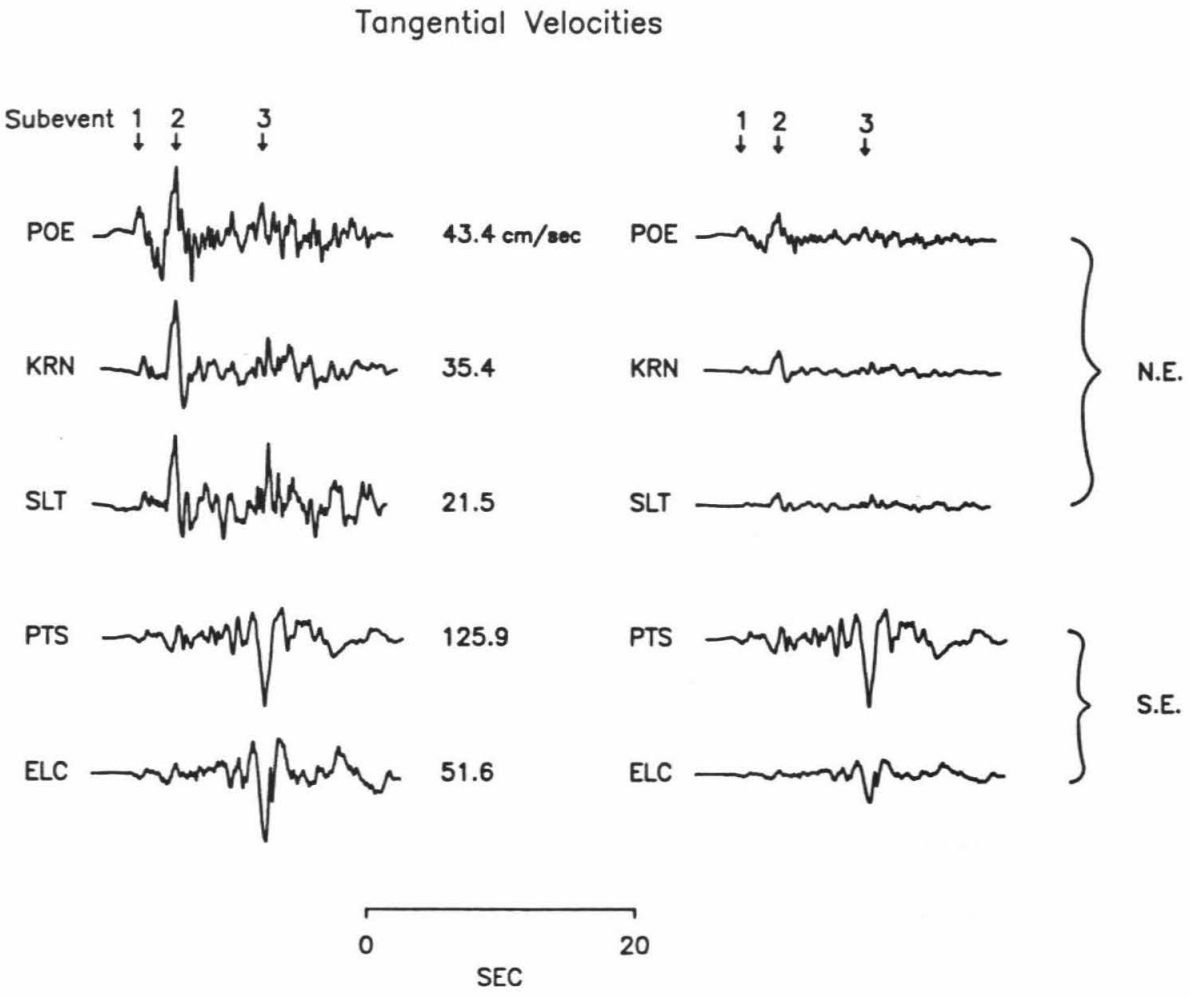

Figure 2.3: Comparison of tangential velocity recordings from stations at northeast (POE, KRN, SLT) and southeast (PTS, ELC) azimuths. The records on the left-hand side are normalized to their peak values. The waveforms on the right are scaled to the peak amplitude of station PTS.

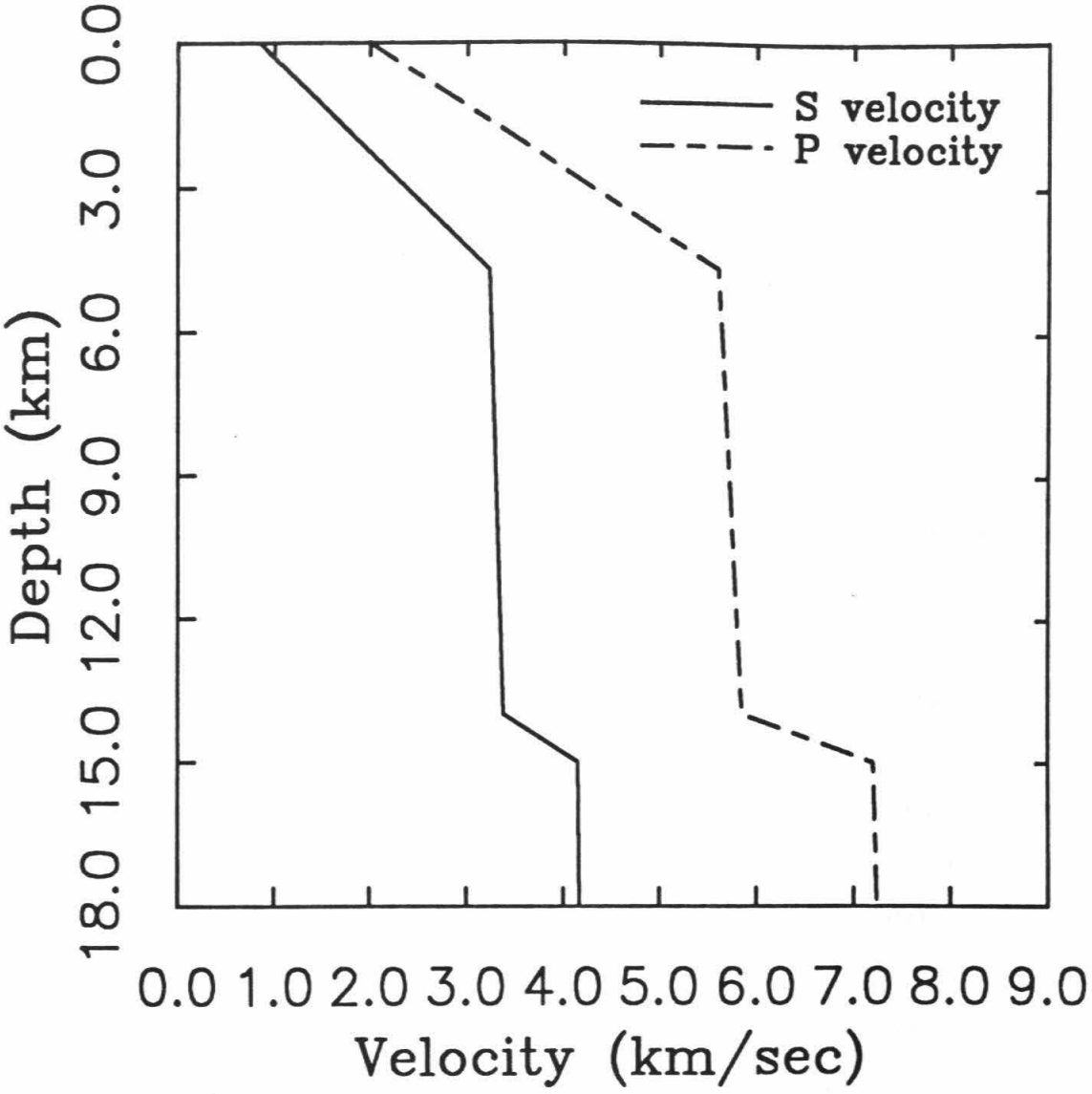

Figure 2.4: Velocity structure used to compute strong-motion synthetics. This model was derived from Fuis *et al.* [1982]. See text for details.

2.4 Fault Rupture Model and Inversion Method

The fault parameterization and modeling procedure we employ is that of Hartzell and Heaton [1983] in their study of the 1979 Imperial Valley earthquake. Faulting is represented as slip on a planar surface, which is discretized into a number of subfaults. The total ground motion computed at a given station can be represented as a linear sum of the contributions of all the subfault elements, each appropriately delayed in time to simulate propagation of the rupture front. Formal inversion procedures are then used to deduce the slip distribution on these subfaults that minimizes the difference between the observed and the synthetic strong motions.

In this study we represent the Superstition Hills earthquake rupture with a vertical fault plane, striking 127°. Previous studies of the teleseismic recordings [Bent *et al.*, 1989; Hwang *et al.*, 1990; Sipkin, 1989; and Dziewonski, *et al.*, 1989] indicate some uncertainty in the dip value but on average suggest a near-vertical fault. These studies indicate little scatter in the fault strike. We also assume only right-lateral, strike-slip motion is significant. The small vertical component of slip and the numerous reversals of northeastward and southwestward scarp directions observed along the surface trace [Sharp *et al.*, 1989] suggest predominantly right-lateral motion on a vertical fault plane. We therefore assume that a vertical fault is the best fault plane representation of the greater part of the moment release. We chose a fault length of 20 km and depth extent of 12 km based on the distribution of aftershocks [Magistrale *et al.*, 1989] with additional constraint on the length by the extent of surface faulting (see Figure 2.1). This area is then discretized into 20 subfault elements along strike and 10 elements downdip, giving each subfault a length of 1 km and a vertical width of 1.15 km.

The ground-motion contribution for each subfault is computed using the Green's function summation and interpolation method of Heaton [1982] and Hartzell and Helmberger [1982]. The subfault synthetics are obtained by summing the responses

of a number of point sources over its area, each delayed in time in order to account for the propagation of the rupture front across the subfault. Thus, each subfault ground motion properly includes the effects of directivity. The point-source responses, or Green's functions, are computed for a gradient velocity model with the discrete wavenumber/finite element (DWFE) methodology of Olson *et al.* [1984] for frequencies up to 3.5 Hz. In practice, we calculate a master set of synthetics for increments of depths from 0.5 to 12 km and for ranges between 0 and 50 km, to allow for the closest and furthest possible subfault-station combinations. Then, for each subfault-station pair, the required subfault response is derived by the summation of 25 point-source responses obtained by the linear interpolation of the closest Green's functions available in the master set. The linear interpolation of adjacent Green's functions is performed by aligning the waveforms according to their shear-wave travel times.

The subfault synthetics are convolved with a dislocation-time history which we represent by the integral of a triangle with a total duration of 0.5 sec and equal rise and fall times. This time function was chosen based on a comparison of the synthetic velocity pulse width for a single subfault with the shortest duration velocity pulse width observed as well as on prior experience with this inversion method. Initially, we tried longer slip durations (0.7 and 0.8 sec), but found them to be inadequate.

The velocity model, shown in Figure 2.4, was chosen from the refraction study of Fuis *et al.* [1982] (Fig. 22, approximately 20 km southeast of shotpoint 13) to represent an average velocity structure for the station paths in this study. This model is clearly an approximation of the true structure. Fuis *et al.* [1982] show significant lateral velocity variations in this region, especially in the vicinity of the Superstition Hills fault, where buried basement scarps and changes of the thickness of sediment cover are evident. The variations in local depth to bedrock in relation to rupture on the Superstition Hills fault is discussed by Magistrale *et al.* [1989], Hwang *et al.*

[1990], and Frankel and Wennerberg [1989].

Although lateral velocity variations will not be incorporated in the present study, as an effort to minimize their effects, we introduce static-delay times in the waveform inversion procedure to account for travel-time differences. These corrections and the effects of complex, local, velocity structure will be discussed in the following section.

The rupture velocity is assumed to be a constant 2.4 km/sec, or 75% of the shear-wave velocity in the greater part of the source region (Figure 2.4). This parameter was varied to test its sensitivity in different inversion runs. Some flexibility in the rupture velocity is obtained by introducing time windows [Hartzell and Heaton, 1983]. In their representation, each subfault slips when the rupture front reaches it and again in two successive time windows, effectively allowing for the possibility of afterslip or a locally slower rupture velocity. In our formulation, we allow each subevent the flexibility of both a locally slower and faster rupture velocity by allowing slip during the time windows preceding and following that of the equivalent, constant-velocity rupture front. Each time window is separated by 0.5 sec.

A constrained, damped, least-squares inversion procedure is used to obtain the subfault-dislocation values that give the best fit to the strong-motion observations. The inversion is stabilized by requiring that the slip is everywhere positive and that the difference in dislocation between adjacent subfaults (during each time window) as well as the total moment is minimized. These constraints have been previously addressed by Hartzell and Heaton [1983].

Both the observations and subfault synthetics are bandpass-filtered from 0.1 to 3.0 Hz with a zero-phase, Butterworth filter and are resampled at a rate of 20 samples per sec. The upper frequency limit is imposed by the the frequency range for which Green's functions can be conveniently calculated. Resampling reduces the number of points required in the point-by-point inversion scheme. Initially the synthetic and observed waveforms are aligned in absolute time when possible (trigger times

were not available for stations CAL, KRN, POE) and are then later adjusted for variations in travel time by aligning the initial shear-wave arrival from subevent 1 with the synthetic shear-wave energy from the subfault containing the initiation of rupture (hypocenter). While this provides an approximate, static-station delay, it will not improve timing errors introduced by lateral variations encountered by subfault-to-station travel paths that vary significantly along the fault.

Station PLC is not included because it is located in a region with a velocity profile significantly different from the average Imperial Valley velocity model used here. Moreover, ray paths from the northwest portion of the fault to PLC traverse a different velocity structure than from the southeast section. A similar argument may be made for station SSM, which sits atop a bedrock nob, but since this site is so close to the fault, energy arriving at this station travels a near-vertical path and can therefore be more easily adjusted with a static correction. All station observations are scaled to a unit amplitude in the inversion in order to insure equal importance of smaller amplitude stations and to downweight possible site effects. Although each station can be individually weighted to adjust for noisier records, all components were weighted equally.

2.5 Inversion Results

The distribution of strike-slip dislocation for each subevent resulting from our preferred rupture model (No. 307) of the Superstition Hills earthquake is shown in Figure 2.5. Slip contours are in intervals of 40 cm, with the maximum value for each subevent indicated in the figure. The large contour interval is used to emphasize robust features in the model and to minimize the importance of smaller details. These dislocations represent the combined slip for the three time windows previously mentioned. This series of subevents can be regarded as a magnitude 5.6 earthquake

Figure 2.5: Northwest-southeast cross section of the fault model showing subfault layout. Contours of strike-slip dislocation in centimeters for model No. 307 are given for each subevent. The contour interval is 40 centimeters. The peak-slip value for each subevent is indicated.

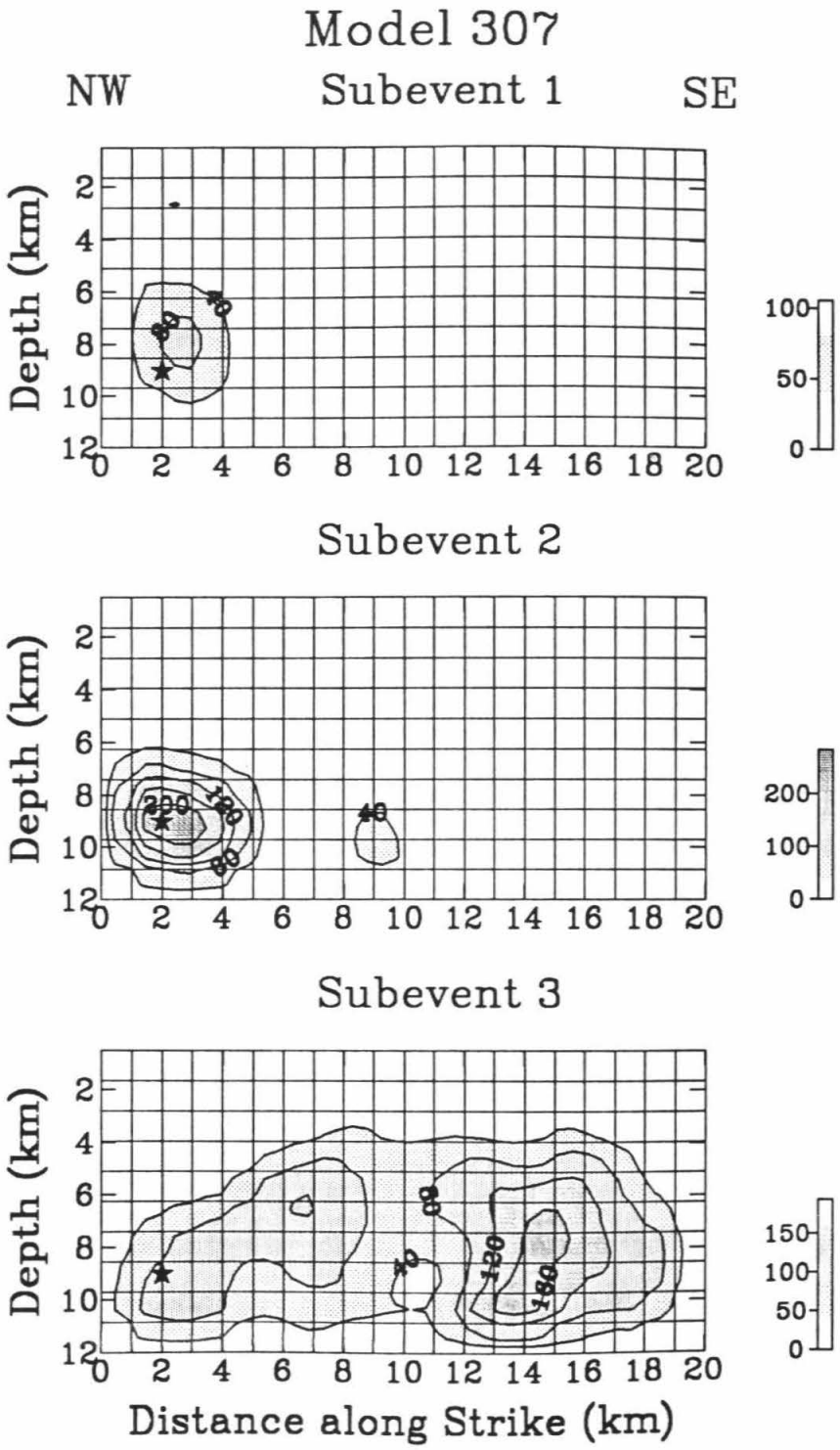
Model 307
NW
Subevent 1
SE
Depth (km)
2
4
6
8
10
12
0 2 4 6 8 10 12 14 16 18 20
100
50
0
Subevent 2
Depth (km)
200
100
0
Subevent 3
Depth (km)
150
100
50
0
Distance along Strike (km)

followed 2.1 sec later by a larger, higher stress-drop event of magnitude 6.0. Finally, after 8.6 sec, the same region ruptured a third time, resulting in a magnitude 6.4 event that continued to rupture over a length of 18 km with considerable slip on the southern section of the Superstition Hills fault. A comparison of the observed velocity records and the synthetic waveforms produced by this model is shown in Figure 2.6.

An attempt was made to determine the most favorable location for the nucleation point of subevent 3. From the small, concentrated rupture area of subevent 2, it seemed reasonable that further slip during the subsequent subevent 3 might have initiated at the southeast edge of the zone that ruptured during subevent 2. However, this assumption gave results inferior to the model in which subevent 3 initiated at the location of the previous subevents. The rupture velocity of our preferred model is 2.4 km/sec. We also modeled faster rupture velocities for both subevent 2 and subevent 3 to evaluate the waveform fits and the resulting slip distribution. Allowing a rupture velocity of 4 km/sec for subevent 2, approaching the 5.3 km/sec value suggested by Frankel and Wennerberg [1989], does not improve our model. Similarly, a rupture velocity of 2.7 km/sec (85% of the local shear velocity) for the third subevent increases the misfit between the observations and the synthetics.

In an effort to resolve an interesting question of whether the first two subevents may have ruptured northeastward [Wald and Somerville, 1988; Frankel and Wennerberg, 1989], we ran an inversion in which rupture begins 2 km from the northwest end of the inferred Superstition Hills fault plane (Figure 2.1) and propagates towards the northeast for both subevents 1 and 2. The resulting slip model produces synthetics with slightly better waveform fits to stations POE, KRN and SLT, but which overpredict the observed subevent 2 amplitudes at these stations. The improvement in waveform fit is partially due to slip occurring on subfaults nearer to those stations, allowing more free-model parameters with which to fit the observations. However,

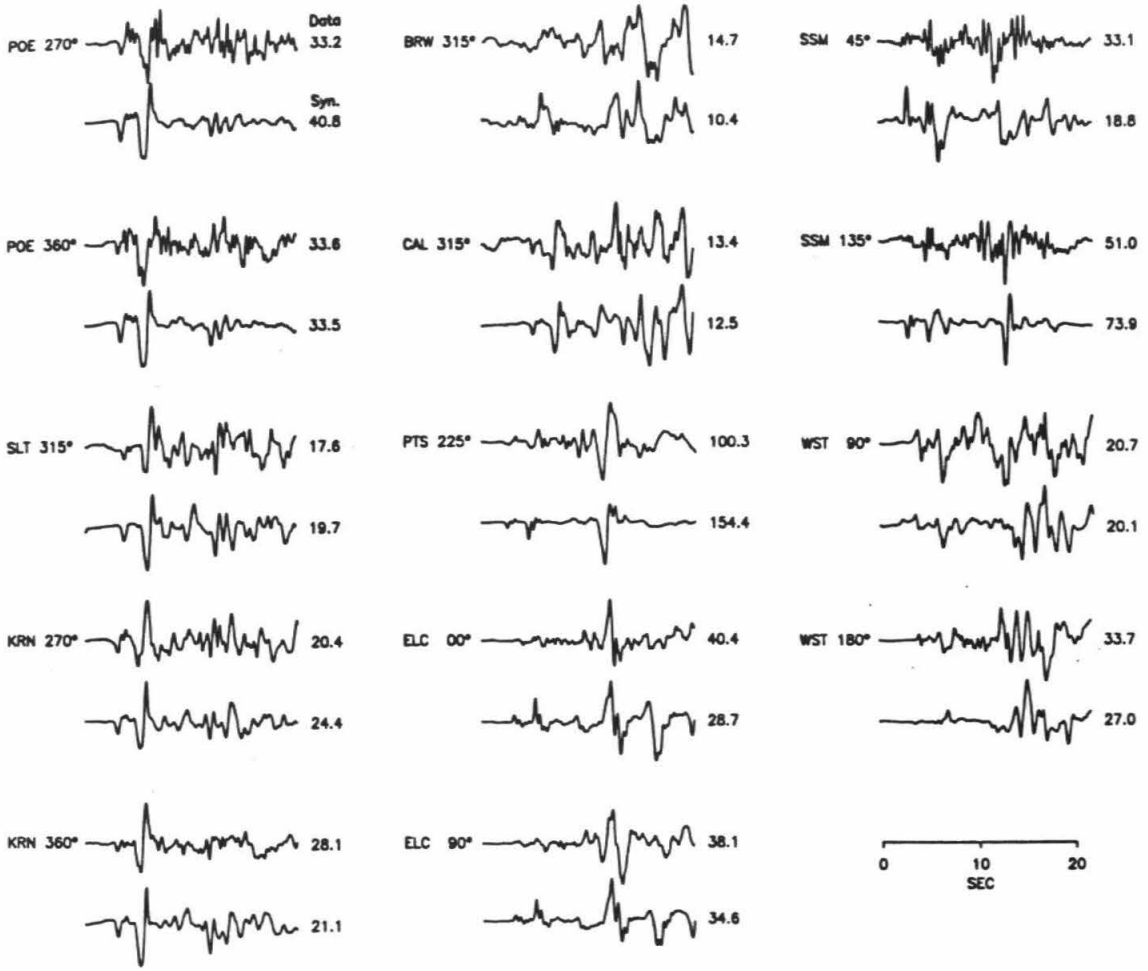

Figure 2.6: Comparison of the observed (top trace) and synthetic (bottom trace) strong-motion velocity records for dislocation model No. 307 (shown in Figure 2.5). Amplitudes are in cm/sec

this model substantially underpredicts the subevent 2 amplitude at SSM, a result also seen in Frankel and Wennerberg's [1989] model for northeast rupture. The absence of aftershocks from the Superstition Hills earthquake along the northeast trend tends to further downplay the possibility of slip on the scale required by subevent 2 [Frankel and Wennerberg, 1989].

Although 3 separate time windows were allowed for each subevent, slip occurred during only the first 0.5-sec window for the first two subevents, implying that the rupture timing of these smaller subevents was adequately modeled with a constant rupture velocity and that the true source-time-function can be adequately simulated with a simple triangle. For the third subevent, significant slip occurred in the first two time windows and minor dislocation during the third window, although almost all subfaults individually had slip in only one of the available time windows (Figure 2.7). This observation suggests that although the slip function for the third subevent can be modeled with a relatively simple time function, the rupture velocity was variable. Rupture on the northern section of the Superstition Hills fault required a velocity slightly slower than the constant value of 2.4 km/sec chosen for the model (Figure 2.7, time window 1), while rupture on the southern section of the fault required a rupture velocity close to the constant value (Figure 2.7, time window 2). The spatial variation in the rupture velocity appears to coincide with a right step-over observed at the surface of the Superstition Hills fault (Figure 2.1). This step-over also delimits a change from northwest to southeast in the physical behavior of fault. At this location there is a change in the depth to basement rock along the fault and a corresponding change in the behavior of the seismicity [Magistrale *et al.*, 1989].

An additional explanation for the necessity of the time windows for the last subevent may be that its extended rupture into the southern section of the Superstitions Hills fault results in a more complex series of propagation paths to each station, creating timing errors in our 1-D Green's functions. This can be seen at ELC, where

Figure 2.7: Subevent 3 dislocations for three time windows 1 (top), 2 (middle) and 3 (bottom). Each time window is separated by 0.5 sec. The contour interval is 40 cm.

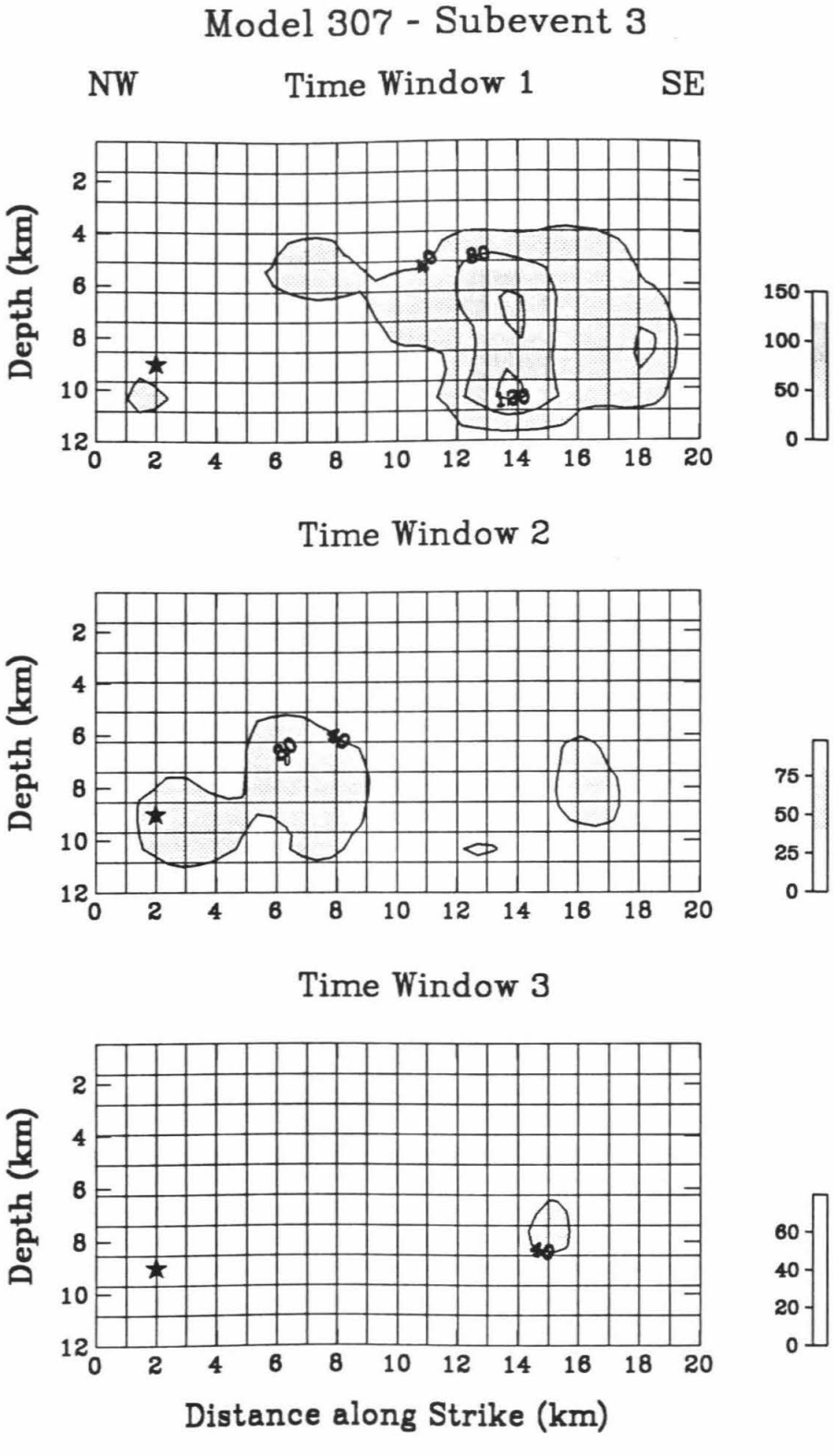
Model 307 - Subevent 3
NW
Time Window 1
SE
Depth (km)
2
4
6
8
10
12
0
2
4
6
8
10
12
14
16
18
20
80
120
150
100
50
0
Time Window 2
Depth (km)
30
75
50
25
0
Time Window 3
Depth (km)
60
40
20
0
Distance along Strike (km)

the synthetic phase *SS* arrives earlier than the corresponding observed phase, and at SSM, where the third subevent arrival on the 45° component arrives slightly late. Processed aftershock data from well-located events would greatly help resolve these discrepancies in timing. Perhaps then the effects of lateral velocity variations on the resulting slip distribution can be evaluated. Note that because of the complexity of the Superstition Hills earthquake there is always the possibility of a tradeoff between the subevent delay time and the location of the subevent nucleation and the rupture velocity. The multiple subevents of this earthquake, each being independent ruptures, make a unique solution difficult to obtain.

The time delay of 2.1 sec between subevents 1 and 2 along with their depths is well constrained. Minor modifications of these parameters result in degradation of the fits to the waveforms. Variations in the delay time between subevents 2 and 3, however, strongly affect the results of the slip distribution for the third subevent (Figure 2.8) without substantially degrading the waveform fits. A short delay (8.1 sec) for subevent 3 allows the rupture to propagate to the southern section of the fault (Figure 2.8, top). As the delay time increases to 8.6 sec, moment release is forced deeper (Figure 2.8, middle). Finally, if delayed by 9.1 sec, bottom of Figure 2.8, slip is forced closer to the point of rupture nucleation along the deep, northwest portion of the fault. In order to resolve the extent of high-frequency radiation toward the southern portion of the Superstition fault, we compare waveforms at selected stations (see Figure 2.9) that are the most sensitive to the subevent 3 slip distribution. This comparison is made for the inversion models shown in Figure 2.8. A summary of the inversion model parameters for different delay times is given in Table 2.2. The misfit between the data and the synthetics is given in terms of the Euclidean norm of the residual vector, ||b-Ax||, and the variance, defined as the square of the Euclidean norm divided by the number of degrees of freedom. The number of degrees of freedom is equal to N - 1, N being the number of data points in the inversion minus the number

Model	$\|$ b-Ax $\|$	Variance	Subevent	Time Lag (sec)	Moment ($x10^{25}$)	Max Slip (cm)
303	18.52	0.0605	1	0.0	0.40	94
			2	2.1	0.84	253
			3	8.1	3.95	241
307	18.78	0.0636	1	0.0	0.44	103
			2	2.1	0.91	270
			3	8.6	3.46	191
312	19.10	0.0654	1	0.0	0.51	121
			2	2.1	1.06	326
			3	9.1	3.00	215

Table 2.2: Inversion models and subevent parameters. Time lag refers to the time of each subevent rupture after initiation of subevent 1.

of nonzero model parameters in the solution. It can be seen from Table 2.2 that in terms of the Euclidean norm and the variance, the difference in waveform fits is not dramatic. Further, the Euclidean norm can be misleading when comparing waveforms dominated by a few large-amplitude arrivals. These factors suggest that other considerations be included in evaluating these models.

The shallow concentration of slip shown in model No. 303 (near 15 km) is not consistent with the lack of observed surface waves at the Pasadena station [Bent *et al.*, 1989, Figure 2] or the moderate level of surface waves at ELC. This shallow slip also overpredicts the peak amplitude at PTS and produces a larger synthetic *SS* phase at ELC (Figure 2.9, 2 sec from end of trace) than the observed phase. It should be noted that the *SS* phase at ELC in the synthetics is also earlier than

the observed phase, indicating that a laterally slowing velocity structure towards ELC may be more appropriate than the 1-D model used here. A longer delay of 8.6 sec (model No. 307 in Figure 2.8) for the start of subevent 3 yields a dislocation model more consistent with the surface-wave observations mentioned above, and has the effect of moderating both the *SS* phase at ELC and the PTS amplitude. Model No. 312 with the longest delay time shown, 9.1 sec, has slip concentrated closer to the rupture nucleation and further reduces the *SS* arrivals at ELC, but it underpredicts the subevent 3 amplitudes at these stations. This results in subevent 3 to subevent 2 amplitude ratios inconsistent with the observations. It also degrades the waveform fit at PTS considerably. From these considerations we favor the rupture model resulting from a delay time of 8.6 sec.

2.6 Discussion And Conclusions

A comparison of our preferred dislocation model (No. 307) with results of previous studies is presented in Figure 2.10 and summarized in Table 2.3. This figure is a northwest-southeast cross section along the Superstition Hills fault. Symbols in Figure 2.10 represent point sources, and line sources are denoted by boldface arrows. The strong-motion, line-source model favored by Frankel and Wennerberg [1989] is depicted as a solid circle leading into two overlapping arrows at a depth of 9 km. The solid circle represents their subevent 1; the circle up to the first arrow displays their subevent 2, starting about 2.5 sec later; and the circle up to the second arrow (to a distance of 10 km), starting 9.7 sec after the first subevent, represents their third subevent. The first two subevents in our model are nearly equivalent to those of Frankel and Wennerberg [1989], considering that the comparison is between one- and two-dimensional fault models. There is, however, a substantial difference in the two strong-motion solutions for the third subevent. While subevent 3 in the Frankel

Model	Subevent	Moment ($x10^{25}$ dyne-cm)	Depth (km)	Time Delay (sec)
Model No. 307	1	0.44	6-9	0.0
	2	0.91	8-10	2.1
	3	3.46	6-10	8.6
Frankel and Wenner. [1989]	2	0.47	9	2.5
	3	1.4	9	9.5
Hwang et al. [1990]	1+2	2.4	4	0.0
	3	5.2*	6	8.1 †
Bent et al. [1989]	1+2	3.6	10	0.0
	3	7.2	> 6	7.5 †
Sipkin [1989]	total	10.0	10	
Dziewonski et al. [1989]	total	7.2	15	

Table 2.3: Comparison of Superstition Hills model parameters. * Hwang et al. [1990] model No.1, 2 point sources. † Time separation with respect to the first teleseismic subevent, which is made up of two subevents, 1 and 2, as seen on the strong ground-motion recordings.

Figure 2.8: Comparison of subevent 3 dislocation models for delay times of 8.1 sec (top, model No. 303), 8.6 sec (middle, model No. 307) and 9.1 sec (bottom, model No. 312). The peak slip values are indicated in cm.

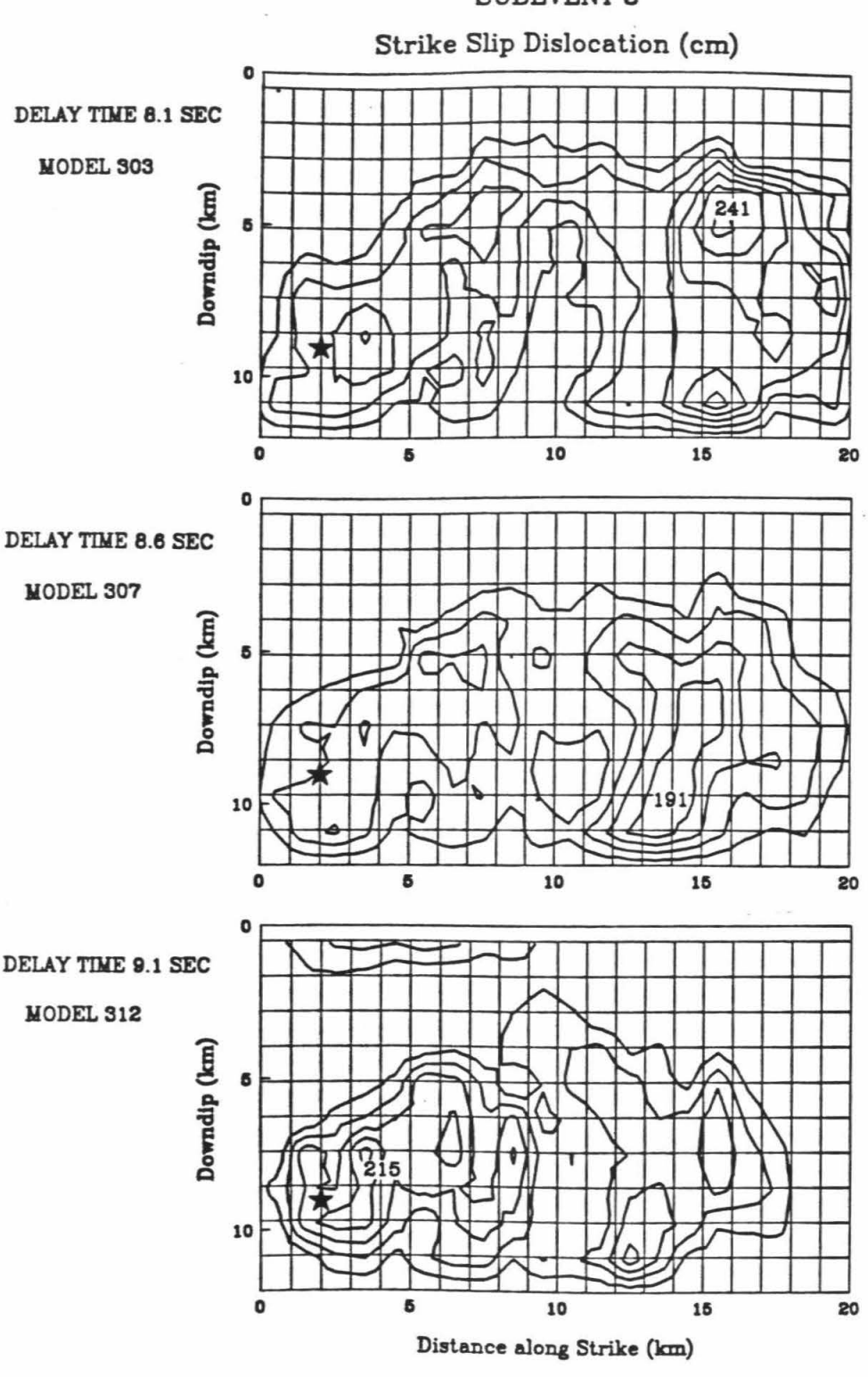
SUBEVENT 3
Strike Slip Dislocation (cm)
DELAY TIME 8.1 SEC
MODEL 303
241
DELAY TIME 8.6 SEC
MODEL 307
191
DELAY TIME 9.1 SEC
MODEL 312
215
Downdip (km)
0
5
10
15
20
Distance along Strike (km)

and Wennerberg [1989] model begins about 9.7 sec after the first subevent and is limited in rupture length to about 8 km, our solution indicates a rupture length of over 18 km delayed by 8.6 sec. Our solution is not so different, however, from the slip distribution presented by Frankel and Wennerberg [1989] for a line source at a depth of 5 km (their Figure 5). In fact, if one were to combine the slip acceleration of both the 5 and 9 km depth line sources depicted by Frankel and Wennerberg [1989] into a two-dimensional fault model, it is quite similar to the spatially extended subevent 3 we describe. Further note that our model No. 312, where we constrain the third subevent lag time to be 9.1 sec, is more limited in length. Model No. 312 is similar to the Frankel and Wennerberg [1989] model for a 9 km deep line source, but produces inferior waveform fits compared to model No. 307 and is further discounted for reasons that follow.

Of the teleseismic studies for this earthquake (Table 2.3), both Bent *et al.* [1989] and Hwang *et al.* [1990] attempt to resolve the spatial and temporal separation of moment release. The model of Bent *et al.*, [1989] is not represented in Figure 2.10, but includes 2 point sources separated in time by 7.5 sec. Their first subevent is located at a depth of 10 km, just below but within the location of our combined subevents 1 and 2. Their second subevent is greater than 6 km in depth and at a distance of more than 10 km from their first subevent. Similarly, Hwang *et al.* [1990] require significant source separations. They present two similar source models, a 2 point source model (large squares in Figure 2.10) and a point source-line source combination (large square and dashed, bold arrow). In both teleseismic models, the first point source is consistent with the combined subevent 1 and 2 sources in our model and in the Frankel and Wennerberg [1989] model, although their 5 km source depth is shallower. However, their rms error shows little change with depths up to 5 km deeper than their chosen depth, indicating that a greater source depth is also consistent with their data. As indicated in Figure 2.10, both the point-source and

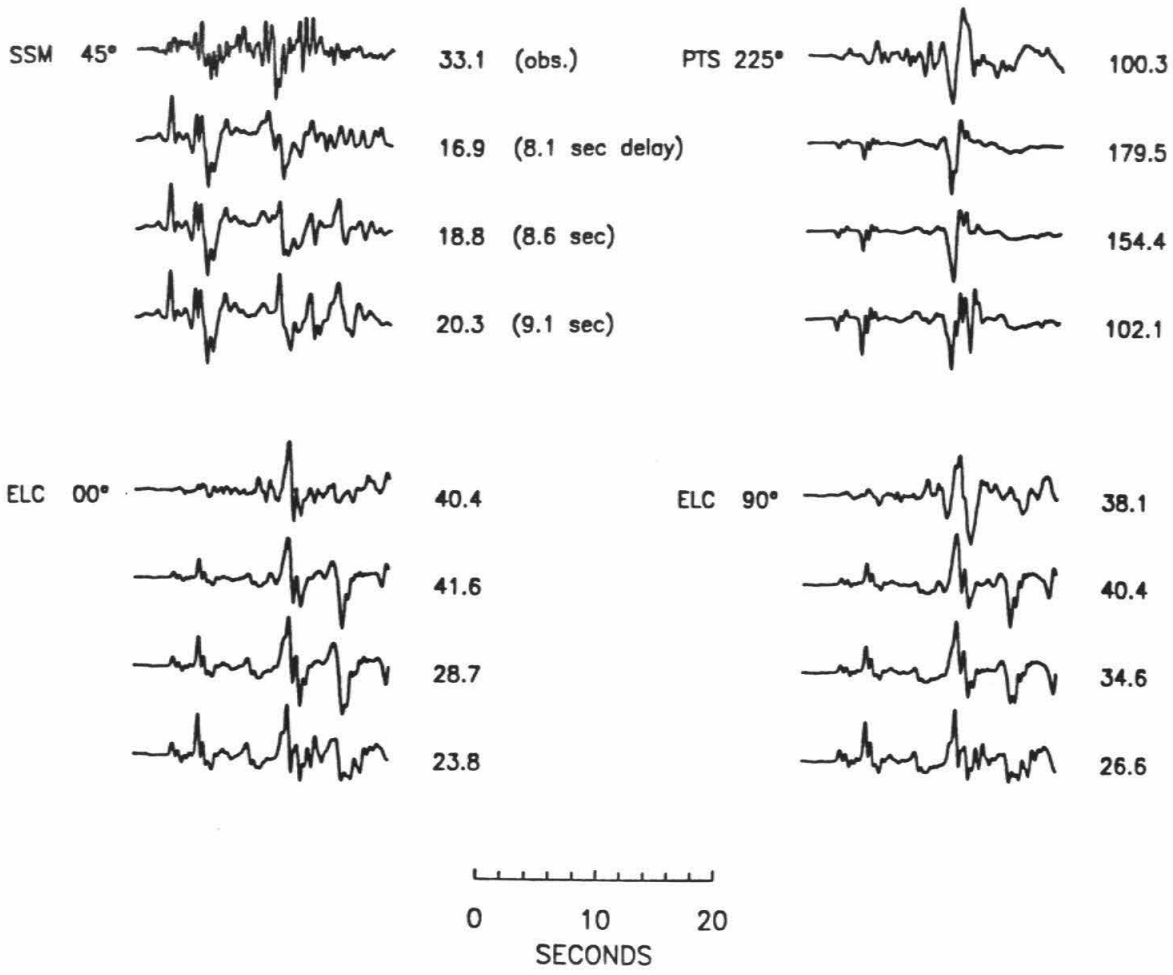

Figure 2.9: Comparison of observed velocity records (top trace) with subevent 3 synthetics produced by the models shown in Figure 2.8 for selected stations. The synthetics shown are for delays of 8.1 sec (2nd trace), 8.6 sec (3rd trace) and 9.1 sec (bottom trace). Amplitudes are in cm/sec.

line-source teleseismic representations of the later moment release overlay the major region of slip in our third subevent, and the time separation is given as 8.1 sec by Hwang *et al.* [1990].

Both these teleseismic studies, as well as our model, suggest significant moment release on the southern section of the Superstition Hills fault. This is consistent with the distribution of the aftershocks, which extend beyond the mapped surface rupture. Furthermore, considerable afterslip at the surface occurred along the southern section [Williams and Magistrale, 1989] shown atop Figure 2.10, suggesting substantial slip at depth. The horizontal scale is common for both the top and bottom portions of this figure. Considerable afterslip occurred on both the northwest and the southeast strands of the fault (Figure 2.1), consistent with our model of dislocation at depth. The agreement between the longer-period teleseismic models, our strong-motion modeling results, and the afterslip at the surface favors moment release along the southern portion of the Superstition Hills fault, radiating both short (1 sec) and long-period (20 sec) energy.

The relative amount of moment release for individual subevents obtained for different studies is shown in Table 2.3. The teleseismically determined, moment ratio of the second to first subsource is roughly 2 to 1, while the strong-motion studies have an average ratio (subevent 3 to subevents 1 and 2 combined) of 3 to 1. We expect the strong-motion studies, with a long period cutoff of 10 sec, might have smaller, overall moment values than observed teleseismically (period of 15-20 sec). The total moment determined from model 307 is 4.8 x 10^{25} dyne-cm, or half the average teleseismic moment of 8.9 x 10^{25} dyne-cm. The total moment of the Frankel and Wennerberg [1989] strong-motion model is 1.87 x 10^{25} dyne-cm, one fifth the average teleseismic moment. Their low moment with respect to our model 307 may reflect the absence of moment release along the southern portion of the Superstition Hills fault in their model.

Figure 2.10: Northwest-southeast cross section parallel to the Superstition Hills fault comparing dislocation model 303 with previous studies. The distribution of slip is shown with contours of 40, 80, 120 and 160 cm for subevent 1 and 2 combined (dark stipple) and subevent 3 (light stipple). The line-source model of Frankel and Wennerberg [1989] is depicted by the circle and arrows (depth of 9 km). The solid squares and dotted line plus arrow represent the two models of Hwang *et al.* [1990]. The top portion of the figure indicates afterslip 1 and 355 days after the earthquake [after Williams and Magistrale, 1989]. See text for details.

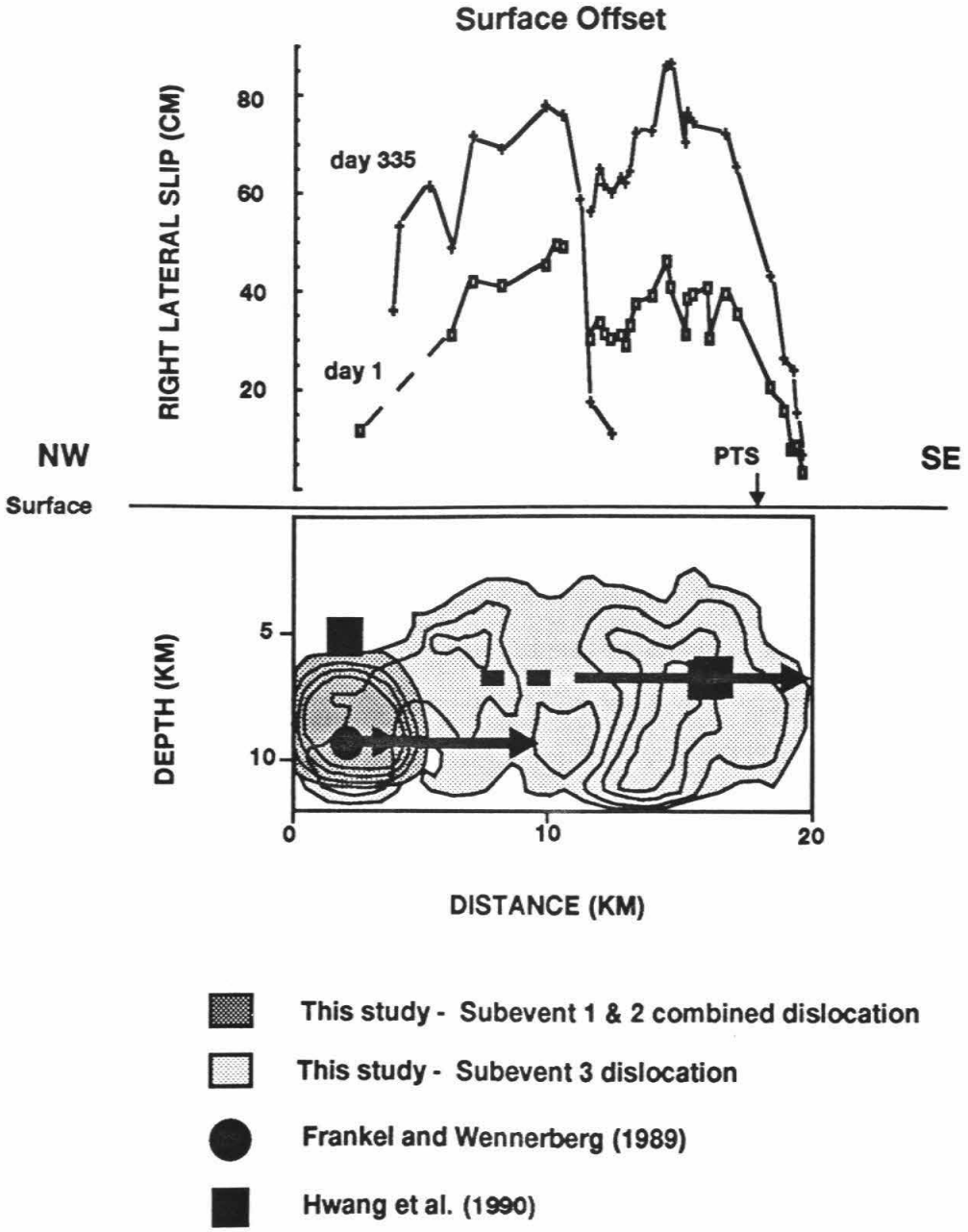

(After Hwang et al., 1990)

We may estimate the stress drop for individual subevents of the Superstition Hills earthquake, keeping in mind that these estimates are clearly dependent on the choice of rupture area. The region of nonzero slip varies with the amount of smoothing constraint chosen in the inversion. Therefore, in these calculations, we assign the area of rupture to be the region with slip greater than 20% of the peak-slip value for that subevent. The stress-drop expression of Eshelby [1957] for a circular fault, $\Delta\sigma = (7\pi\mu\overline{u})/(16a)$, where μ is the rigidity, $\overline{u}$ is the average dislocation and a is the radius, is suitable for subevents 1 and 2, considering their spatial distribution of slip (Figure 2.5). For subevent 1, using $\mu = 3.3 \times 10^{11}$ dyne/cm^2, $\overline{u} = 40$ cm and a=2.8 km, we find a stress drop of 64 bars. Subevent 2, with $\overline{u} = 145$ cm and a=3.1 km, has a stress drop of 207 bars. Subevent 3 has a stress drop of 87 bars, using the same expression for a circular rupture and choosing a radius of 4.6 km and an average slip of 90 cm for the high-slip area between 10 and 20 km (see Figure 2.5, bottom). An alternative expression for stress drop for the entire subevent 3 rupture area is given by Knopoff [1958] for a long, shallow strike-slip fault, $\Delta\sigma = (2\mu\overline{u})/(\pi w)$, where w is the fault width or depth. For $w = 9.5$ km and $\overline{u} = 70$ cm, the stress drop for subevent three over its entire rupture length is 15 bars.

Figure 2.11 shows the well-located aftershocks (M > 3.0) of the Superstition Hills earthquake projected on the inferred fault plane together with the slip distribution of the major subevents as shown in Figure 2.10. The aftershocks tend to cluster along the shallow northern region and along a vertical section of the central portion of the fault. Aftershocks in the central portion of the fault separate regions of major slip on the northwestern and southwestern segments of the fault, and underlie the fault stepover shown in Figure 2.1 and discussed earlier. The concentration of aftershocks outside regions of large slip has been observed for most earthquakes for which the coseismic slip has been determined from modeling. This observation has been interpreted by Mendoza and Hartzell [1988b] as resulting from the redistribution

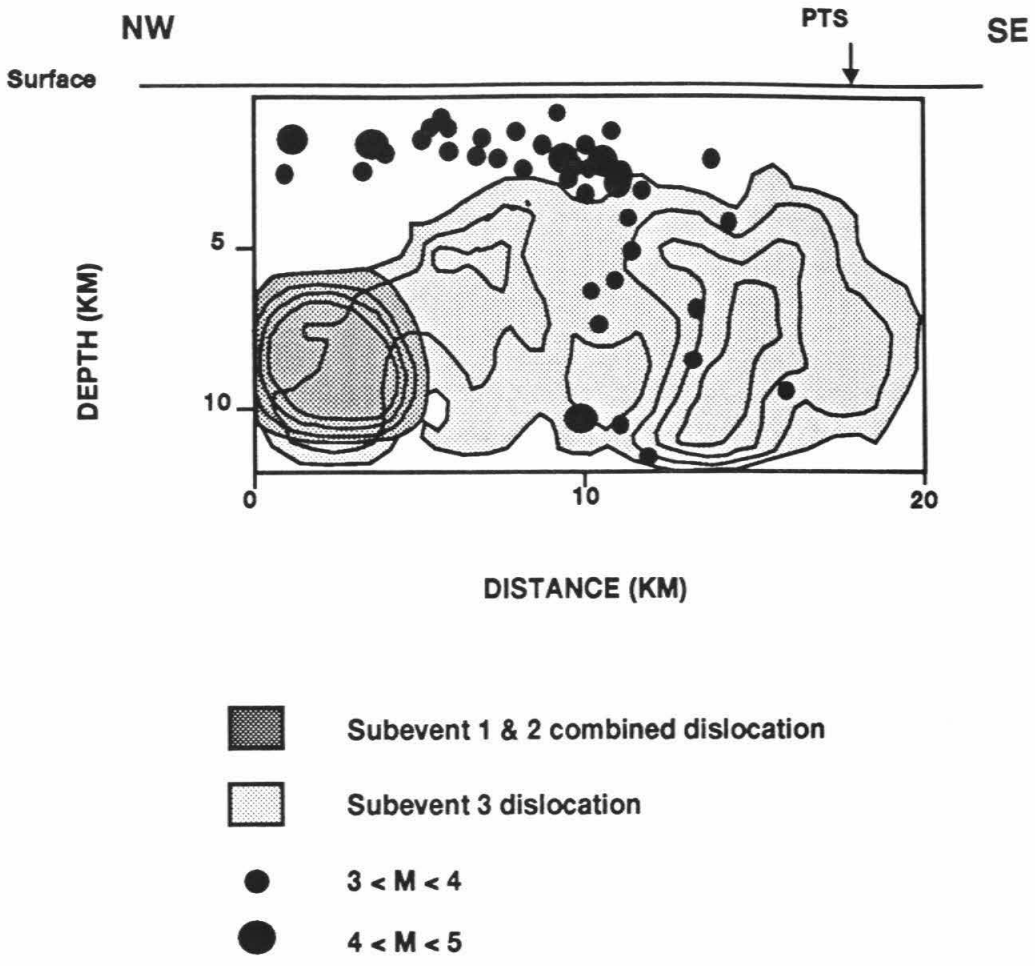

Figure 2.11: Cross section of fault showing aftershocks ($M \geq 3.0$) projected onto the fault plane. Also shown are the combined subevent 1 and 2 slip contours and the subevent 3 contours as shown in Figure 2.9. Contour interval is 40 cm.

of stress following the primary failure on the fault plane. The relationship between aftershocks and regions of large slip during the Superstition Hills earthquake as seen in Figure 2.11 is clear, but is perhaps not as dramatic as seen in the examples presented by Mendoza and Hartzell [1988b].

Chapter 3

Loma Prieta Earthquake

3.1 Abstract

We have used 24 broadband teleseismic and 48 components of local, strong-motion velocity records of the 1989 Loma Prieta earthquake in a formal inversion to determine the temporal and spatial distribution of slip. Separate inversions of the teleseismic data (periods 3-30 sec) and strong-motion data (periods 1-5 sec) result in similar models. The data require bilateral rupture with relatively little slip in the region directly updip from the hypocenter. Slip is concentrated in two patches; one centered 6 km northwest of the hypocenter at a depth of 12 km, with an average slip of 250 cm, and the other centered about 5 km southeast of the hypocenter at a depth of 16 km, with an average slip of 180 cm. The bilateral nature of the rupture results in large-amplitude ground motions at sites located along the fault strike, both to the northwest and the southeast. However, the northwestern patch has a larger moment and overall stress drop and is, consequently, the source of the largest ground motion velocities, consistent with the observed recordings. This bilateral rupture also produces relatively modest ground motion amplitudes directly updip from the hypocenter, which is in agreement with the velocity ground motions

observed at Corralitos. There is clear evidence of a foreshock (magnitude about 4.5 to 5.0) or a slow-rupture nucleation about 2 sec before the main part of the rupture; the origin time implied by strong-motion trigger times is systematically nearly 2 sec later than the time predicted from the high-gain, regional-network data. The seismic moment obtained from either of the separate data sets or both sets combined is about 3.0×10^{26} dyne-cm, and the seismic potency is 0.95 km^3. Our modeling results indicate that the rupture model determined from the teleseismic broadband data alone, independent of the strong-motion data, is adequate to predict many of the characteristics of the local strong-motion recordings.

3.2 Introduction

In this study, we use a linear, least-squares inversion of strong-motion and teleseismic waveform data to solve for the temporal and spatial distribution of slip vectors during the 1989 Loma Prieta earthquake ($M_s = 7.1$). Although the geometry of the fault plane is fixed in the inversion, it is chosen to be compatible with teleseismic waveforms and the distribution of aftershocks. Our estimates of the spatial and temporal distribution of slip will enhance studies of fault segmentation and earthquake recurrence [King *et al.*, 1990; Working Group on California Earthquake Probabilities, 1988], which depend on reliable estimates of the rupture dimensions and amplitude of slip. Furthermore, the variation in rake angle as a function of position along strike and downdip on the fault plane is critical to analyses of the complicated fault interactions within the Sargent-San Andreas system [Schwartz *et al.*, 1990; Dietz and Ellsworth, 1990; Seeber and Armbruster, 1990; Olson, 1990].

The method we employ is that of Hartzell and Heaton [1983], which has been shown to provide valuable insight into the rupture history of other California earthquakes [Hartzell and Heaton, 1983; Hartzell and Heaton, 1986; Mendoza and Hartzell,

1988a; Wald *et al.*, 1990], as have other finite-fault approaches [Olson and Apsel, 1982; Archuleta, 1984; Beroza and Spudich, 1988]. In addition to providing an estimate of the rupture history for individual earthquakes, these studies also provide new insight into the general characteristics of the rupture process that are common to many events. After studying slip models from several earthquakes, Mendoza and Hartzell [1988b] suggested that large gaps in aftershock patterns often coincide with the regions of relatively large slip. From the distribution of slip, we can also place constraints on the location and depth extent of significant energy release and characterize the distribution of stress changes on the faults. These results provide a starting point for calculating ground motions for future events comparable in size to the Loma Prieta earthquake. Such ground-motion calculations are important for augmenting the sparse data base of near-source, strong-motion recordings of crustal earthquakes having magnitudes of 7 or larger.

The Loma Prieta earthquake was well recorded at both local strong-motion and teleseismic broadband stations. The strong-motion velocity recordings used here are dominated by energy in the range of 1-5 sec, while the broadband, teleseismic recordings range from 3-30 sec. This wealth of data provides an opportunity to compare rupture models that are derived independently from either the strong-motion or the teleseismic waveforms with models derived from the combined data sets and over a wide range of frequencies. Our results provide insight into the limitations and constraints provided by previous studies that have less extensive data sets.

3.3 Data

Ground motions from the Loma Prieta earthquake were recorded over a wide range of frequencies and distances, from high-frequency waveforms on local accelerometers and regional seismic networks to very low frequencies observed in teleseismic

surface waves and geodetic line-length changes. Unfortunately, deterministic waveform inversion of high-frequency motion (> 3 Hz) requires an accurate and detailed knowledge of the wave propagation in the geologically complex structure in the Loma Prieta region. Furthermore, inversion of high frequencies requires a proliferation of free variables that significantly increase the computation time and decrease the stability of the inversion process. Therefore, we have chosen to concentrate our study on the lower-frequency part of the rupture history. Near-source, low-pass, filtered strong-motion and teleseismic body waves seem to be the most suitable data sets to study the general characteristics of the slip history. Geodetic data can also provide important constraints on an earthquake slip-distribution model. Unfortunately, we were not able to obtain enough geodetic data at the time of this study to justify its inclusion in the formal inversion process.

3.3.1 Teleseismic

The teleseismic stations chosen for this study are listed in Table 3.1. The data are digital recordings obtained from Chinese Digital Seismograph Network (CDSN), GEOSCOPE and Incorporated Research Institution for Seismology (IRIS) broadband components, and Global Digital Seismograph Network (GDSN) intermediate-period components. These stations provide a uniform azimuthal coverage of the focal sphere and also contain several near-nodal observations for both P and SH source radiation (Figure 3.1). In this analysis, instrument responses were deconvolved from the original recordings to obtain true ground velocities.

3.3.2 Strong Motion

The distribution of near-source ground velocities used in this study is displayed in Figure 3.2, Figure 3.3 and Figure 3.4. Station abbreviations, station geometries with respect to the epicenter, and trigger times (when available) are given in Ta-

Figure 3.1: Global-station distribution for teleseismic records shown by takeoff angles plotted on focal spheres. The P (left) and *SH* (right) radiation patterns are given for a mechanism with strike, dip and rake equal to 128°, 70°, 138°, respectively. For *SH*, up refers to clockwise motion.

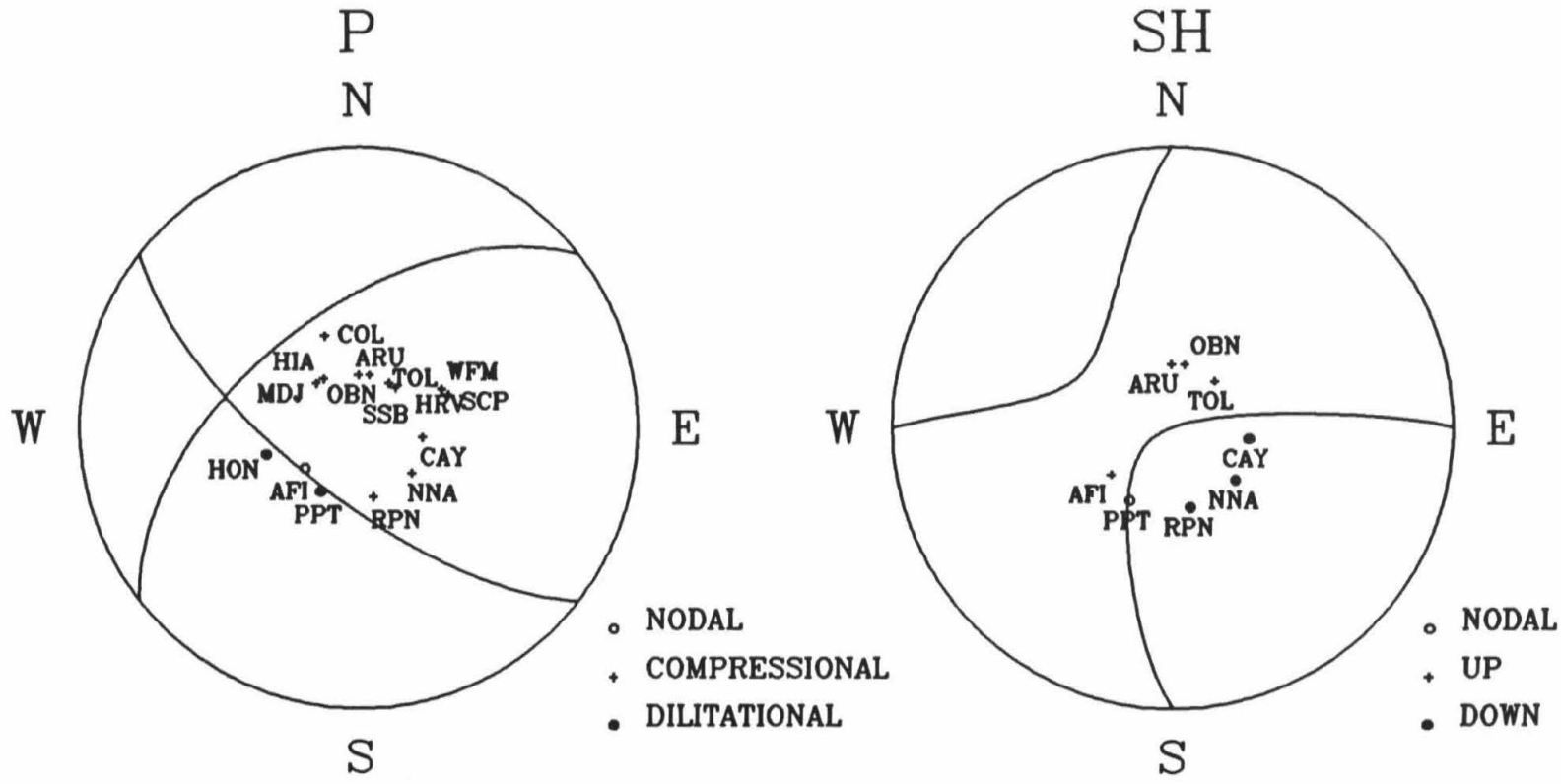
P
N
W
E
S
COL
HIA
ARU
TOL
WFM
MDJ
OBN
SSB
HRV
SCP
CAY
HON
AFI
NNA
PPT
RPN
NODAL
COMPRESSIONAL
DILITATIONAL
SH
N
W
E
S
OBN
ARU
TOL
CAY
AFI
NNA
PPT
RPN
NODAL
UP
DOWN

Station	Distance (Degrees)	Azimuth	Back Azimuth	Phases Used
AFI	69.2	232.6	40.8	P,SH
ARU	86.9	359.7	0.4	P,SH
CAY	70.8	98.6	307.6	P,SH
COL	31.8	339.4	138.5	P
HIA	77.9	324.0	45.9	P
HON	35.0	253.5	55.2	P
HRV	38.5	65.7	279.2	P
MDJ	76.0	305.2	51.3	P
NNA	64.8	130.1	321.5	P,SH
OBN	85.1	11.9	343.0	P,SH
PPT	60.5	210.6	25.2	P,SH
RPN	65.2	167.7	349.0	P,SH
SCP	34.1	67.8	278.3	P
SSB	84.6	34.7	319.8	P
TOL	84.3	43.0	314.8	P,SH
WFM	38.5	65.6	279.1	P

Table 3.1: Loma Prieta teleseismic stations.

Figure 3.2: Location map showing strong-motion stations (solid triangles). The shaded region represents the surface projection of the model fault plane used in this study. The epicenter is shown with a star. Radial ground velocities are displayed for each of the stations. Peak amplitudes are in cm/sec. The faults are a digitized version of major Quaternary faults of Jennings [1975].

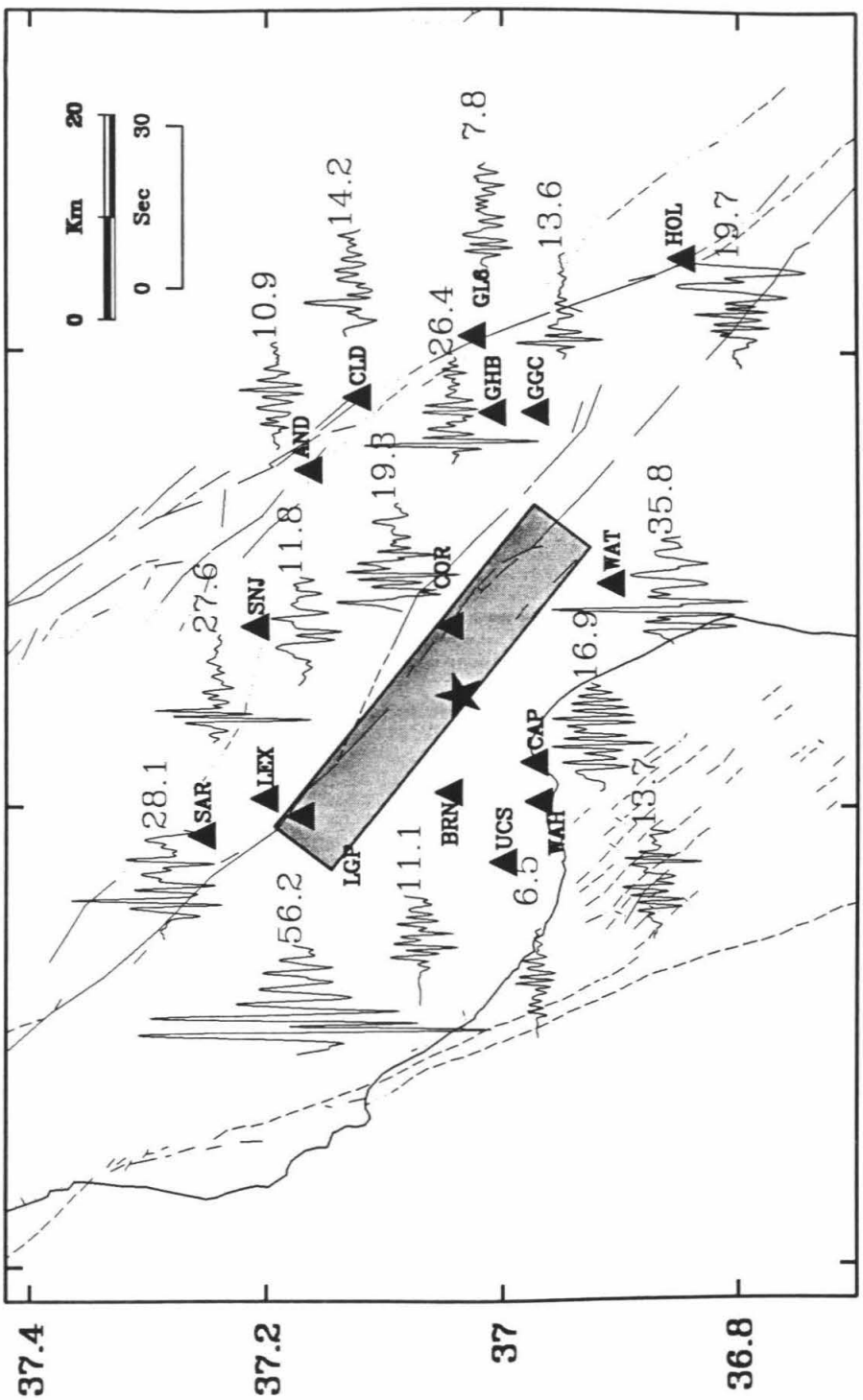
Radial Ground Velocities
0 Km 20
0 Sec 30
SAR
LEX
SNJ
AND
CLD
GHB
GLB
GGC
HOL
LGP
BRN
UCS
MAH
CAP
COR
WAT
28.1
27.6
11.8
10.9
14.2
26.4
7.8
13.6
19.7
19.8
35.8
16.9
13.7
11.1
6.5
56.2
37.4
37.2
37
36.8
-122.5
-122
-121.5

Figure 3.3: Same as Figure 3.2 except that tangential ground velocity is shown. Also shown is the distribution of aftershocks.

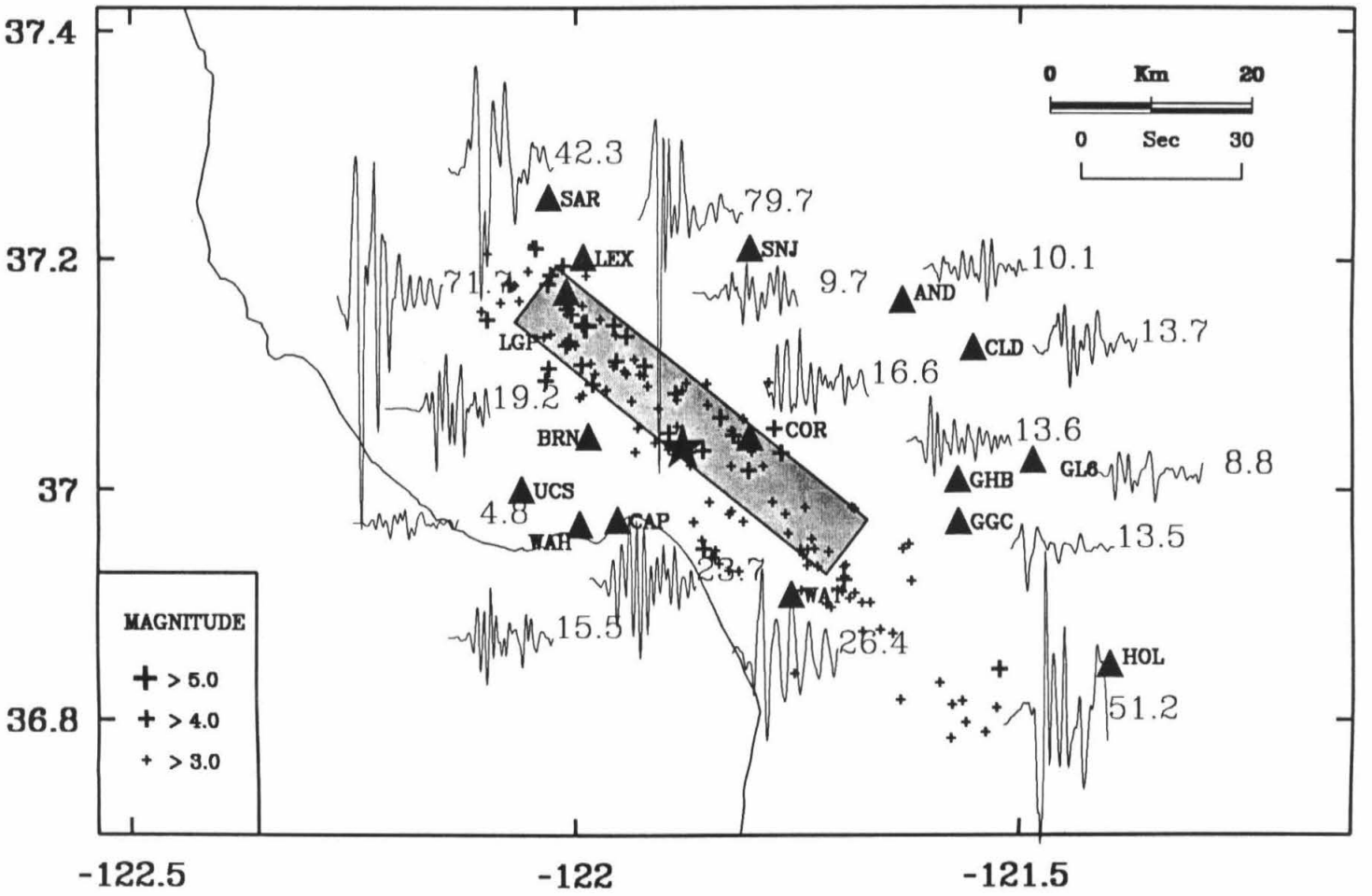
Tangential Ground Velocities
37.4
37.2
37
36.8
-122.5
-122
-121.5
0 Km 20
0 Sec 30
42.3
SAR
79.7
SNJ
LEX
71.3
9.7
AND
10.1
LGP
CLD
13.7
16.6
19.2
BRN
COR
13.6
GHB
GLS
8.8
UCS
4.8
CAP
GGC
WAH
13.5
23.7
WAT
15.5
26.4
HOL
51.2
MAGNITUDE
> 5.0
> 4.0
> 3.0

Figure 3.4: Same as Figure 3.2 except that vertical ground velocity is shown. Also shown is the Modified Mercalli isoseismal contour separating regions of intensity VII and VIII [from Stover *et al.*, 1990].

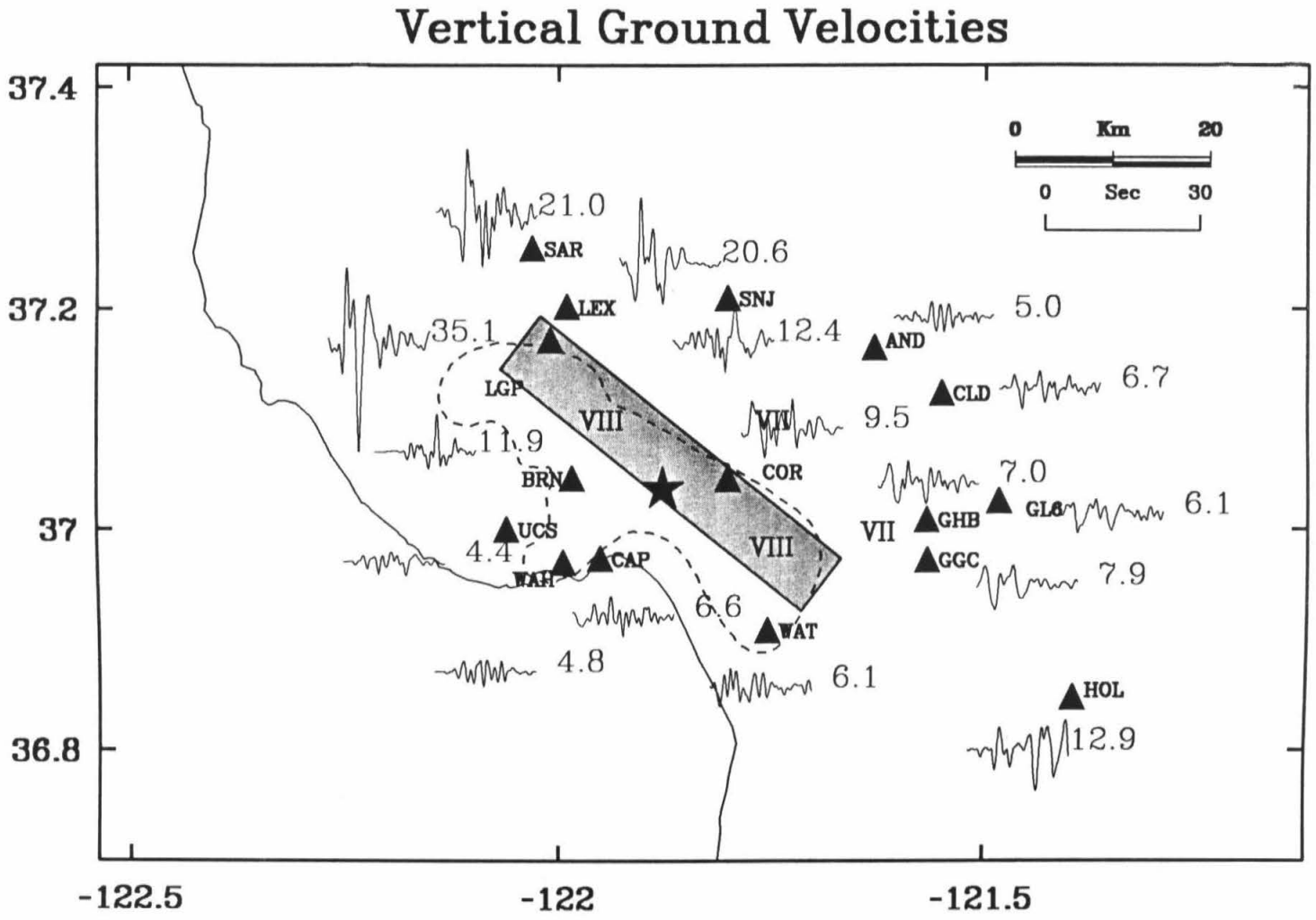
Vertical Ground Velocities
37.4
37.2
37
36.8
-122.5
-122
-121.5
0 Km 20
0 Sec 30
21.0
SAR
20.6
SNJ
LEX
35.1
12.4
5.0
AND
LGP
VIII
CLD
6.7
9.5
11.9
BRN
COR
7.0
UCS
GLA
6.1
4.4
GHB
VII
CAP
GGC
7.9
WAH
6.6
WAT
4.8
6.1
HOL
12.9

ble 3.2. The velocity waveforms were obtained by integrating corrected acceleration recordings provided by the C.D.M.G. [Shakal *et al.*, 1989] and the U.S.G.S. [Maley *et al.*, 1989] and uncorrected recordings from the University of California Santa Cruz (U.C.S.C.). The velocity waveforms were bandpass-filtered between 0.1 to 1.0 Hz using a zero-phase, third-order, Butterworth filter. The horizontal components are rotated with respect to the epicenter to obtain "radial" and "tangential" components. While this rotation is correct for the energy originating near the epicenter, it is only approximate for source regions farther northwest and southeast along the fault.

Two criteria were used to select stations to include in the inversion: the observations should be close to the aftershock zone and also well distributed in azimuth. Within the epicentral region, peak-ground motions are relatively independent of surface geology [Benuska, 1990]. Care was also taken to avoid stations that seemed to have unusual site responses. For this reason, the C.D.M.G. station Agnew was not used, although fortunately, it is at a similar distance and azimuth as station LEX. U.C.S.C. stations BRN, LGP, UCS and WAH were included to provide important station coverage to the west and southwest of the epicenter. Unfortunately, the U.C.S.C. stations did not record absolute time and required additional processing to remove glitches in the raw-acceleration data. The deglitching process may be inadequate at high frequencies, but provides useful velocity recordings at the frequencies of interest in this analysis (0.1 to 1 Hz). The station LGP acceleration recording exhibited a permanent step on the vertical component, which does not carry through in our bandpassed data. The horizontal components were apparently unaffected. Station BRN was set for 0.5 g maximum amplitude, and since amplitude reached close to that value, the accuracy of the response is unknown. We will address the issue of estimating absolute time for these stations in the section on the inversion method.

Code	Station Name	Data Source	Dist (km)	Az	Station Delay	Trig Time	Trig -O.T.
AND	Anderson Dam	USGS	26.1	57.6	0.0	23.0	7.8
BRN	Branciforte Drive	UCSC	9.5	275.4	-	-	-
CAP	Capitola Fire Sta.	CDMG	9.7	222.0	-	-	-
CLD	Coyote Lake Dam	CDMG	30.7	72.1	0.0	24.5	9.3
COR	Corralitos	CDMG	6.8	83.5	0.0	20.4	5.2
GGC	Gavilan College	CDMG	28.6	104.8	-0.4	23.9#	8.7
GHB	Gilroy Hist. Bld.	CDMG	27.8	96.9	-0.2	23.4	8.2
GL6	Gilroy Array #6	CDMG	35.2	92.4	0.7	26.0	10.8
HOL	Hollister - Pine St	CDMG	47.9	116.3	1.9	27.5	12.3
LEX	Lexington Dam	CDMG	19.1	331.0	-0.3	21.1	5.9
LGP	Los Gatos Pres. Cnt.	UCSC	18.8	321.7	-	-	-
SAR	Saratoga - Aloha Av	CDMG	27.5	330.6	-	-	-
SNJ	San Jose - Harry Rd	CDMG	20.1	19.6	-0.2	18.3	3.1*
UCS	U. C. Santa Cruz	UCSC	16.8	255.0	-	-	-
WAH	Walter's House	UCSC	12.9	233.4	-	-	-
WAT	Watsonville	CDMG	18.1	142.8	0.3	21.6	6.4

Table 3.2: Loma Prieta strong-motion stations. Distance and azimuth are with respect to the epicenter at 37 2.37' N 121 52.81' W. Station delay is the adjustment to absolute time in sec—see text for details. Trig time refers to trigger time in sec after 00 04 00.0 GMT October 18, 1989, and O.T, origin time is 00 04 15.21 GMT October 18, 1989. - indicates station did not record absolute time. # Time was accurately estimated from time on Gilroy 1. * refers to Digital Instrument with memory before trigger time (P wave at 1.7 sec).

3.4 Fault-Rupture Model

The fault parameterization and modeling procedure we employ is that described by Hartzell and Heaton [1983] in their study of the 1979 Imperial Valley earthquake. Faulting is represented as slip on a planar surface that is discretized into a number of subfaults. The ground motion at a given station can be represented as a linear sum of subfault contributions, each appropriately delayed in time to simulate fault rupture. Formal inversion procedures are then used to deduce the slip distribution on these subfaults that minimizes the difference between the observed and synthetic waveforms.

In this study we represent the Loma Prieta rupture area as a 40 km-long plane striking N 128° E and dipping 70° toward the southwest. The fault extends from a depth of 1.5 km to 20.3 km, giving a downdip width of 20 km (Figure 3.5). As a point of reference, the northernmost corner of our assumed fault plane in at 37.193 north latitude and 122.020 west longitude. We chose the overall dimensions of the fault to enclose the region of major aftershock activity [Dietz and Ellsworth, 1990], although there has been some discussion about the possibility of vertical strike-slip faulting on a second plane extending past the southern end of our inferred rupture area. This possibility is discussed later. The strike and dip value of our fault plane were chosen from the broadband-inversion results of Kanamori and Satake [1990]. This fault plane is also consistent with the aftershock lineation [Dietz and Ellsworth, 1990], the focal mechanism determined from first-motion data [Oppenheimer, 1990], and the P and *SH* teleseismic waveforms shown in Figure 3.6. Slight discrepancies in strike and dip would have little effect on our model results and conclusions.

The fault-plane geometry chosen for this study differs somewhat from the geometry used by Lisowski *et al.* [1990] to model the geodetic data. Although they also used a dip of 70°, they found that a strike of N 136° E (8° more northerly than ours) was necessary to explain their data. Furthermore, their fault plane was shifted

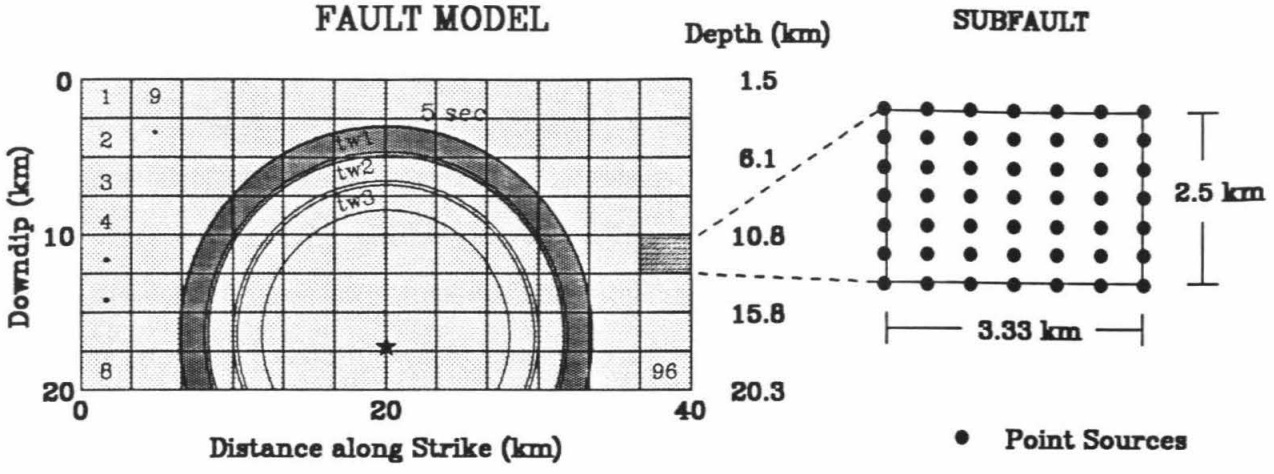

Figure 3.5: Northwest-southeast cross section of the fault-rupture model along the fault plane indicating subfault layout. The subfault enlargement displays the distribution of point sources for each subfault. The largest circle radiating outward from the hypocenter (star) represents the position of the rupture front after 5 sec. Smaller concentric circles delimit the (slightly overlapping) fault regions slipping in time windows 1 (tw1 - shaded), 2 (tw2) and 3 (tw3).

about 2 km westward of our assumed plane, which was chosen to coincide with the aftershock distribution. In general, the geodetic data are more sensitive to fault geometry than the waveform data, but are not as powerful in resolving details of the slip distribution. Differences in the fault geometry inferred from the static offsets, when compared with waveform studies, may reflect complexities in the nature of the rupture, such as a nonplanar fault or multiple fault rupture. These complexities are not considered in this study.

Our fault area is discretized into 12 subfault elements along strike and 8 elements downdip, giving each subfault a length of 2.5 km and a vertical width of 3.33 km (Figure 3.5). This subfault area is a compromise chosen to give sufficient freedom to allow rupture variations necessary to model the ground motions successfully and yet minimize computational time. The computation time for the inversion is proportional to the cube of the number of unknown parameters, in this case the number of subfault-slip values to be determined.

3.4.1 Synthetic Green's Functions

The synthetic ground motion contribution for each subfault is computed using the Green's function summation and interpolation method of Heaton [1982] and is summarized only briefly here. The subfault motions are obtained by summing the responses of a number of point sources distributed over the subfault. We sum 25 equally spaced point sources (see Figure 3.5) appropriately lagged in time to include the travel-time difference that is due to the varying source positions and to simulate the propagation of the rupture front across each subfault. In all, 2400 point sources are summed to construct the teleseismic and strong-motion synthetics at each station for both a pure strike-slip and a pure dip-slip mechanism. Thus, each subfault includes the effects of directivity.

The point-source responses, or Green's functions, for teleseismic P or SH body-

wave, synthetic seismograms are computed using the generalized ray method [Langston and Helmberger, 1975]. We include the responses of all rays up to two internal reflections in a layered velocity model, including free-surface and internal phase conversions. A Q operator [Futterman, 1962] is applied with the attenuation time constant t^* equal to 1 and 4 sec for P and SH waves, respectively.

The point-source responses for the strong motions are computed for a layered velocity model with the discrete wavenumber/finite element (DWFE) methodology of Olson *et al.* [1984] for frequencies up to 3.5 Hz. In practice, we calculate a master set of synthetics for increments in depth from 1.5 to 20.3 km and for ranges between 0 and 75 km, to allow for the closest and furthest possible subfault-station combinations. Then for each subfault-station pair, the required subfault response is derived by the summation of 25 point-source responses obtained by the linear interpolation of the closest Green's functions available in the master set. The linear interpolation of adjacent Green's functions is performed by aligning the waveforms according to their shear-wave travel times. Subfault contributions from both a pure dip-slip and pure, right-lateral strike-slip mechanism are computed using the assumed fault geometry. The relative weights of these fundamental mechanisms, as well as the amount of slip on each subfault, are determined in the inversion process described later.

3.4.2 Velocity Model

The velocity model used to compute the DWFE Green's functions is given in Table 3.3. The P-wave velocities were obtained by averaging the two velocity-depth profiles in this region given by Dietz and Ellsworth [1990] for regions northeast and southwest of the San Andreas fault. We have also added a thin, slower layer to this model to better approximate elastic properties just beneath the strong-motion stations. S-wave velocities were obtained by assuming that the structure is a Poisson

Vp (km/sec)	Vs (km/sec)	Density (g/cm^3)	Thickness (km)	Depth (km)
1.73	1.00	1.50	0.1	.1
3.38	1.95	1.55	0.4	.5
4.29	2.48	1.85	0.5	1.0
4.80	2.77	2.05	2.0	3.0
5.37	3.10	2.26	2.0	5.0
5.74	3.31	2.45	2.0	7.0
6.15	3.55	2.58	2.0	9.0
6.25	3.61	2.62	4.0	13.0
6.27	3.62	2.63	5.0	18.0
6.67	3.85	2.77	7.0	25.0
8.00	4.62	3.28	50.	

Table 3.3: Loma Prieta velocity structure.

solid.

The velocity model used to compute the teleseismic Green's functions is a 5-layer approximation of the velocity model given in Table 3.3. Heaton and Heaton [1989] discuss difficulties that arise when seismic moments derived from different velocity models are compared. Fortunately, the seismic velocities are nearly constant for both the teleseismic and strong-motion velocity models in the depth range from 7 km to 18 km (the region of highest slip). This favorable coincidence means that a simple comparison of seismic moments derived from teleseismic and strong-motion inversions is approximately valid.

3.4.3 Source-Time Function and Rupture Velocity

The subfault synthetics are convolved with a dislocation-time history which we represent by the integral of an isosceles triangle with a duration of 0.7 sec. This slip function was chosen on the basis of a comparison of the synthetic velocity-pulse width for a single subfault with the shortest duration velocity pulse width observed, as well as on prior experience with this inversion method [Heaton, 1990]. As Hartzell and Mendoza [1991] point out, resolution of the slip function is difficult, although we are required by the strong-motion recordings to employ a relatively short (< 0.8 sec) duration.

The rupture velocity is assumed to be a constant 2.7 km/sec, or 75% of the shear-wave velocity in the main part of the source region (Table 3.3). Many observations, including the absence of tectonic surface slip [U.S. Geological Survey Staff, 1990], indicate that little dislocation occurred above a depth of about 4 km. The position of the rupture front 5 sec after the nucleation time is shown in Figure 3.5.

Some flexibility in the rupture velocity and slip-time history is obtained by introducing time windows [Hartzell and Heaton, 1983]. In all inversions, each subfault is allowed to slip in any of three identical 0.7-sec time windows following the passage of the rupture front, thereby allowing for the possibility of a longer slip duration or a locally slower rupture velocity. Hartzell and Mendoza [1991] obtained very similar dislocation models for the 1978 Tabas, Iran earthquake ($M_s = 7.4$), using both a linear inversion parameterizing slip with three time windows (as is done here), and also a nonlinear iterative inversion, which allows a single rupture at each point on the fault, but allows the rupture velocity to vary.

In this study each time window is separated by 0.6 sec, allowing a small overlap of the 0.7-sec duration subfault, source-time-function. Thus, as depicted in Figure 3.5, the region of the fault that is allowed to slip 5 sec (for example) after the nucleation of rupture is within concentric bands occupied by the 3 time windows. We did not

test for the possibility of a faster rupture velocity since initial indications from our modeling showed that regions towards the northwest required slightly slower rupture velocities than 2.7 km/sec, which can be approximated, given the flexibility allowed for by the three time windows.

3.5 Inversion Method

A constrained, damped, linear, least-squares inversion procedure is used to obtain the subfault dislocation values that give the best fit to the strong-motion velocity waveforms. The inversion is stabilized by requiring that the slip is everywhere positive and that the difference in dislocation between adjacent subfaults (during each time window) as well as the total moment is minimized. These constraints have been previously discussed by Hartzell and Heaton [1983].

Smoothing, or minimizing, the difference in slip between adjacent subfaults, is required to avoid instabilities as well as to downplay the role in the inversion played by starting and stopping phases associated with each subfault. If large variations in slip are allowed, such phases dominate, yet represent artifacts of the subfault discretization. Since numerous subfaults are required to resolve the spatial variations in slip, smoothing constraints are needed. We expect the smoothing required for teleseismic and strong-motion data to be different in that the number of subfaults and their size remain fixed for each data set, yet the dominant period of the energy varies.

The teleseismic data can usually be fit with somewhat isolated spikes of large slip, which would predict enormous (unphysical), localized slips and excessive high-frequency radiation. So in practice, we increase the spatial-slip smoothing until there is a degradation to the waveform fits. Since the strong-motion inversion is more sensitive to higher-frequency radiation, it automatically limits extreme vari-

ations in rupture, which produce excessive short-period radiation. Therefore, the strong-motion inversion needs minor additional smoothing. And in fact, substantial smoothing would degrade the strong-motion waveform fits.

In essence then, the teleseismic-rupture model may represent a lower bound on the actual fault roughness and therefore represents a lower limit to high-frequency radiation. Similarly, we might expect the strong-motion model, derived from velocity waveforms, to underestimate much higher-frequency accelerations, but may be adequate for frequencies slightly higher than used in the inversion, perhaps up to 5 Hz.

Both the strong-motion observations and subfault, synthetic seismograms are bandpass-filtered from 0.1 to 1.0 Hz with a zero-phase Butterworth filter and are resampled at a uniform time step of 10 samples per sec. The teleseismic data were similarly filtered from 0.02 to 1.0 Hz. The upper-frequency limit is imposed by the nature of the strong-motion recordings. In general, there is more coherence in the waveforms at periods greater than 1 sec than at higher frequencies. Originally, the strong-motion data were low-pass-filtered at 3 Hz, but we found indications of significant complication apparently caused by local site-response effects. We modeled the first 25 sec of the record for teleseismic data and between 14 to 22 sec of the strong-motion records (depending on the individual record).

3.5.1 Timing

The initial alignment in time of the observed and synthetic seismograms is a critical issue in modeling waveform data in order to determine the temporal and spatial distribution of slip on the fault plane. In this type of study, two approaches can be taken. One approach (commonly used for teleseismic waveform inversions) is to time-shift the synthetic waveform from a point-source hypocenter until the first significant motion of the synthetic is aligned with that of the observed recording. Later

source contributions (from the developing rupture process) can then be determined by modeling the remaining features of the record. This method is adequate when 1) the observed first-arrival time is not ambiguous, and 2) it is clear that the initial arrival is actually from the locally determined hypocenter (including the origin time). Unfortunately, the first arrivals (observed on local seismic networks) for waves from the hypocenter may be too small to be seen teleseismically or on strong-motion recordings. These first arrivals are, however, used to determine the hypocenter and origin time of the earthquake. Serious problems arise if it is erroneously assumed that the first arrival on a teleseismic or strong-motion record is from the hypocenter determined from local seismic-network data. Hartzell and Heaton [1983] show how this is a serious problem when interpreting the 1979 Imperial Valley, California, earthquake.

In the second approach, all correlations are done in absolute time, with appropriate time delays to accommodate errors introduced by inadequacies of the assumed velocity model. At teleseismic distances, these delays can be substantial, so master-event techniques must be employed [e.g., Hartzell and Heaton, 1983]. For the local strong-motion data, the use of absolute time is preferable if it is known for a majority of the recordings. We use this second approach in this strong-motion modeling study.

When the trigger time on local strong-motion records is available (see Table 3.2) synthetic and observed waveforms are aligned in absolute time. Slight adjustments are also made to allow for variations in travel time not predicted by the assumed 1-D velocity structure (Table 3.2, station delays). While this provides an approximate static-station delay, it will not improve timing errors introduced by lateral variations encountered by subfault to station travel paths that vary significantly along the fault. This issue can be addressed later with the analysis of aftershock recordings at strong-motion sites when these data are made available.

For stations without absolute time, synthetic and observed waveforms are aligned on the basis of the assumption that the initial P-wave triggers the instrument. The stations with timing are weighted heavily in the inversion, and those without are downweighted, effectively removing them from the inversion. Using the preliminary inversion results, synthetic waveforms are calculated for those stations without timing, and new time estimates are obtained by comparing synthetic and observed waveforms. At some stations (UCS and WAH) the forward prediction was insufficient to estimate the timing, and these stations were not given significant weighting in subsequent inversions. We did, however, continue to compute waveforms for these for comparison with the observed waveforms and for later analysis.

3.6 Teleseismic Modeling

3.6.1 Preliminary Analysis

To date, several broadband teleseismic studies of the Loma Prieta earthquake have been made. The overall conclusions of many of these studies are well summarized by Wallace *et al.* [1991]. As pointed out by Choy and Boatwright [1990], three distinct arrivals can be recognized on most of the broadband teleseismic, velocity recordings. In Figure 3.6 (top traces) we mark these separate arrivals at selected stations with arrows. The first arrival is quite small but can be seen on the P-wave records, about one sec into the trace, at stations ARU, OBN and TOL. The first subevent is at the threshold of resolution for waveform modeling for the teleseismic data.

In general, previous teleseismic models describe this earthquake as a simple two-point source combination representing two later, dominant subevents. The seismic moments determined in these broadband studies range from $2.0 - 3.0 \times 10^{26}$ dyne-cm and show a large variation in the ratio of the relative moments for subevent 3 compared with subevent 2, depending on the assumptions of the individual researcher.

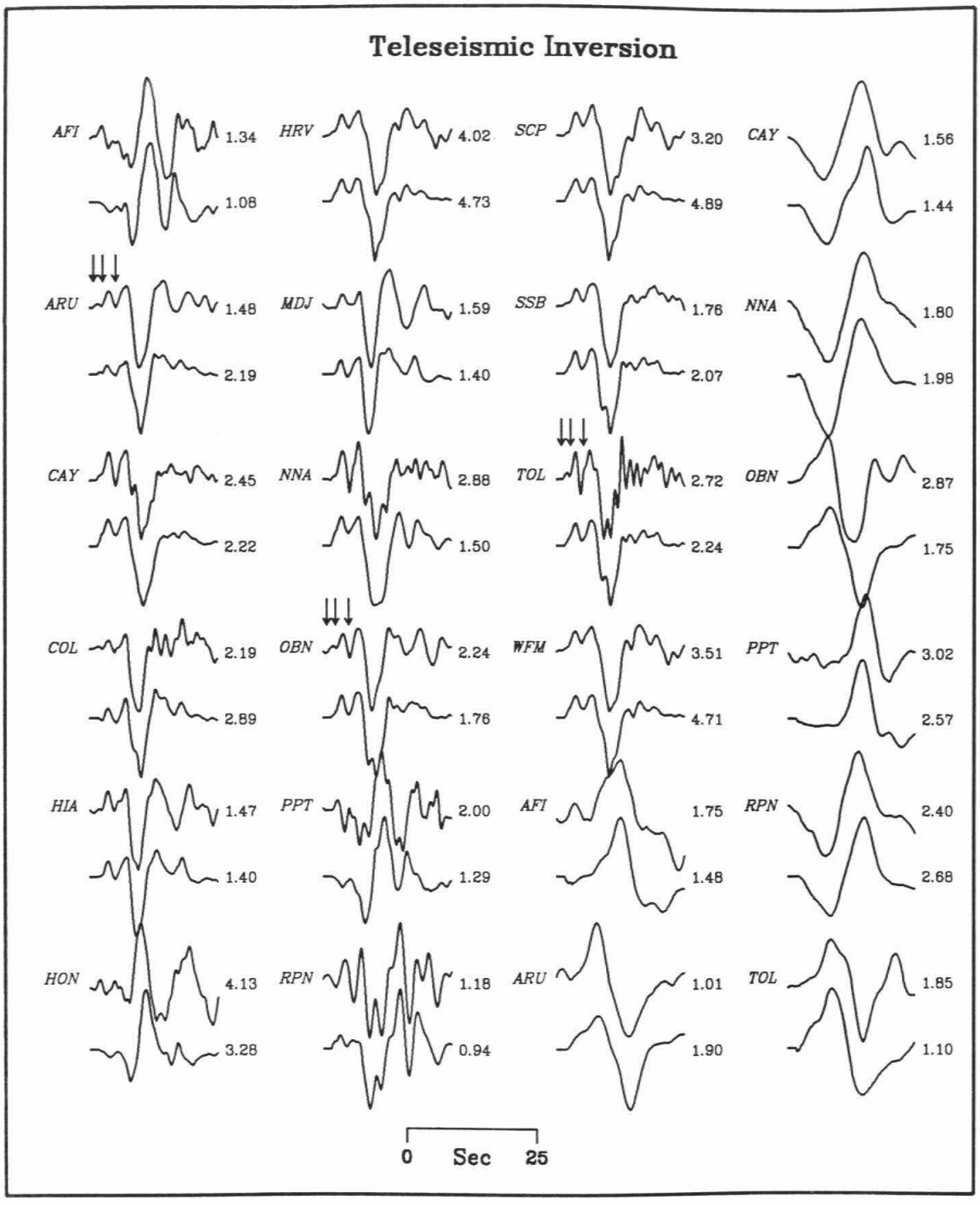

Figure 3.6: Comparison of observed (top) and synthetic (bottom) teleseismic velocity records. The first 16 stations are P waves and the last 8 stations are SH waves. Amplitudes are in microns/sec. The arrows indicate the three subevents as identified by Choy and Boatwright [1990].

In addition, there is a wide spread in the estimate of the best point-source depths for the second and third subevents, or for a single estimate of the centroid location. This suggests that the rupture, although over a finite area, was not extensive enough to be easily resolved teleseismically (i.e., less than about 35 km), consistent with the limited extent of rupture inferred from the aftershock distribution alone [Dietz and Ellsworth, 1990].

When teleseismic-velocity waveforms are integrated into displacements, it becomes difficult to distinguish arrivals from individual subevents. In particular, the arrival from the second subevent appears as a subtle inflection in the large pulse from the third subevent. Although very similar results were obtained by modeling the teleseismic-displacement waveforms, we find it easier to compare synthetic and observed velocity waveforms.

3.6.2 Inversion Results

The spatial distribution of slip obtained from inversion of only the teleseismic data is shown in Figure 3.7. The slip contours are in intervals of 50 cm, and increased shading indicates larger slip as displayed in the legend shown at the right of each diagram. We use a large contour interval to emphasize robust features in the model and to minimize the importance of smaller details. The dislocations shown represent the combined slip for the three time windows previously mentioned.

Our teleseismic model has a seismic moment of 2.8×10^{26} dyne-cm. Comparison of the observed teleseismic records (top) and the synthetic seismograms (bottom) predicted by the teleseismic dislocation model are shown in Figure 3.6. The amplitudes are given in microns-per-sec. The main features of this model are 1) a two-lobed bilateral rupture with a slightly larger slip to the northwest; 2) the largest slips are concentrated at a depth of 11 km for the northwestern patch and slightly deeper for the southeastern patch, and 3) there is little slip in the region updip from

Figure 3.7: Northwest-southeast cross section of the fault model showing contours of dislocation for strike-slip (top), dip-slip (middle) and oblique-slip (bottom) resulting from the teleseismic inversion. Contour interval is 50 cm. Shading values indicating slip in cm are given by the scale to the right of each diagram.

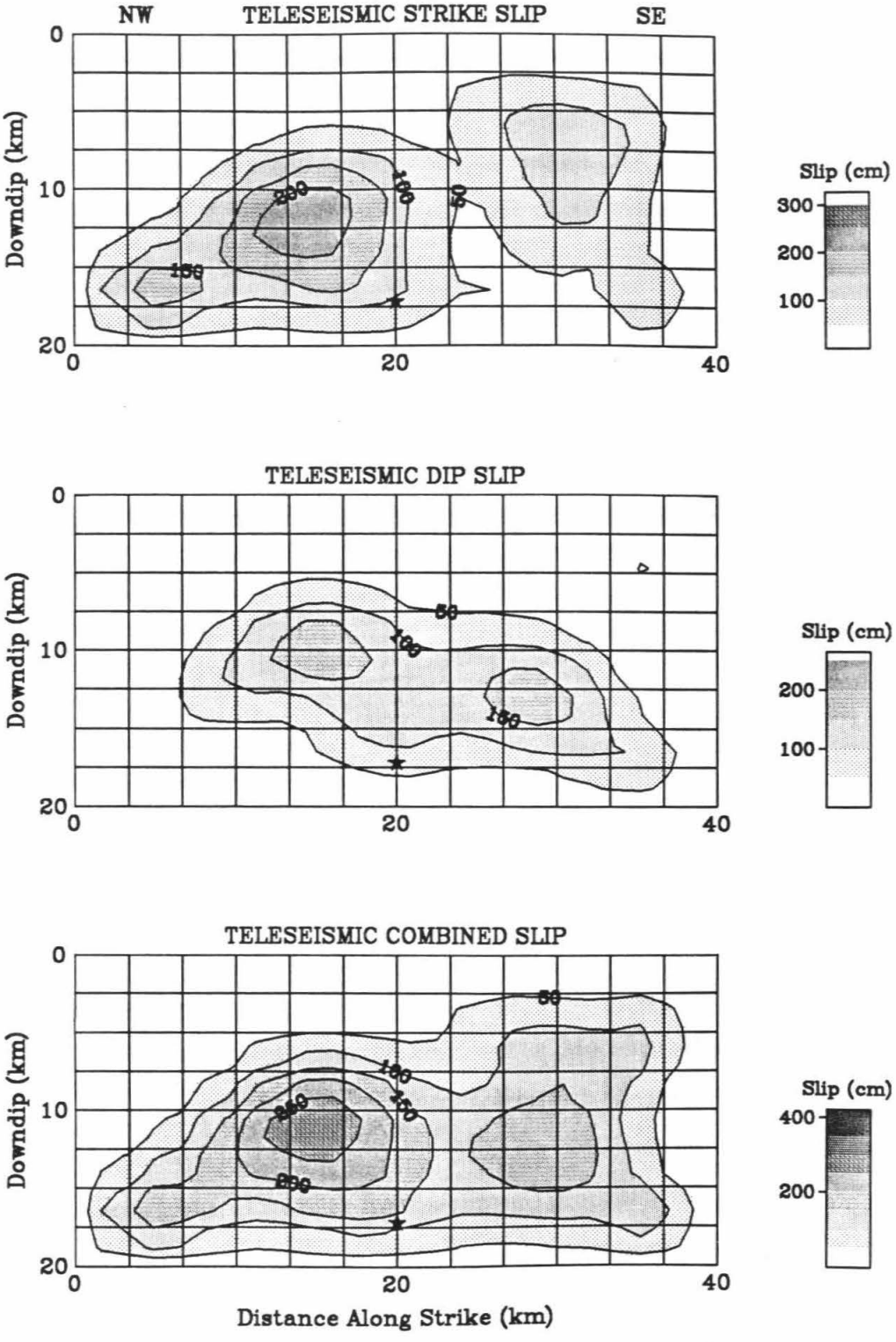
NW
TELESEISMIC STRIKE SLIP
SE
Downdip (km)
0
10
20
0
20
40
Slip (cm)
300
200
100
TELESEISMIC DIP SLIP
Downdip (km)
Slip (cm)
200
100
TELESEISMIC COMBINED SLIP
Downdip (km)
Slip (cm)
400
200
Distance Along Strike (km)

the hypocenter.

Directivity controls the waveform and amplitude only when the rupture front progresses at a velocity comparable to the phase of interest. For this reason, the teleseismic body waves, all having steep takeoff angles, are limited in their ability to resolve rupture directivity along strike, but are quite sensitive to up- or downdip rupture propagation. The lack of vertical directivity in our solution is apparent. Since the teleseismic data do not allow significant slip updip or downdip from the hypocenter, the majority of slip must occur along strike from the hypocenter. Bilateral rupture is indicated by the timing of the second and third arrivals and by the absence of significant azimuthal arrival time differences between the two dominant arrivals. As will be discussed in the following section, this model explains many features observed in the local strong-motion data.

3.7 Strong-Motion Modeling

3.7.1 Preliminary Analysis

PEAK MOTIONS. Inspection of the pattern of near-source, peak, ground velocities (Figures 3.2, 3.3, 3.4) reveals that the largest motions occurred at stations located near the northwest (LEX, LGP, SAR) and southeast (HOL, WAT, GHB) ends of the aftershock zone. Tendency for large motions at both ends of the aftershock zone, particularly to the northwest, can be seen in the Modified Mercalli intensity VII isoseismal map [Stover *et al.*, 1990]. This contrasts with the relatively low amplitudes recorded at COR, which is directly updip from the hypocenter, a location at which we expect to see strong directivity from a rupture propagating updip.

Additional evidence for bilateral rupture can be seen in the timing and similarity of the velocity recordings at GGC and SAR (Figure 3.8, middle 6 traces). As seen in Figure 3.2, these stations are symmetrically located about the fault plane and

are at nearly the same epicentral distance. Polarities for the radial and vertical components for station SAR have been reversed to correct for the change in sign of the P-SV radiation pattern in order to enhance the comparison. Although absolute time was not available for SAR, its timing was estimated by noting the similarity of the S waveform with LEX (Figure 3.2) and then correcting for the additional shear-wave propagation time from LEX to SAR. The timing and waveforms of the main arrivals at GGC and SAR are similar, although they are slightly earlier at GGC than at SAR. However, the peak amplitudes are considerably larger at SAR (Figure 3.2). These observations demand a nearly symmetric, bilateral rupture with considerably more 1 Hz energy radiated towards the northwest. A single asperity centered at or above the hypocenter could also explain the symmetry in timing and waveform at these stations, but is inconsistent with the small velocity amplitudes observed at stations located near the center of the aftershock region (BRN, CAP, COR, UCS, and WAH) that otherwise should be enhanced in amplitude by a slip concentration in the center of the fault. Further, a central asperity cannot easily account for the larger-amplitude velocities observed towards the northwest and smaller velocities observed towards the southeast. These observations agree with the main features found from the inversion of the teleseismic data.

TRIGGER TIMES AND RUPTURE INITIATION. The hypocentral parameters we use are from Dietz and Ellsworth [1990] and are given in Table 3.2. In Figure 3.9, we compare the theoretical P-wave travel times for each station with the corresponding trigger times. Because only vertical motions trigger the strong-motion accelerometers, it is likely that they were triggered by P-wave arrivals. However, the accelerometers were actually triggered nearly 2 sec later than the P-wave arrival time predicted from the hypocentral parameters of Dietz and Ellsworth [1990]. At COR, nearly directly above the hypocenter, the observed trigger time is about 1.8 sec after the P-wave arrival time predicted using the velocity model shown in Table 3.3.

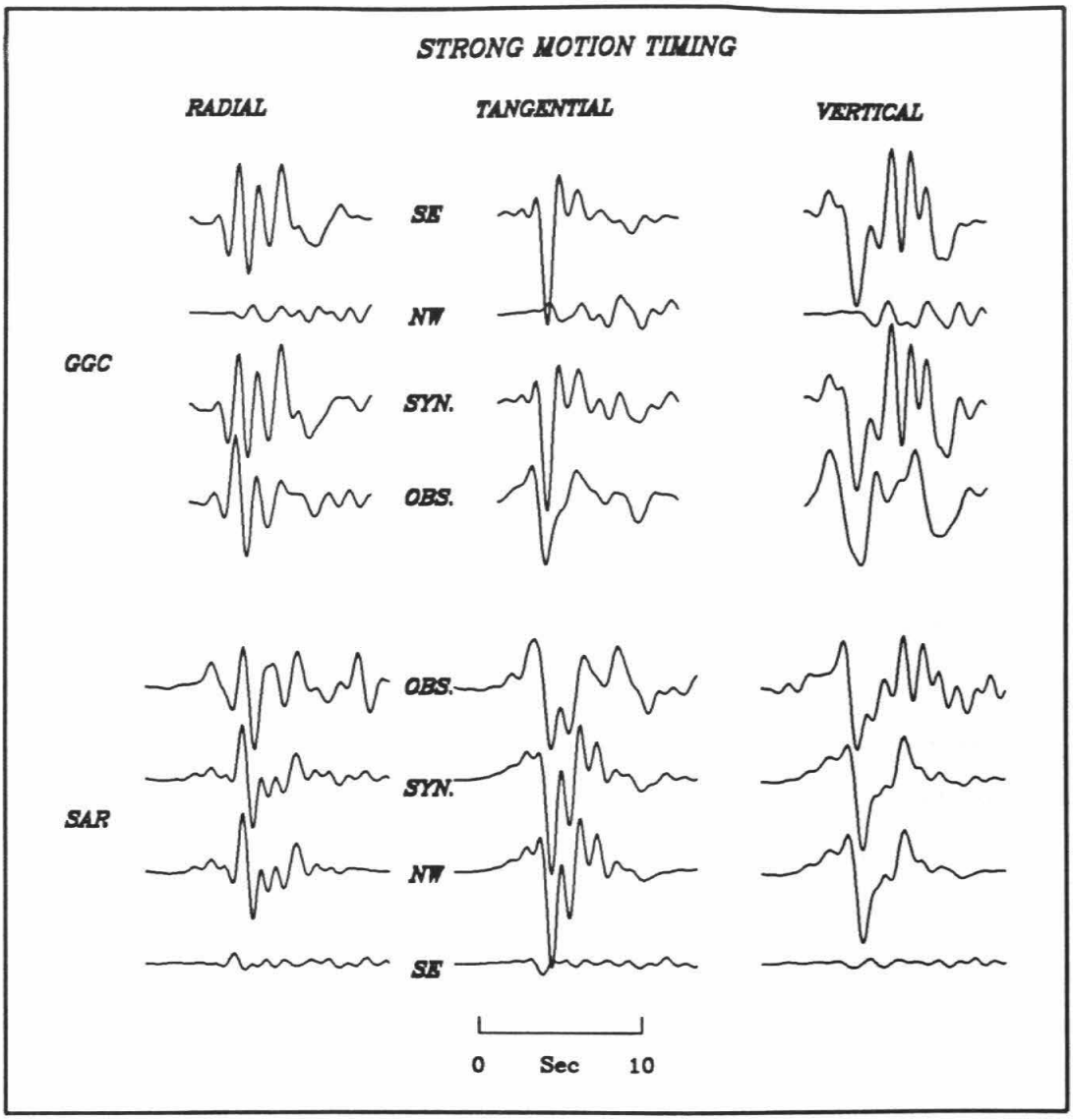

Figure 3.8: Comparison of velocity recordings for stations GGC and SAR aligned vertically in absolute time. Polarities of the radial and vertical components for station SAR have been reversed to enhance the comparison. The synthetic contribution from the northwest (NW) and southeast (SE) halves of the fault model are shown in addition to the complete synthetic velocity (SYN). For each component, the records are on the same scale and normalized to the peak value. The observed records (OBS) are adjacent to each other in the center of the figure.

Other stations show similar delays. We examine this delay in Figure 3.10 by displaying the waveforms and timing of data from a variety of instrument types. The low- and high-gain vertical components at CALNET station BSR are shown at the top of the figure, followed by teleseismic station TOL, strong-motion station SAR and station SAO (San Andreas Geophysical Observatory), a U. C. Berkeley broadband Streckeisen instrument. The waveforms for stations BSR and SAO are aligned on their first motions, and TOL and SAR are aligned according to our interpretation of the rupture initiation. That is, the simplest explanation for this 2-sec delay is that a foreshock, whose magnitude was too small (less than about 5) to trigger the strong-motion instruments, occurred about two sec before the main part of the rupture, and it is this foreshock that was located as the hypocenter using the high-gain regional network data. However, we suggest that the initial two sec represents the initial stage of rupture, perhaps a smooth, slow-growth episode [Wald *et al.*, 1991]. As shown in Figure 3.10, the initial stage of rupture clipped the nearby high-gain station BSR, but shows a long-period component as seen in the low-gain component. The low-gain component clipped after about 1.6 sec. It is after this time that 1) the first teleseismic energy becomes visible, 2) the strong-motion stations begin to trigger and 3) the local broad-band stations change character from a long-period one-sided waveform and dramatically clip. These observations can be interpreted as a slow rupture nucleation that generated insufficient long-period energy to be seen teleseismically and insufficient high-frequency radiation to trigger the strong-motion instruments.

The observation that led to the discovery of this timing problem was the initial inversion of the strong-motion waveforms using absolute time. The resulting slip-distribution model required a two-lobed pattern similar to the teleseismic results, but the centers of these lobes were forced toward the sides of the fault. The slip distribution was inconsistent with that derived from the teleseismic data and also

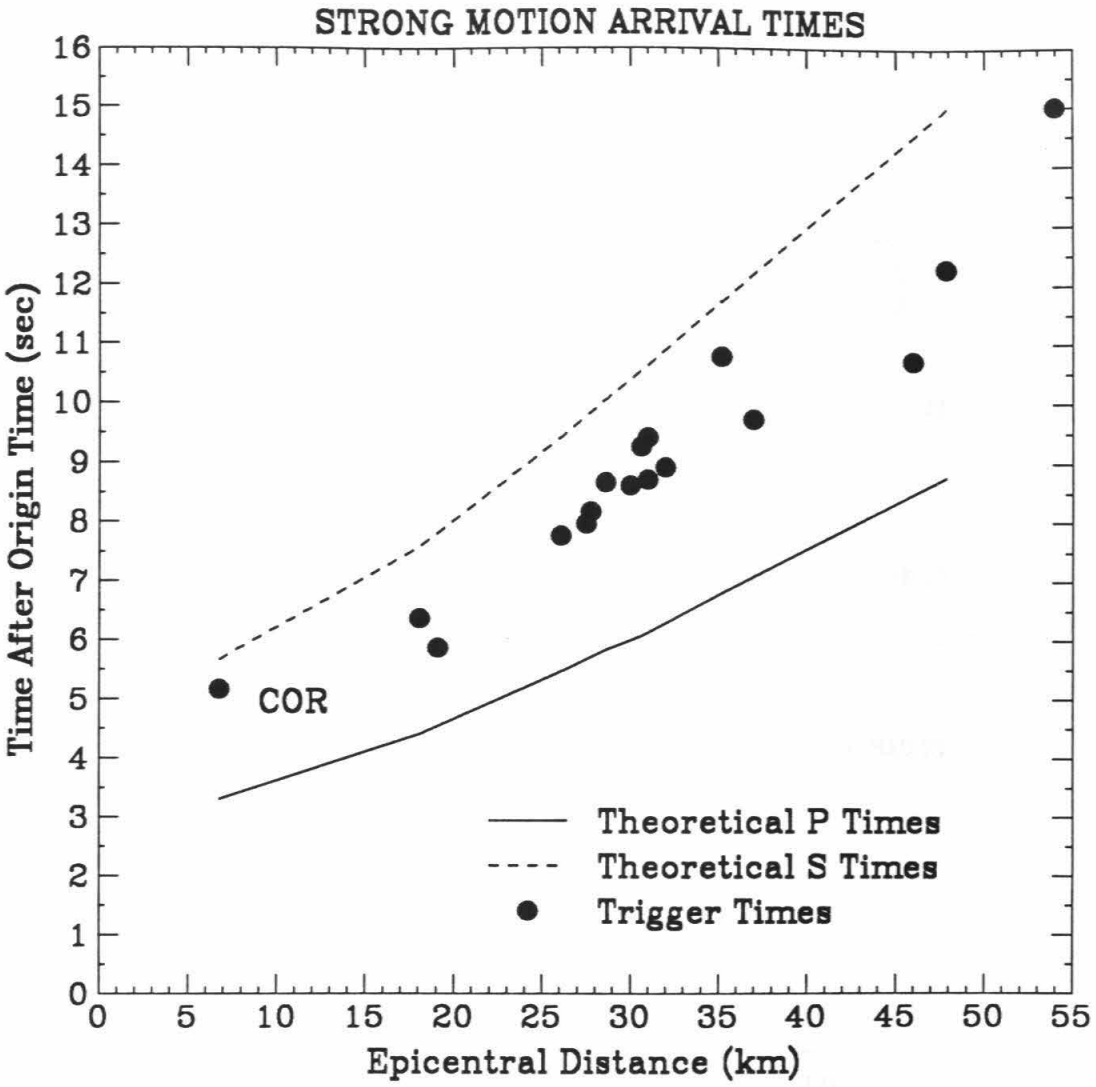

Figure 3.9: Comparison of strong-motion trigger times (stars) with the predicted *P*-wave arrival times (solid line) for the velocity model given in Table 3 based on the published hypocentral time (00 04 15.21 GMT). The predicted *S*-wave arrival time is given for reference.

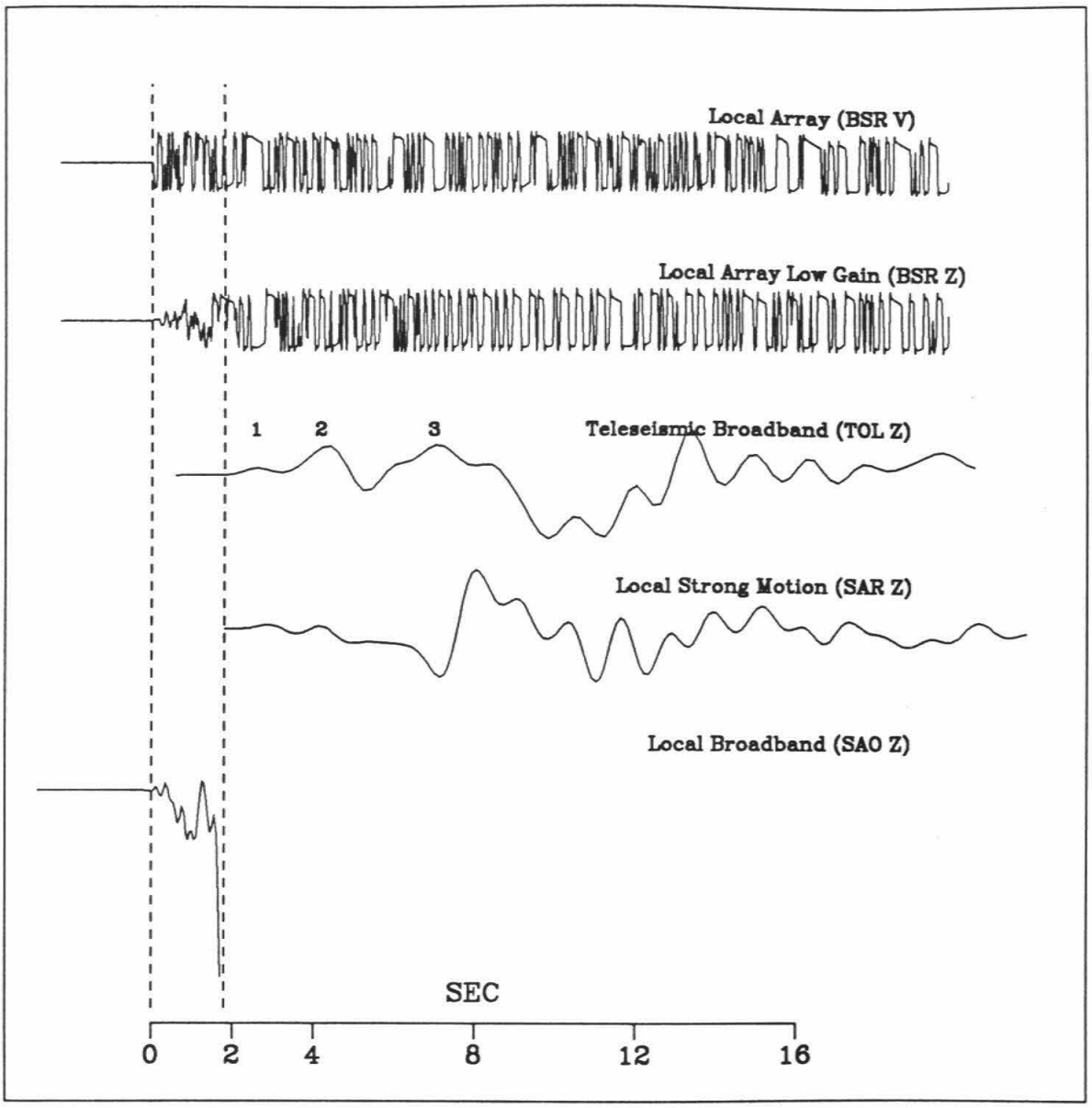

Figure 3.10: Comparison of waveforms indicating delay to main portion of the rupture. Data for stations BSR and SAO are aligned according to the first arrival, and stations TOL and SAR are aligned according to our interpretation of the rupture initiation (see text for details).Dashed lines correspond to times of 0.0 and 1.8 sec. Arrivals 1, 2 and 3 labeled on the TOL record refer to arrivals shown by arrows in Figure 3.6.

with the source region suggested by the aftershock pattern [Dietz and Ellsworth, 1990]. Furthermore, it generated inferior fits to the strong-motion data.

Thus, failure to account for this delay can seriously affect source models based on waveform inversion, using absolute timing. In particular, the modeled rupture front would have already progressed 5 km away from the hypocenter during this 2-sec interval, when, in fact, there was probably very little rupture propagation during this period. Owing to the initial weak 1.8 sec of rupture, the strong-motion records appear to be delayed by 1.8 sec with respect to the Dietz and Ellsworth [1990] origin time. We thus chose to ignore the foreshock or rupture initiation and we began modeling at the time of the first significant strong-ground motion. We assume that the main rupture began at or near the network hypocenter location and then allowed rupture to propagate out from that location. This approach is consistent with our analysis of the teleseismic data, which also begins with the first significant rupture, since the initial rupture or foreshock was too small to be recorded teleseismically.

It is not uncommon for the hypocenter determined from high-gain, regional network data to represent a foreshock or an earlier stage of rupture not observed on other data sets. Wald *et al.* [1990] discuss the rupture process of the 1987 Superstition Hills earthquake and suggest that the network hypocenter represents an earlier foreshock and not the main-rupture initiation. Hence, as seen on the strong-motion and teleseismic data, that event began rupturing in a different location than the hypocentral coordinates determined from the regional-network data.

3.8 Inversion Results

The distribution of slip from the inversion of only the strong-motion velocities is shown in Figure 3.11. Comparison of the observed (top) and synthetic (bottom) strong-motion velocities is shown in Figure 3.12, Figure 3.13 and Figure 3.14, The

Model	Moment ($\times 10^{26}$)	Maximum Slip (Cm)	Radius (Km)	Average Slip (Cm)	Stress Drop (Bars)
STRONG MOTION					
Northwest	1.9	350	7.2	209	138
Southeast	1.2	460	6.2	148	114
Total	3.1	460		134	46
TELESEISMIC					
Northwest	2.0	347	6.3	210	155
Southeast	0.8	420	5.8	129	105
Total	2.8	420		118	41
COMBINED					
Northwest	2.2	491	5.3	248	218
Southeast	0.8	371	6.2	181	136
Total	3.0	491		141	

Table 3.4: Inversion model summary. Radius refers to asperity radius (Figure 3.22) for stress-drop calculations. Stress drop is given for asperities in northwest and southeast halves of the fault shaded in Figure 3.22 and for the total fault area.

strong-motion rupture model is similar to that derived from the teleseismic inversion (Figure 3.7). Again, slip is concentrated in two patches, one centered about 8 km northwest of the hypocenter at a depth of 12 km, with a maximum slip of 350 cm, and the other centered about 6 km southeast of the hypocenter at a depth of 16 km, with a maximum slip of 460 cm. These parameters are summarized in Table 3.4. As for the teleseismic inversion, the largest, localized slip concentrations are northwest of the hypocenter.

Figure 3.11: Northwest-southeast cross section of the fault model showing contours of dislocation for strike-slip (top), dip-slip (middle) and oblique-slip (bottom) resulting from the strong-motion inversion. Contour interval is 50 cm. Shading values indicating slip in cm are given by the scale to the right of each diagram. Aftershocks with $M > 4.0$ projected onto the fault plane are represented as solid circles.

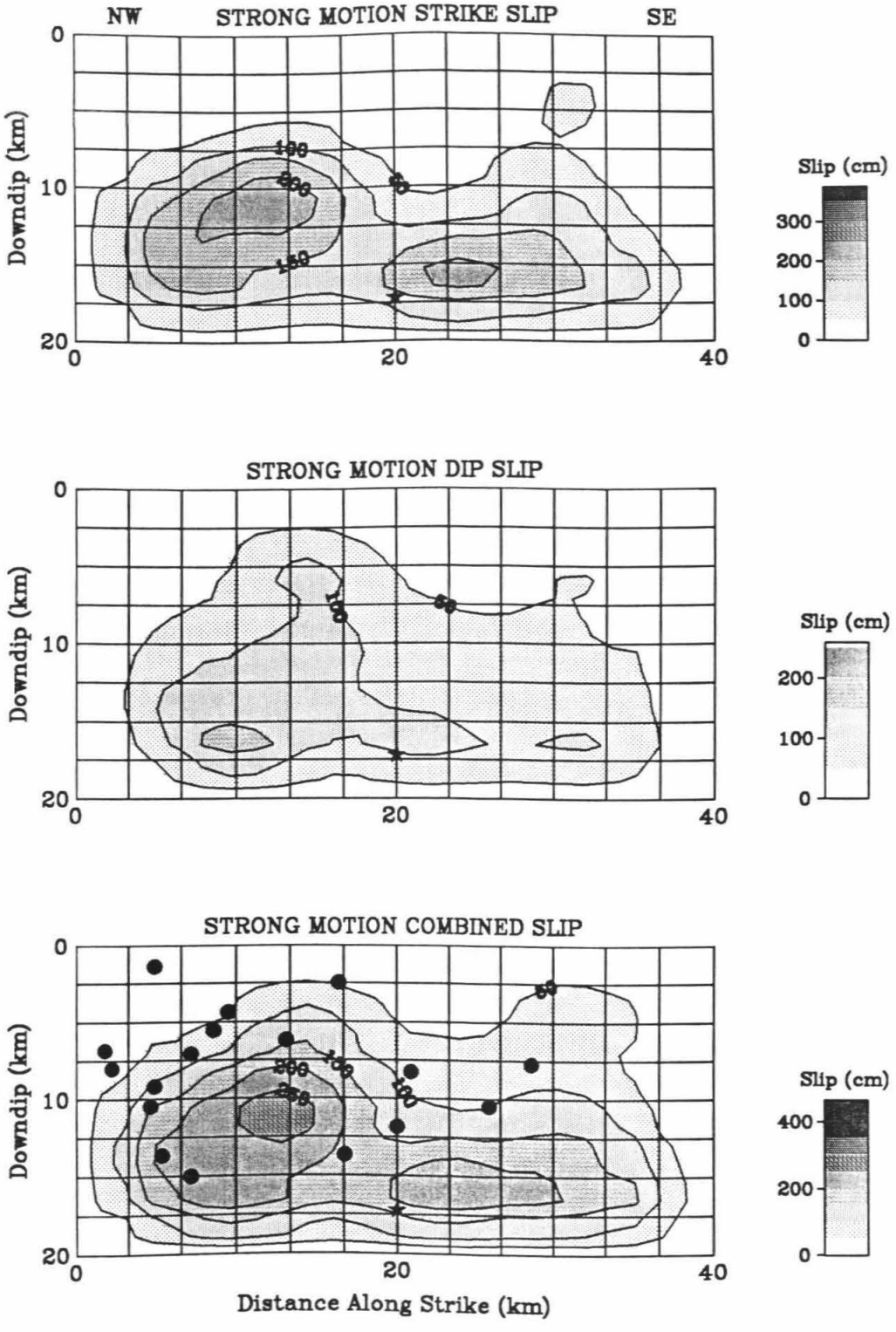
NW
STRONG MOTION STRIKE SLIP
SE
Downdip (km)
0
10
20
0
20
40
100
200
150
50
Slip (cm)
300
200
100
0
STRONG MOTION DIP SLIP
Downdip (km)
0
10
20
0
20
40
100
50
Slip (cm)
200
100
0
STRONG MOTION COMBINED SLIP
Downdip (km)
0
10
20
0
20
40
50
100
200
250
150
Slip (cm)
400
200
0
Distance Along Strike (km)

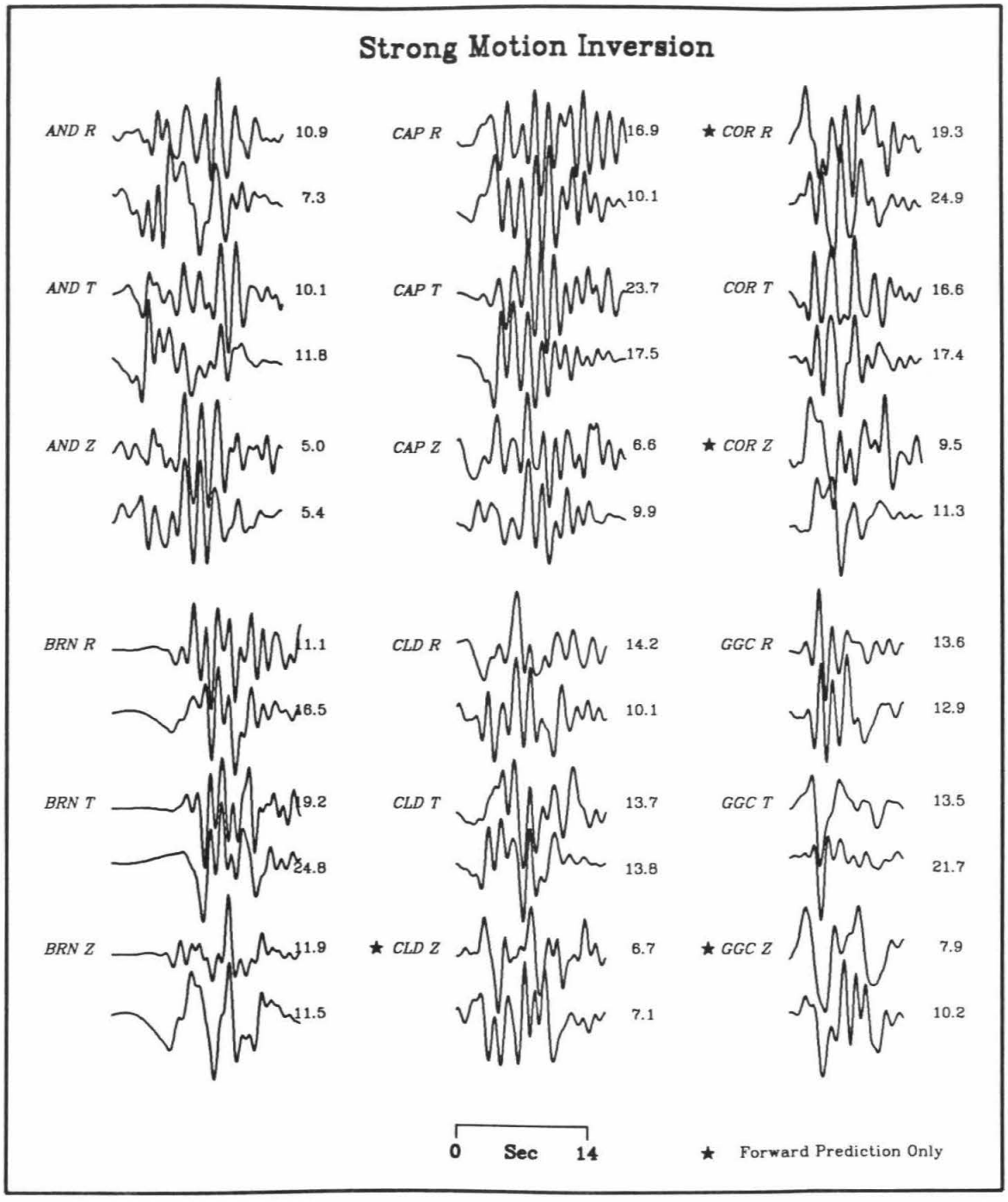

Figure 3.12: Comparison of observed (top) and synthetic (bottom) strong-motion records. Amplitudes are in cm/sec. Stars indicate data not used in the inversion.

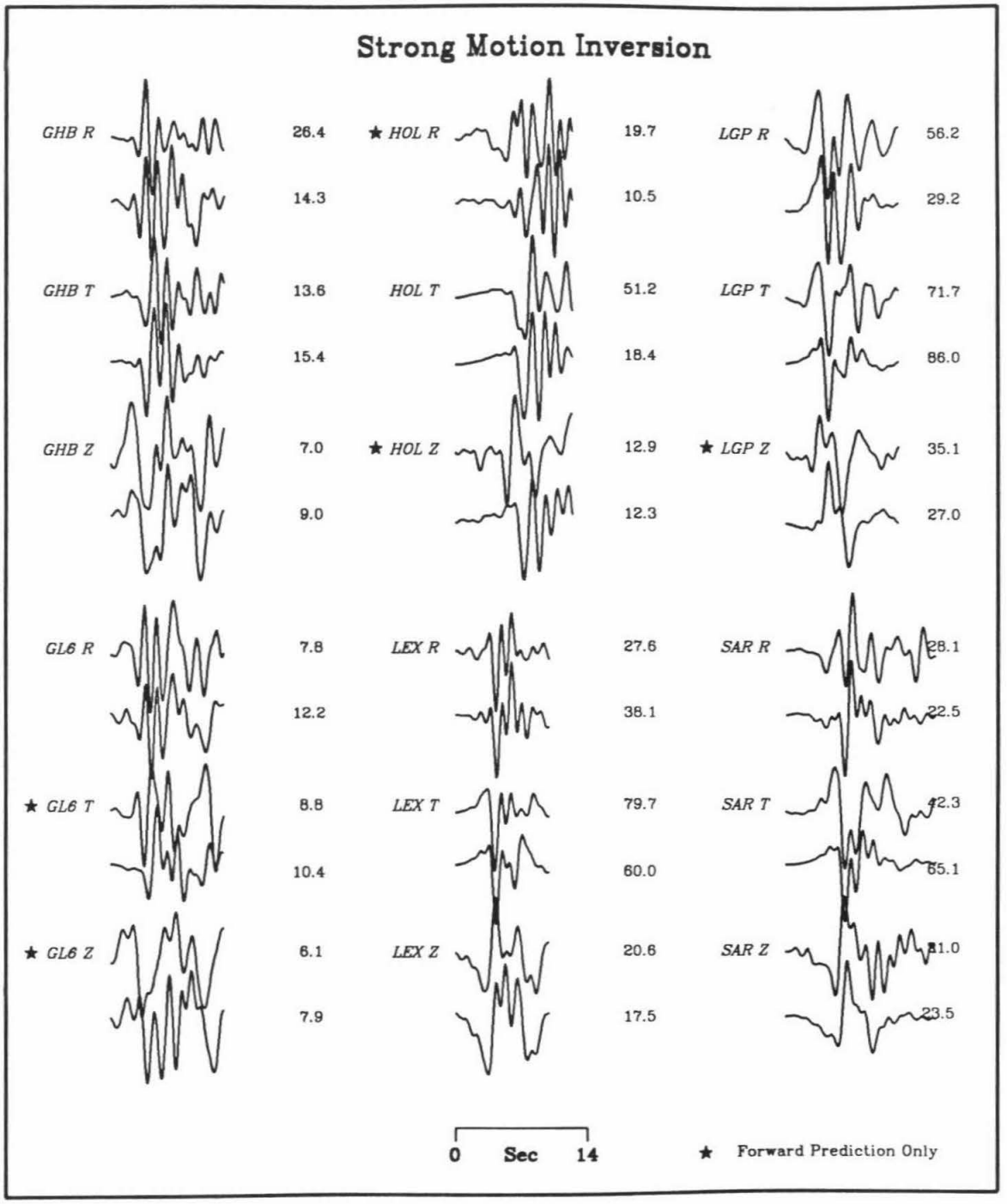

Figure 3.13: Comparison of observed (top) and synthetic (bottom) strong-motion records. Amplitudes are in cm/sec. Stars indicate data not used in the inversion.

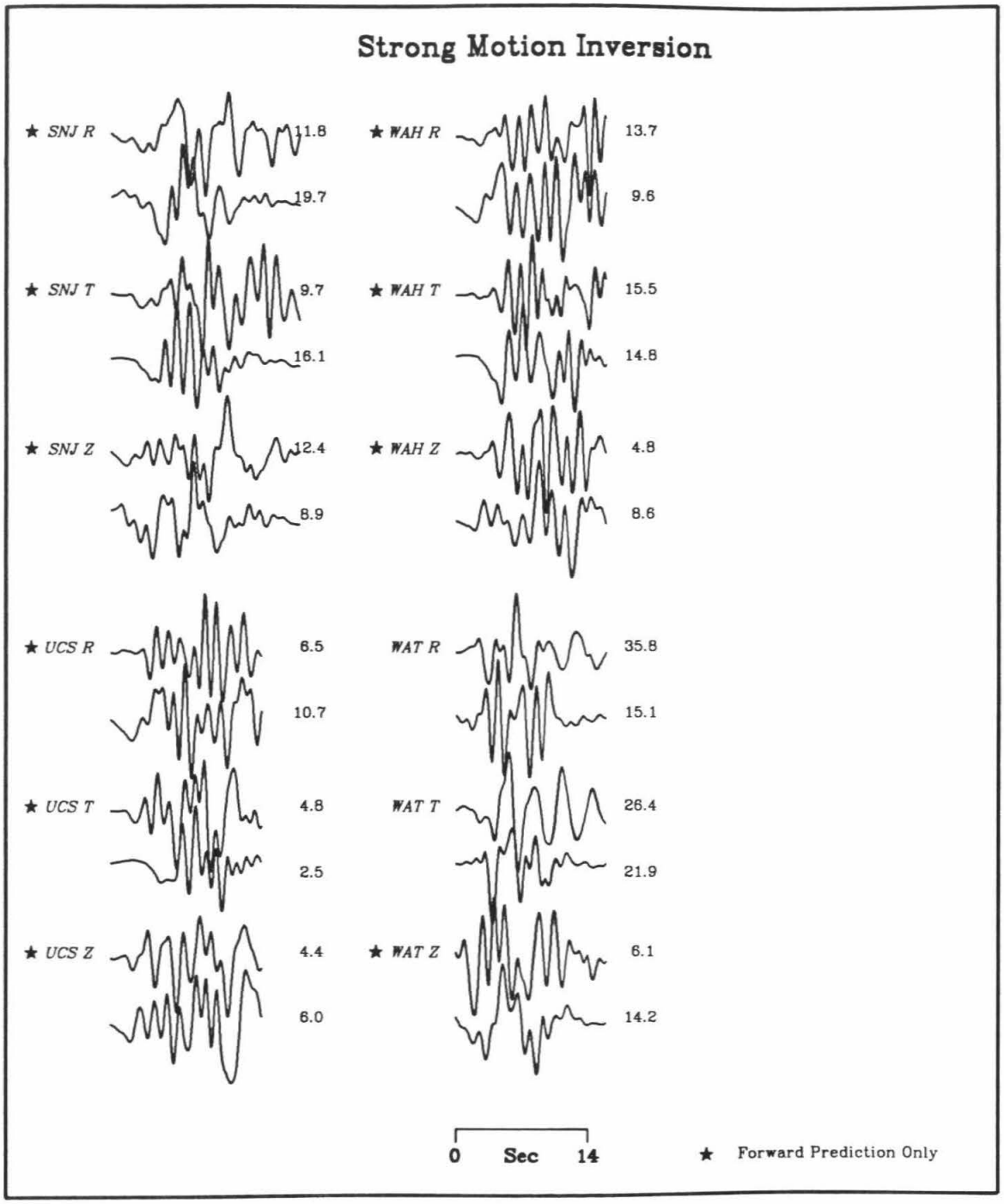

Figure 3.14: Comparison of observed (top) and synthetic (bottom) strong-motion records. Amplitudes are in cm/sec. Stars indicate data not used in the inversion.

The overall pattern of the strong-motion duration and waveform complexity can be explained by the relative position of individual stations with respect to the two lobes of concentrated slip. In Figure 3.15, for selected, strong-motion stations, we display in map view the observed (top-trace) and the synthetic (second-trace) velocities along with the surface projection of the fault plane and strong-motion slip distribution. To better understand our synthetic waveforms, we also show synthetics that result from rupture on only the northwest (NW - third-trace) and southeast (SE - bottom-trace) halves of the fault. A similar breakdown of the synthetic ground motions for all components at stations GGC and SAR is shown in Figure 3.8. Velocities at stations located nearly along strike (LEX, SAR, GGC, GHB) are controlled by the nearby slip concentration and show little contribution from the farther lobe. This is attributable to both the additional distance from the farther lobe of concentrated slip and the favorable source directivity for stations in the direction of rupture. For this reason, the waveforms at along-strike stations are simple, large in amplitude, and short in duration. Stations in the central portion of the fault (CAP, COR) show smaller amplitudes and more waveform complexity, resulting from the lack of rupture directivity and the interference of contributions from the northwest and southeast regions of large slip. We expect these waveforms to be the most difficult to model, since the synthetic seismograms are controlled by the interference of the wavefields from two propagating rupture fronts that are diverging from one another.

Sensitivity To Station Coverage. Of concern when inverting waveform data for source-rupture processes is the consideration of possible contamination from site effects and flawed data. It has been suggested [J. Vidale, personal communication, 1991] that the strong-motion instrument at station LGP moved during the mainshock, resulting in data of questionable reliability. Although we believe that the data from this station are well behaved on the basis of its waveform, frequency content and amplitude similarities to data from neighboring stations LEX and SAR (see

Figure 3.15: Display of strong-motion data (top trace), complete synthetic seismograms (second trace) and contributions from the northwest half (third trace - NW) and southeast half (bottom trace - SE) of the model fault. For each station, all traces are scaled to a common-peak value in cm/sec. The surface projection of the strong-motion slip distribution is also shown.

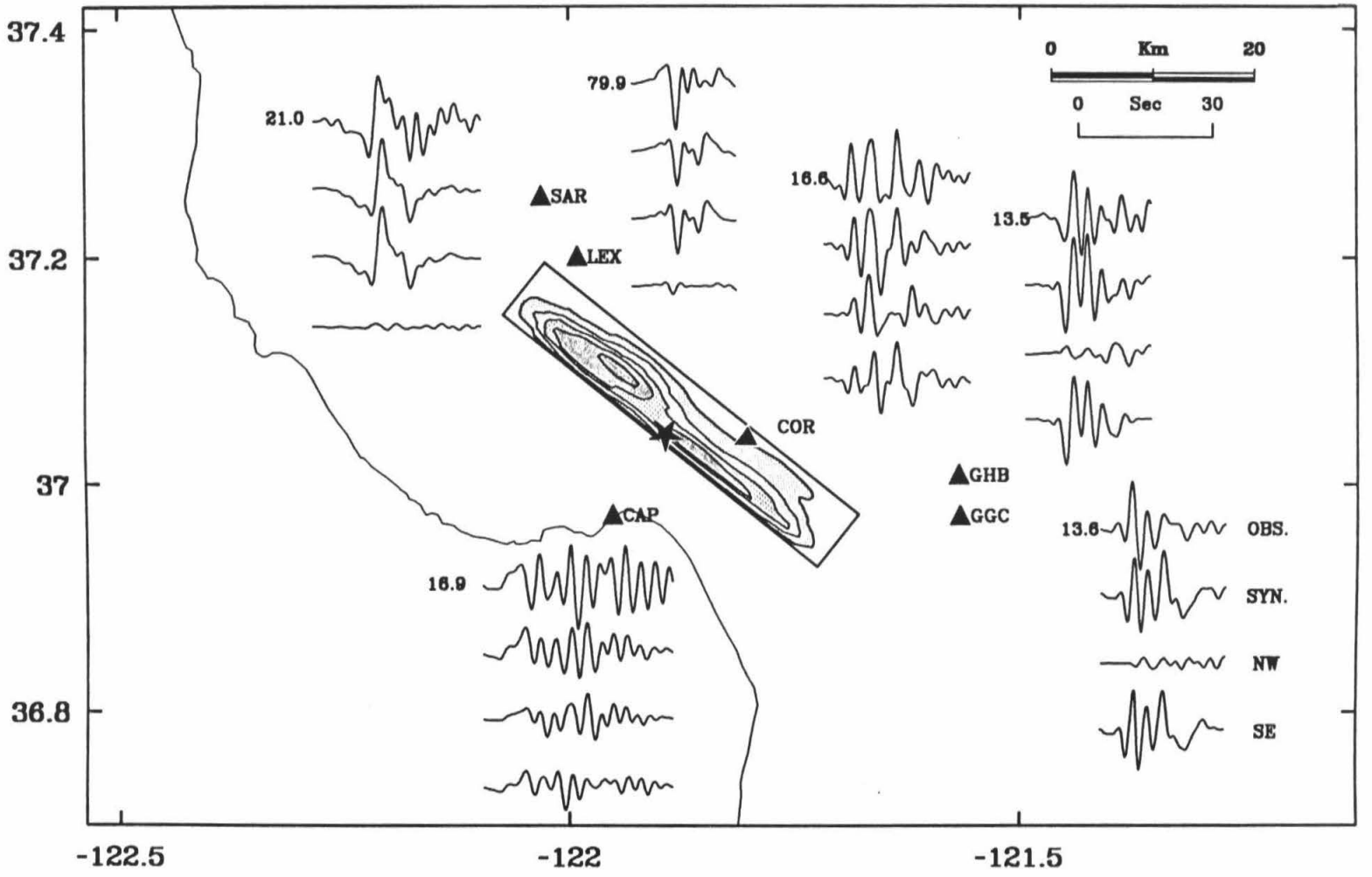
Strong Motion Contributions
37.4
37.2
37
36.8
-122.5
-122
-121.5
0 Km 20
0 Sec 30
21.0
79.9
16.6
13.5
SAR
LEX
COR
GHB
GGC
CAP
16.9
13.6
OBS.
SYN.
NW
SE

Figure 3.3 and Figure 3.4), we performed a test inversion excluding the data from LGP, to be certain of the role of that station in the final solution. The result indicated that removal of data station LGP has almost no effect on the source model. This result might have been anticipated, since any one station has only a limited role in the total solution and in particular, the data from LGP are nearly redundant, considering that the waveforms at adjacent stations SAR and LEX require a similar source contribution. In fact, the forward prediction of LGP with the solution determined without considering those data fit that record well, confirming our observation that the waveform is properly behaved and is dominated by useful source information.

3.9 Joint-Teleseismic and Strong-Motion Inversion

Although there are several features that the teleseismic and strong-motion models have in common, variations in the results are apparent. The teleseismic model has considerably more strike-slip in the shallow, southeast region of the fault. In addition, the overall depth of the slip concentration in the southeast half of the fault is deeper in the strong-motion model.

In order to test the compatibility of the teleseismic and strong-motion data and to establish a model consistent with both, we have performed a combined inversion of both data sets. In the combined inversion we used the average of the smoothing weights used in the separate inversions. Also, because of the relatively small source dimensions, the near-source, strong-motion data have more resolving power than the teleseismic data. The teleseismic data are dominated by a single velocity pulse, which is not as sensitive to subtle changes in the details of the rupture process as are the higher-frequency, strong-motion data. Accordingly, we have chosen to weight the strong-motion results by a factor of two over the teleseismic data in the combined

inversion.

The slip distribution resulting from the joint inversion of the strong-motion and teleseismic models (Figure 3.16) is very similar to that resulting from the inversion of either the strong motion or teleseismic waveforms. This could have been anticipated since our previous models, which were derived from these independent data sets, are so similar. The combined inversion model is our preferred model, and it represents a compromise between our two previous source models. However, in order to best satisfy both data sets, slip is more concentrated in the central portion of the northwest lobe of dislocation when compared with the more distributed slip seen in the previous models. There is little degradation to teleseismic-waveform matches, and the strong-motion synthetic seismograms suffer only slightly from the increased smoothing constraints.

3.10 Forward-Prediction, Ground-Motion Estimates

In this section, we make use of our finite-fault, source-inversion results for the purpose of characterizing ground motions in a more general sense. First, we are interested in determining whether or not the teleseismic, broadband data alone are sufficient to resolve adequately the source characteristics necessary to predict local, strong-ground motions. In a forward-modeling sense, this was tested by predicting the strong motions using the teleseismically derived source model. We then compared the spectral response of the strong motions predicted by the teleseismic model with the strong motions produced from the source model, derived by inverting the strong-motion data set.

Second, we show that the strong-motion inversion model is useful for estimating the nature of ground motions over the entire source region. The overall distribution of the strong-motion velocity amplitudes was characterized by predicting ground mo-

Figure 3.16: Northwest-southeast cross section of the fault model showing contours of dislocation for strike-slip (top), dip-slip (middle) and oblique-slip (bottom) resulting from the combined strong-motion and teleseismic inversion. Contour interval is 50 cm. Shading values indicating slip in cm are given by the scale to the right of each diagram.

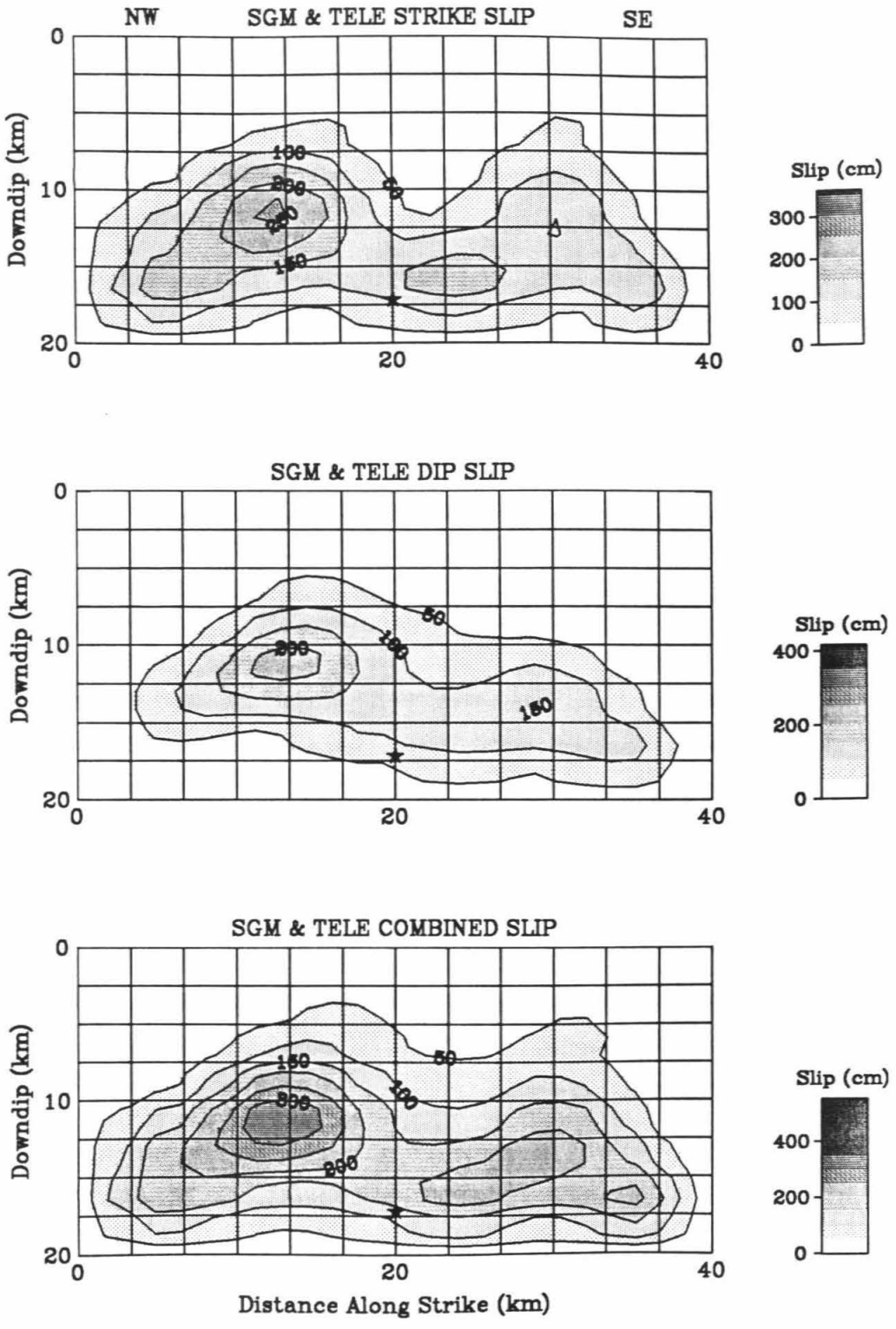
NW
SGM & TELE STRIKE SLIP
SE
Downdip (km)
0
10
20
0
20
40
100
200
250
150
50
Slip (cm)
300
200
100
0
SGM & TELE DIP SLIP
Downdip (km)
0
10
20
0
20
40
50
100
200
150
Slip (cm)
400
200
0
SGM & TELE COMBINED SLIP
Downdip (km)
0
10
20
0
20
40
150
50
100
200
250
Slip (cm)
400
200
0
Distance Along Strike (km)

tions at a variety of sites not represented by strong-motion recordings. In addition, we modified the source-rupture model and analyzed the overall effect of fault geometry and rake on the resulting ground motions. Specifically, we preserved the slip distribution of the strong-motion model, constrained the slip to be strike-slip on the adjacent vertical, shallow segment of the San Andreas Fault, and then compared the resulting ground motions to those from the dipping, oblique-slip Loma Prieta rupture. The vertical strike-slip rupture scenario is plausible for a future rupture on this segment of the San Andreas, and might be considered a lower bound on the ground motions likely experienced during the 1906 San Francisco earthquake.

3.10.1 Ground-Motion Prediction from a Teleseismic Model

Given the rupture model determined from modeling the broadband, teleseismic data exclusively (Figure 3.7), it is straightforward to compute the local ground motions at the 16 stations that recorded the strong motions (Table 3.2). We simply replace the strong-motion slip model with the teleseismic slip model and compute, in a forward sense, the resulting ground velocities. Recall that the fault-model parameterization is identical for both the strong-motion and teleseismic data sets; only the spatial smoothing and final slip distribution, including the relative weights within each of the three time windows, vary.

We might expect that given the similarities of the teleseismic model to the strong-motion model (Figure 3.7 and Figure 3.11), a comparable set of strong motions would be produced. In Figure 3.17 we compare, for selected stations, the observed ground-motion velocities (top) with the synthetic waveforms produced by the strong-motion model (middle) and the teleseismic model (bottom). The stations displayed in Figure 3.17 were chosen since they are representative of regions above the northwest, center and southern portions of the fault. The waveform comparison indicates that the teleseismic synthetic ground motions (bottom) fit the overall amplitude and du-

rations of the observed ground motions quite well. We should expect the amplitude and phases of individual arrivals to be different from the strong-motion data, considering that this phase information was not part of the teleseismic inversion. We do note, however, that there is a slightly longer-period character to the teleseismic-source ground motions (bottom) than for the strong-motion synthetics (middle) and the data (top). This shift to longer periods is particularly noticeable at station LEX (Figure 3.17).

For a more systematic comparison, we can quantify the misfit to the observations for both the strong-motion and the teleseismic-source models by examining the difference in the response spectra of the observed and synthetic ground motions. We employ the methodology of Abrahamson *et al.* [1990] used to evaluate the uncertainty in numerical, strong-motion predictions as appropriate for applications in engineering. We take the natural logarithm of the spectral acceleration at 5 percent damping on each horizontal component and then average the log spectra for the two horizontal components. As shown by Abrahamson *et al.* [1990], the estimated model bias is given by the mean error as a function of frequency:

$$\varepsilon(f) = \frac{1}{N} \sum_{i=1}^{N} lnSA_i^o - lnSA_i^s$$

where SA_i^o is the observed and SA_i^s is the synthetic, spectral acceleration for the i^{th} recording, and N is the total number of recordings used. We compute the mean error only for frequencies within the bandpass of the inversion (0.2 to 1.0 Hz).

The mean error averaged over for both horizontal components of all stations and the 90% confidence interval of the bias are shown in Figure 3.18. The left plot displays the model bias for the strong-motion source model and the right side shows the model bias from the teleseismic source model. The model is considered unbiased if the bias is not significantly different from zero at the 90% confidence level [Abrahamson *et al.*, 1990]. Over this frequency range, there is very little bias

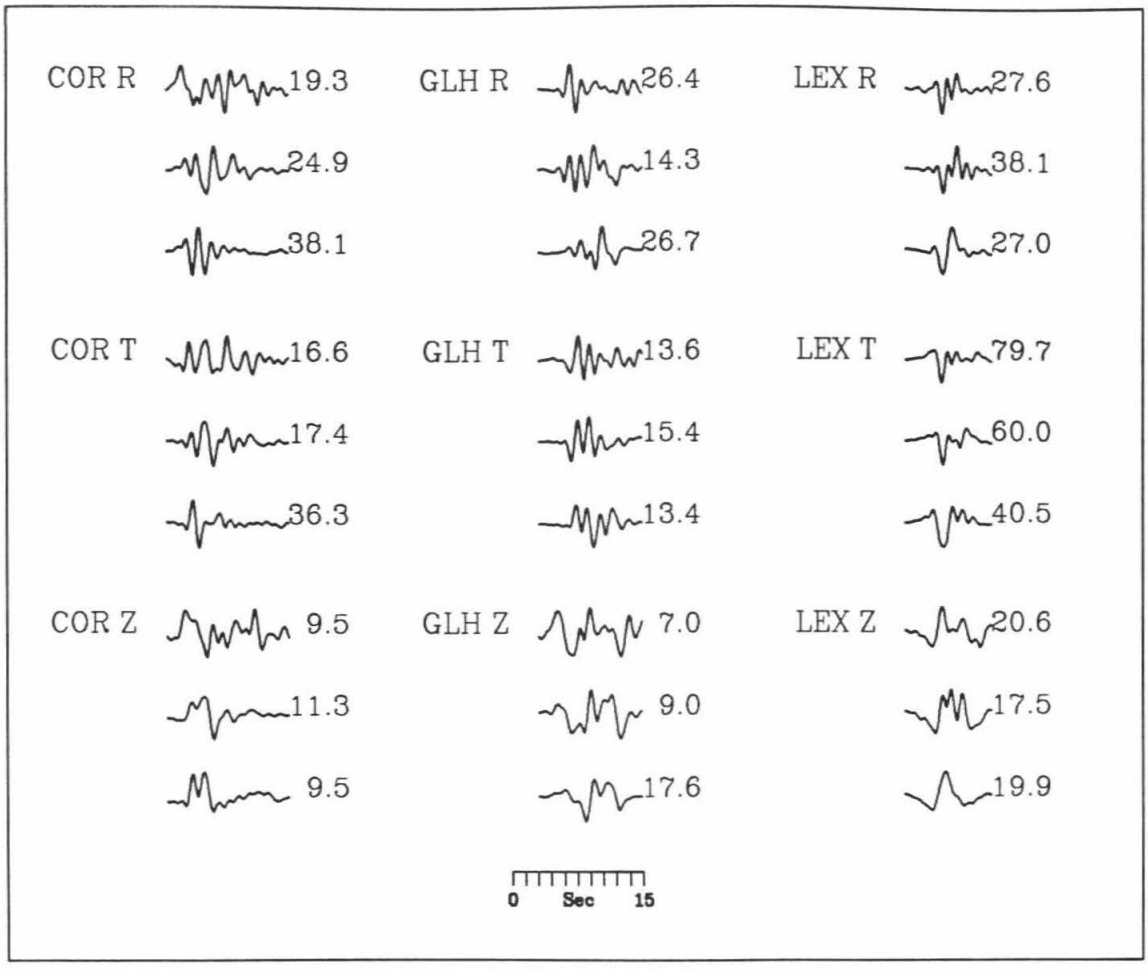

Figure 3.17: Comparison of observed (top), strong-motion synthetics produced with the strong-motion, dislocation model (middle) and strong-motion synthetics produced using the teleseismic-dislocation model (bottom) for selected stations. Amplitudes are in cm/sec.

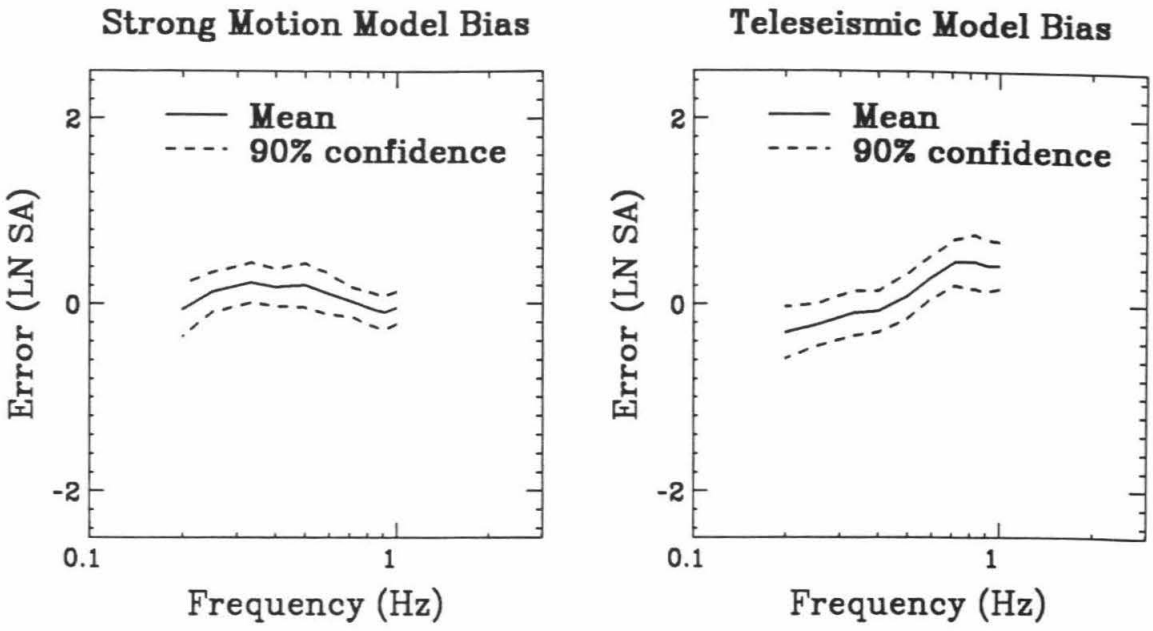

Figure 3.18: Model error and 90% confidence interval of the bias for the strong-motion model (left) and the teleseismic model (right).

for the strong-motion synthetics compared with the data. Of course, this is expected, considering that the solution was determined using a least-squares fit between the strong-motion observations and the strong-motion synthetics.

For the teleseismic model within the 90% confidence interval, the bias is only marginally different from zero. The synthetics slightly overpredict the data at frequencies less than 0.4 Hz, and slightly underpredict for higher frequencies. This indicates, though, that the broadband, teleseismic solution, determined independently from the strong-motion data, can provide a means for predicting the near-fault ground motions for comparable earthquakes that might lack strong-motion recordings.

It should be noted that the forward prediction of strong-motion data from the teleseismic data are sensitive to the spatial smoothing chosen for the teleseismic model. For this reason, the Loma Prieta earthquake, with abundant teleseismic as well as local data, presents a unique chance to examine the relationship between these parameters. Since there is a general tendency for inversions of teleseismic data alone to prefer solutions with numerous isolated, large-slip subfaults, significant smoothing was required to minimize the variation of slip between adjacent subfaults. Thus, as presented, the teleseismic model represents a lower estimate of the fault-slip heterogeneity. The net effect is a noticeable underprediction of the higher frequencies (> 0.7 Hz) as shown in Figure 3.18, and a slight overprediction at longer periods ($<$ 0.4 Hz).

It appears that our estimation of the smoothing required for the teleseismic model is reasonable, considering the sufficient fit to the strong-motion predictions (Figures 3.17 and 3.18). In future work we hope to examine more fully the relationship between the *a priori* spatial smoothing used for teleseismic modeling and the effects on estimations of higher-frequency radiation.

3.10.2 Estimated Peak Ground-Velocity Distribution

With the dislocation model presented from the inversion of the teleseismic and/or strong-motion data, it is also possible to characterize the ground motions for a site at any location within the source region. For example, Hartzell and Iida [1990] used their rupture model of the 1987 Whittier Narrows earthquake, derived from the inversion of local strong-motion data, to forward-predict the ground motions over the entire epicentral region. When using this approach, we are limited only by the farthest distance to which adequate Green's functions are available. For the Loma Prieta source area, we computed synthetic ground velocities over a grid of stations (crosses in Figure 3.19) with east-west separations of 9 km and north-south separations of 5 km. In all, ground motions were computed at 64 locations in addition to the 16 original station locations (Table 3.2). The peak value of ground velocity was determined at each grid station, and then these values were contoured over the region. In all, ground motions were computed at 64 locations in addition to the 16 original station locations (Table 3.2). The peak value of ground velocity was determined at each grid station, and then these values were contoured over the region. The contours of peak velocity are shown in Figure 3.19 with an interval of 10 cm/sec. Two lobes of large peak values are apparent, one in the southeast portion of the fault; the other in the northwest portion. The largest amplitude simulations, over 70 cm/sec, are concentrated above the northwest portion of the fault. The two lobes represent the combined effects of the two asperity depths and locations (Figure 3.11) together with the source-radiation pattern. The oblique mechanism, with an average rake of 142°, favors radiation towards the northwest even for a uniform distribution of slip.

The overall pattern of peak velocities (Figure 3.19) agrees well with many of the observed indicators of strong ground shaking during the Loma Prieta earthquake, confirming that the regions above the northwestern portion of the fault experienced

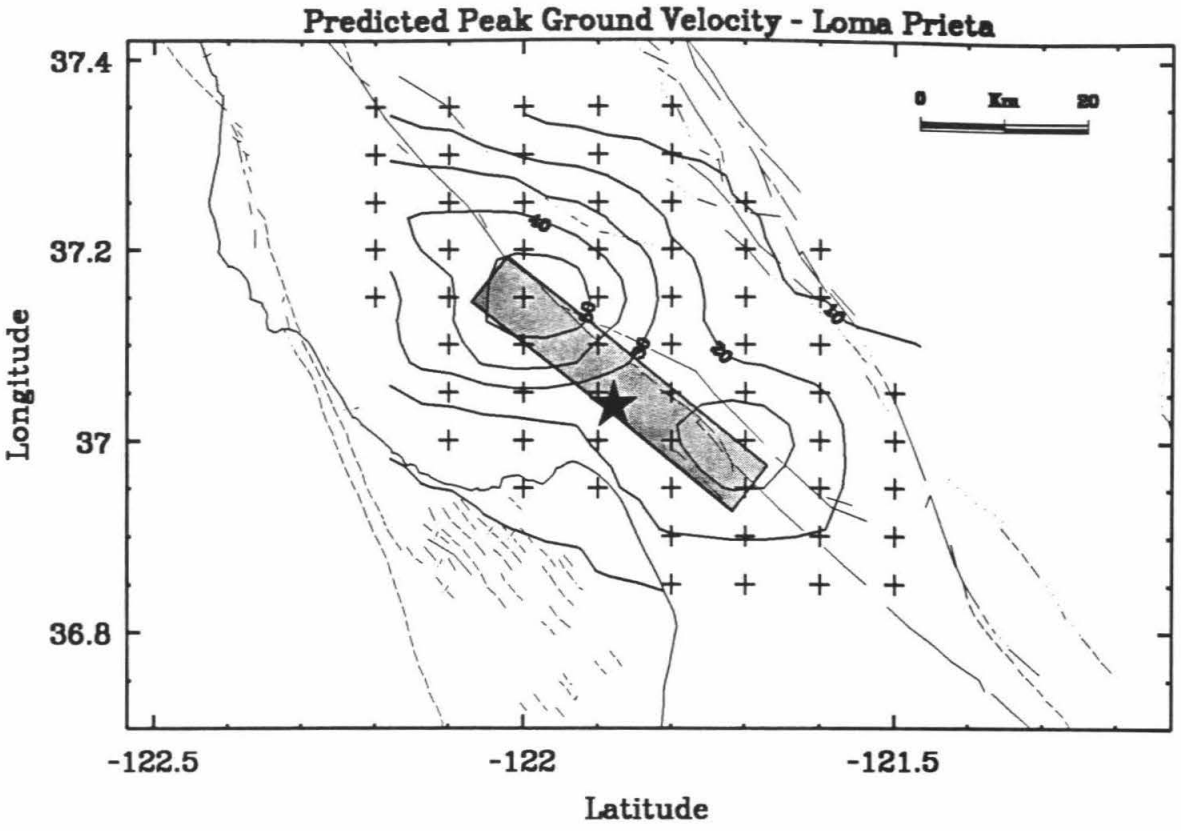

Figure 3.19: Predicted distribution of ground velocities from the strong motion derived source model. Crosses show locations of the grid of stations for the forward prediction. Contour interval 10 cm/sec. The shaded region represents the surface projection of the model fault plane.

the strongest shaking. The largest observed ground velocities were located at stations (LEX, LGP and SAR) within the northwest lobe of high-amplitude computed ground motions. Further, the Modified Mercalli intensity map of Stover *et al.* [1990] shows a localized concentration of intensity VIII observations within the northwest lobe of large computed ground motions. This region of the southern Santa Cruz Mountains, was also the location of the majority of ground ruptures and fissures formed during the earthquake, particularly along Summit Road and Skyline Ridge. Ponti and Wells [1991] attributed these displacements to shaking-induced, gravitational spreading of ridges and downslope movement. They also noted that the greatest damage to competent structures and the highest concentration of topped trees, displaced boulders and seismically activated landslides occurred in this region.

Finally, to further characterize the ground-motion hazards in this region, we modified the strong-motion rupture model to simulate a vertical strike-slip rupture along the San Andreas fault, having a comparable slip distribution to the Loma Prieta strong-motion model. By rotating the model fault to a vertical plane and constraining the dislocation to be pure, right-lateral strike-slip, we approximate rupture along the San Andreas fault. To be consistent with the average depth of significant slip from other strong-motion, waveform inversions of California, vertical strike-slip earthquakes [Hartzell and Heaton, 1983; Hartzell and Heaton, 1986; Beroza and Spudich, 1988; Wald *et al.*, 1990], we needed to decrease the asperity depth compared to the Loma Prieta model. This was done by bringing the top of the fault to within 0.5 km of the surface and translating the slip (shown in Figure 3.11) 5 km closer to the top of the fault (Figure 3.20). The strike was kept identical to that of the Loma Prieta model, giving a minor discrepancy of the model fault (the straight line in Figure 3.21) strike compared to the strike of the San Andreas fault. The absolute amount of slip was preserved, resulting in a slightly smaller overall moment (that was due to the reduced rigidity at the depths of the shallower slip). The slight difference

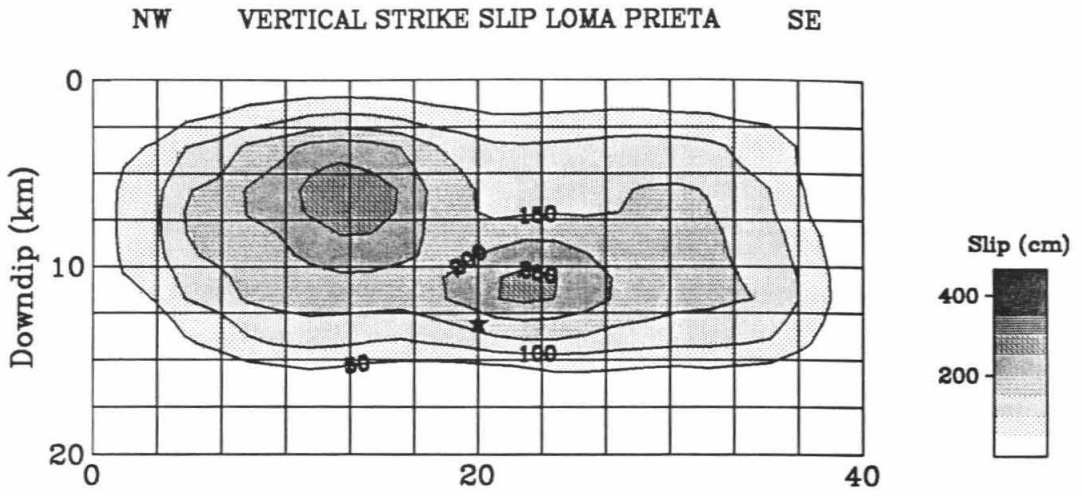

Figure 3.20: Northwest-southeast cross section of the fault model, showing contours of dislocation for the vertical strike-slip derived from the strong-motion slip distribution. Contour interval is 50 cm.

in the contours (Figures 3.11 and Figure 3.20) was a result of compressing the fault width over which the slip occurred.

The overall pattern of the resulting peak ground velocities computed with the vertical, strike-slip fault model (Figure 3.20) is shown in Figure 3.21. The contour interval is in cm/sec. Note that the overall amplitudes are larger than the Loma Prieta model. The maximum velocity is over 90 cm/sec. The larger amplitudes can be attributed to the relatively shallow slip relative to the Loma Prieta model. Note that the asperity towards the northwest portion of the fault is shallower than the one

towards the southeast (Figure 3.20). This suggests that near-source ground motions during the Loma Prieta earthquake were moderated by the relatively large average depth of significant slip.

3.11 Discussion

Up to this point, we have presented our slip models using contour maps that have been spatially smoothed to de-emphasize the abrupt subfault boundaries used in our inversion scheme. In order to show a more detailed comparison of our inversion models, we show slip vectors for individual subfaults in Figure 3.22. Maximum values for the absolute slips are given in Table 3.4. The average rake angles, based on the relative components of strike-slip and dip-slip for the strong-motion, teleseismic and combined inversions are 142°, 144°, and 145°, respectively. This agrees well with the range of values given in the teleseismic, point-source studies of other researchers and with geodetic-modeling results [Lisowski *et al.*, 1990].

Inversion of only the teleseismic data does not result in systematic spatial variations of the rake angle (Figure 3.22, middle). However, inversions using the strong-motion data (Figure 3.22 top, bottom) show a clear tendency for more vertical rake angles for slip that is northwest of the hypocenter and for more horizontal rake angles for slip that is to the southeast. Although our models assume that all slip occurs on a single, 70° dipping plane, this systematic change in rake angle coincides with an apparent change in the dip of the aftershock zone from about 70° for the segment northwest of the hypocenter to nearly vertical near the southeastern edge of the fault plane [Dietz and Ellsworth, 1990].

One shortcoming of our model is its failure to produce the large-amplitude, transverse motions observed at HOL (Figure 3.13), although site-response studies do indicate significant site amplifications at this station [K. Aki, personal communication,

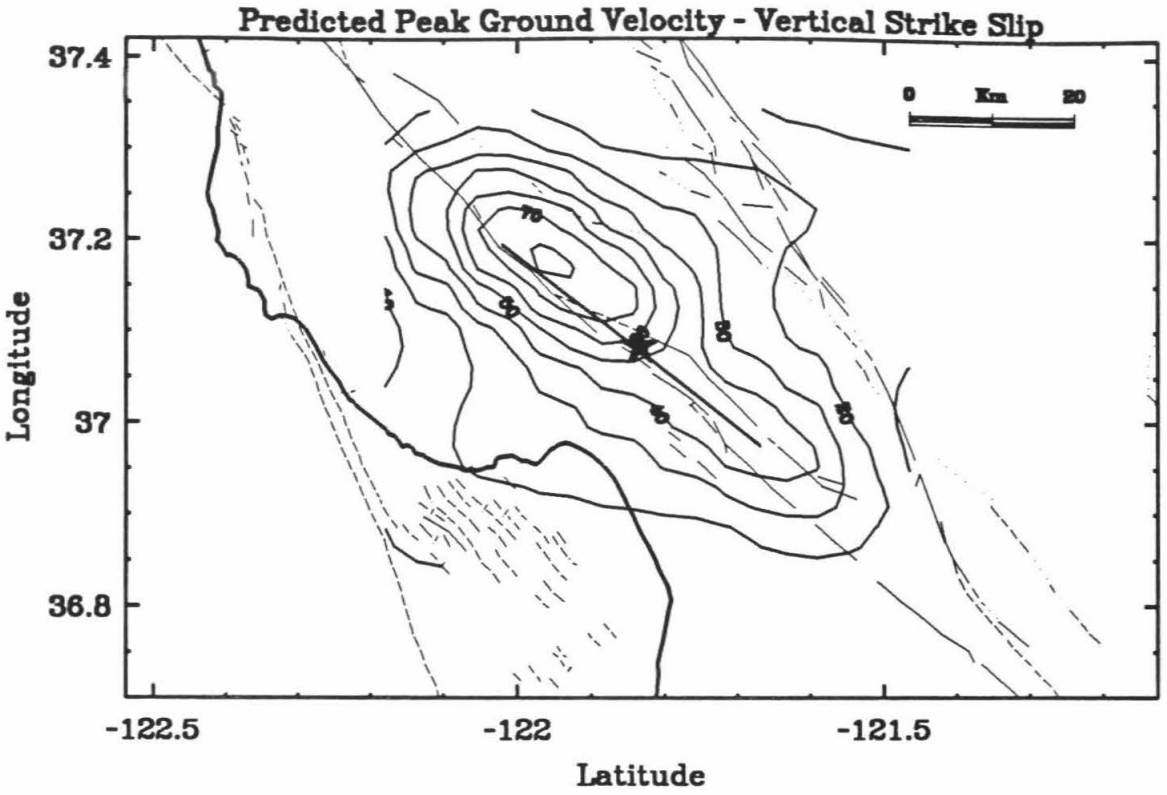

Figure 3.21: Predicted distribution of ground velocities from a vertical strike-slip rupture along the San Andreas with the Loma Prieta slip distribution. Contour interval 10 cm/sec. The model fault location and length is depicted by the straight line.

Figure 3.22: Northwest-southeast cross section of the fault model showing the rake angle for each subfault as determined in each inversion. The length of the vector is proportional to the amount of slip, each normalized by the peak slip on the fault plane.

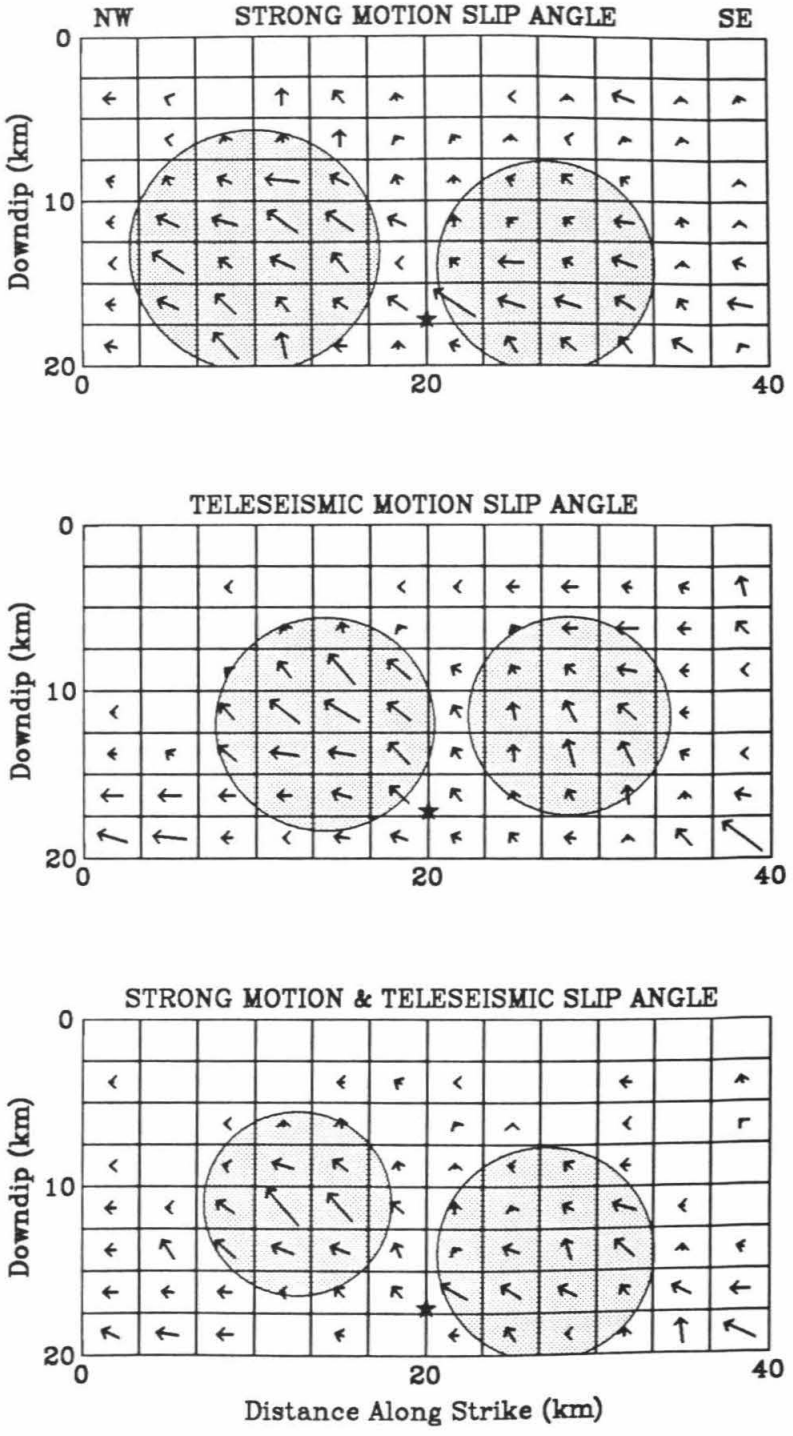
NW
STRONG MOTION SLIP ANGLE
SE
Downdip (km)
0
10
20
0
20
40
TELESEISMIC MOTION SLIP ANGLE
Downdip (km)
0
10
20
0
20
40
STRONG MOTION & TELESEISMIC SLIP ANGLE
Downdip (km)
0
10
20
0
20
40
Distance Along Strike (km)

1991]. HOL is located along the southeast projection of the fault, and it has an unusually large motion perpendicular to the fault strike (Figure 3.13). Strike-slip faulting on a separate vertically dipping, southeast trending fault plane located at the southeast end of the aftershock area (perhaps the San Andreas fault) is suggested by this waveform. The radiation pattern from a vertical, strike-slip mechanism would greatly enhance the tangential component and yet not contribute to the near-nodal radial and vertical components. Such a model is consistent with the near-vertical aftershock distribution and strike-slip mechanisms near the southeastern edge of the inferred rupture zone [Dietz and Ellsworth, 1990]. Pure strike-slip motion occurs on the shallow, southeastern section of our fault inferred from the teleseismic data (Figure 3.22, 2.5-7.5 km downdip, 23-36 km along strike), but is not seen in models inferred from strong-motion data.

To estimate the stress drop for the regions of concentrated slip, we approximate their area with a circular region and calculate the average slip within that region. The choice of regions for stress-drop calculations are the shaded regions in Figure 3.22. The stress-drop expression of Eshelby [1957] for a circular fault, $\Delta\sigma = (7\pi\mu\overline{u})/(16a)$, where μ is the rigidity, $\overline{u}$ is the average dislocation and a is the radius, is used for this calculation. Using $\mu = 3.4 \times 10^{11}$ dyne/cm^2, we obtain the stress-drop values given in Table 3.4. For the entire fault rupture, it is more appropriate to use the relationship of Parsons *et al.* [1988] for a long, buried, strike-slip fault, $\Delta\sigma = (C\mu\overline{u})/(w)$, where w is the downdip fault width and C is a constant dependent on the fault-plane dimensions. Using our fault dimensions, their results require C to be approximately equal to 1.75. We use $w = 17$ km and have tabulated the stress drops for all three inversions in Table 3.4.

In general, the rupture dimensions of significant slip agree well with the overall slip dimensions based on the active perimeter of the aftershock zone [Dietz and Ellsworth, 1990]. This result is consistent with the observation of Mendoza and Hartzell [1988b]

that aftershocks often cluster along the margin of regions of the fault that experienced large, coseismic slips. The regions of major slip in our models coincide with a region of relatively few aftershocks in the central portion of the aftershock zone. However, our model suggests less updip rupture than was inferred by Dietz and Ellsworth [1990] from the aftershock distribution alone. Hence, while the general features of the rupture may often be inferred from the aftershock activity, significant features of the rupture may be obscured in the aftershock patterns. The exact details of the aftershock pattern for this earthquake vary significantly, depending on the time duration chosen for the analysis [see, for example, Dietz and Ellsworth, 1990, Figures 3a, 3b, and 3c). Consequently, we consider only the larger ($M > 4.0$) aftershocks, including those within the first 34 minutes of the mainshock [Simila *et al.*, 1990], and find a tendency for aftershocks to cluster around the major slip concentrations in our models (Figure 3.11, bottom), particularly in the northwest region of the fault.

The use of three time windows (each having a duration of 0.7 sec) allows us to make general observations about the nature of the rupture velocity and slip-time history. We expect regions requiring a locally slower rupture velocity to make use of the later time windows in order to compensate for the slower, fixed-rupture velocity. Likewise, regions with a faster rupture velocity would take advantage of only the first rupture window. Overall, in both the strong-motion and teleseismic inversion, slip in the first window dominates, with minor slip occurring in the second and third windows (Figure 3.23) over much of the fault. This implies that the rupture timing in our model satisfies the data, and that large variations in the rupture velocity are unnecessary. There is some suggestion of locally slower rupture velocity or somewhat longer slip duration along the outer northwest margin of the northwestern asperity, the same region that exhibits the majority of $M > 4.0$ aftershocks.

The fact that most of the slip is concentrated in the first time window indicates that our models prefer short slip durations (less than 1 sec) for a given point on the

Figure 3.23: Separate oblique-slip contributions for time window 1 (top), 2 (middle) and 3 (bottom) resulting from the strong-motion inversion. Each time window is separated by 0.6 sec. Contour interval is 25 cm.

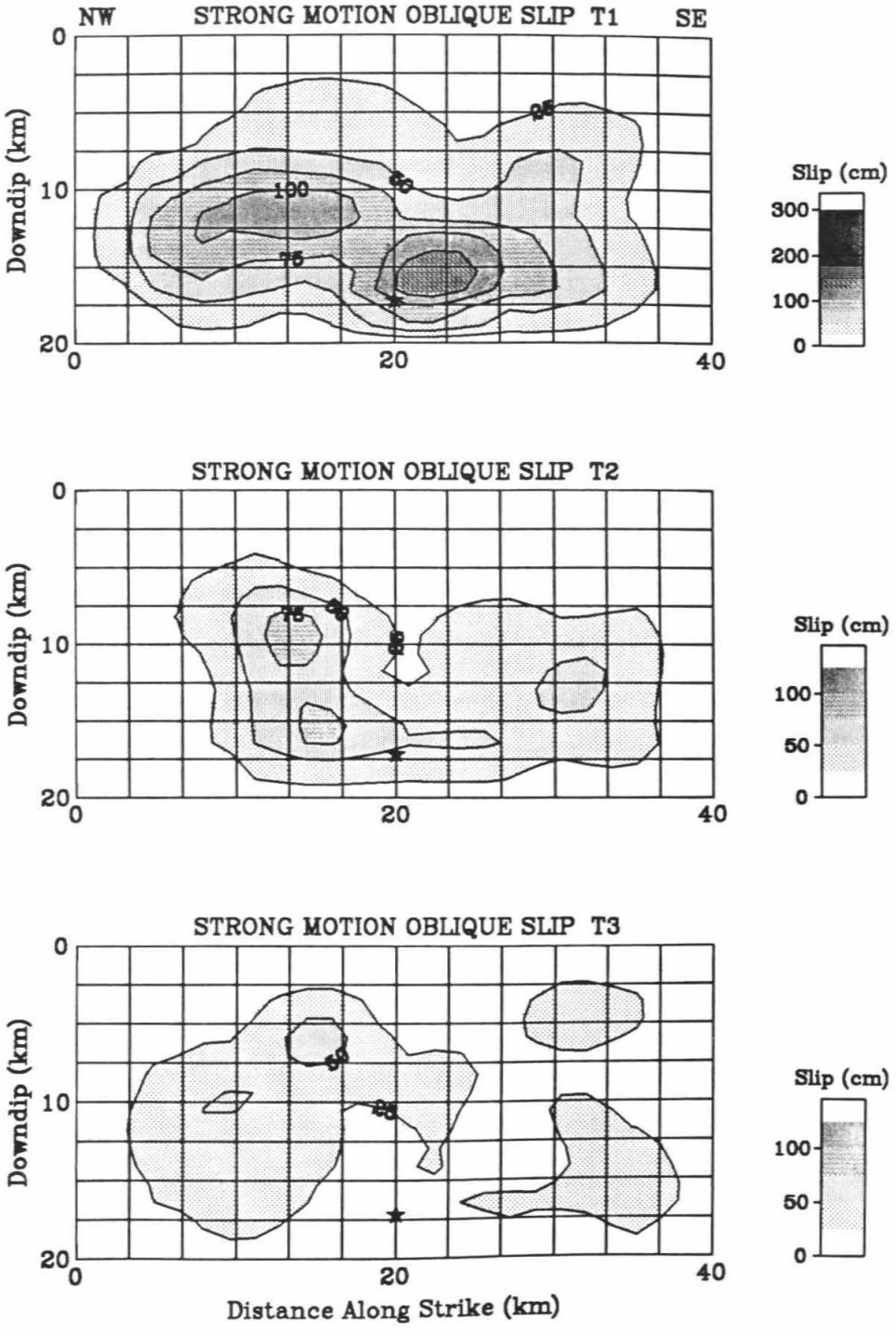
NW
STRONG MOTION OBLIQUE SLIP T1
SE
Downdip (km)
0
10
20
0
20
40
25
100
75
Slip (cm)
300
200
100
0
STRONG MOTION OBLIQUE SLIP T2
Downdip (km)
75
Slip (cm)
100
50
0
STRONG MOTION OBLIQUE SLIP T3
Downdip (km)
Slip (cm)
100
50
0
Distance Along Strike (km)

fault. This implies that only a small portion of the entire rupture surface is slipping at any given time. For example, the portion of the fault rupturing 5 sec after the nucleation time is depicted in Figure 3.5 as the shaded area within time window 1. Short slip durations have been inferred for other earthquakes and they have an important implication for rupture mechanics [Heaton, 1990].

3.12 Conclusions

From analysis of the three inversion results, we find a bilateral dislocation pattern with two main regions of oblique slip. One region is centered about 6-8 km northwest of the hypocenter at a depth of 11-13 km and the other is centered at 7-9 km southeast of the hypocenter near a depth of 15-16 km. The northwestern patch has a larger moment, a higher average slip, and consequently, a larger overall stress drop (Table 3.4). It is also the source of the largest observed strong-motion velocities recorded about 20 km northwest of the epicenter (see Figures 3.2, 3.3, 3.4 and 3.15). Dominant radiation toward the northwest is also confirmed by the overall damage patterns and landslides concentrated in regions northwest of the epicenter [Benuska, 1990]. Likewise, there is an azimuthal dependence on the peak ground motions as observed by Boore, Seekins and Joyner [1989; see Figure 6]. They note a tendency for high residuals relative to predicted peak values at rock sites toward the northwest compared to all other azimuths.

We now compare our slip model with the other finite-fault dislocation models for this earthquake [Beroza, 1991; Hartzell *et al.*, 1991; Steidl *et al.*, 1991]. Although there are significant differences in the amplitude and direction-of-slip vectors between our model and others, there is also remarkable agreement in these models concerning the overall nature of this rupture. All researchers conclude that bilateral rupture with relatively little slip updip from the hypocenter best explains the waveforms.

All researchers find that the majority of slip occurred in two relatively small patches nearly equidistant from the hypocenter; one to the northwest, and one to the southeast. All studies indicate that a fairly uniform rupture velocity of approximately 80% of the local shear-wave velocity together with a relatively short slip duration at any point (less than about 1.5 sec) best explains the waveforms.

Although our model is similar in most respects to the others presented in this volume, it differs substantially in two aspects. First, the local rake vectors vary significantly among the models discussed here. On average, the rake vectors in the region southeast of the hypocenter for our model and that of Hartzell *et al.* [1991] agree and are about 145°. Both these models have similar, oblique rake components in the northwestern asperity. In contrast, the southeastern asperity in the models of Beroza [1991] and Steidl *et al.* [1991] shows rake angles indicating nearly pure, strike-slip (rake approximately $160 - 170°$), yet have almost pure thrusting rake vectors ($80 - 90°$) within the northwestern asperity. These two models require an approximately 80° change in rake vector from the southern to northern halves of the fault with no corresponding change in dip. It should also be emphasized that although the slip distributions of Hartzell *et al.* [1991] and Beroza [1991] look similar, the rake vector in the region of dominant slip for these models (the southeast asperity) is different by about 40° and would likely produce substantially different near-field ground motions.

Second, in addition to the variation in the local rake directions, the partitioning of the total slip along strike in asperities northwest and southeast of the epicenter in our model requires more slip in the northwest region (Figures 3.7, 3.11 and 3.16; Table 3.4); the other models require the greater part of the slip in the southeast asperity. Considering that rise times, rupture velocities and source geometries are similar among the various models, disparities in the resulting slip-distribution models most likely reflect variations in the data sets employed. Other parameters being

comparable, station coverage and weighting are perhaps the most critical elements controlling the slip partitioning. A source of dominant radiation northwest of the epicenter is required by the strong-motion data used in our study (see Figures 3.2, 3.3, 3.4). In particular, the large, coherent arrivals at stations SAR, LEX and LGP require significant slip and directivity in that direction. A comparison of waveform fits at station SAR by the various models is particularly revealing and reflects the differences in modeling strategy.

The strategy adopted by Steidl *et al.* [1991] was to obtain the largest possible azimuthal coverage by including stations out to 60 km. Thus, they modeled a number of distant stations to the north (FRE, FMS, WFS, CSS and CSP) quite well, while doing a relatively poor job at SAR in fitting both waveform and amplitude. They did not use LEX and LGP, the two stations with the largest observed ground velocities, and therefore the wavefield at these ray parameters is down weighted relative to distant samples. If their Green's functions are adequate for these distant stations and ours prove less than desirable at LEX, SAR and LGP, then they have a more reasonable interpretation. A detailed study of aftershock recordings at the various stations is one way to resolve this particular issue, since local receiver structures can be recognized, and the adequacy of the theoretical Green's functions may be examined.

It is not so clear why the slip distribution model of Beroza [1991] has different characteristics from ours. Although he does not use the vertical components of the ground motion, his station selection in the northwest region of the fault is similar to that in our study. Waveform fits at his northwestern stations show significant differences from those of our model. Perhaps the slip-distribution variability is partially due to the differences in the applied Green's functions, as he suggests; we employed the complete layered space solutions, whereas he used only geometric-ray approximations. Again, a comparison of near-field and far-field Green's functions with simple

aftershocks at SAR and other stations should help resolve this issue.

Slip in the southeastern asperity is obviously constrained by the southeastern stations as described in Figure 3.15. We used station WAT and a few of the Gilroy stations. We observed that the other Gilroy stations have complex receiver functions and we omitted them. The data sets from the other studies excluded WAT and used additional stations from the Gilroy Array. The use of a dense set of stations over a limited distance and azimuthal ranges provides redundant coverage and may favor slip in the southern portion of the fault plane.

Clearly, the teleseismic data have less resolving power along strike than the strong-motion data, as can be observed by comparison of *P* and *SH* waveforms from this study and those of Hartzell *et al.* [1991]. Although the slip models are quite different—indeed they are nearly northwest-southeast reversed—they produce very similar teleseismic-waveforms, suggesting a lack of resolution from this data set. The teleseismic data, however, do resolve updip directivity and require a bilateral rupture with little updip slip. Again, it is most likely that the differences in the teleseismic models result from variations in station coverage. Hartzell *et al.* [1991] use teleseismic stations similar to ours, but add several additional stations, particularly in the northwestern and northeastern azimuths. These additions do not substantially augment azimuthal coverage and may actually bias the results. Removal of these stations from their inversion results in a model similar to our results, favoring northwestern slip [S. Hartzell, personal communication, 1991].

It is important to note that even though the slip distribution and rake vectors vary, the net sum of any of these models will be very similar at long periods. This can be explained by the fact that the bilateral rupture radiates from both asperities simultaneously. Hence, as long as the net rake vector and total moment are preserved, the resulting models should produce similar and adequate teleseismic waveform matches. This, however, is not true for the near-field data. That the waveform comparisons

for all the strong-motion models are less than remarkable may reflect the need for a more complex rupture surface than the idealized flat planar models used here.

In general, the rupture process of the Loma Prieta earthquake was fairly simple for a magnitude 7.1 earthquake, rupturing only a relatively short (< 35 km) fault segment [Kanamori and Satake, 1990]. The relatively short duration of strong motion can be partially attributed to the bilateral nature of the rupture. Further, the relatively large depth of slip concentrations had the effect of moderating the size of the ground velocities in the near-source region.

Most of our current knowledge of fault-asperity characteristics has been derived from ground-motion frequencies that are lower (less than 1 Hz) than the frequency range of most interest in earthquake engineering. Wald *et al.* [1987, 1988] found that large-scale asperity models derived from longer-period velocity data also explained many characteristics of the higher-frequency accelerograms. Our results here indicate that the asperities that control the broadband, teleseismic waveforms (3-30 sec), also dominate the higher-frequency strong motions (1-5 sec).

In an effort to understand the radiation of the higher-frequency motions during the Loma Prieta earthquake, we have performed an inversion with the observations and synthetic seismograms bandpassed-filtered from 0.1 to 3 Hz. We used a finer discretization of the fault plane, with 200 subfaults, each having dimensions of 2.0 km along strike and 2.0 km downdip. We also reduced the duration of the source-time-function to 0.5 sec. Our results indicate that the same regions of large slip that control the longer-period, teleseismic waveforms and the strong-motion velocities up to 1 Hz are also responsible for higher-frequency (> 1.0 Hz) radiation. We also note that the inversion using higher-frequency data appears to favor slightly more concentrated asperities. Understanding the relationship between long-period source models of large earthquakes and the radiation of high frequencies is critical for the prediction of ground motions in the frequency range of engineering interest. Future

work will further address the nature of the high frequency radiation. This will require more sophisticated timing corrections based on the aftershock data recorded at many of the strong-motion stations used here, and a more detailed treatment of the variations in propagation paths and site effects of individual stations.

Chapter 4

Sierra Madre Earthquake

4.1 Abstract

Short-period and broadband, teleseismic waveform data and three-component strong-motion records were analyzed to obtain the source parameters of the 1991 Sierra Madre earthquake. Close-in, strong-motion velocity records (analyzed from 5 sec to 5 Hz) show two distinct pulses about 0.35 sec apart, requiring some rupture complexity. The near-field, shear-wave displacement pulse from this event has a relatively short duration (about 1 sec) for the magnitude of the event, requiring a particularly high average stress drop. To further constrain the rupture process, the data were used in a finite fault source inversion to determine the temporal and spatial distribution of slip. We chose a fault plane orientation striking S 62° W and dipping 50° toward the northwest as required by the distribution of aftershocks, the first motion mechanism and the teleseismic, body-wave point-source inversion. In addition to the aftershock locations, depth constraints are provided by teleseismic short-period and broadband recordings which require a centroid depth of 10–11 km. Our inverse modeling results indicate that both the teleseismic and strong-motion data sets can be fit with a compact rupture area, about 12 km^2, southwest and updip

from the hypocenter. The average slip is approximately 50-60 cm, and the maximum slip is 120 cm. The seismic moment obtained from either of the separate data sets or both sets combined is about $2.8 \pm 0.3 \times 10^{24}$ dyne-cm, and the potency is 0.01 km^3. Using the area of significant slip estimated from the finite-fault inversion, the resulting stress drop is on the order of 150–200 bars.

4.2 Introduction

The 1991 Sierra Madre, California earthquake (M_L=5.8) of June 28 occurred under the San Gabriel Mountains about 18 km northeast of Pasadena. The location and mechanism of the mainshock, the geometry of the aftershock distribution, and the surface projection of the inferred fault plane (Figure 4.1) suggest that the Clamshell-Sawpit fault is the likely candidate for the causative structure [Hauksson and Jones, 1991a]. If so, only a small portion of the fault ruptured during this earthquake.

The near-field, shear-wave displacement pulse from this event has a relatively short duration (about 1 sec) for the magnitude of the event, requiring a particularly high, overall stress drop [Kanamori *et al.*, 1991]. Moreover, source parameters determined from regional and local waveforms substantiate the short duration and compact nature of the source [Dreger and Helmberger, 1991]. Hence, we are interested in quantifying the spatial and temporal distribution of slip in order to better understand the source of damaging ground motions from this thrust fault and other potential blind-thrust earthquakes. The recent series of deep strike-slip and blind-thrust events within and around the heavily populated Los Angeles metropolis [Hauksson, 1991; Hauksson and Jones, 1991b] and the potential for similar and larger events in the future mandate a careful examination of data recorded from the Sierra Madre earthquake.

Fortunately, a large number of acceleration recordings were recovered for this

Figure 4.1: Model fault geometry compared to aftershock distribution. (*a*) Map view of aftershock distribution. Mainshock first-motion mechanism is located at the epicenter. Rectangle depicts surface projection of inferred fault plane. (*b*) Cross section A-A' with side view of fault plane as seen from the southwest. (*c*) Cross section B-B', showing view of fault surface from the southeast. Seismicity plot courtesy of E. Hauksson.

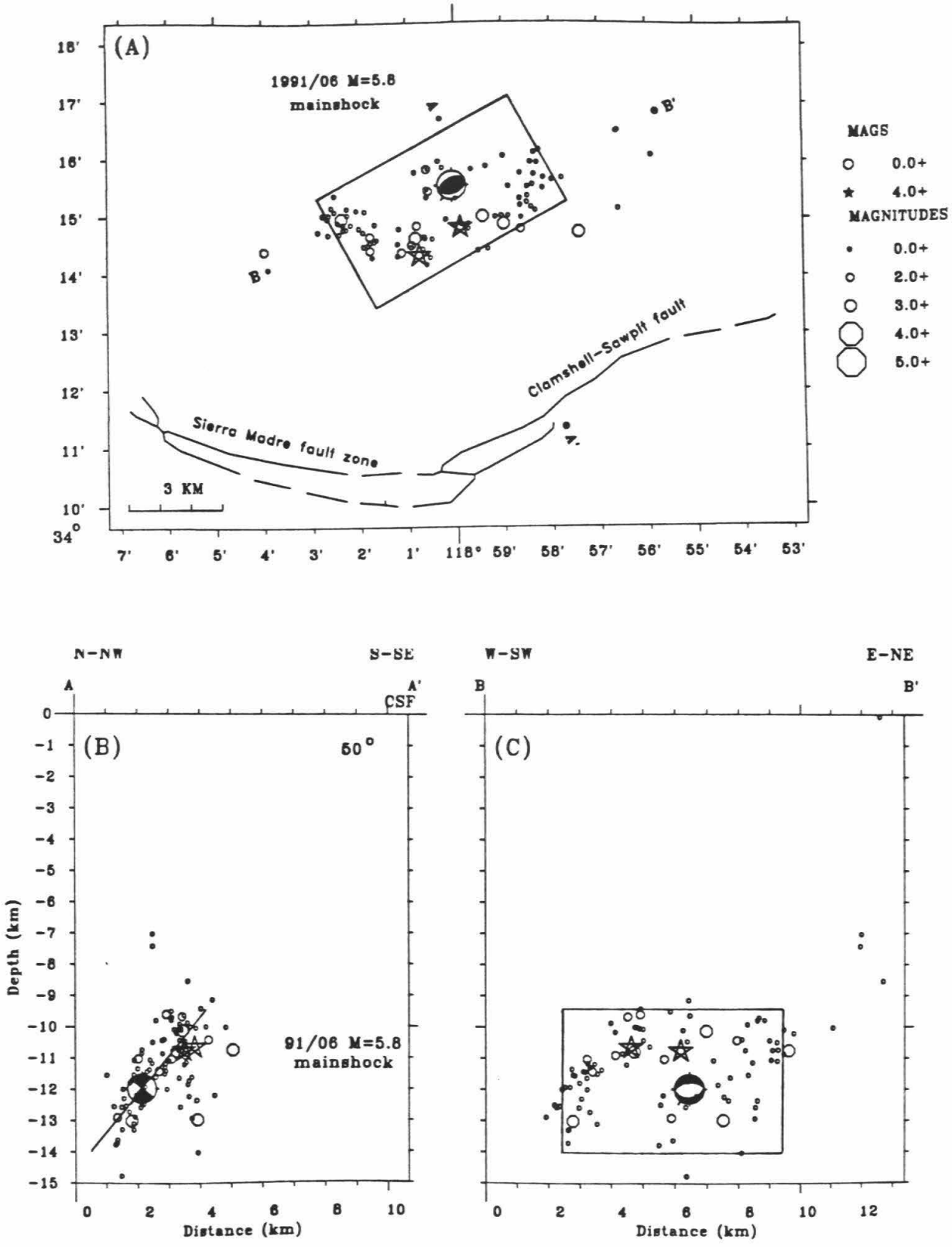
(A)
1991/06 M=5.8
mainshock
B'
B
Clamshell-Sawpit fault
Sierra Madre fault zone
3 KM
MAGS
0.0+
4.0+
MAGNITUDES
0.0+
2.0+
3.0+
4.0+
5.0+
18'
17'
16'
15'
14'
13'
12'
11'
10'
34°
7'
6'
5'
4'
3'
2'
1'
118° 59'
58'
57'
56'
55'
54'
53'
N-NW
S-SE
A
A'
CSF
(B)
50°
91/06 M=5.8
mainshock
Depth (km)
Distance (km)
W-SW
E-NE
B
B'
(C)
Distance (km)

earthquake because of the density of CDMG and USGS instruments in the epicentral area. The 1987 Whittier Narrows earthquake (M_L=5.9) also produced useful, local, strong-motion data, which were analyzed by Hartzell and Iida [1990]. They modeled the overall rupture area from the Whittier Narrows earthquake as approximately 70 km^2, with slip concentrated over a smaller region of perhaps 25 km^2. Here we are testing the resolving power of the strong-motion data and teleseismic data for a somewhat smaller source dimension than for the Whittier Narrows earthquake, but it will be useful to compare the rupture process of these two blind-thrust-style earthquakes in the Los Angeles region.

In order to better understand the ground-motion behavior and hazards in Los Angeles, it is very helpful to remove the contribution of the effects of source finiteness and rupture heterogeneity from the effects of ground-motion amplification that is due to propagation and site response. When these source effects are distinguished from others, it is possible to scale up the source of moderate-sized events like the 1987 Whittier Narrows and the 1991 Sierra Madre earthquakes and to make reasonable estimations of ground motions and attenuation relationships specific to the Los Angeles region from larger, anticipated earthquakes [Saikia, 1992]. Here we attempt to characterize the source contribution of the Sierra Madre earthquake by modeling local ground-motion and teleseismic waveforms. Some independence from the effects of local path and site contamination is provided by the teleseismic data, which are less likely to be seriously contaminated by site effects, and in general, show more stability in overall amplitude than the strong-motion data. But it is also important to consider only those strong-motion stations that have coherent waveforms and appear to be relatively free from site effects. The strong-motion velocity records we model are dominated by energy with frequencies of about 3–5 Hz. This frequency band is at the cross-over between longer periods which, on average, show amplification of soil sites relative to rock sites, and higher frequencies for which the relationship is

reversed [Aki, 1988]. Therefore, we expect some independence from site amplification from the near-source, strong-motion data used here because of the band-limited nature of the velocity-waveform observations.

4.3 Data

4.3.1 Strong Motion

The distribution of near-source, ground-motion stations used in this study is displayed in Figure 4.2. Station abbreviations, locations and geometries with respect to the epicenter are given in Table 4.1. The surface projection of the assumed fault plane is shaded. At the time of this study, digital strong motions were available for U.S.G.S. stations GSA, UPL and GRV. All other records were provided by the C.D.M.G. [Huang *et al.*, 1991] and the U.S.G.S. [Salsman *et al.*, 1991] as paper records, which were then digitized at Caltech. The digitizing system includes a 400 dpi scanner and automated digitizing algorithm. By visual waveform comparison with the digital recordings, we find that our digitized accelerograms are accurate for frequencies up to at least 10 Hz, more than adequate for the purpose of this study. Velocity waveforms were obtained by integrating digitized-accelerogram recordings. The velocity time histories were then bandpass-filtered between 0.2 and 5.0 Hz, using a zero-phase, third-order Butterworth filter, and the horizontal components were rotated with respect to the epicenter to obtain radial and tangential components. This rotation is only approximate for stations directly above the inferred fault plane (COG and MTW). The rotated, filtered velocity data are displayed in Figure 4.3. In addition, the tangential waveforms are displayed in Figure 4.2 with a common vertical scale to show the relative amplitudes as a function of distance and azimuth from the epicenter. Note that the updip projection of the model fault plane is parallel to and surfaces near the Clamshell-Sawpit Fault trace; thus stations ETN and GSA are

Station	Location	Distance	Azimuth	Back Azimuth
COG	Cogswell Dam	3.9	118.1	298.1
ETN	Eaton Canyon Park, Altadena	12.8	222.8	42.8
GSA	U.S.G.S., Pasadena	18.0	219.9	39.9
GVR	Garvey Reservoir	25.9	204.7	24.7
MOR	Morris Dam	15.1	132.2	312.2
MTB	Mt. Baldy Elementary School	31.5	95.8	275.8
MTW	Mt. Wilson - Caltech Station	6.6	230.7	50.7
PAC	Pacoima Dam - Kagel Canyon	34.5	274.9	94.9
PAL	Pearblossom - Pallet Creek	23.4	21.4	201.4
PUD	Puddingstone Dam	26.0	136.7	316.7
UPL	Upland	30.6	114.1	294.1
VAL	Valermo Forest Station	24.2	35.2	215.2
VSQ	Vasquez Rocks Park	38.7	310.9	130.9
WRW	Wrightwood - Swarthout Val.	33.8	69.4	249.4

Table 4.1: Strong Motion Stations. Distances (km) and azimuths are with respect to epicenter at 34° 15.7' North latitude, 118° 00.1' West longitude.

directly updip (Figure 4.2).

Although there is fairly good azimuthal coverage of the source from the strong-motion stations shown in Figure 4.2, there is less adequate coverage for stations within 20 km of the epicenter. In our waveform inversions we initially gave more weight to the close-in stations by considering the vertical, radial and tangential components, whereas for the more distant stations, normally we use only the tangential component. This approach is justified since the close-in stations show very simi-

Figure 4.2: Location map showing USGS (triangles) and CDMG (circles) strong-motion stations and and corresponding, observed, tangential-ground velocities. The epicenter is shown with a star. The shaded region represents the surface projection of the model fault plane used in this study. The faults (light lines) are a digitized version of major Quaternary faults of Jennings [1975].

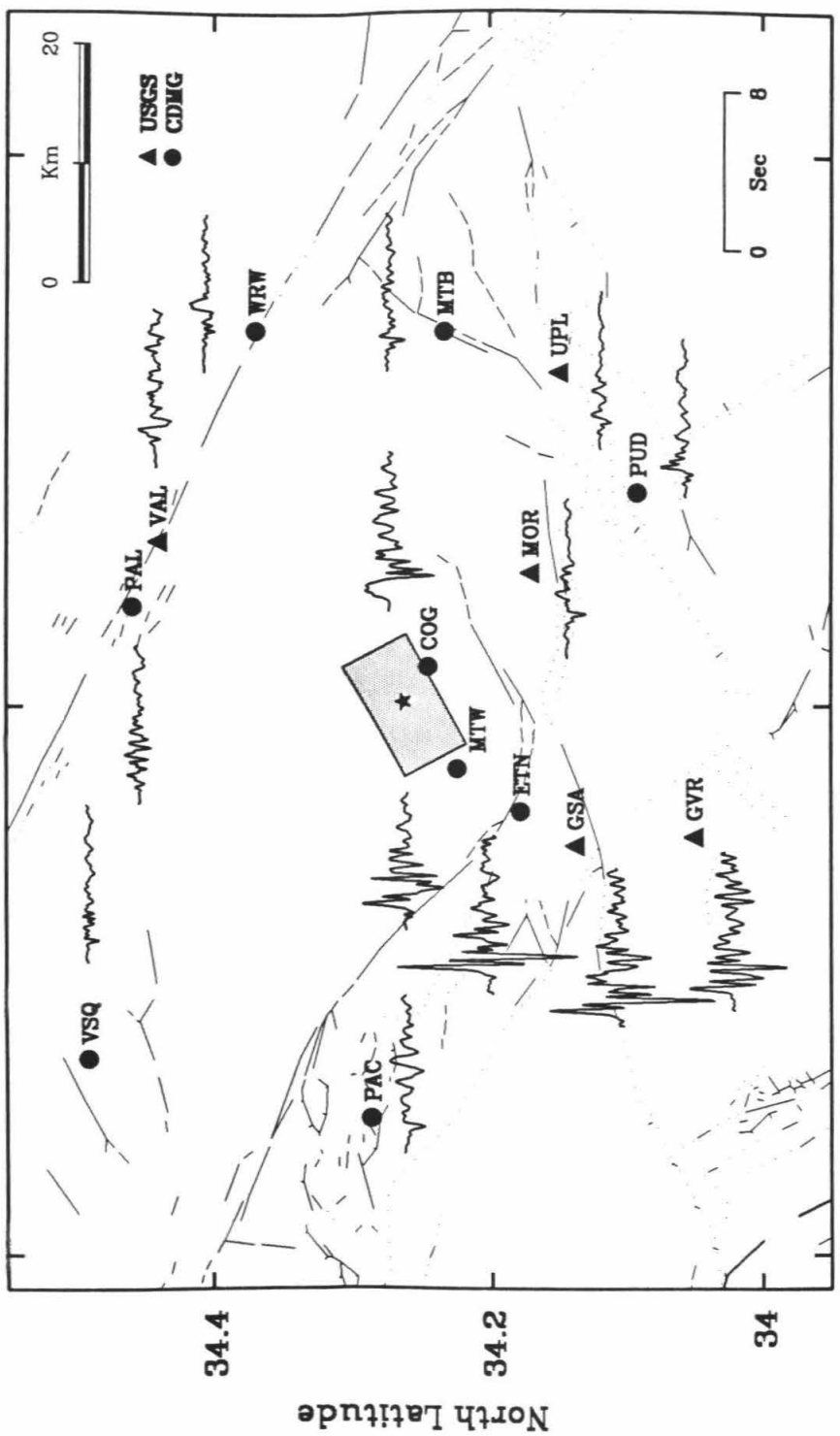
0
Km
20
USGS
CDMG
0
Sec
8
VSQ
PAC
PAL
VAL
WRW
COG
MTW
ETN
GSA
MOR
GVR
PUD
UPL
MTB
34.4
34.2
34
-118.5
-118
-117.5
North Latitude
West Longitude

lar, larger-amplitude waveform features, which are not easily identified in the more distant, smaller-amplitude stations (Figure 4.3). In subsequent modeling we also gave equal weight to the distant stations to analyze their contribution to the source model. Note the similarity of waveforms from the close-in stations. In particular, the tangential records at COG, ETN, GSA, GVR and MTW begin with distinct, double SH arrivals easily traced from record to record (Figure 4.3). The time separation between the two arrivals is nearly identical at these stations, consistently 0.35 sec. The same feature is observed on the radial components but is not as clearly recognized. Further, note the corresponding feature on the tangential components at stations MOR, MTB, and UPL.

Examination of aftershocks at stations MTW and GSA indicates that several of the aftershocks also exhibit double arrivals at the time of the direct *SH* wave. The two arrivals for the aftershocks were, in general, roughly 0.15 to 0.20 sec apart but show some variability. Initially, we attributed the second of the two arrivals to a reflection from a deeper, near-source velocity interface. If so, the variation in time separation was due to varying source depths and hence varying relative locations with respect to the reflecting interface. However, the double-arrival nature of the mainshock velocity records cannot be attributed to propagation complexities alone. Since this feature is observed at stations ranging in location from directly above the source area (COG and MTW) as well as along a southwest profile of stations (ETN, GSA, and GVR in Figure 4.2) at distances up to at least 26 km from the epicenter, a near-source reflection is not a likely candidate. While it is possible to generate a reflection comparable in amplitude to the incident phase with a simple dipping structure and a reasonable impedance contrast, it requires a near-critical incidence and hence will not be sufficient for producing comparable reflection amplitudes over the range of distances at which this feature is observed. Moreover, the relative timing between the phases would vary systematically as a function of distance, and

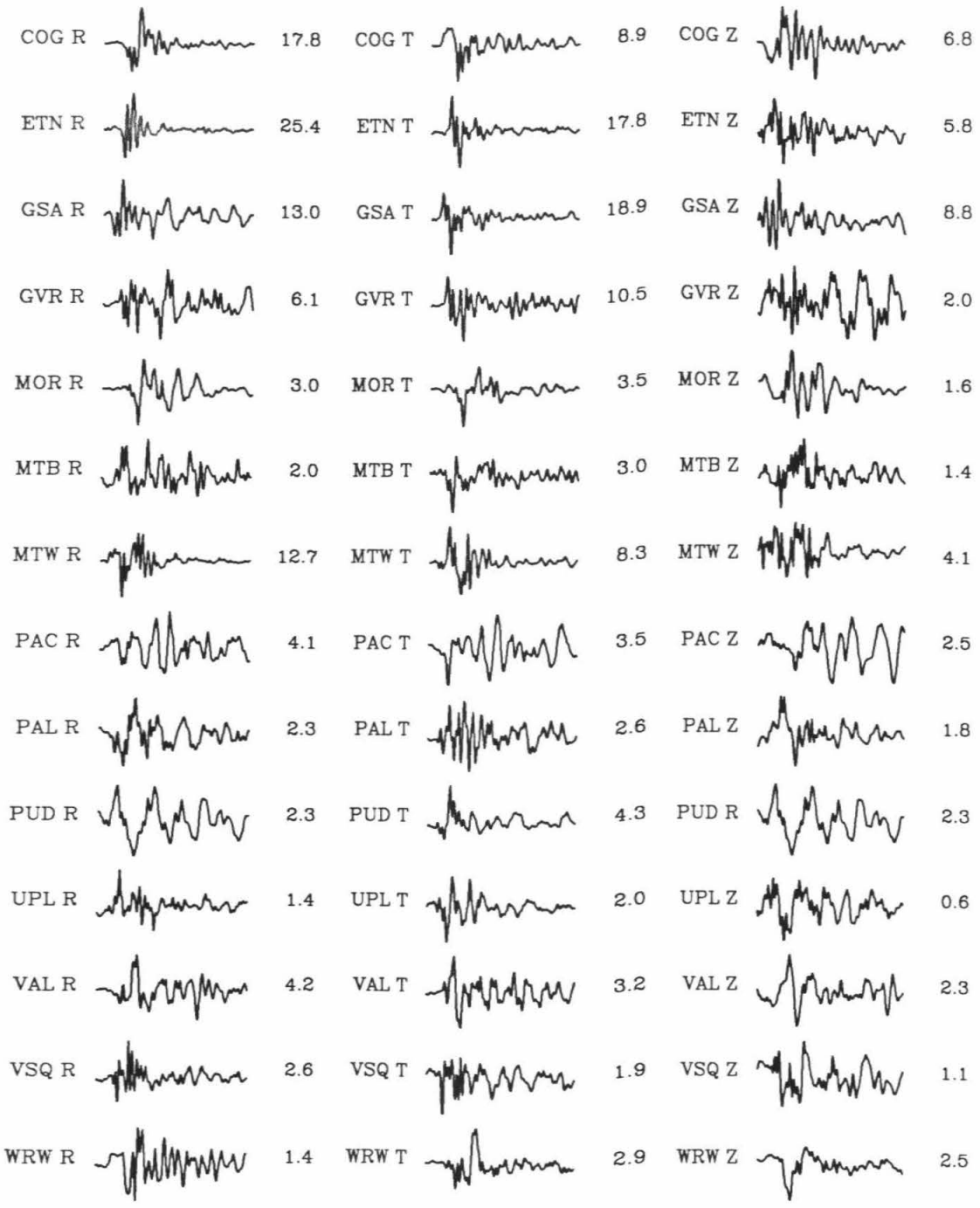

Figure 4.3: Radial (R), tangential (T) and vertical (Z) recorded ground velocities for the stations listed in Table 4.1. Amplitudes are in cm/sec.

a characteristic phase shift would be apparent. It is also difficult to reproduce the comparable relative amplitudes of the two arrivals from a reflection below the source at stations almost directly above the source. From these considerations, we attribute the double arrival of the mainshock to source complexity. The source of the double arrivals observed on some of the aftershocks remains yet unresolved.

4.3.2 Teleseismic

As the Sierra Madre earthquake is only a moderate-sized event, there are limited teleseismic data available, and the azimuthal coverage is incomplete (Figure 4.4). Broadband teleseismic waveforms were available for the stations listed in Table 4.2. Although other stations were available, most had low signal-to-noise ratios and were not considered useful. The instrument response for each station was deconvolved to obtain ground displacements. For the point-source inversion, we inverted ground displacement; one time derivative was taken to obtain true ground velocities for input into the finite-fault inversions. We find that the depth phases are more easily distinguished visually in the velocity recordings than the displacement records.

The short-period Canadian stations allow an accurate depth determination, although the pP and sP surface reflected phases may be complicated by the mountainous topography above the source region, and the depth may be relative to the average bounce-point elevation. Figure 4.5 shows the observed (solid) and synthetic (dashed) short-period seismograms at station FBC for depths ranging from 8 to 12 km. It is clear that the data require the best point-source depth to be close to 10–10.5 km in order to match the time separation between direct P and the surface reflection sP.

Figure 4.4: Global station distribution for teleseismic stations listed in Table 4.2.

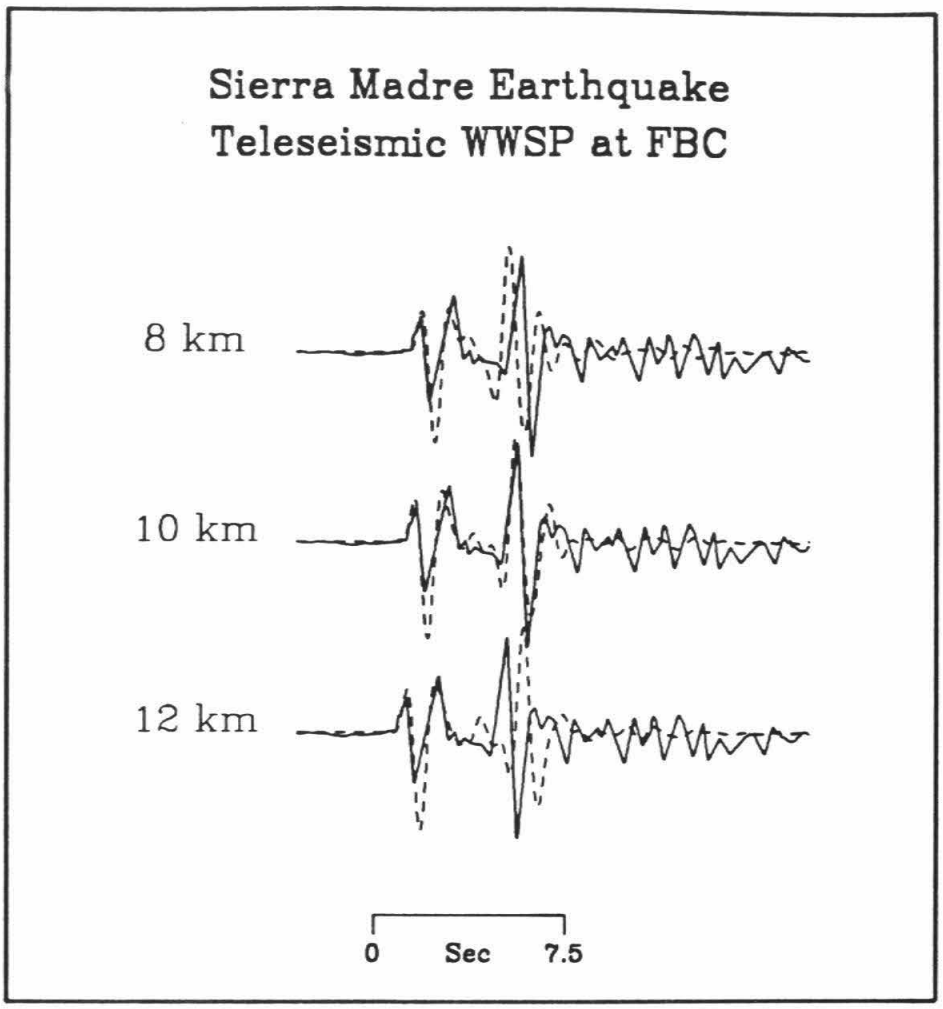

Figure 4.5: Comparison of observed (solid) and synthetic (dashed) waveforms for Canadian short-period station FBC (delta = 42.2°) for point-source depths of 8, 10 and 12 km.

Station	Delta	Back Azimuth	Azimuth
ALE	51.901	240.28	7.93
COL	35.568	134.97	338.63
HIA	82.315	44.97	326.01
HRV	36.942	272.88	63.09
KONO	76.935	317.64	24.40
MAJO	80.030	54.76	307.42
YKW1	28.339	186.10	3.42
SCH	40.784	261.31	43.69
FBC	42.182	249.79	30.28

Table 4.2: Teleseismic Stations. SCH and FBC are short-period Canadian stations.

4.4 Fault Model

The fault-parameterization and modeling procedure we employ is that described by Hartzell and Heaton [1983] in their study of the 1979 Imperial Valley earthquake. Faulting is represented as slip on a planar surface that is discretized into a number of subfaults. The ground motion at a given station can be represented as a linear sum of subfault contributions, each appropriately delayed in time to simulate fault rupture. Formal inversion procedures are then used to deduce the slip distribution on these subfaults that minimizes the difference, in a least-squares sense, between the observed and synthetic waveforms.

In this study we represent the Sierra Madre rupture area as a 7 km-long plane striking S 62° W and dipping 50° toward the northwest (Figure 4.1a). The fault extends from a depth of 9.4 km to 14.0 km (Figures 4.1b,c), giving a downdip width of 6 km. We fix the hypocentral depth to a value of 12.0 km determined by Hauksson

and Jones [1991a], using the Southern California Seismic Network (SCSN) short-period array, and we chose the overall dimensions of the fault to enclose the region of major aftershock activity. The hypocentral depth is slightly shallower than the best point-source depth as determined from the short-period data, suggesting an updip rupture propagation. The strike and dip values of our fault plane were chosen from our point-source, broadband, teleseismic inversion results, discussed in a later section. This geometry is nearly identical to that determined from the first motion solution determined from the short-period array [Hauksson and Jones, 1991a] and fits neatly into the distribution of aftershocks (Figure 4.1). We discretized the fault area into 10 subfault elements along strike and 10 elements downdip, giving each subfault a length of 0.7 km and a downdip width of 0.6 km. The subfault elements are shown as a gridded overlay on later figures, which display the modeled slip distribution.

The synthetic ground-motion contribution for each subfault is computed using the Green's function summation and interpolation method of Heaton [1982] and is only briefly summarized here. The subfault motions are obtained by summing the responses of a number of point sources distributed over the subfault. We sum nine equally spaced point sources appropriately lagged in time to include the travel-time difference that is due to the varying source positions and to simulate the propagation of the rupture front across each subfault. In all, 900 point sources are summed to construct the teleseismic and strong-motion synthetics at each station. We fix the rake at 82°, nearly pure thrusting, with the northwest side moving up and to the southwest. A variable rake was tested, but the results indicated very little variation from the constrained value, so we prefer the fixed model, since it has fewer free parameters.

The point-source responses, or Green's functions, for teleseismic P or SH body-wave synthetic seismograms are computed using the generalized ray method [Langston and Helmberger, 1975]. We include the responses of all rays up to two internal re-

flections in a layered velocity model, including free-surface and internal phase conversions. An attenuation operator [Futterman, 1962] is applied with the attenuation time constant t^* equal to 0.75 and 3.5 sec for P and SH waves, respectively.

The point-source responses for the strong motions, including near-field terms, are computed for a layered velocity model for frequencies up to 10 Hz using the frequency-wavenumber (FK) methodology. This method allows the computation of complete waveforms and also includes the effects of attenuation. In practice, we calculate a master set of Green's functions for increments in depth from 9 to 15 km and for ranges between 0 and 45 km to allow for the closest and farthest possible subfault-station combinations. Then for each subfault-station pair the required subfault response is derived by the summation of nine point-source responses obtained by the linear interpolation of the closest Green's functions available in the master set. The linear interpolation of adjacent Green's functions is performed by aligning the waveforms according to their shear-wave travel times. The amount of slip on each subfault is determined in the waveform inversion.

The velocity model used to compute the FK Green's functions is given in Table 4.3. The P-wave velocities were obtained by Hauksson and Jones [1991a], using a joint inversion of the aftershock data for location and velocity structure. We have also added a thin, slower layer to this model to better approximate the average site velocity just beneath the strong-motion stations. S-wave velocities were obtained by assuming that the structure is a Poisson solid. The Q structure in Table 4.3 was estimated, based on the velocity structure and was made to be consistent with the determinations for the total-path attenuation to TERRAscope station PAS for this earthquake [K. F. Ma, personal communication, 1991]. The velocity model used to compute the teleseismic Green's functions does not include the shallowest 0.3 km thick layer employed for the local, strong-motion modeling.

The subfault synthetics are convolved with a dislocation-time history, which we

Vp (km/s)	Vs (km/s)	Density (g/cm^3)	Thickness (km)	Depth (km)	Qp	Qs
3.35	1.67	2.50	0.3	0.3	100	50
4.61	2.66	2.62	3.7	4.0	200	100
6.18	3.57	2.80	4.0	8.0	600	300
6.45	3.72	2.85	8.0	16.0	600	300

Table 4.3: Sierra Madre velocity structure.

represent by the integral of an isosceles triangle with a duration of 0.2 sec. This slip function was chosen based on a comparison of the synthetic velocity-pulse width for a single subfault with the shortest-duration velocity-pulse width observed. As suggested by Heaton [1990], this is likely a maximum duration for the slip function, and in fact, using a 0.1-sec triangle matches the data equally well. Slip durations longer than 0.2 sec, however, substantially increase the waveform misfit.

The rupture velocity is assumed to be a constant 2.7 km/sec, or about 75% of the shear-wave velocity in the source region (Table 4.3). Some flexibility in the rupture velocity and slip-time history is obtained by introducing time windows [Hartzell and Heaton, 1983]. Each subfault is allowed to slip in any of three identical 0.2-sec time windows following the passage of the rupture front, thereby allowing for the possibility of a longer slip duration or a locally slower rupture velocity. In this study each time window is separated by 0.1 sec, allowing a small overlap of the 0.1-sec duration, subfault source-time function. With a constant rupture velocity this model implies that at most, a ribbon having a width of 1.1 km is slipping at any one time.

Because of the short-duration and high-frequency nature of the ground velocities,

the slight travel-time inaccuracies inevitable in synthetics from a one-dimensional model would result in poor alignment between synthetics and observations and thus would detract from the inversion for slip distribution. For this reason, we align the synthetics with the impulsive initial *S*-wave arrival in the data (best seen in the recorded accelerations), and we do not try to match the absolute timing.

A constrained, damped, linear, least-squares inversion procedure is used to obtain the subfault dislocation values that give the best fit to the strong-motion velocity waveforms. The inversion is stabilized by requiring that the slip is everywhere positive and that the difference in dislocation between adjacent subfaults (during each time window) as well as the total moment is minimized. These constraints have been previously discussed by Hartzell and Heaton [1983].

Both the strong-motion observations and subfault synthetic seismograms are bandpass-filtered from 0.2 to 5.0 Hz with a zero-phase Butterworth filter and are resampled at a uniform time step of 20 samples/sec. The teleseismic data were similarly filtered from 0.025 to 2.5 Hz and are resampled at 10 samples/sec. We modeled the first 3 sec of the strong-motion records and 10 sec of the teleseismic data.

4.5 Results

4.5.1 Teleseismic, Point-Source Inversion

To be certain that the fault geometry suggested by the aftershock distribution and local first-motion mechanism adequately reflects longer-period moment release for this earthquake, we first performed a point-source inversion of the available *P* and *SH* broadband-displacement waveforms using the methodology of Kikuchi and Kanamori [1991]. Initially we constrained the time function to be a simple 0.75-sec triangle and determined the best-fitting mechanism and the source depth. The observed (top) and synthetic (bottom) waveforms resulting from this inversion are shown in Figure 4.6.

The best point source was determined to be at a depth of 10.7 km with a moment of 2.8×10^{24} dyne-cm. The mechanism, as shown, has a strike, dip, and rake determined to be 243°, 49°, and 82°, respectively. Although most of the *SH* waveforms are not impressive for this event, the nodal nature of this arrival at MAJO and the *SH* waveform at ALE do play roles in constraining the mechanism (Figure 4.6). Next, by fixing the mechanism and allowing for multiple point-source locations relative to the hypocenter, the data required all the energy release to be updip and southwest of the hypocenter.

4.5.2 Teleseismic, Finite-Fault Inversion

After constraining the fault geometry with a point-source teleseismic inversion, we set up the finite-fault inversion. Initially, we inverted only the teleseismic-velocity waveforms. The resulting distribution of slip is shown in Figure 4.7. The slip contours are in intervals of 20 cm, and increased shading indicates larger slip as displayed in the legend shown at the right of the diagram. The dislocations shown represent the slip with a fixed rake of 82°. The solution is largely controlled by the time separation of the surface reflections *sP* and *pP*, requiring the depth of concentrated energy release to be near 10–11 km, consistent with the point-source inversion. There is a slight tendency for the slip to be forced southwest of the hypocenter in order to improve the match to the relative amplitudes as a function of distance and azimuth.

4.5.3 Combined Strong-Motion and Teleseismic Inversion

The distribution of slip from the inversion of combined strong-motion and teleseismic velocities is shown in Figure 4.9. Comparison of the observed (top) and synthetic (bottom) strong-motion velocities is shown in Figure 4.8 and the observed (top) and synthetic (bottom), teleseismic waveforms are given in Figure 4.9. We show only those stations and components that were given significant weight in the final inver-

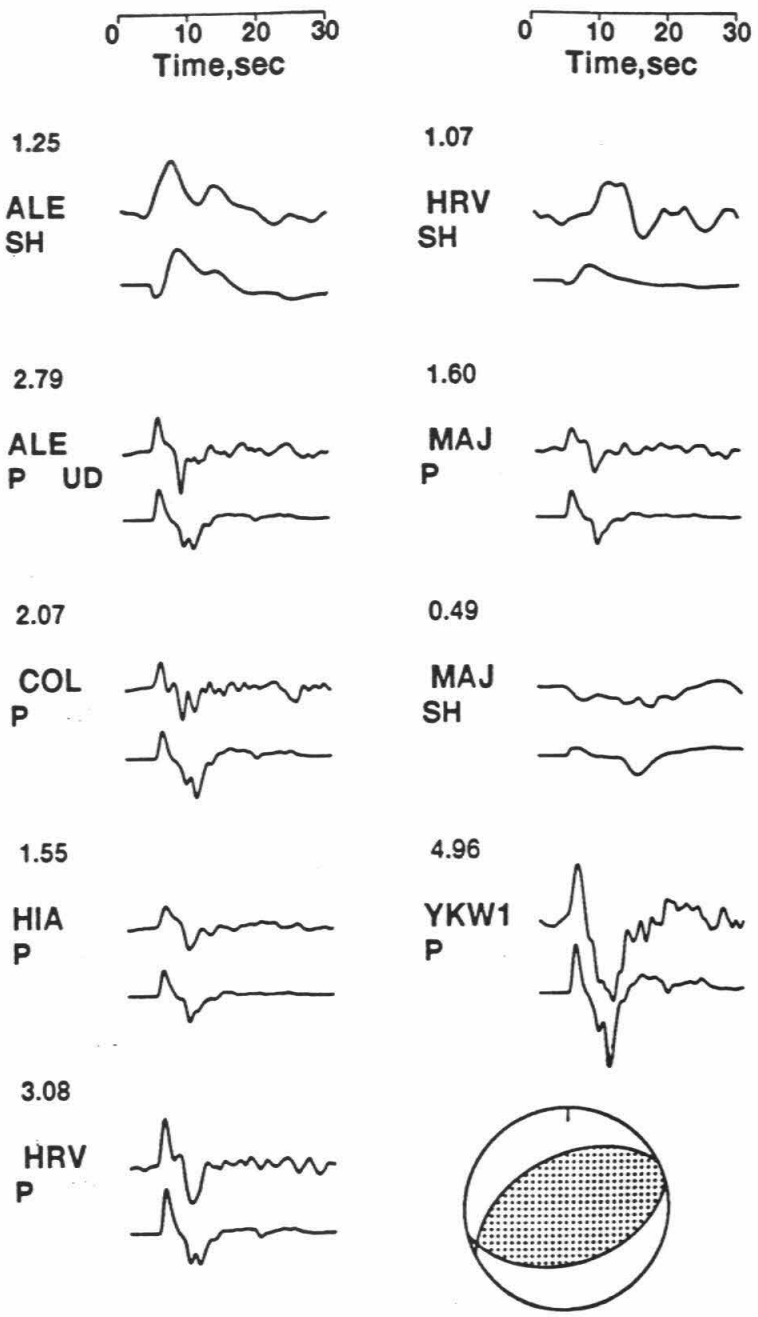

Figure 4.6: Comparison of observed (top) and synthetic (bottom) teleseismic *P* and *SH* displacement records for the point-source solution represented by the focal mechanism shown. All waveforms are on the same scale, and the peak observed amplitude in microns is given for each station.

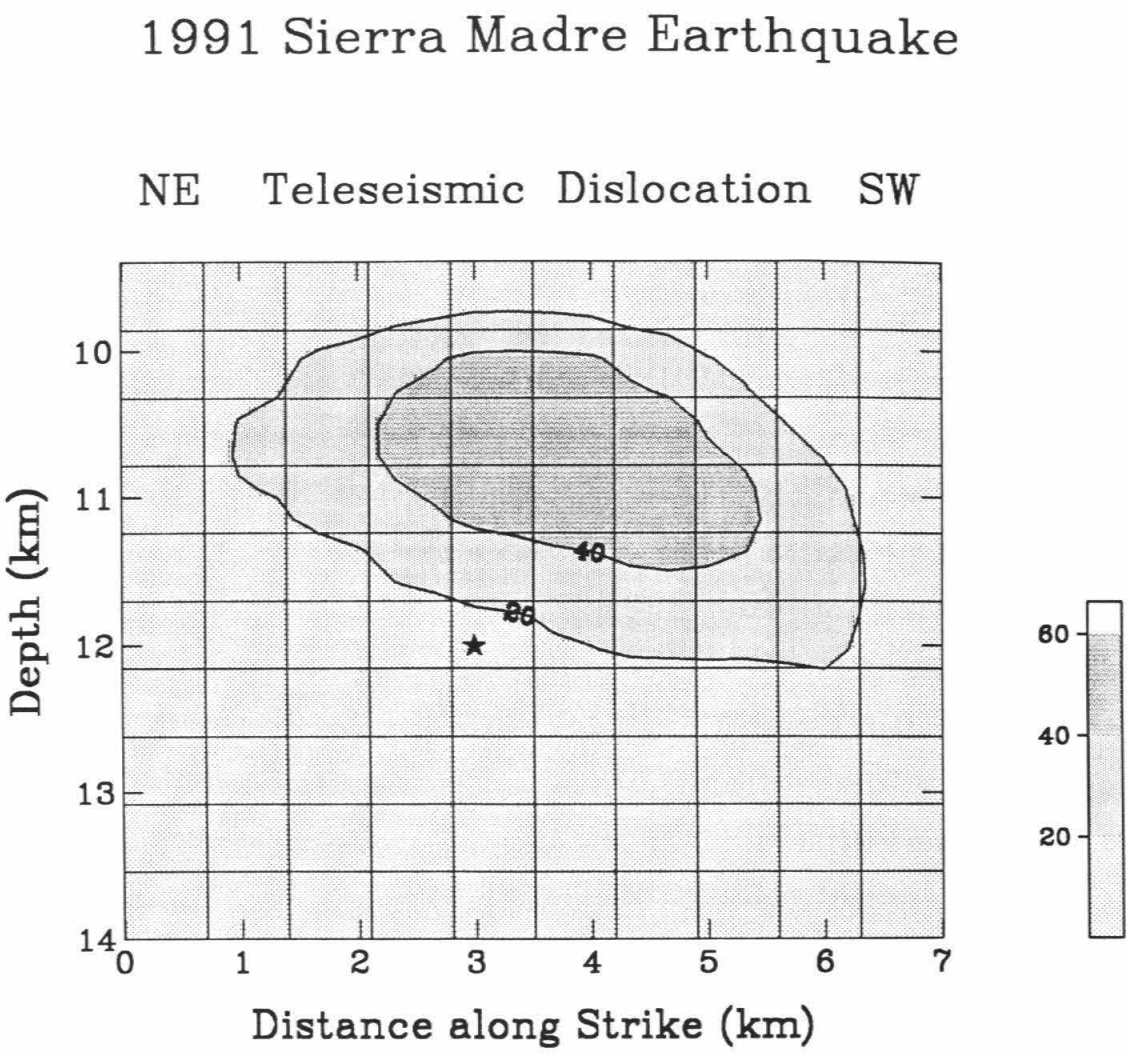

Figure 4.7: Northeast-southwest cross section of the fault model showing contours of dislocation resulting from the teleseismic inversion. Contour interval is 20 cm. Shading values indicating slip in centimeters are given by the scale on the right of the diagram.

sion. In general, the overall waveform fit and amplitude comparison are favorable. Recall that the frequency band (0.2–5 Hz) being modeled here is significantly higher than previous finite-fault inversions for larger earthquakes (e.g., Hartzell and Heaton [1983], Hartzell and Iida [1990]). The addition of the rest of the stations shown in Figure 4.2 does not particularly change the concentrated asperity in the solution, but minor amounts of slip are distributed at the outer edges of the inferred fault plane, quite separate from slip in the main source region. Requiring the model to fit arrivals that result from complicated path effects degrades the overall waveforms at the close-in stations where we know the waveforms are more dominated by source effects. For this reason, we prefer the simpler model (Figure 4.8) to the more random slip distributions, controlled by the addition of distant stations, which we believe result from mapping unmodeled propagational effects back into the source model. The source model shown in Figure 4.8 is quite robust, and is representative of the results of inversions using various weighting schemes for the close-in stations.

The combined strong-motion and teleseismic-rupture model is similar to that derived from the teleseismic data alone in that slip is concentrated updip and towards the southwest. Again, the region of substantial slip is very limited in size, but more so than from the teleseismic data alone. The moment is 2.8×10^{24} dyne-cm. There is a trade-off between the fit to the strong-motion data and the relatively narrow depth interval required to fit the depth phases of the teleseismic waveforms. Inverting only the strong-motion data yields an asperity similar to the combined inversion, although the centroid is forced slightly deeper (12 km) and southwest of the hypocenter rather than southwest and updip.

Examination of the combined-data, teleseismic and strong-motion inversion solution indicates that the double arrival seen at most close-in strong-motion stations was modeled by employing the time windows. Figure 4.11 shows the slip contributions during time window 1 (top), 2 (middle) and 3 (bottom). The initiation of time

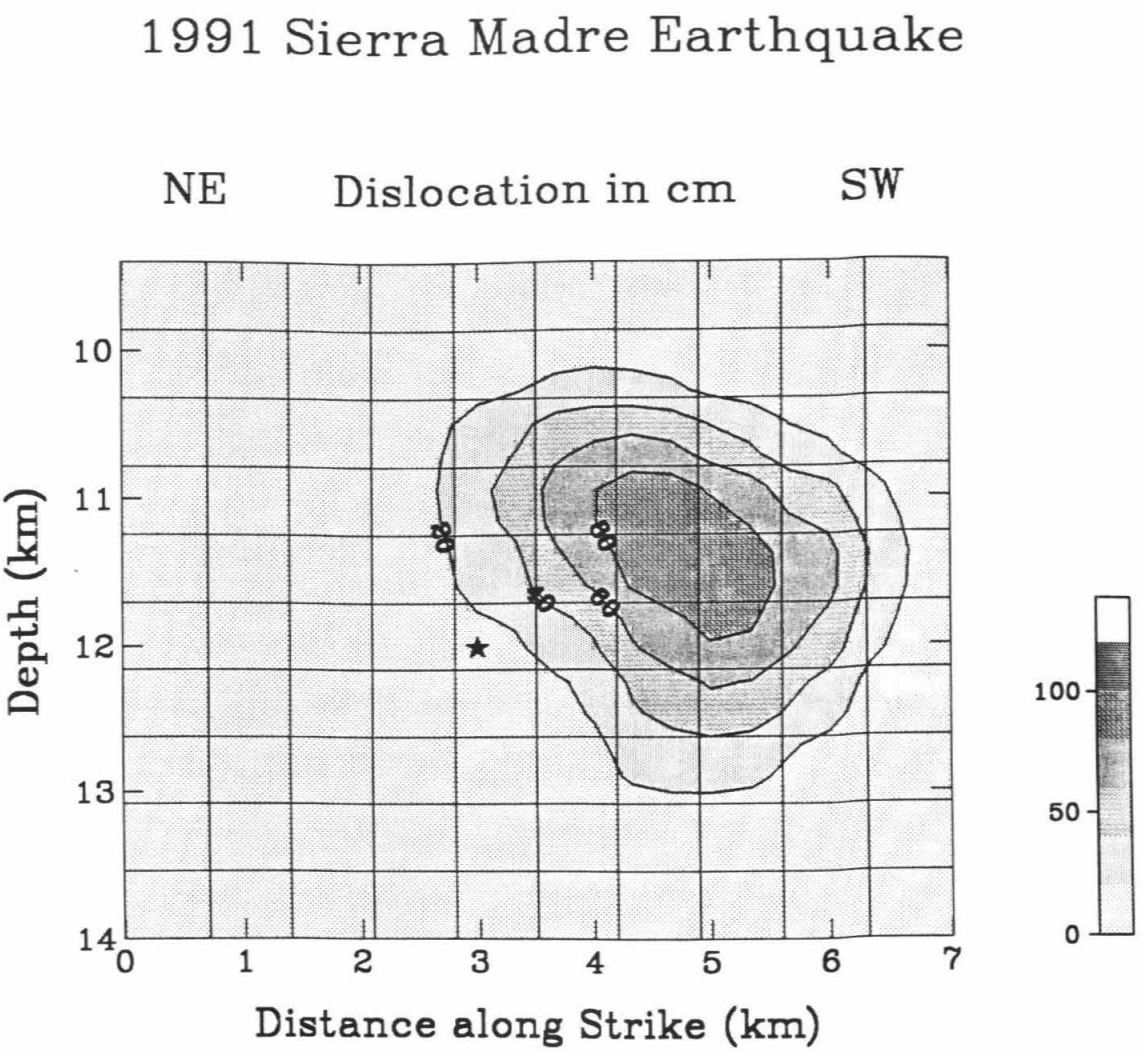

Figure 4.8: Northeast-southwest cross section of the fault model showing contours of dislocation resulting from the combined strong-motion and teleseismic inversion. Contour interval is 20 cm. Shading values indicating slip in centimeters are given by the scale on the right of the diagram.

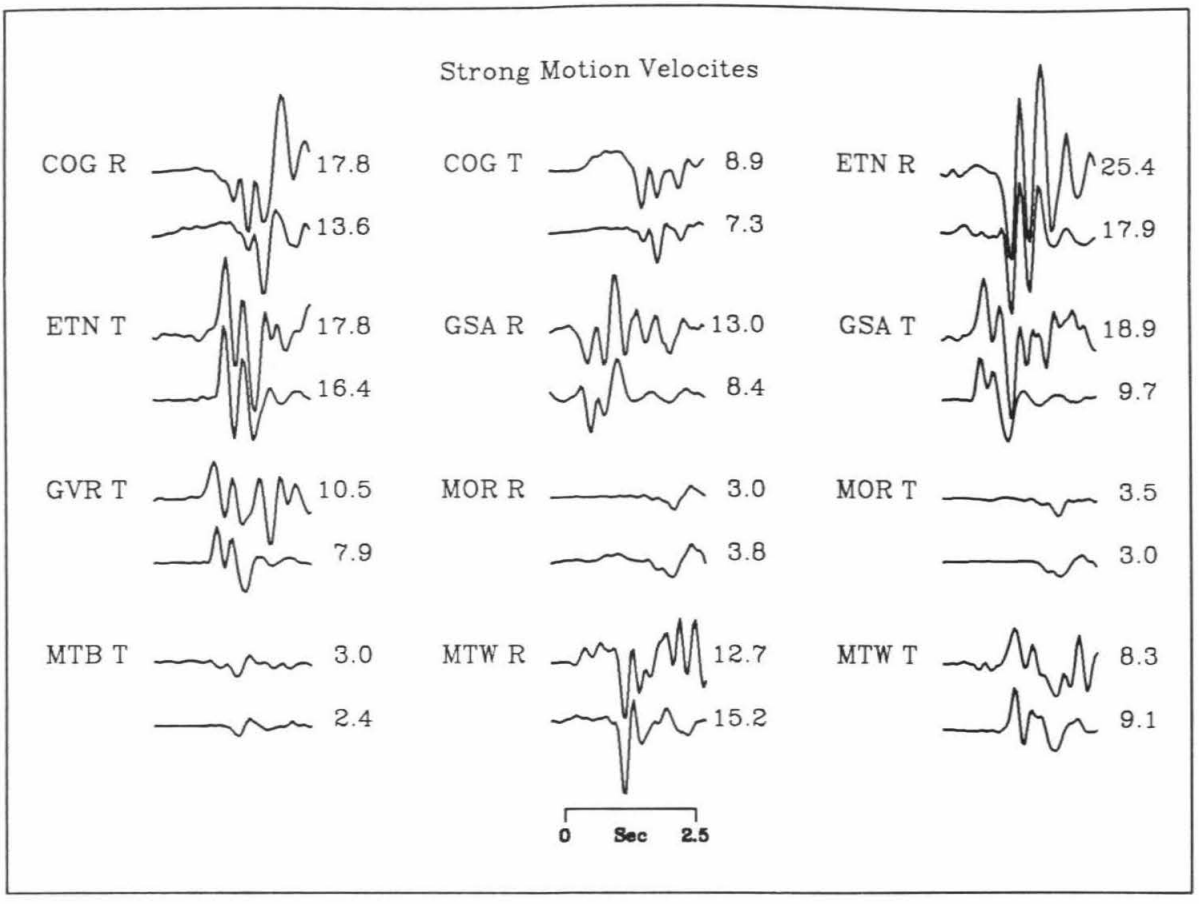

Figure 4.9: Comparison of observed (top) and synthetic (bottom) strong-motion records from the inversion of the combined data set. Amplitudes are in cm/sec.

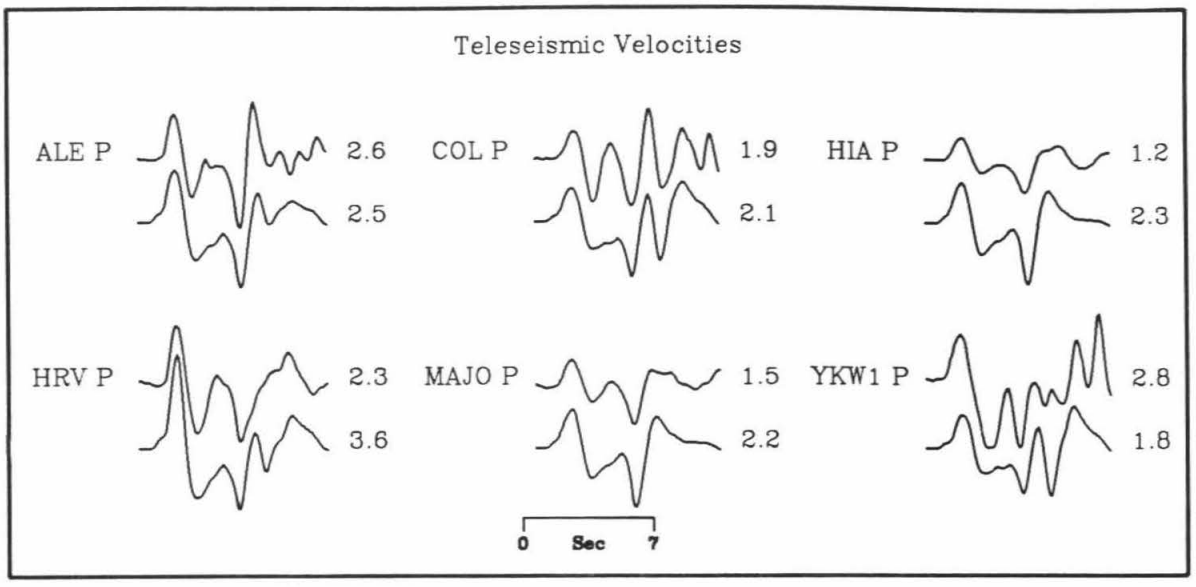

Figure 4.10: Comparison of observed (top) and synthetic (bottom) teleseismic records from the inversion of the combined data set. Amplitudes are in microns/sec.

window 2 is 0.1 sec after time window 1; time window 3 begins 0.2 sec later than window 1. The 0.35-sec time separation between the two arrivals is obtained in the model by rupturing two adjacent fault regions (Figure 4.11), top and bottom slip concentrations). The total time separation of 0.35 sec is obtained from the combined effects of a 0.15-sec delay that is due to rupture across the additional distance to the region shown in the bottom of Figure 4.11 relative to the region at the top of the figure, and a 0.2-sec time delay between time window 3 and time window 1. This may be considered to be a complex slip function or a local retardation of the rupture front. The alternative to a complicated slip function or locally variable rupture velocity is to allow only one time window and to force two slip concentrations separated in time by 0.35 sec. This is not as favorable as the more complex scenario, since it failed to predict the observed waveforms adequately.

Considering that slip occurs in all 3 time windows, the total slip duration in the region of the largest slip is 0.4 sec. As the peak slip is slightly greater than a meter, this requires a slip velocity of over 2 meters/sec. Similar slip velocities are demanded by models for other well-studied earthquakes [Heaton, 1990]. We also investigated the effect of different rupture velocities on the slip distribution. Although rupture velocities of 3.0 and 3.3 km/sec, corresponding to roughly 80% and 90% of the source-region, shear-wave velocity, were tried, they did not produce any improvement in the match to the observed waveforms. Thus, slightly faster rupture velocities are not favored, or ruled out. The fact that the earlier time window contributes a large portion of the slip suggests that a slower rupture velocity is not appropriate.

4.5.4 Forward Regional Waveform Modeling

Regional waveforms from the Sierra Madre earthquake recorded on broadband TERRAscope instruments were modeled by Dreger and Helmberger [1991], using a point source, a 1.0-sec source duration and a seismic moment of 2.5×10^{24} dyne-cm. In

Figure 4.11: Separate slip contributions for time window 1 (top), 2 (middle) and 3 (bottom) resulting from the strong-motion inversion. Each time window is separated by 0.1 sec. Contour interval is 20 cm. The concentric circles depict the location of the rupture front at 0.25 sec intervals. See text for details.

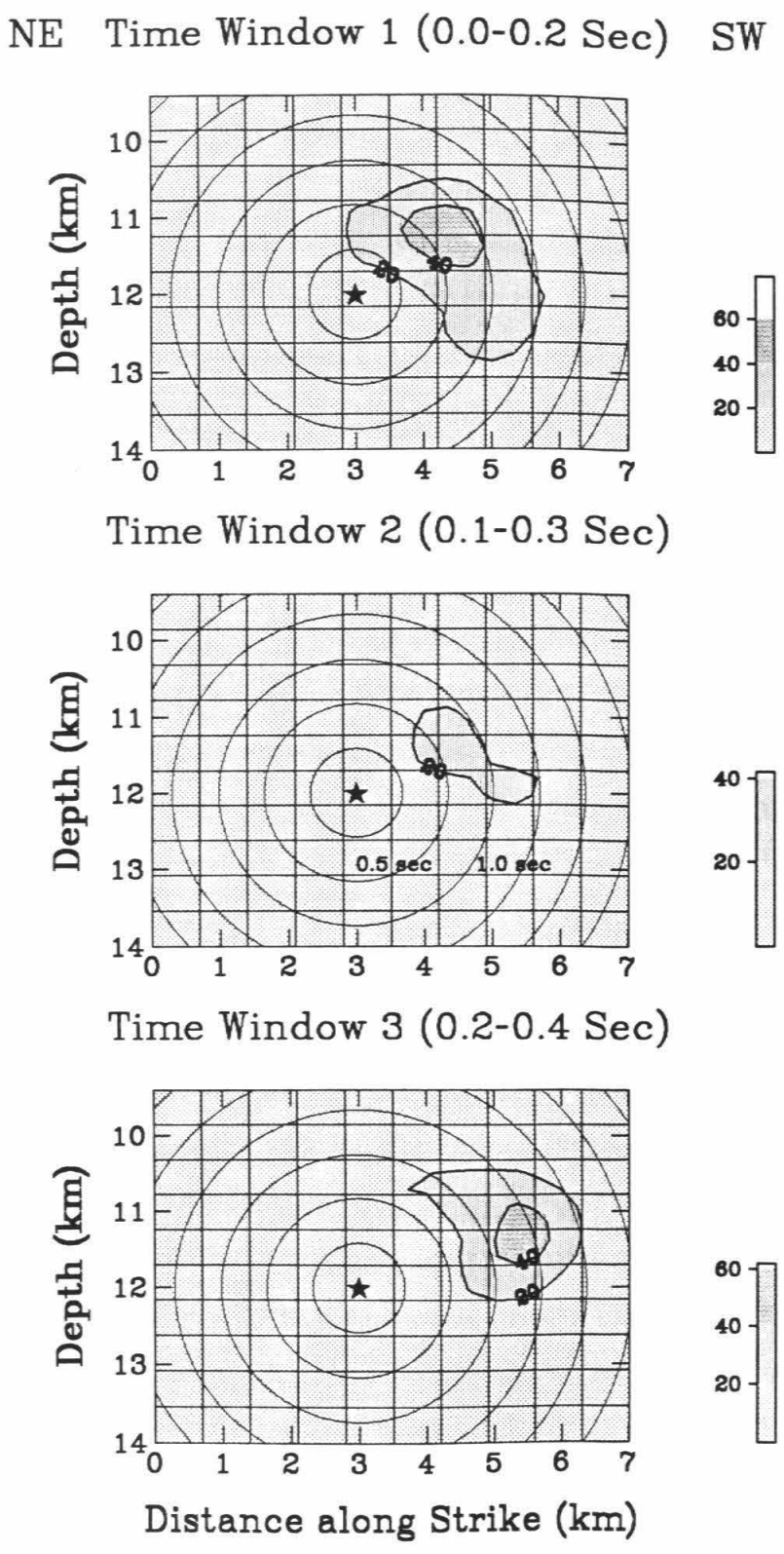
NE Time Window 1 (0.0-0.2 Sec) SW
Depth (km)
10
11
12
13
14
0 1 2 3 4 5 6 7
60
40
20
Time Window 2 (0.1-0.3 Sec)
Depth (km)
0.5 sec
1.0 sec
40
20
Time Window 3 (0.2-0.4 Sec)
Depth (km)
60
40
20
Distance along Strike (km)

this section we describe the prediction of those regional waveforms with an approximation of the slip distribution determined from the joint inversion of strong-motion and teleseismic data discussed above and shown in Figure 4.8. The distributed slip is approximated by lagging in time and summing point-source responses over a grid with the same area as our fault model. We model stations GSC, PFO, and ISA, all (coincidently) at distances of about 159 km, but at varying azimuths of 44°, 117° and 344°, respectively. It is advantageous to try modeling these stations, recognizing that GSC and ISA are at azimuths not well covered by close-in, strong-motion stations. The regional waveform modeling procedure we employ uses complete FK Green's functions and is discussed in detail by Dreger and Helmberger [1991]. In modeling the waveforms, we simulated three different, finite-fault rupture scenarios, the results of which are shown in Figures 4.12, 4.13 and 4.14. Amplitudes are displacements in centimeters. Immediately below the three components of observations at the top of Figures 4.12, 4.13 and 4.14 are the synthetics produced by a model that approximates the slip distribution determined above (slip updip and to the southwest of the hypocenter - SW). The next series of records results from a distribution of slip updip and towards the northeast (NE). The last row of synthetics were produced with slip concentrated directly downdip of the hypocenter. The dashed vertical lines mark the arrival times of important phases, *Pn*, *sPmP*, and *SmS*.

The waveforms most similar to the observations result from the model "SW", which best approximates the solution determined independently of regional waveforms by the inversion of teleseismic and strong-motion records. In particular, note the improvement to the *SmS* arrivals on the tangential and vertical components at station GSC and the similarity to the observed *P*-wave train on the radial and vertical components at all three stations. This exercise supports the finite-fault solution obtained above and suggests that the broadband, regional waveforms contain sufficient information to extract source information pertaining to rupture directivity and

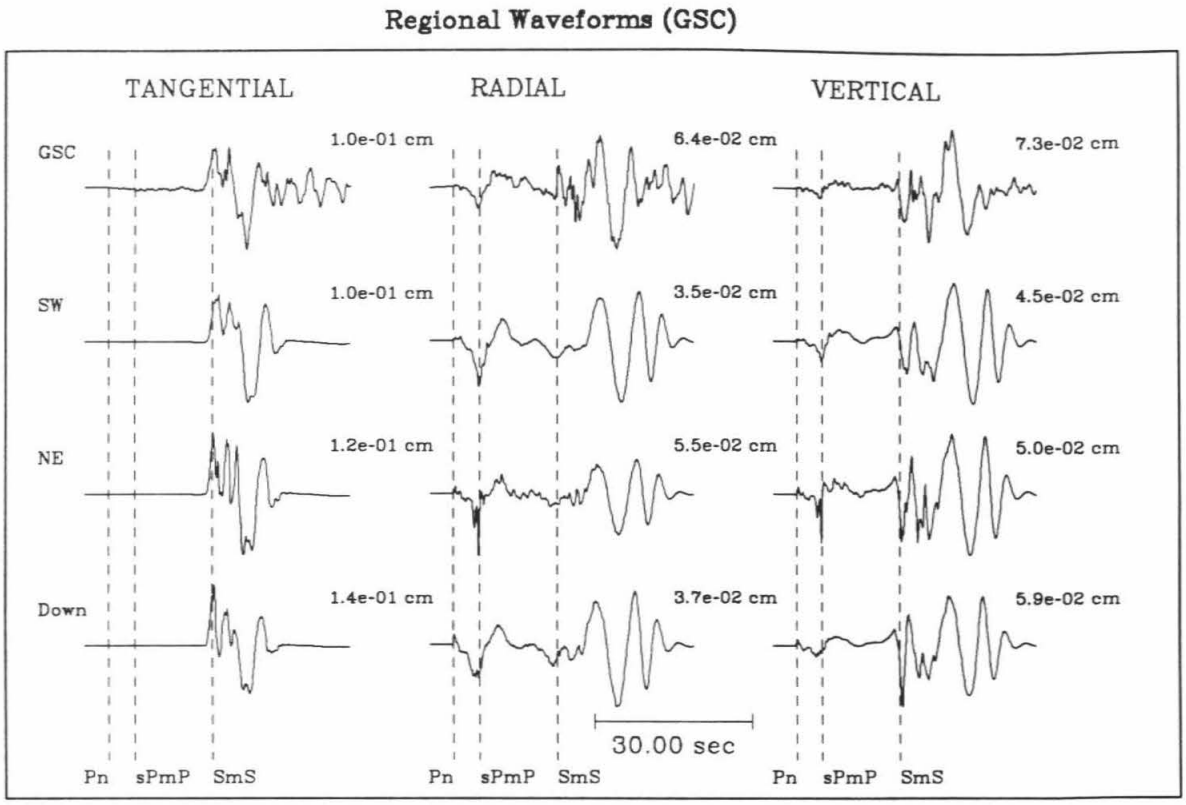

Figure 4.12: Comparison of observed regional waveforms (top) with synthetics for slip concentrated updip and to the southwest (SW), updip and to the northeast (NE) and downdip (Down) from the hypocenter for station GSC. The waveforms are normalized with the peak amplitudes given in centimeters.

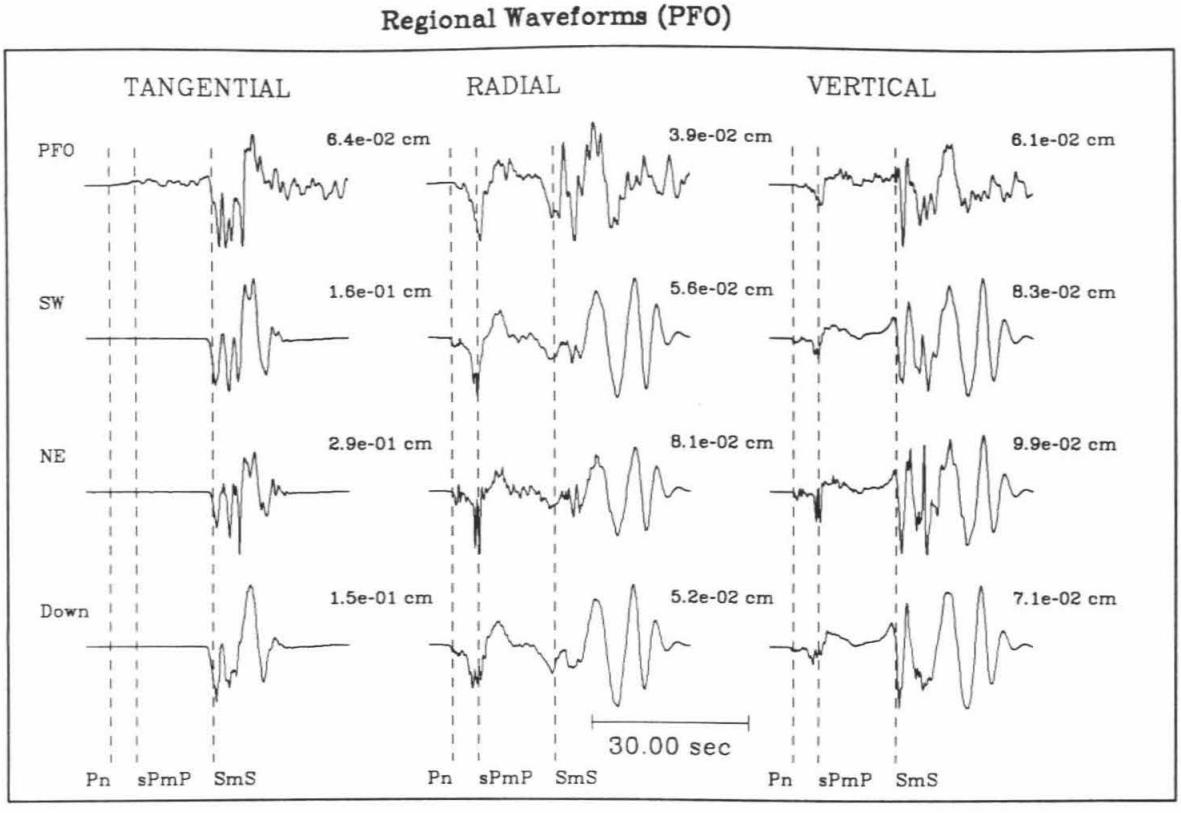

Figure 4.13: Comparison of observed regional waveforms (top) with synthetics for slip concentrated updip and to the southwest (SW), updip and to the northeast (NE) and downdip (Down) from the hypocenter for station PFO. The waveforms are normalized with the peak amplitudes given in centimeters.

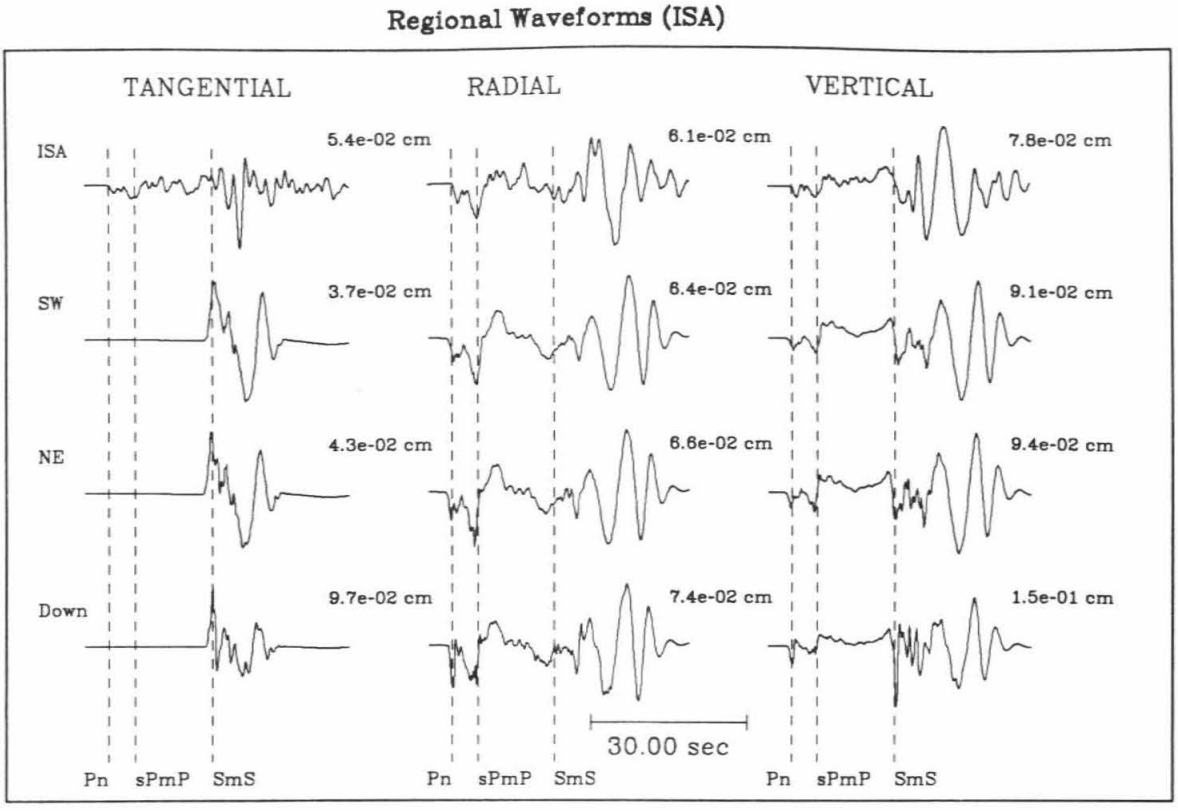

Figure 4.14: Comparison of observed regional waveforms (top) with synthetics for slip concentrated updip and to the southwest (SW), updip and to the northeast (NE) and downdip (Down) from the hypocenter for station ISA. The waveforms are normalized with the peak amplitudes given in centimeters.

relative slip location in addition to focal mechanism and seismic moment. Note that the tangential component at ISA is close to a radiation node for the Sierra Madre mechanism and is dominated by off-azimuth, multipathed arrivals; thus, it is not well fit by any of the models.

4.5.5 Forward Prediction of Surface-Displacement Field

Given the model of dislocation determined from the inversion of the seismic data, we can estimate the amount of coseismic uplift that occurred during the Sierra Madre earthquake. The Green's function summation technique used for the time histories can also be used to calculate theoretical, static displacements at the surface for a three-dimensional, finite fault buried in a halfspace. The half-space rigidity is 3.9×10^{11} dyne/cm^2, consistent with the velocity structure in the source region (Table 4.3). Once again, we subdivide the fault into a grid of subfaults, each having constant dislocation within the subfault, but which vary along the grid. The analytic expressions of Mansinha and Smylie [1971] are used to compute the surface displacement resulting from a constant dislocation on each subfault. The total displacement at a surface location is the sum of the displacement contributions from all subfaults, each subfault weighted by the amount of slip determined from the combined strong-motion and teleseismic inversion. By iterating over a grid of surface station locations, we can contour the resulting static offsets. The vertical component of surface displacement is shown in Figure 4.15. The peak vertical uplift is 14 mm and is centered about 2.5 km northeast of Mt. Wilson. For comparison, the peak uplift that was due to the 1987 Whittier Narrows earthquake was observed to be 50 mm (Lin and Stein, 1989).

We noted that the static displacements are not very sensitive to the location and concentration of the slip on the inferred fault plane. The location, amplitude and shape of the uplift pattern are more sensitive to the fault geometry and total slip

Figure 4.15: Vertical component of surface displacement computed from the combined strong-motion and teleseismic model of slip distribution. Contour interval is 2 mm.

Estimated Vertical Uplift from Sierra Madre Earthquake

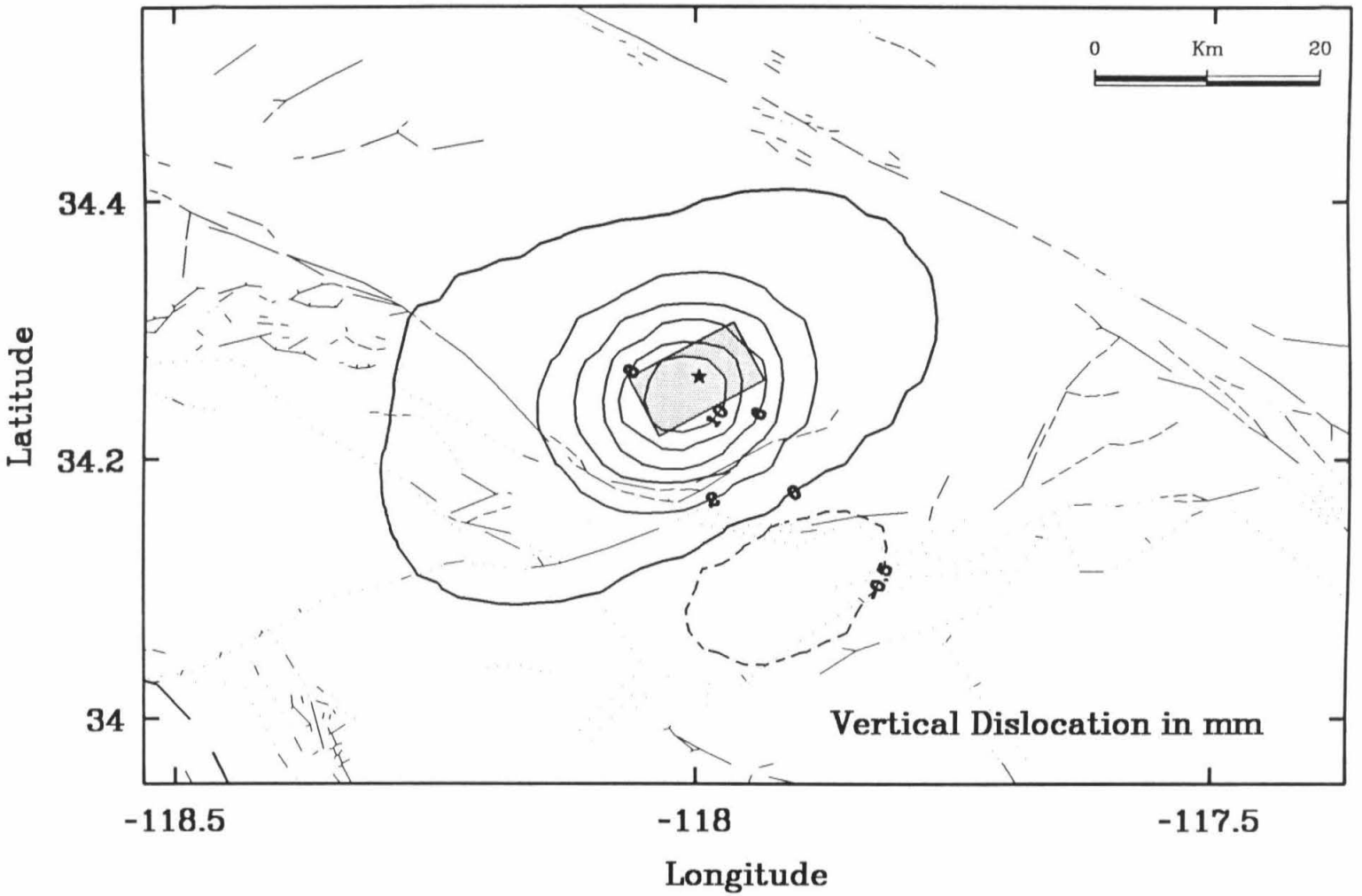

than its relative location updip or along strike. This suggests that only with a very dense network of geodetic monuments would it be possible to resolve variations of slip on a buried fault plane with dimensions comparable to that of the Sierra Madre earthquake (7 km by 6 km).

4.6 Discussion And Conclusions

There is an overall consistency of the ground motions predicted by our rupture model with the damage patterns, Modified Mercalli intensities [Stover and Reagor, 1991], and peak ground accelerations [M. Trifunac, personal communication, 1991] all of which indicate greater effects of ground motion to the south and west of the epicenter. Note that the largest amplitude recordings are directly updip and towards the southwest, and are not the closest stations (Figure 4.2). The largest-amplitude, strong motions are limited to a rather narrow, azimuthal window (Figure 4.2). In our model, it is the effect of radiation pattern and source directivity that focuses energy updip and toward the southwest. In general, of course, the above ground-motion indicators are a complicated interaction of source, path, and site effects, and population density, and the contribution of these factors must be evaluated.

The updip, southwestward rupture in our model is also incompatible with other observations. First, the hypocentral depth is slightly deeper than the point-source depth of the teleseismic data requiring propagation updip. Second, the broadband regional waveform data, which independently provide updip and downdip rupture constraints, are best modeled with updip slip. Finally, the location of the hypocenter with respect to the aftershock distribution and the extent of the distribution itself indicate probable updip extent to the slip (Figure 4.1).

Figure 4.16 indicates that many of the aftershocks surround the central asperity found in our dislocation model. Most noteworthy, the two largest aftershocks (both

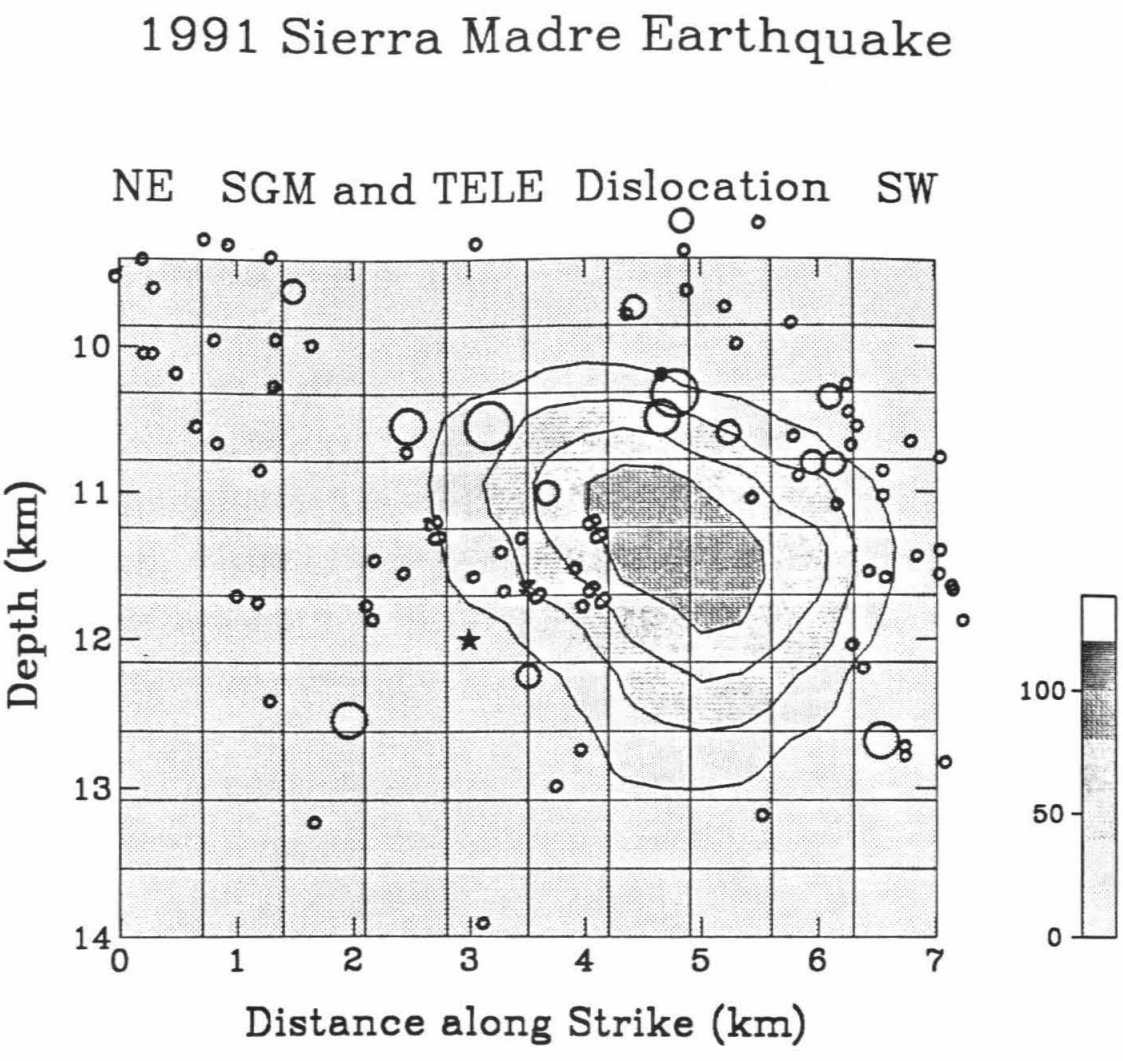

Figure 4.16: Northeast-southwest cross section of the fault model showing contours of dislocation for the combined strong-motion and teleseismic inversion. Aftershock seismicity is projected to the fault surface. The focal mechanism represents the location of the mainshock hypocenter. The two largest circles represent aftershocks both with magnitudes of 4.0.

magnitude 4.0) outline the edge of the significant coseismic slip inferred from our waveform modeling (Figure 4.16). This result is consistent with the observation of Mendoza and Hartzell [1988b] that aftershocks for many earthquakes often cluster along the margin of regions of the fault that experienced large, coseismic slips. They attribute the aftershock patterns to a secondary redistribution of stress following primary failure on the fault. Note that the overall dimensions of the active aftershock perimeter of the Sierra Madre earthquake define an area substantially larger than the modeled coseismic region.

From teleseismic and local strong-motion, waveform modeling, we find that only a small portion of the fault was responsible for producing significant ground motions, implying a substantial stress drop. It is often difficult to estimate stress drop since one must normally make assumptions concerning the relationship of the rupture duration and the rupture area. The finite-fault approach allows us to determine both the amount of slip and the area over which it occurred. In this case, the stress-drop expression of Eshelby [1957] for a circular fault is appropriate, $\Delta\sigma = (7\pi\mu\overline{u})/(16a)$, where μ is the rigidity, $\overline{u}$ is the average dislocation, and a is the radius. Using $\mu = 3.9 \times 10^{11}$ dyne/cm^2, $\overline{u} = 57$ cm, and $a = 2.0$ km, we obtain the stress drop of 150 bars. Since the choice of the area of significant rupture is still subjective, we also evaluate the stress drop for a slightly smaller rupture area. For $a = 1.8$ km, the stress drop becomes 190 bars. This event consists of a relatively high stress drop region with relatively little additional slip in the surrounding regions.

There are serious ramifications to our observation that damaging ground motion radiation can be attributed to such a compact fault region. It is often considered that fault segmentation limits the maximum size of earthquakes that can occur along a given fault zone. The relatively large localized slip in the Sierra Madre earthquake suggests that thrust faults of even limited dimensions are capable of producing potentially hazardous ground motions. This is substantiated by the high stress drops

and substantial ground motions from the 1987 Whittier Narrows (M_L=5.9), 1988 Pasadena (M_L=4.9), and 1990 (M_L=5.5) Upland earthquakes. The localized slip concentrations and the heterogeneous nature of the final dislocation imply that strain was released on only a small area of each fault. Further, the large gradients in slip modeled from the Sierra Madre earthquake (this study) and from the Whittier Narrows earthquake [Hartzell and Iida, 1990] suggest that regions immediately adjacent to the main asperities of these events likely experienced stress increases during the earthquake and are therefore more likely to fail now than prior to the earthquake. Recall that the area that actually slipped is substantially smaller than the region that experienced aftershocks.

It is worthwhile to compare and contrast the Sierra Madre earthquake and our rupture model with the 1987 Whittier Narrows earthquake (M_L=5.9) and seismological studies of that event. Both events were deep-thrust earthquakes and both were costly to the residents of metropolitan Los Angeles. The felt area for the Sierra Madre event was approximately 59,000 km^2, considerably less than the 110,000 km^2 felt area for the Whittier Narrows earthquake [Stover and Reagor, 1991]. For comparison, the 1987 Whittier earthquake had a seismic moment of about 1.0×10^{25} dyne-cm as estimated from strong-motion data [Hartzell and Iida, 1990] and 1.1 to 1.4×10^{25} dyne-cm based on teleseismic waveforms [Bent and Helmberger, 1989], roughly 4–5 times the moment of the Sierra Madre earthquake.

Estimates of the rupture area for the Whittier Narrows earthquake (and thus stress drop) vary considerably. Hauksson and Jones [1989] show that the overall aftershock area was approximately 25–30 km^2, but proposed a rupture area of 13 km^2 based on the temporal and spatial clustering of the aftershocks. Wald *et al.* [1988], using a semi-empirical, forward-modeling technique, inferred that a rupture area of about 20 km^2 could adequately simulate the acceleration recordings. Hartzell and Iida estimate that the total rupture area from the Whittier earthquake is approxi-

mately 70 km^2, with more concentrated slip isolated over a smaller region of perhaps 25 km^2. Still, the majority of the coseismic slip was contained within the overall aftershock distribution. For the Sierra Madre earthquake, nearly all the slip lies within an area of 13 km^2, with most of the moment release within a region on the order of 4 km^2, easily confined to a small portion of the total active aftershock perimeter. For both the Whittier Narrows and the Sierra Madre events, the hypocenter is located in a region of the fault at the edge of an asperity, not within the major slip area.

Note, however, that although the total moment was a factor of 4–5 lower than that of the Whittier earthquake, the peak ground velocity of 25 cm/sec recorded at station ETN from the Sierra Madre earthquake is comparable to that recorded during the Whittier Narrows earthquake at stations WTR (26 cm/sec) and DOW (28 cm/sec). The relatively large ground motions for the Sierra Madre earthquake may reflect the highly localized nature of the source. Of course, damage resulting from the Sierra Madre earthquake was greatly moderated by the relative remoteness of the epicentral region and areas of high ground motion relative to the heavily populated area of the Whittier Narrows earthquake.

Chapter 5

1906 San Francisco Earthquake

5.1 Abstract

All quality teleseismic recordings of the great 1906 San Francisco earthquake archived in the 1908 Carnegie Report by the State Earthquake Investigation Commission were scanned and digitized. First-order results were obtained by comparing complexity and amplitudes of teleseismic waveforms from the 1906 earthquake with well-calibrated, similarly located, more recent earthquakes [1979 Coyote Lake, 1984 Morgan Hill and 1989 Loma Prieta earthquakes) at nearly co-located modern stations. Peak-amplitude ratios for calibration events indicated that a localized moment release of about $1 - 1.5x10^{27}$ dyne-cm was responsible for producing the peak of the teleseismic bodywave arrivals. At longer periods (50-80 sec), we found that spectral-amplitude ratios of the surface waves require a total moment release between $4 - 6x10^{27}$ dyne-cm for the 1906 earthquake, comparable to previous geodetic and surface-wave estimates [Thatcher, 1975]. We then made a more detailed source analysis using Morgan Hill S bodywaves as empirical Green's Functions in a finite-fault, subevent summation. The Morgan Hill earthquake was deemed most appropriate for this purpose, as its mechanism is that of the 1906 earthquake in the central por-

tion of the rupture. From forward and inverse empirical summations of Morgan Hill Green's functions, we obtained a good fit to the best-quality, teleseismic waveforms with a relatively simple source model having two regions of localized strong radiation separated spatially by about 110 km. Assuming the 1906 epicenter determined by Bolt [1968], this corresponds with a large asperity (on the order of the Loma Prieta earthquake) in the Golden Gate/San Francisco region and one about three times larger located northwest along strike between Point Reyes and Fort Ross. This model implies that much of the 1906 rupture zone may have occurred with relatively little 10-20 sec radiation, similar to the 1990 Philippines ($M_S = 7.8$) earthquake, but in contrast to the extreme complexity of the 1976 Guatemalan ($M_S = 7.5$) event. Consideration of the amplitude and frequency content of the 1906 teleseismic data allowed us to constrain the scale length of the largest asperity to be less than about 40 km.

With constraints on the largest asperity (size and magnitude), we produced a suite of estimated, synthetic-ground velocities. For purposes of comparison with the recent, abundant, Loma Prieta strong-motion data set, we "moved" the largest 1906 asperity into the Loma Prieta region. Peak-ground velocity amplitudes are substantially greater than those recorded during the Loma Prieta earthquake, and are comparable to those predicted by the attenuation relationship of Joyner and Boore [1988] for a magnitude $M_W = 7.7$ earthquake.

5.2 Introduction

The great 1906 San Francisco earthquake began an era in earthquake seismology. Following this earthquake, direct observations of surface displacement combined with the analysis of the surrounding crustal deformation led Reid to formulate the elastic-rebound theory. Although much has been learned from the numerous studies of the

1906 earthquake, a systematic analysis of the recorded teleseismic body and surface waveforms has not been made. Yet, the seismic recordings of the 1906 earthquake have been well preserved in the Atlas of the 1908 Carnegie Report by the State Earthquake Investigation Commission [Lawson, 1908], hereafter referred to as the *Atlas* or the *Report.* It is the authoritative reference and summary of the 1906 earthquake, including geological observations, the effects of ground shaking and all the data collected following the earthquake. In this study, we revisit the waveform data set contained in the *Atlas* and analyze the data in the context of modern source analysis.

The need to understand the ground-motion hazard potential from earthquakes in the San Francisco area has been rekindled by the occurrence of and damage from the 1989 Loma Prieta earthquake. The Loma Prieta event has provided a valuable strong-motion data set for analysis of source complexity and ground-motion damage from a magnitude 7 earthquake. Unfortunately, local, strong-ground motion data from the (much larger) 1906 earthquake were limited to one off-scale, partial recording on the Ewing three-component seismograph at Mt. Hamilton [Boore, 1977]. Few strong-motion recordings have been made from any large strike-slip earthquakes. However, it is possible to obtain source information relevant to understanding the local strong motions through analysis of the teleseismic data.

In a separate study of the Loma Prieta earthquake, Wald *et al.* [1991] inverted the broadband teleseismic and local strong motion to determine the temporal and spatial distribution of slip. Separate inversions of the teleseismic data (periods 3-30 sec) and strong-motion data (periods 1-5 sec) resulted in similar rupture models. Hence the broadband teleseismic data has the capability of providing important constraints on the nature of the strong motions at long periods, independent of the strong-motion recordings. In the study that follows, we apply this insight to the 1906 earthquake, though clearly the quality and bandwidth of the historic data are not as impressive

as the modern digital, broadband data.

Our study focuses on several important, unresolved issues relevant to the 1906 rupture. Was the 1906 rupture complex or were there large portions of the fault where rupture was fairly uniform? What were the nature and location of fault asperities? As we will show, the body waveforms are fairly simple, considering the rupture duration expected for such a large rupture length (at least 300, and likely 430 km). Did the Loma Prieta section of the fault have a dip-slip component? The geodetic study of Segall and Lisowski [1990] requires a few meters of strike-slip motion for 1906 along the Loma Prieta segment of the fault, but their data do not rule out a thrust component comparable to the Loma Prieta earthquake at greater depths. Is there evidence for a dip-slip component in this or other portions of the fault? We address these issues in this study.

Processing and interpreting the turn-of-the-century seismic data recorded presented many challenges. However, we believe that the historic data are valuable in spite of their limitations, and thus, it is desirable to try to obtain as much information as possible from them considering the societal and scientific importance of the 1906 San Francisco earthquake. Hence, we have revisited the data available for the 1906 earthquake in an effort to place constraints on the nature of that rupture, relate the radiated seismic energy to fault breakage and geodetic-offset measurements, and to try to determine its relationship to the Loma Prieta rupture.

Although the records alone of the 1906 earthquake may be insufficient to resolve the above questions, the use of records from the Loma Prieta , Morgan Hill and Coyote Lake earthquakes first as calibration events, and then as empirical Green's functions assists in extracting important information from this unique data set. The analysis of the teleseismic data proves useful in answering questions about fault-rupture style on the San Andreas Fault and asperity positions, in addition to allowing an estimation of strong ground motions likely experienced during the 1906

earthquake.

5.3 Overview of Previous Studies

The enormity and significance of the 1906 earthquake resulted in careful collection and mapping of the geologic, geodetic, seismic and sociological data. A wealth of investigations have been made, and scientific studies of this event still appear occasionally in the geophysical literature. The occurrence of the 1989 Loma Prieta earthquake rejuvenated interest in previous San Francisco Bay area earthquakes, particularly the 1906 event. Most recently, reanalysis has been made of both the geodetic [Segall and Lisowski, 1990] and surface offset data [Prentice and Schwartz, 1991]. Constraints on the rupture characteristics are provided by previous studies of the epicenter, surface offset, geodetic slip and mapped isoseismal distributions.

5.3.1 Surface Offset and Geodetic Observations

The 1906 surface rupture is known to have ruptured about 300 km from near San Juan Bautista (or Chittenden) to Point Arena (Figure 5.1). That the rupture continued offshore for 140 km to Cape Mendocino is commonly assumed and was initially based on an observation of surface rupture at Shelter Cover (near Point Delgada, Figure 5.1). The amount of slip at Point Delgada was never documented, and it might not be of tectonic origin. Other equivocal evidence for offshore rupture is suggested by other observations, but the question of the offshore extension of rupture has not been eliminated. Observations that support the extension of rupture offshore include the impressive ground shaking and damage in the Cape Mendocino region as shown by the 8-9 Modified Mercalli isoseismal values (Figure 5.2). In addition, a linear zone of strong shaking (X on the Rossi-Forel scale), narrower but similar to regions along the fault trace farther south, is evident in the *Atlas* map of apparent intensi-

ties but is not so clear because of the limited number of data points in Figure 5.2. The *Report* also documents many strongly felt aftershocks within the same region, many of which occurred locally, considering that they were not reported at locations towards the southeast. Further, geodetic modeling by Thatcher and Lisowski [1987a] favors about 4-6 meters of displacement to a depth of 10 km on the offshore region to satisfy the distortion of the geodetic network onshore to the east.

Alternatively, the strong shaking along the extension of the northwest terminus of a rupture propagating over 200 km in that direction would be expected from the effects of source directivity. Likewise, aftershocks commonly occur well off the end of the rupture zone (i.e., the 1990 Philippines earthquake) and thus do not necessarily reflect the true source dimension. Concerning the geodetic evidence for large 1906 offsets offshore, the data of Thatcher and Lisowski [1987a] spanned a very long duration from about 1880-1940 and were of course limited to a one-sided, onshore network well east of the rupture. Therefore, their resolution is not good, and any displacement observed was not necessarily coseismic. There is no clear, documented evidence for tectonic-surface rupture associated with the 1906 earthquakes at the northernmost end of the assumed rupture, nor have any paleo-earthquakes been associated with the San Andreas north of Point Arena [D. Merrits, personal communication, 1991]. Further, McLaughlin *et al.* [1979] discuss adularia veins (dated older than 10 million yrs. BP) that cross the terraine boundary at Point Delgada. According to McLaughin *et al.* [1979] these northeast striking veins, are crossed with a steeply dipping, northwest-striking fault that many workers regard as the on-land extension of the San Andreas Fault. However, the mineralization and cross-cutting relation of the faults, which show little or no offset, indicate that no significant motion has occurred along the purported San Andreas Fault trace since late-middle Miocene time. Lastly, the commonly assumed connection of the San Andreas Fault from Point Arena to Point Delgada requires a bend in the San Andreas strike more significant ($> 20°$)

Figure 5.1: Location map showing rupture length (thick line) of the 1906 San Francisco earthquake. Arrows refer to significant changes in the strike of the San Andreas Fault. The epicenter of Bolt [1968] is represented as a star. Focal mechanisms indicate location and faulting geometry of calibration events.

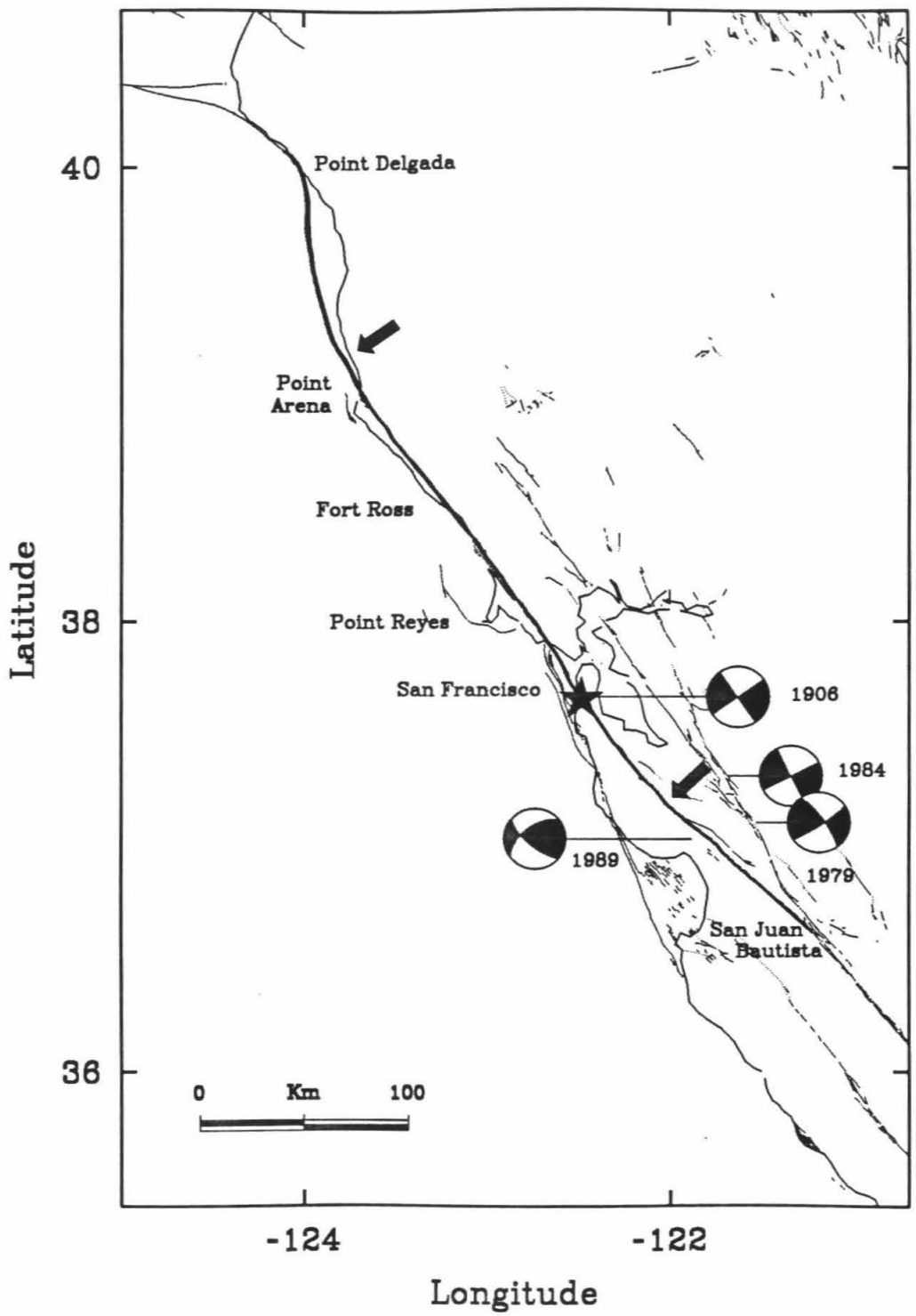
Point Delgada
Point
Arena
Fort Ross
Point Reyes
San Francisco
1906
1984
1989
1979
San Juan
Bautista
0
Km
100
40
38
36
-124
-122
Latitude
Longitude

than anywhere else along the northern portion of the fault. It might be expected to behave as a source of high-frequency radiation during a rupture that traversed such a geometric obstacle. There is not substantial evidence for later radiation in the teleseismic recordings. The shorter (300 km) rupture length is more consistent with the effective rupture length of 240 km determined by Ben-Menahem [1978] for this earthquake on the basis of surface-wave analysis. This is not to suggest that the rupture did not continue to offshore, but rather to point out that any conclusion on this issue is not without question.

In order to model this event, we divided the rupture length into three segments: the northwest, central and southeast portions of the full rupture. The arrows on Figure 5.1 depict the boundaries between these segments. Note that there is a significant change in strike between the segments going from N15°W in the northeast to N35°W in the central section to N50°W in the southeast. In the central portion of the rupture, surface offset averaged nearly 4 meters from south of San Francisco to Point Arena, where it heads offshore. In the southeastern section, the surface offset is difficult to quantify and is much smaller than to the northwest. The historical data provide no unequivocal estimates of surface slip, though offset in Wright's tunnel amounts to 1 to 1 1/2 meters and is considered one of the more reliable measurements [Prentice and Schwartz, 1991]. The geodetic data require the slip at depth to be about 2 to 3 meters from San Juan Bautista through the Loma Prieta section and between about 5 and 7 meters along the central segment [Thatcher, 1975].

5.3.2 Seismic Data

Epicenter

For modeling purposes, we chose the epicenter given by Bolt [1968], which was based on local timing observations, stopping of astronomical clocks, a local, strong-motion recording at Mt. Hamilton and teleseismic P and S-P travel times. The location is

Figure 5.2: Modified Mercalli shaking intensity map [from Toppozada and Parke, 1982]. The thick line represents the trace of the San Andreas Fault, and the extent of intensity VII+ is indicated with a dashed line.

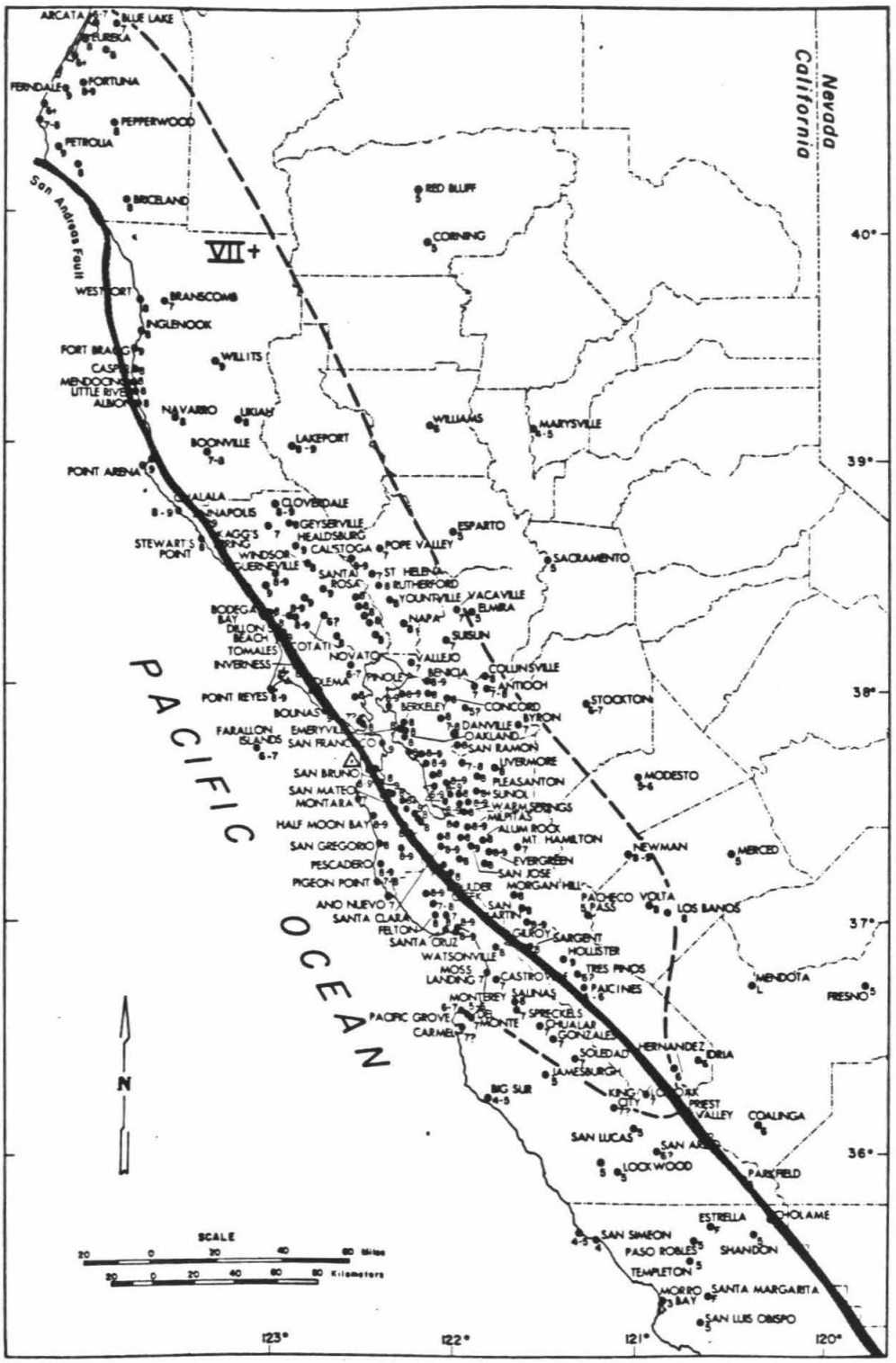
Nevada
California
San Andreas Fault
VII+
PACIFIC OCEAN
ARCATA
BLUE LAKE
EUREKA
FERNDALE
FORTUNA
PEPPERWOOD
PETROLIA
BRICELAND
RED BLUFF
CORNING
WESTPORT
BRANSCOMB
INGLENOOK
WILLITS
NAVARRO
LIGIAN
BOONVILLE
LAKEPORT
WILLIAMS
MARYSVILLE
POINT ARENA
CLOVERDALE
GEYSERVILLE
HEALDSBURG
CALISTOGA
POPE VALLEY
ESPARTO
SACRAMENTO
STEWARTS POINT
WINDSOR
GUERNEVILLE
SANTA ROSA
ST HELENA
RUTHERFORD
YOUNTVILLE
VACAVILLE
ELMIRA
NAPA
SUISUN
BODEGA BAY
DILLON BEACH
TOMALES
PETALUMA
NOVATO
VALLEJO
INVERNESS
POINT REYES
BENICIA
COLLINSVILLE
ANTIOCH
STOCKTON
BERKELEY
CONCORD
BYRON
BOLINAS
FARALLON ISLANDS
EMERYVILLE
SAN FRANCISCO
OAKLAND
DANVILLE
SAN RAMON
LIVERMORE
MODESTO
SAN BRUNO
SAN MATEO
MONTARA
PLEASANTON
SUNOL
WARM SPRINGS
MILPITAS
ALUM ROCK
MT HAMILTON
HALF MOON BAY
SAN GREGORIO
PESCADERO
EVERGREEN
NEWMAN
MERCED
SAN JOSE
PIGEON POINT
MORGAN HILL
PACHECO PASS
VOLTA
LOS BANOS
ANO NUEVO
SANTA CLARA
FELTON
SAN MARTIN
GILROY
SARGENT
SANTA CRUZ
HOLLISTER
WATSONVILLE
TRES PINOS
MOSS LANDING
CASTROVILLE
PAICINES
MENDOTA
FRESNO
MONTEREY
SALINAS
SPRECKELS
PACIFIC GROVE
CHUALAR
GONZALES
CARMEL
SOLEDAD
HERNANDEZ
ORIA
JAMESBURGH
BIG SUR
KING CITY
PRIEST VALLEY
COALINGA
SAN LUCAS
SAN ARDO
LOCKWOOD
PARKFIELD
ESTRELLA
CHOLAME
SAN SIMEON
PASO ROBLES
SHANDON
TEMPLETON
MORRO BAY
SANTA MARGARITA
SAN LUIS OBISPO
N
SCALE
20 0 20 40 60 Miles
20 0 20 40 60 80 Kilometers
40°
39°
38°
37°
36°
123°
122°
121°
120°

near that of the 1957 Daly City earthquake ($M = 5.7$) epicenter and is shown as an asterisk in Figure 5.1. Our subsequent modeling of the body waves supports this location.

Strong Motions

The only strong-motion data written during the 1906 earthquake was on a Ewing three-component seismograph at Lick Observatory on Mt. Hamilton, an epicentral distance of about 85 km. Although the traces went off scale after only 10 sec, Boore [1977] was able to model features of the recording and to determine that the polarities and timing were consistent with the epicenter determined by Bolt [1968]. Boore [1977] also concluded that the most massive faulting responsible for the strong motions at Mt. Hamilton came from at least 75 km away and were dominated by surface waves. In addition to the Mt. Hamilton strong-motion recording, several Ewing duplex-pendulum recordings were preserved. The records at Mt. Hamilton and Berkeley were useful to Boore [1977] in corroborating waveform polarities at the Mt. Hamilton station.

Local Magnitude

The duplex-pendulums records mentioned above, in addition to several others (Alameda, San Jose, Oakland and Carson City, Nev.) and a simple pendulum at Yountville were used by Jennings and Kanamori [1979] to estimate the local magnitude by extrapolating the seismoscope-style recordings to the maximum response of the standard Wood-Anderson instrument. The Wood-Anderson response is most appropriate for quantifying the nature of strong ground motions, since its period and damping are such that it is sensitive to motions in the frequency range of most interest to earthquake engineering. Considering the uncertainties involved, Jennings and Kanamori assigned an M_L range of $6\frac{3}{4}$ to $7\frac{1}{4}$, though analysis of the Carson City recording,

deemed to be most reliable, gave an $M_L = 7.2$. It is fortunate to have an M_L estimate for 1906 to compare with other large, strike-slip earthquakes since the local magnitude determination is made at distances relatively near the source, and hence, the time history input to the instrument is more representative of the duration and frequency content of near-source ground motions than other magnitude scales.

Surface-Wave Magnitude

An important issue that arose during this study involved the value of the surface-wave magnitude (M_S) for the 1906 earthquake. The M_S value of 8 $\frac{1}{4}$ (or 8.3) often quoted for 1906 is an overestimate, as stated by Abe and Noguchi [1983], and can be explained by two factors. First, there is an azimuthul bias towards larger M_S values from California to stations in Europe and second, the bias is exacerbated by the use of undamped instrument during that time period. The azimuthal bias can be demonstrated with M_S determinations for the 1979 Imperial Valley and 1989 Loma Prieta earthquakes (Figure 5.3). The M_S values are plotted as a function of station azimuth as given in the monthly Preliminary Determination of Epicenters (PDE's) for the Loma Prieta and Imperial Valley events, and directly from Richter's notebook for the 1906 values.

Note that within the narrow range of azimuths from which the 1906 M_S determination was made (20° to 90°), the other events have very large M_S values and would provide a biased estimate of the average M_S value. Using only magnitude values within this azimuthal range yields an $M_S = 7.4$ for the 1989 Loma Prieta earthquake, while the computed value should be 7.0. As a side note, for the individual station M_S values published in the PDE's and shown in Figure 5.3, the average Loma Prieta M_S is 7.0, not 7.1 as is commonly accepted. Similarly, the 1979 Imperial Valley M_S value of 6.9 was determined largely from European stations, yielding a biased value. For azimuths limited from 20° to 90°, the M_S would be 7.1. Also note

Figure 5.3: Surface-wave magnitudes (M_S) as a function of station azimuth for the (a) 1989 Loma Prieta earthquake, (b) 1979 Imperial Valley earthquake, and (c) the 1906 San Francisco earthquake. Open circles are values that were not used in the computation of the official PDE $M_S = 7.1$ calculation.

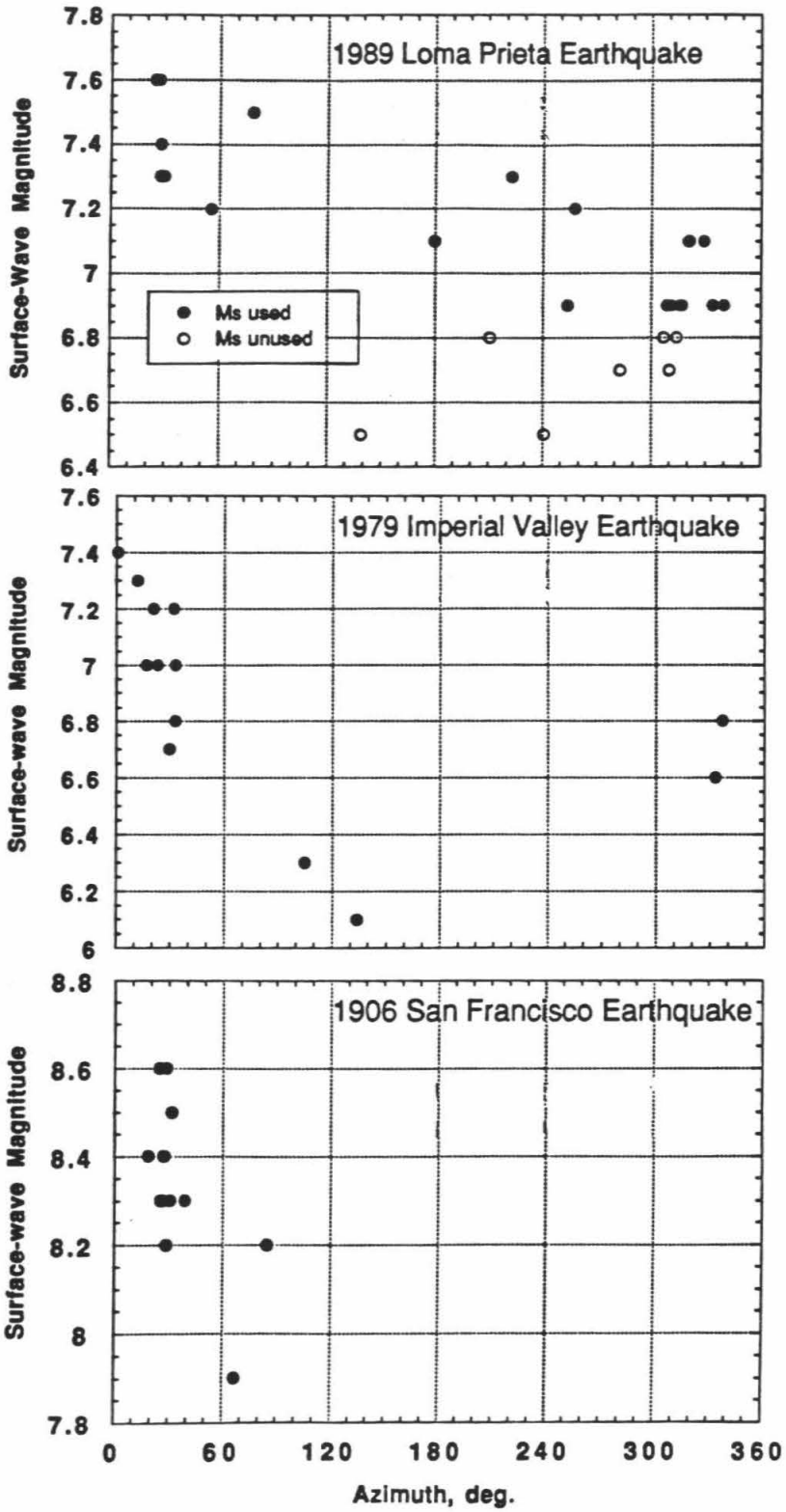
1989 Loma Prieta Earthquake
Ms used
Ms unused
Surface-Wave Magnitude
7.8
7.6
7.4
7.2
7
6.8
6.6
6.4
1979 Imperial Valley Earthquake
Surface-wave Magnitude
7.6
7.4
7.2
7
6.8
6.6
6.4
6.2
6
1906 San Francisco Earthquake
Surface-wave Magnitude
8.8
8.6
8.4
8.2
8
7.8
0
60
120
180
240
300
360
Azimuth, deg.

that for these two events, the moment magnitudes M_W computed from the seismic moments determined from waveform modeling are significantly smaller than the M_S. Since most events in this magnitude range M_S are approximately the same as M_W, the above disparity between M_S and M_W for these two events suggests that the M_S values for these two events are overestimated.

We found that this azimuthal trend holds true for all other moderate-to-large California earthquakes (with the exception of the 1980 $M_S = 8.0$ Eureka event) and is thus likely to be independent of focal mechanism. Loma Prieta has a good distribution of stations and only a slight azimuthal bias, and therefore, only a 0.2 unit difference between M_S and M_W. Imperial Valley has a considerable azimuthal bias and consequently shows a 0.4 unit difference between M_S and M_W.

Finally, the 1906 M_S determination has both a severe azimuthal bias and in addition is further biased by the use of undamped instruments as suggested by the work of Abe and Noguchi [1983]. They recognized that M_S determinations during the period from 1904-1906 were 0.5 magnitude units too large. They attributed this bias to the combined use of damped and undamped seismographs (the undamped were slowly phased out). Abe and Noguchi [1983] used (undamped) Milne instrument recordings with a correction for damping and obtained $M_S = 7.8$ for the San Francisco earthquake. At the time, Milne instruments had a better worldwide (hence azimuthal) coverage than damped instruments for 1906. Most M_S magnitudes based on damped instruments relied heavily on European stations, which clearly show a path bias for events from California [Gutenberg, 1955].

An M_S value of $7\ \frac{3}{4}$ is consistent with the $M_W = 7.7$ estimate of Thatcher [1975] based on amplitudes of 50-100 sec period surface waves at (stations ZIE, UPP and GOT). It is also in agreement with the geodetic data that gave an $M_W = 7.7$ [Thatcher and Lisowski, 1987b] from their estimated moment of $5x10^{27}$ dyne-cm. Ben-Menahem [1978] found the seismic potency to be 25,000 m-km^2, on the basis of

modeling 50-100 sec surface waves. Using the same average rigidity, $\mu = 3.0$ x 10^{11} dyne/cm^2, as Thatcher [1975], this implies a seismic moment of $7.5x10^{27}$ dyne-cm ($M_W = 7.9$).

The implication of the lower $M_S = 7\frac{3}{4}$ is very important, in that the moment-magnitude equivalent of $M_S = 7\frac{3}{4}$ requires an average slip based on the estimated rupture area on the order of several meters, compatible with surface and geodetic observations. A moment magnitude of $8\frac{1}{4}$ requires an average of about 15 m over the entire rupture length, even assuming rupture along the maximum-estimated length (450 km) and a conservatively large average width of 15 km. This is much larger than the geodetic- and surface-offset observations allow.

5.4 Data

5.4.1 1906 Historical Data

The 1906 earthquake was recorded at 96 stations around the world. The data from these stations were preserved in the *Report* and nearly all at the original recording size. Absolute time was preserved at most stations; time corrections from G.M.T. were provided along with instrument damping, magnification and free period constants. An example of the quality of the original analogue data contained in the *Atlas* is shown in Figure 5.4 for the station Göttingen, Germany, as recorded on a Wiechert inverted-pendulum instrument.

5.4.2 Digitizing System

A substantial portion of this project involved generating usable, digitized waveforms from the historic and modern data sets. The waveforms were scanned and digitized on a digitizing system developed at Caltech. Care was taken to remove the instrument pen arc and to preserve absolute timing. The software includes an interactive

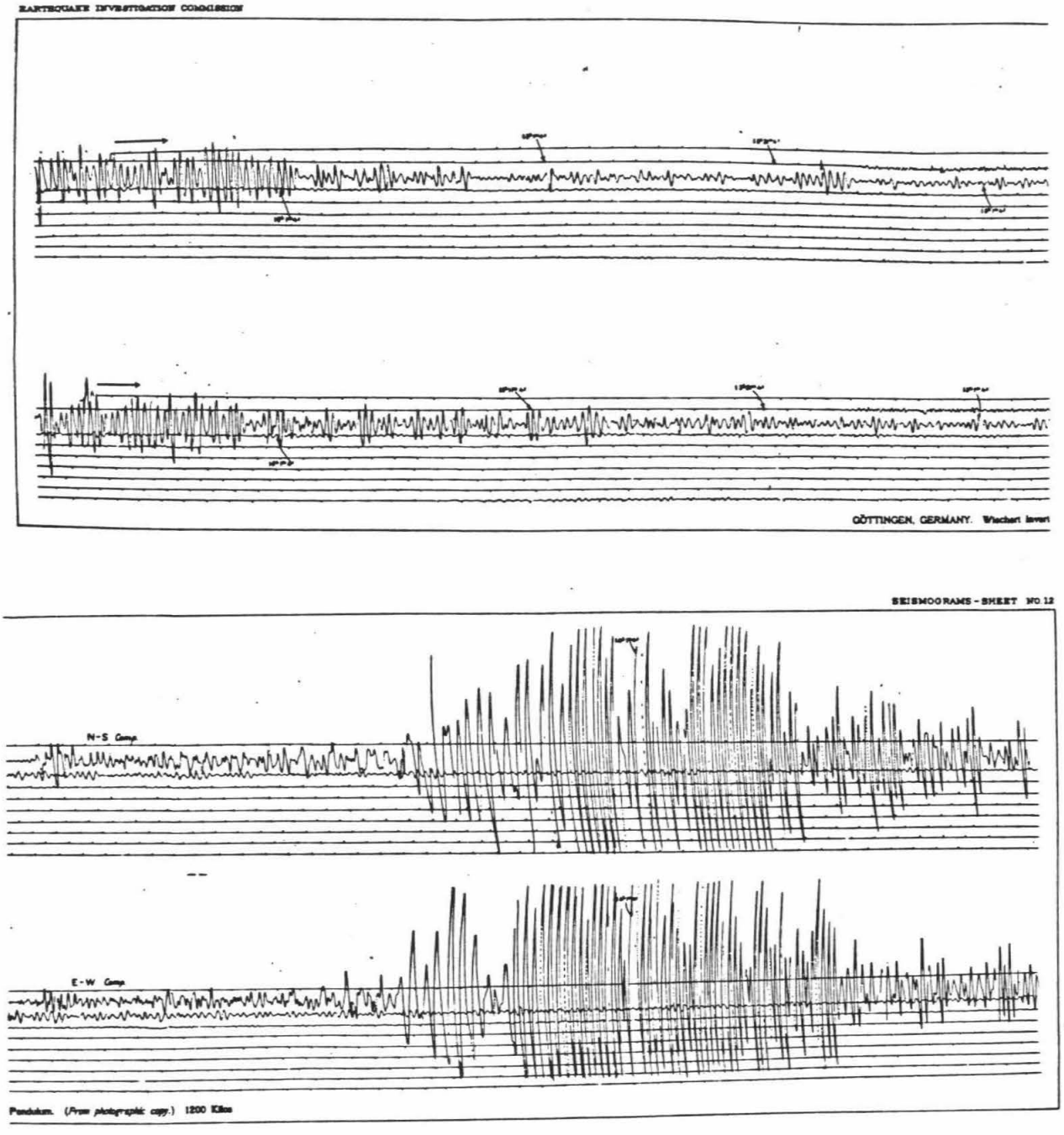

Figure 5.4: Example from the *Atlas* of the original analogue recording at Göttingen, Germany. Only a portion of entire seismogram is shown because of the scale. The record is original-sized and uncut in the *Atlas*.

trace-following algorithm (developed by Neil Humphreys). The digitized trace is converted to SAC format. In addition to the 1906 San Francisco data, many more analogue recordings of more recent events were digitized from long-period World-Wide Standardized Seismic Network (WWSSN) stations to be used for calibration and empirical Green's functions. Those data will be discussed in a later section.

5.4.3 Instrument Responses

Useful data were obtained for 12 stations, the locations of which are given in Table 5.1 and shown in Figure 5.5. The most useful records were written by Wiechert and Bosch-Omori instruments. The Wiechert instrument response can be accurately reproduced; the free period is about 5-15 sec, and the magnification is on the order of 150 times. The Bosch-Omori instruments have free periods ranging from 20-30 sec and magnifications near 20 times. The pendulum period, T_o, and damping constant, h, for each component are given in Table 5.2. The damping constant, h, is related to the damping ratio, ϵ, given in the *Report* by the expression [e.g., Richter, 1958, p. 219],

$$\epsilon = \exp \frac{\pi h}{\sqrt{1-h^2}}.$$

All values were contained in the *Report*, with the exception of the several damping constants given in Table 5.2 as .20. These values, estimated to be near .20 and reasonable deviations from this value, modify the waveforms only slightly; the conclusions obtained in this study do not rely on the few stations with unknown damping constants. For the purpose of this study, we removed the mechanical instrument response and convolved in the WWSSN long-period response (with a gain of 1500) to facilitate comparisons with the recent calibration events. Therefore, the waveforms shown, unless otherwise stated, are as if recorded on a WWSSN long-period instrument, and amplitudes are given in millimeters.

Remarkably, the same instrument that recorded the 1906 earthquake at Göttingen,

Figure 5.5: Global station map (left) and European (upper-right) and Asian (lower-right) station locations. Filled triangles represent historic-station locations and shaded triangles represent modern stations.


RSNY
OGD
THL
BLA
SJG
TOL

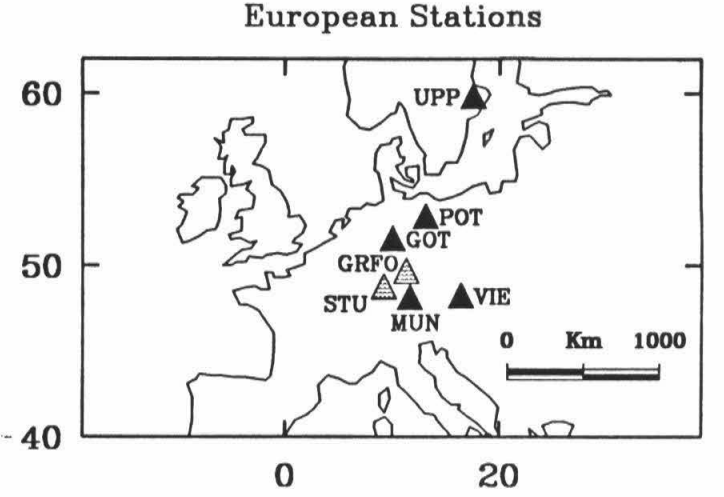
European Stations
UPP
POT
GOT
GRFO
STU
MUN
VIE
0 Km 1000
60
50
40
0
20

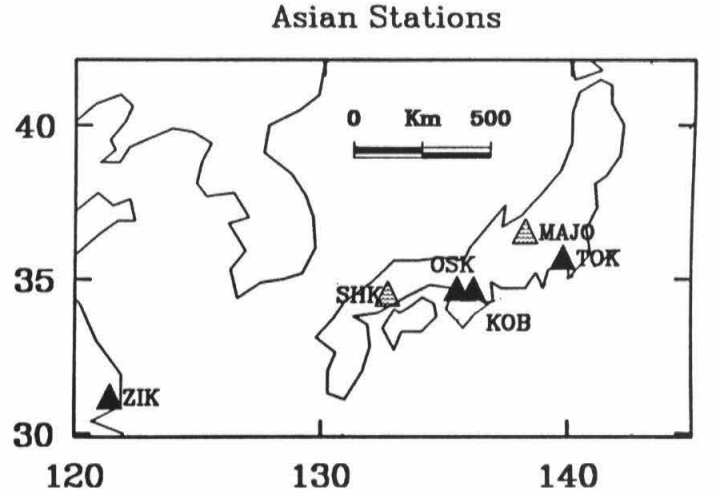
Asian Stations
0 Km 500
MAJO
TOK
OSK
SHK
KOB
ZIK
40
35
30
120
130
140

Station Abbrev.	Location	Latitude	Longitude	Distance (Deg.)	Az	Back Az
ALB	Albany, New York	42.65	-73.75	37.2	66.6	270.1
CHL	Cheltenham, MD	38.733	-76.842	35.6	73.9	282.9
GOT	Göttingen, Grm.	51.55	9.967	81.9	27.7	323.7
KOB	Kobe, Japan	34.683	136.167	77.5	304.2	52.8
MUN	Munich, Grm.	48.150	11.608	85.3	28.9	324.1
OSK	Osaka, Japan	34.70	135.517	78.0	304.5	52.5
POT	Potsdam, Germany	52.883	13.067	81.9	25.4	325.9
PTR	Puerto Rico, W. I.	18.133	-65.433	53.2	95.0	303.8
TAC	Tacubaya, Mexico	19.40	-99.20	27.3	125.5	316.8
TOK	Tokyo, Japan	35.708	139.767	74.6	303.2	54.7
UPP	Uppsala, Sweden	59.858	17.626	77.4	19.4	328.6
ZIK	Zi-ka-wei, China	31.20	121.433	89.7	309.7	45.5

Table 5.1: Station abbreviations and parameters for 1906. Distances and azimuths are with respect to the epicenter determined by Bolt [1968] at 37.667 North latitude, 122.480 West longitude.

Station	Instrument Type	Period (To) NS EW	Damping (h) NS EW	Magnification NS EW
ALB	Bosch-Omori	30,30	.20,.20	10,10
CHL	Bosch-Omori	20,25	.20,.20	10,10
GOT	Wiechert	14,13	.39,.36	172,152
KOB	Omori	35, -	.20, -	10, -
MUN	Wiechert	12,12	.50,.50	200,200
OSK	Omori	- ,27	- ,.20	- ,20
POT	Wiechert	14,14	.46,.46	130,130
PTR	Bosch-Omori	21,21	.15,.15	10,10
TAC	Bosch-Omori	17,17	.20,.20	15,15
TOK	Omori	- ,42	- ,.20	- ,30.
UPP	Wiechert	6.8,5.3	.33,.33	270,230
ZIK	Omori	- ,33	- ,.25	- ,15

Table 5.2: Intrument constants for 1906 recordings.

Germany, recorded the 1989 Loma Prieta earthquake ($M_W = 6.9$). Although the instrument constants were given for 1906 in the *Report* and were available for 1989, they were nearly the same as in 1906, with a slight change in the T_o, the natural period of the pendulum. Comparison of the two earthquake recordings is shown in Figure 5.6. The travel times are shown for body-wave phases, using Jeffreys-Bullen [1958] travel times and assuming the epicentral parameters for the 1906 earthquake of Bolt [1968]. Note the changes in the vertical scale and the difference in the noise levels between the two events. Also note the change in the shear waveforms: The Loma Prieta S waveform is short in duration and is indicative of an oblique mechanism, while the San Francisco S wave has a much longer duration and an amplitude on average nearly 5 times larger. Observing the Loma Prieta S wave on this instrument well above the noise level indicates that we should expect to see many subevents for 1906 on such an instrument if the San Francisco earthquake was comprised of many Loma Prieta-style subevents.

Figure 5.7 shows the north and east components for station GOT after instrument normalization and convolution with the WWSSN long-period response. Again, expected body-wave phase-arrival times are given. The start-time labels refer to seconds after the origin time. There is a close correspondence of observed and predicted arrival times. Figure 5.8 shows the data from station UPP with a similar format. Both stations show a complicated S wave train indicative of complex faulting.

Figure 5.9 displays the radial component of motion recorded at San Jose, Puerto Rico, for both the 1906 San Francisco (top) and 1984 Morgan Hill (bottom) earthquakes. Note that the dominant S wave arrival is very similar in character, even in the overall frequency content. However, the main 1906 S phase is delayed relative to the the Morgan Hill S wave, even though the P wave is nearly aligned. This is explained in a later section and is due to source finiteness and complexity for the 1906 earthquake. The amplitude ratio of the 1906 S wave compared to that of the

Figure 5.6: Comparison of the 1989 Loma Prieta and 1906 San Francisco digitized recordings from the Wiechert seismograph at GOT.

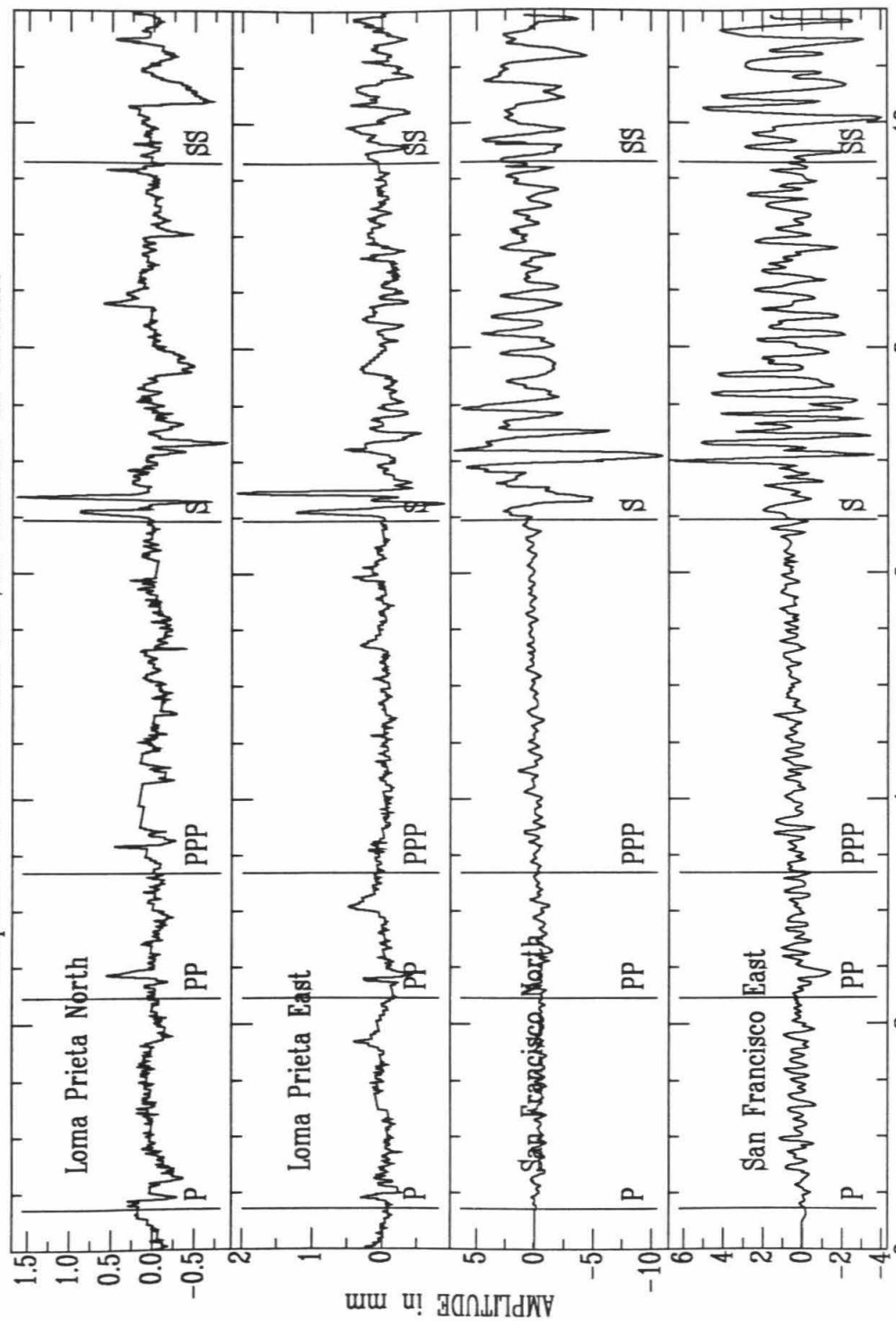
Comparison of Loma Prieta and San Francisco on Wiechtert
Loma Prieta North
Loma Prieta East
San Francisco North
San Francisco East
P
PP
PPP
S
SS
AMPLITUDE in mm
X 10+2
TIME - Seconds

Figure 5.7: Digitized 1906 recording at Göttingen, Germany (GOT) after instrument normalization and convolution with the WWSSN long-period response.

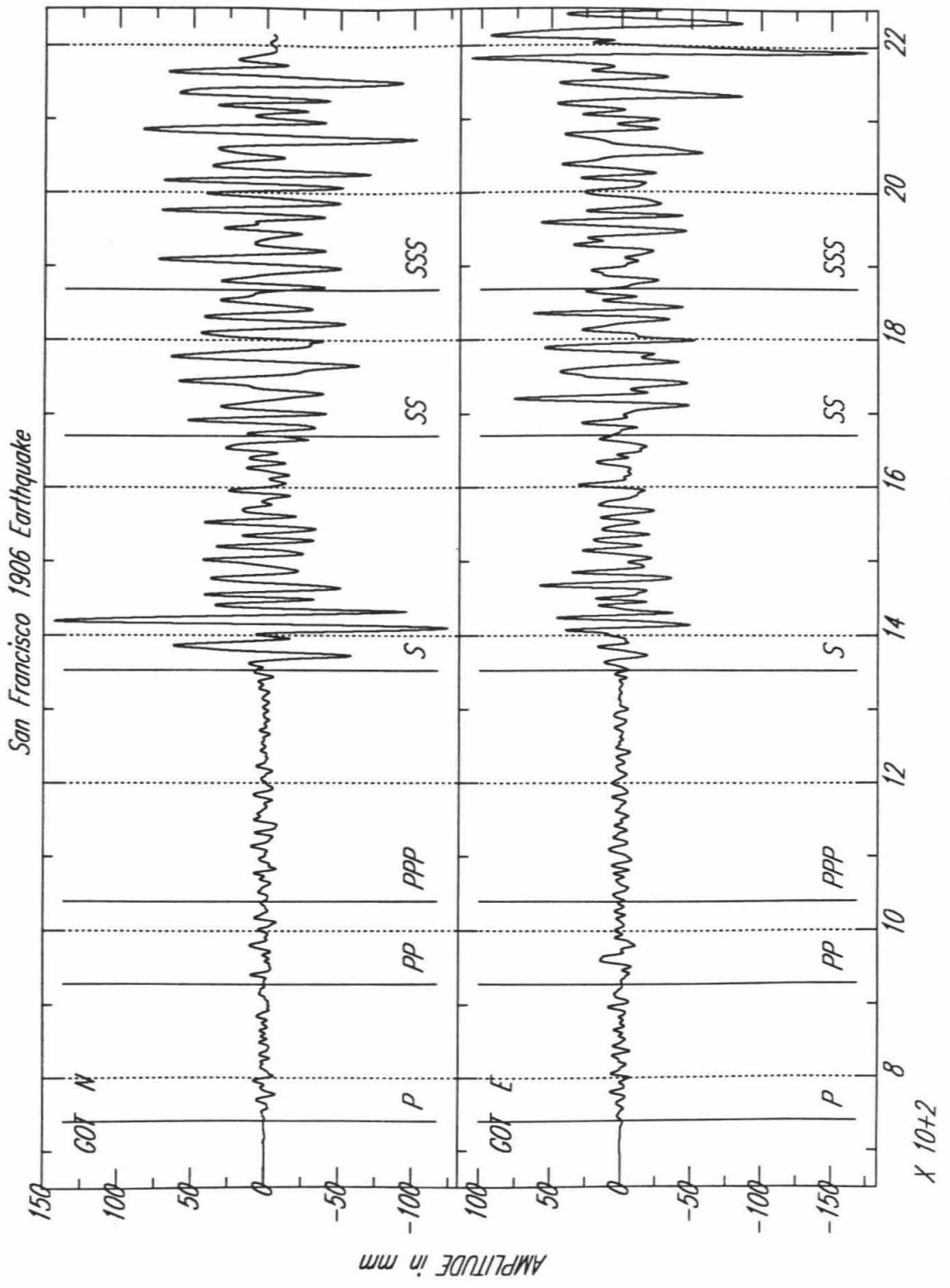
San Francisco 1906 Earthquake
GOT N
GOT E
P
PP
PPP
S
SS
SSS
AMPLITUDE in mm
150
100
50
0
-50
-100
-150
8
10
12
14
16
18
20
22
X 10+2
TIME - Seconds x 100

Figure 5.8: Digitized 1906 recording at Uppsala, Sweden (UPP), after instrument normalization and convolution with the WWSSN long-period response.

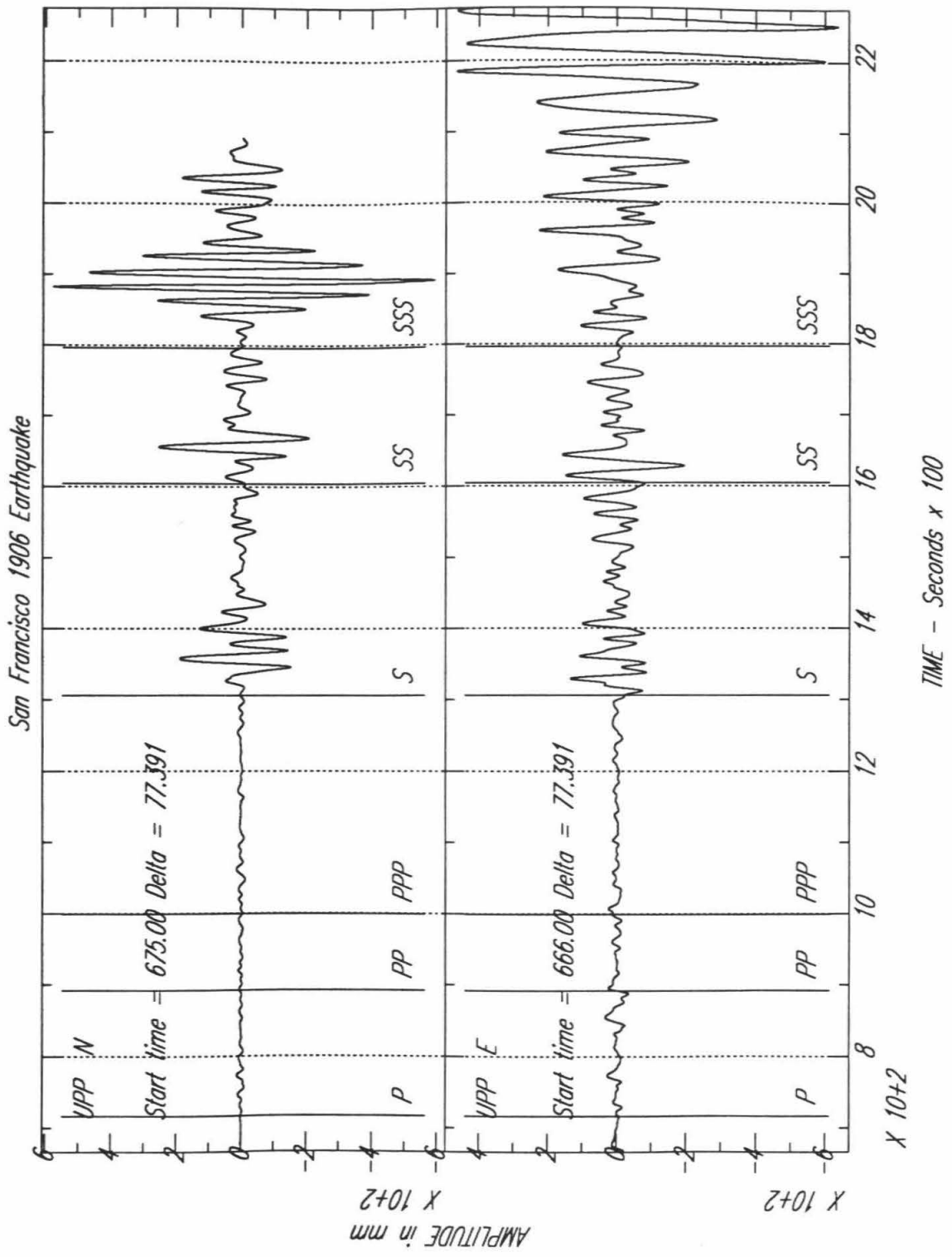
San Francisco 1906 Earthquake
UPP N
Start time = 675.00 Delta = 77.391
P
PP
PPP
S
SS
SSS
UPP E
Start time = 666.00 Delta = 77.391
P
PP
PPP
S
SS
SSS
AMPLITUDE in mm
X 10+2
X 10+2
X 10+2
TIME - Seconds x 100

Morgan Hill earthquake is nearly a factor of 35.

The complete set of S teleseismic body waves deemed usable for this study are shown in Figure 5.10. The vertical arrows indicate the predicted S-arrival times. The locations of these stations on SH and SV focal spheres for a vertical, strike-slip fault striking with the azimuth along the central portion of the 1906 rupture zone (145°) are shown in Figure 5.11.

It is quite apparent that there are limitations with the 1906 data set. The body wave information is predominantly direct S waves and multiples (SS and SSS). There is only a single, vertical component Wiechert instrument (at Göttingen). It has a good P wave, which can be compared with those from other large strike-slip events, but that is the only teleseismic, vertical recording. Hence, we are basically limited to shear body waves. To compound this, the European stations, for which we have highest-quality Wiechert recordings, are nearly SH nodal (Figure 5.11). Unfortunately, these are noticeably contaminated by shear-coupled PL waves (SPL), which can often obscure the direct S waveforms on teleseismic seismograms [Baag and Langston, 1985]. In order to model these waveforms for the purpose of source determination, it is necessary to address the effects of SPL contamination.

5.4.4 Modern Events for Calibration and Green's Functions

Since the availability and quality of data for the 1906 earthquake are poor relative to modern standards, a detailed study of modern events is critical for analyzing and placing constraints on the nature of San Francisco data. The events chosen were the Loma Prieta (1989), Morgan Hill (1984) and Coyote Lake (1979) earthquakes. The criteria for selection were that the events must be nearly co-located (as far as teleseismic distances are concerned), have similar focal mechanisms and have been recorded at modern stations with comparable locations to the historical stations of 1906. The modern-station locations are shown in Figure 5.5 with shaded triangles;

Figure 5.9: Comparison of the 1906 San Francisco (top) and 1984 Morgan Hill (bottom) radial waveforms at Puerto Rico.

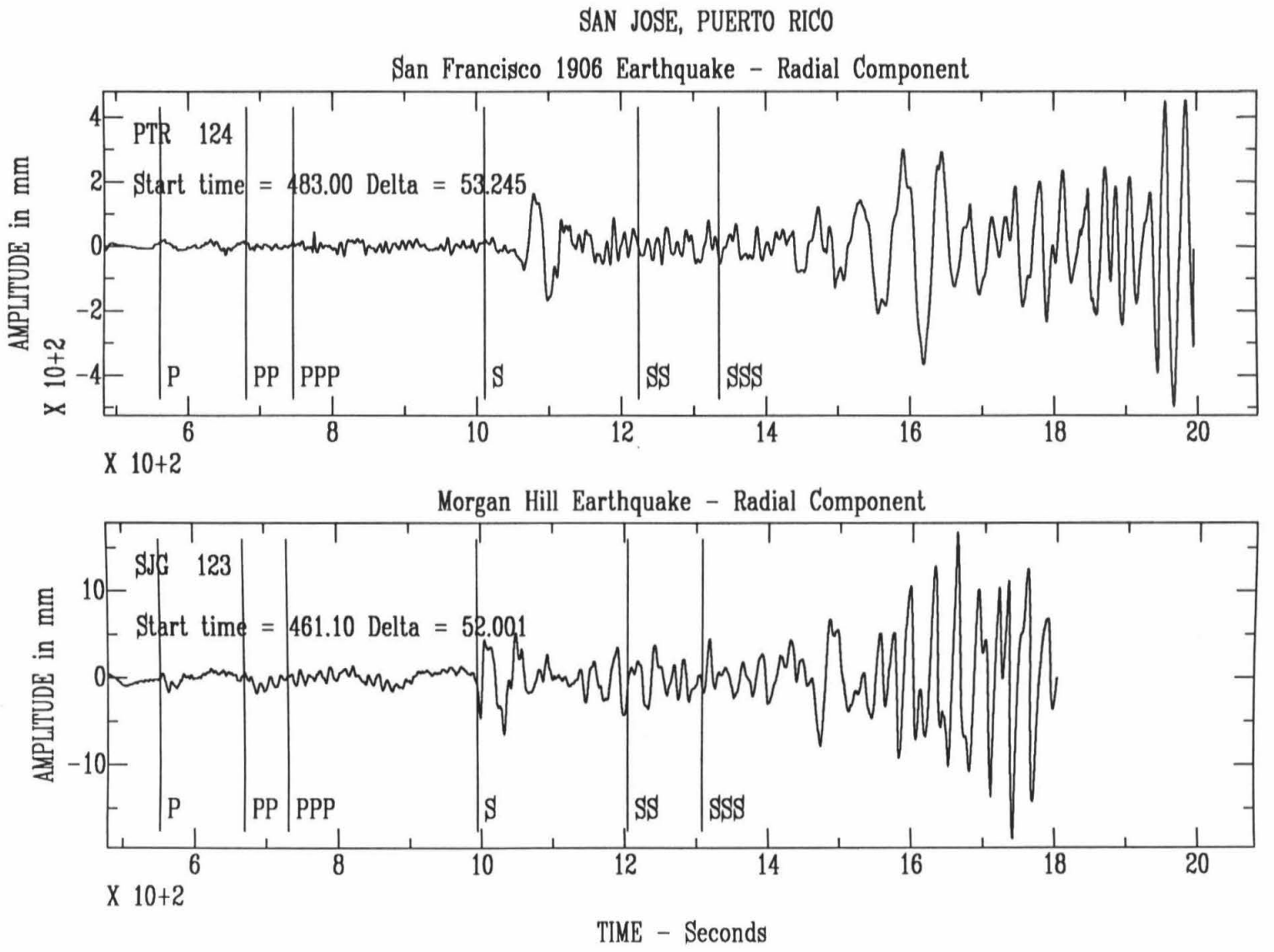
SAN JOSE, PUERTO RICO
San Francisco 1906 Earthquake - Radial Component
PTR 124
Start time = 483.00 Delta = 53.245
AMPLITUDE in mm
X 10+2
4
2
0
-2
-4
P
PP
PPP
S
SS
SSS
6
8
10
12
14
16
18
20
X 10+2
Morgan Hill Earthquake - Radial Component
SJC 123
Start time = 461.10 Delta = 52.001
AMPLITUDE in mm
10
0
-10
P
PP
PPP
S
SS
SSS
6
8
10
12
14
16
18
20
X 10+2
TIME - Seconds

Figure 5.10: Available set of teleseismic S waves. The arrows indicate the predicted arrival time of the S wave.

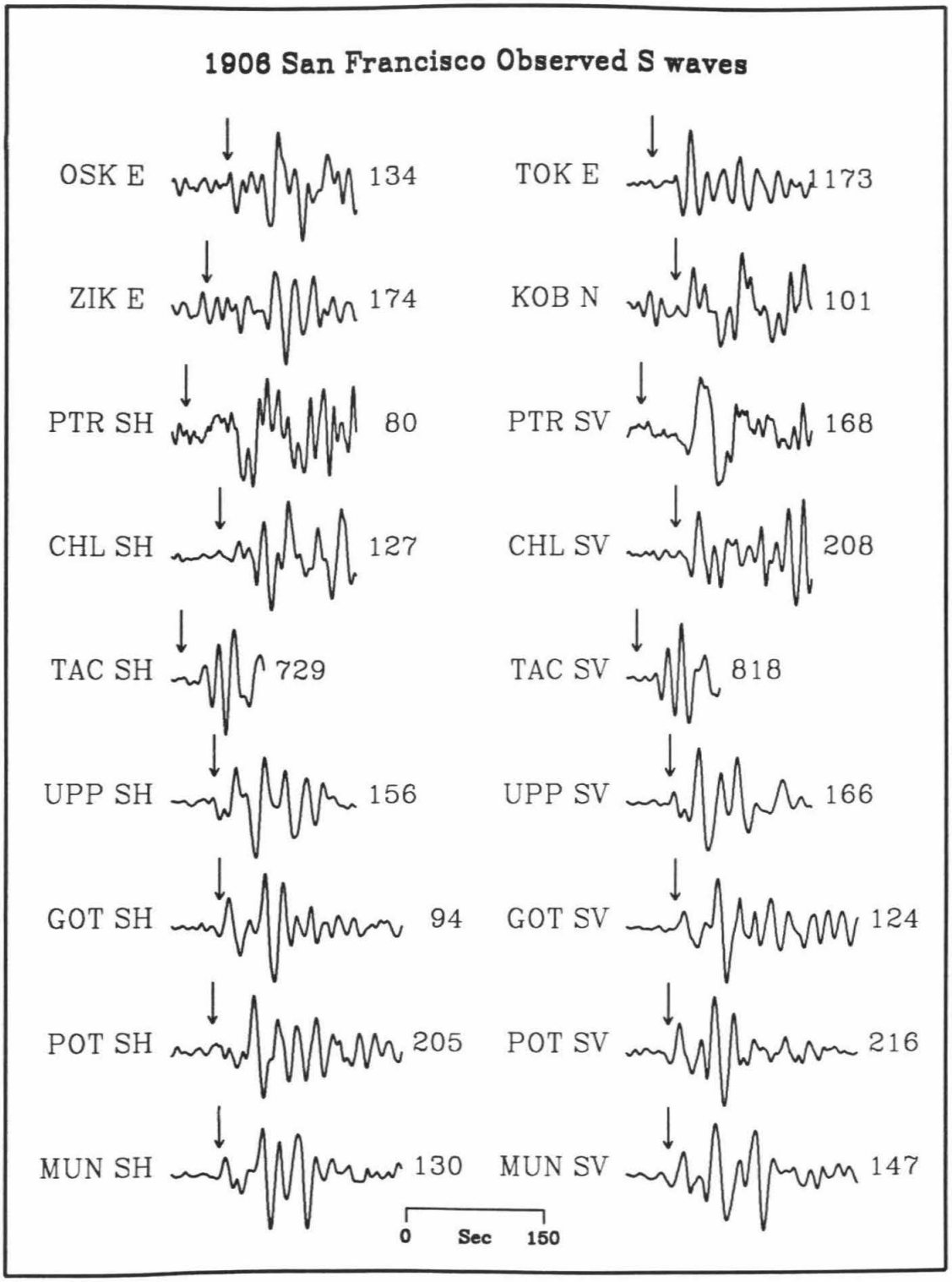
1906 San Francisco Observed S waves
OSK E
134
TOK E
173
ZIK E
174
KOB N
101
PTR SH
80
PTR SV
168
CHL SH
127
CHL SV
208
TAC SH
729
TAC SV
818
UPP SH
156
UPP SV
166
GOT SH
94
GOT SV
124
POT SH
205
POT SV
216
MUN SH
130
MUN SV
147
0
Sec
150

Figure 5.11: *SH* and *SV* nodal planes for vertical strike-slip on the central portion of the San Andreas Fault. Stations are plotted as a function of azimuth and takeoff angle.

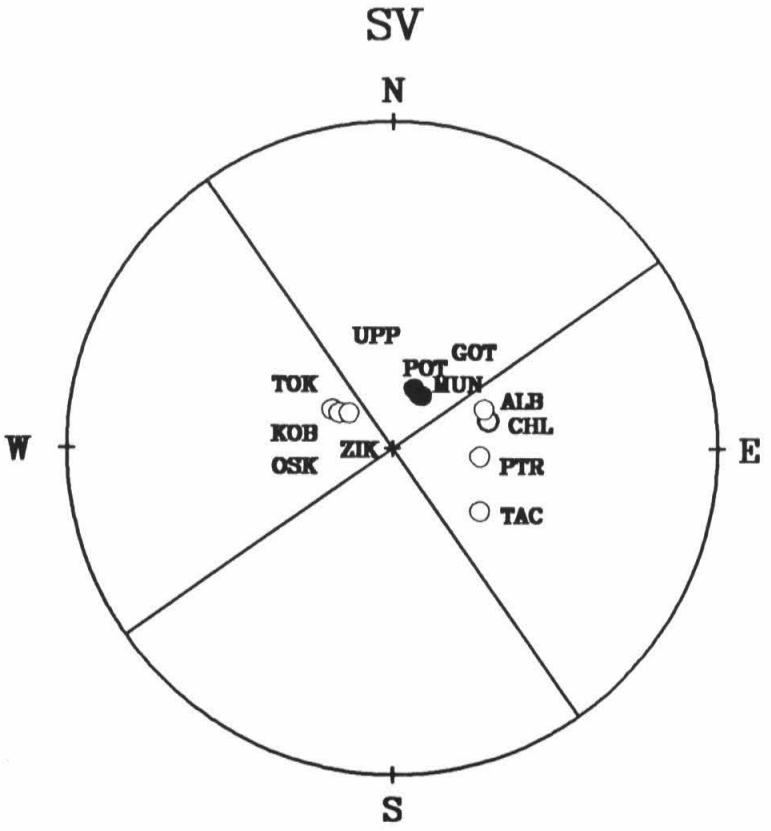
SV
N
W
E
S
UPP
GOT
POT
MUN
TOK
ALB
CHL
KOB
ZIK
OSK
PTR
TAC

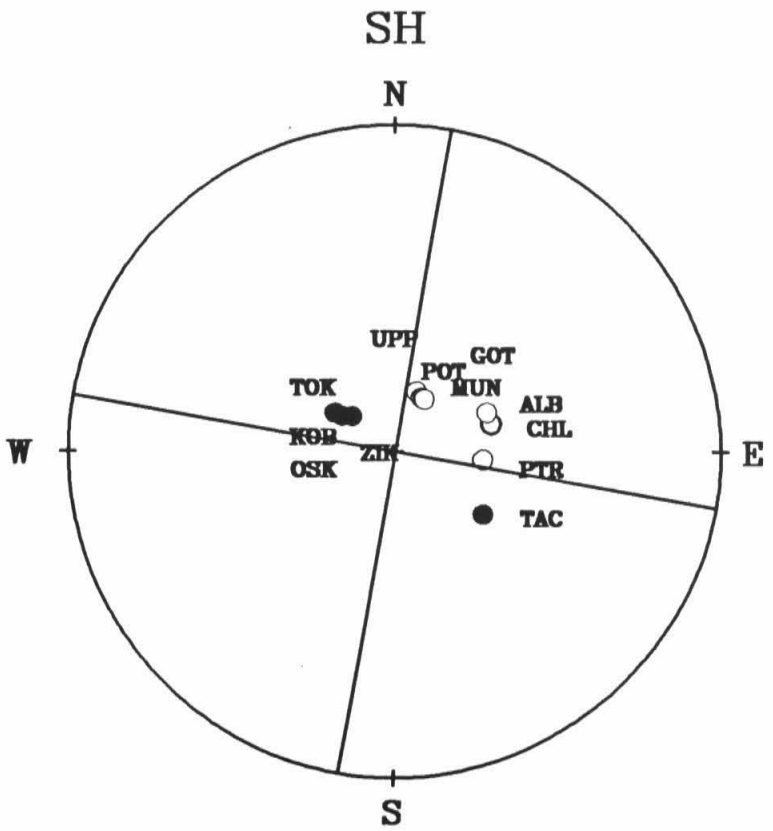
SH
N
W
E
S
UPP
GOT
POT
MUN
TOK
ALB
CHL
KOB
ZIK
OSK
PTR
TAC

the historical stations are indicated by filled triangles. The European and Asian stations used in this study are shown with an enlarged scale at the right of Figure 5.5. For stations UPP and GOT the modern and historical stations occupy the same site. In Puerto Rico, stations PTR (historical) and SJG (WWSSN) are very closely situated (Tables 5.1 and 5.3). The locations and focal mechanisms of the calibration events are depicted in Figure 5.1, and the station parameters are given in Table 5.3. All three calibration events have been well modeled in earlier source studies, so good estimates of source mechanism, seismic moment, time duration and slip distribution are available in the literature [e.g., Beroza and Spudich, 1988; Ekström, 1984; Hartzell and Heaton, 1986; Liu and Helmberger, 1983; Wald *et al.*, 1991]. By analyzing these smaller events at stations close to those that recorded 1906, we can estimate the amount and effect of *SPL* contamination. Unfortunately, there is not always an identical station location for modern and older instruments, and *SPL* is often quite site-specific. This makes it difficult in some cases to quantify the *SPL* contamination. Ideally, we would like to be able to examine the smaller, calibration events with simple, known source time histories in order to determine the amount of *SPL* contamination and then empirically to include this site response. However, the calibration stations available must be close enough to the station of interest, or the site effects may not be representative enough. Unfortunately, there are no usable, long-period recordings of the calibration events in the vicinity of the 1906 TAC recording in Mexico City, and the amplitude of that recording is suspect. It is therefore difficult to make use of the TAC recording even though it is at a very desirable azimuth along strike of the San Andreas Fault towards the southeast.

Examination of the Morgan Hill and Coyote Lake shear waves gives us an indication of just how important the *SPL* phases can be. The source mechanisms are very similar, although the Coyote Lake geometry shows a slight non-vertical dip (see Figure 5.1). Hence, we expect the waveforms to be quite compatible. Figure 5.12

Station Abbrev.	Location	Latitude	Longitude	Distance (Deg.)	Az	Back Az
UPP	Uppsala, Sweden	59.858	17.627	77.5	19.7	327.8
MAJO	Matsushiro, Japan	36.542	138.209	75.8	305.1	54.1
RSNY	Adirondack, NY	44.548	-74.530	35.9	63.3	275.1
GRFO	Graefenberg, Grm.	49.69	11.22	83.9	28.6	324.0
BLA	Blackburg, VA	37.21	-80.42	32.7	77.4	283.0
OGD	Ogdensburg, NJ	41.07	-74.62	36.3	69.2	279.8
SHK	Shiraki, Japan	34.530	132.678	80.6	306.3	51.1
SJG	San Juan, P.R.	18.112	-66.150	52.0	95.7	303.5
STU	Stuttgart, Grm.	48.771	9.193	83.8	30.2	322.7

Table 5.3: Station abbreviations and parameters for Morgan Hill earthquake. Distances and azimuths are with respect to the epicenter determined at latitude 37.317 North and longitude 121.682 West.

shows the recorded and synthetic *SH* and *SV* waveforms at Uppsala, Sweden, for both events displaying similarity of the waveforms. It is also interesting to observe that the amplitudes for these recordings are very small (less than 1 mm on the original paper records), yet the scanning/digitizing system we employ can recover the details remarkably well. The waveform similarity suggests that these magnitude-6 events can be effectively used as Green's functions for a much larger event. They differ only in amplitude, the ratio reflecting the moment ratio of Morgan Hill with respect to Coyote Lake (between 3.5 to 4.5). The *SH* waveforms are clearly less contaminated than the SV, but are not immune from *SPL* coupling.

Synthetic waveforms were produced for the Morgan Hill earthquake, using the finite-fault slip distribution of Hartzell and Heaton [1986]; for the Coyote Lake simulations of the source model of Liu and Helmberger [1983] were employed. As can be seen in the synthetic waveforms in Figure 5.12, the source contribution to the waveform complexity is negligible. The synthetic waveforms predict only the simple first arrival on the *SH* component. Since the entire duration of either event is less than 7 sec, it can be approximated as a point source when viewed through the long-period WWSSN response (peaked at 15 sec period). The later-arriving energy is *SPL* energy. In order to investigate the later part of the shear wave train for the 1906 records, it is critical that we include the site-specific *SPL* contamination. Otherwise, we may not be able to attribute later arrivals in the *S* wave train to complexities of the source-rupture process.

5.5 Body-Wave Analysis

Examination of the 1906 shear-wave data (Figure 5.10) indicates that there is a small, initial *S*-wave arrival at the time of the predicted *S*-wave arrival (shown with the vertical arrows), followed by a dominant, larger phase about 30-40 sec later.

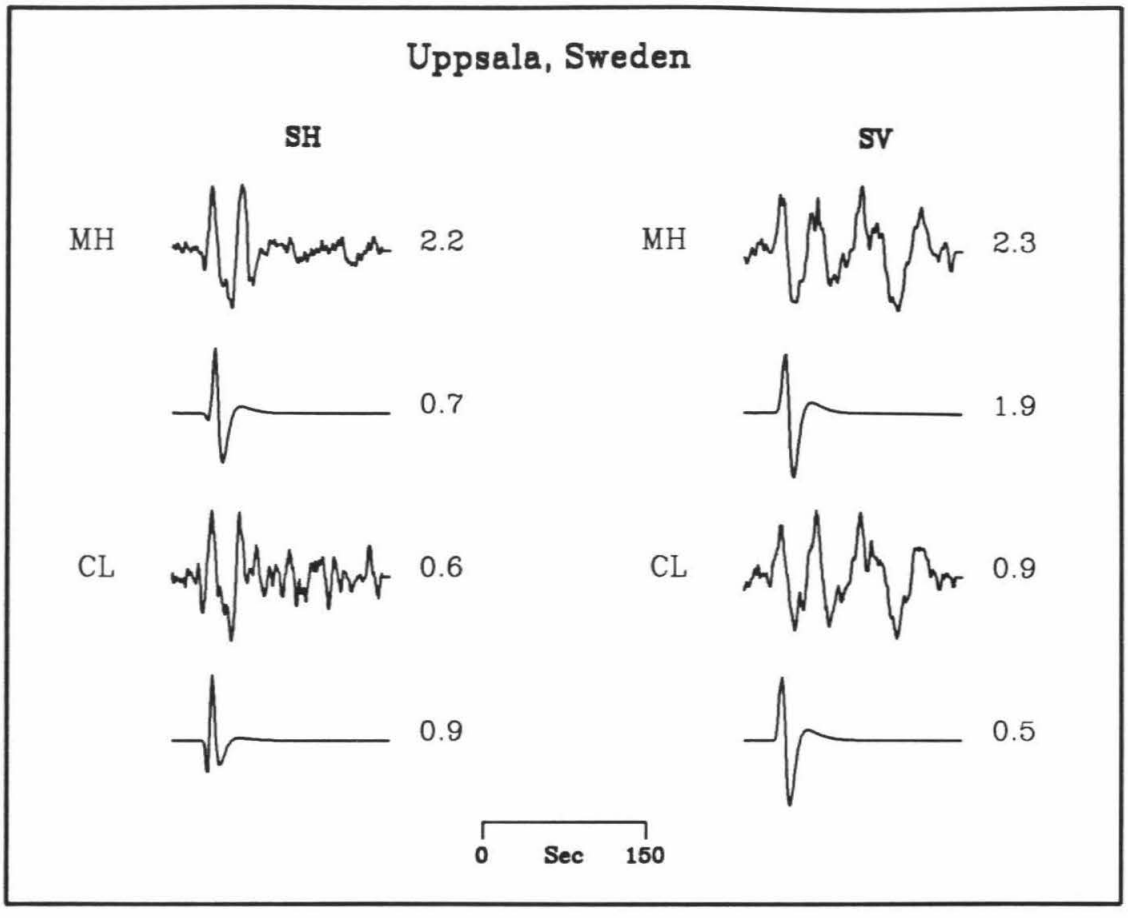

Figure 5.12: WWSSN long-period recordings for calibration events Morgan Hill (MH) and Coyote Lake (CL) showing *SPL* contamination. Observed recordings are above the synthetics seismograms.

There is a clear time difference of these two arrivals as a function of azimuth ranging from 36 sec at KOB and 39 sec at GOT to nearly 45 sec at PTR. As will be further discussed, this is consistent with two sources separated along the strike of the San Andreas Fault.

5.5.1 Amplitude Comparisons With Green's Functions

First-order results were obtained by simply making comparisons of teleseismic waveform complexity and amplitudes of the 1906 recordings with the Coyote Lake , Morgan Hill , and Loma Prieta S waves. The durations of the 1906 teleseismic S waves are relatively short, and the complexity of the waveforms is not great (Figure 5.10), considering that the rupture length was at least 300 km. On average, the largest 1906 S waves are about 3-5 times larger than the largest Loma Prieta S waves as recorded at the same stations (GOT and UPP). Neglecting the differences in source-radiation pattern, this requires an excitation of 5-15 sec energy several times that of Loma Prieta along some limited portion of the 1906 rupture. Comparing the 1906 and Morgan Hill S waves gives an average amplitude ratio of about 40; the ratio for Coyote Lake is approximately 135. With the seismic moments determined for the calibration events, we can estimate the size of the dominant asperity of the 1906 earthquake. These values are summarized in Table 5.4. This, of course, is not the total moment for 1906, just an estimate of the portion of the fault responsible for producing the largest amplitude 5-20 sec body waves.

5.5.2 Forward Modeling

A straightforward approach to modeling the 1906 recordings is to use the Morgan Hill S-wave recordings as Green's functions and to lag and sum them to produce 1906 simulations. Previous examples of the use of empirical, teleseismic summations include the 1987 Superstition Hills, California earthquake [Bent *et al.*, 1989] and

Calibration Earthquake	Seismic Moment ($x10^{25}$ dyne-cm)	Scaling Factor (N)	1906 Asperity Moment ($x10^{27}$ dyne-cm)
Loma Prieta	30	3	0.9
Morgan Hill	2.5	40	1.0
Coyote Lake	0.5	135	0.8

Table 5.4: Estimates of the main 1906 asperity size from comparison with calibration-event amplitudes. See text for details.

the 1927 Lompoc, California earthquake [Helmberger, 1992]. Here we are fortunate in having a subevent (Morgan Hill) with the appropriate source mechanism and a known seismic moment. The radiation pattern is nearly that of the 1906 rupture along the central portion of the San Andreas Fault (Figure 5.1). The Coyote Lake earthquake is not used for an empirical simulation because its mechanism is slightly different from the one in 1906, and perhaps more importantly, its seismic moment was about 3-4 times smaller than that of the Morgan Hill event, and thus has fewer well-recorded signals at teleseismic distances. Loma Prieta was very well recorded teleseismically, but the faulting geometry is significantly different from the vertical strike-slip (Figure 5.1) and therefore cannot be used without a correction for the radiation pattern and the associated (and unknown) effect on the *SPL* signals. Although appropriate for the central part of the 1906 rupture zone, the Morgan Hill mechanism is slightly discrepant in strike for subevents along the northwest and southeast sections. It is also possible that a substantial portion of oblique thrusting occurred in the Loma Prieta segment of the fault, in which case the Morgan Hill Green's functions are not appropriate.

In a forward-modeling sense, we determine the best locations and amplitudes for

subevents along the trend of the San Andreas fault in order to fit the recorded 1906 teleseismic waveforms and amplitudes. By assuming a constant rupture velocity V_r of 2.7 km/sec, we compute the delay at each station, Δt_i, for a number of subevent positions along strike within the onshore rupture zone. For a distance D along strike from the epicenter,

$$\Delta t_i = \frac{D}{V_r} - Dcos(\phi_o - \phi)P,$$

where V_r is the assumed rupture velocity, ϕ_o is the station azimuth, ϕ is the fault strike and P is the ray parameter. We then determined the best multiplicative amplitude-scaling factor, N, to weight each subfault Green's function by, in order to obtain the observed 1906 amplitudes.

Using the relationship equating seismic moment to fault slip

$$M_o = \mu A \overline{u},$$

where μ is the rigidity, A is the area and $\overline{u}$ is the average dislocation, we can estimate the average slip and the area over which it occurred for the Morgan Hill earthquake. Given the strong-motion inversion models of Hartzell and Heaton [1986] and Beroza and Spudich [1988], we assume a rupture approximately 12 km in length and 10 km deep having a seismic moment of $2.5x10^{25}$ dyne-cm. Using $\mu = 3.2$ x 10^{11} dyne/cm^2, on the basis of their crustal models, we find the average slip to be about 65 cm. This allows us to relate the scale factor, N, for the number of Morgan Hill Green's functions to the approximate slip on the fault we allow it to represent.

Initially, we computed the teleseismic body-wave signal on the basis of the geodetic slip model of Thatcher [1975]. Using the above conversion from a single Morgan Hill Green's function to slip, we summed the appropriate number of Green's functions to approximate the geodetic slip model. The geodetic model of Thatcher [1975] is shown as a function of position along strike with filled triangles in the bottom portion of Figure 5.13. The observed surface offset, also from Thatcher [1975], is also shown

with filled squares. Note that the distance corresponds to km from the epicenter south of San Francisco and increases along strike to the northwest. Atop Figure 5.13 is a schematic diagram of the fault-slip model used to approximate the geodetic slip. The subfault weights correspond to the multiplicative-weighting factor N. There are 28 subfaults, numbered from northwest to southeast, beginning at Point Arena. The hypocenter, indicated with a star, is located in subfault 22. The area of each subfault corresponds to the effective rupture area of the Morgan Hill subevent. Note that we do not model the offshore region (205-340 km) in our simulations. As described above, there is little evidence in the later part of the teleseismic records of substantial 5-20 energy release from this portion of the fault.

Figure 5.14 shows the observed 1906 S waves modeled with the corresponding S waves computed with the Morgan Hill , empirical Green's function scaled to the geodetic slip. For each component, the top trace is the observation, the middle trace is the synthetic, and the third trace shows an overlay of the two for comparison, the synthetic being distinguished with a dashed line. Notice that the overall amplitudes of the synthetics for the geodetic model are about 50% of the observed amplitudes, suggesting the need for more intense slip variations. In general, there is fair agreement with the data for some features of the waveforms, though the timing of the largest arrival does not fit the data. Further, the synthetic traces are often longer period than the data.

Next, in a forward-modeling sense, we determined the best simple, rupture model in order to satisfy the observation of the relatively small, initial phase at the S-wave arrival time and the larger arrival 35-45 sec later seen in Figure 5.10. The best model found by trial and error came from a relatively simple summation consisting of two regions of strong radiation separated in time by an average of about 38 sec. The relative-weighting factor N was determined to be about 14 for the hypocentral subfault and 30 for subfault 10. This corresponds to about 110 km of separation

Figure 5.13: Schematic of the geodetic fault model (top) showing subfault layout. The numbered subfaults were allowed to contribute to the teleseismic signal. Shading is proportional to fault slip through the weighting factor N as shown by the scale bar (see text). The geodetic slip is shown below as filled triangles, and the surface offset is given with filled squares [from Thatcher, 1975]. The distance given is along strike from the hypocenter (star in subfault No. 22).

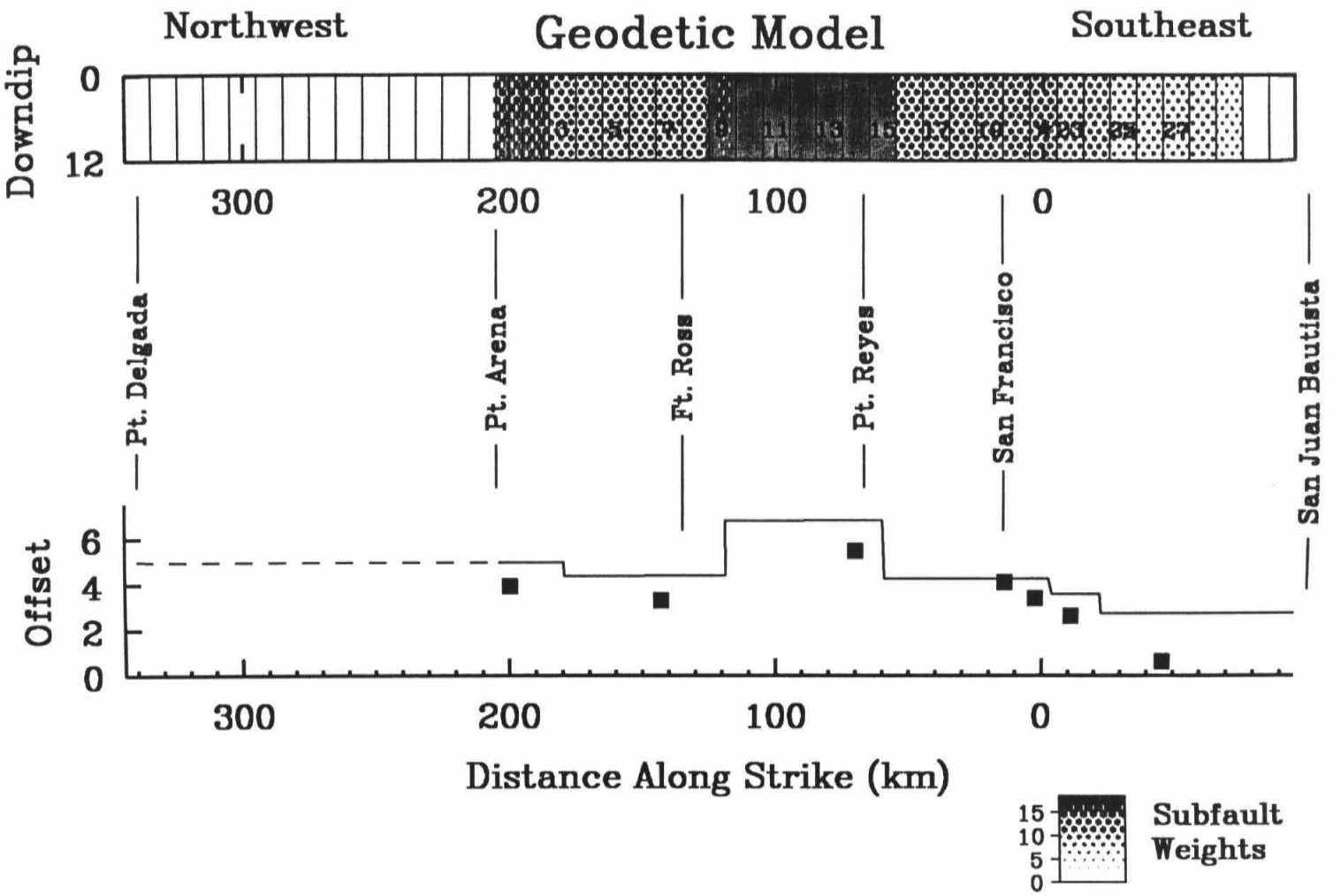
Northwest
Geodetic Model
Southeast
Downdip
0
12
300
200
100
0
Pt. Delgada
Pt. Arena
Ft. Ross
Pt. Reyes
San Francisco
San Juan Bautista
Offset
6
4
2
0
300
200
100
0
Distance Along Strike (km)
15
10
5
0
Subfault
Weights

Figure 5.14: Observed 1906 S waves (top) and the corresponding synthetic seismogram (middle) from the geodetic model. The overlay (bottom) shows both traces superimposed with the synthetic trace dashed.

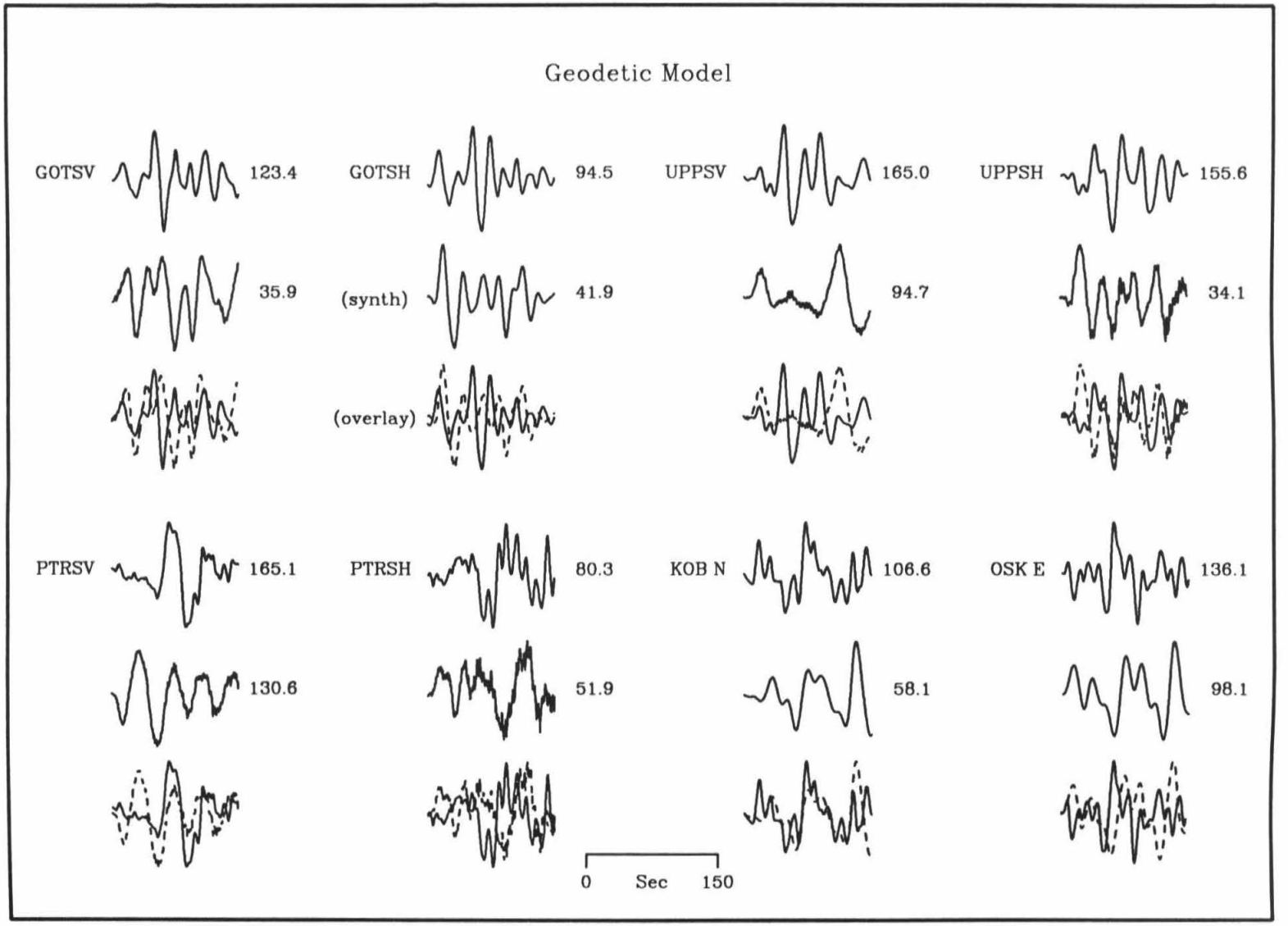
Geodetic Model
GOTSV
123.4
35.9
GOTSH
94.5
(synth)
41.9
(overlay)
UPPSV
165.0
94.7
UPPSH
155.6
34.1
PTRSV
165.1
130.6
PTRSH
80.3
51.9
KOB N
106.6
58.1
OSK E
136.1
98.1
0
Sec
150

between the two major regions of strong radiation at these periods (about 5-20 sec), placing the largest between Point Reyes and Fort Ross.

In short, we see that the teleseismics can be explained by about 14 Morgan Hill events summed near the epicenter, a region where the amount of slip changes quite abruptly according to surface offset, and about 30 Morgan Hill events concentrated at about 110 km from the epicenter, where the geodetic and surface slip is near its greatest (Figure 5.15). The synthetics from the empirical summation are shown in Figure 5.16. A good portion of the shear-wave train is fit at most stations. We find the data at KOB to be inconsistent with many of the other observations.

5.5.3 Source Inversion

Solving for the location and scale-factor subevents to best satisfy the timing and amplitude of the observed waveforms can be set up as a least-squares inversion. Again, we assume a fixed rupture velocity of 2.7 km/sec, and solve for the over-determined system of linear equations

$$Ax \cong b$$

, using linear, least-squares to determine x, the solution vector of subfault weights. Here the matrix A consists of synthetics (empirical Green's functions) of equally weighted subfault responses strung end to end, each lagged according to its rupture and travel-time delay, and b is the data vector.

The result of the inversion, shown in Figure 5.17, is nearly that of the forward estimation also showing two main regions of radiation, though several more subfaults contribute to the solution. The waveform fits are given in Figure 5.18. In a formal sense, the solution from the inversion has a slightly lower misfit to the data, but there are features in waveforms produced by the forward that are more favorable.

As shown in the forward and inverse models, the arrival in the data corresponding to the largest subsource can be fit well with a very limited dimension along strike. In

Figure 5.15: Schematic of the forward-model results. The bottom portion of the figure is the same as in Figure 5.13.

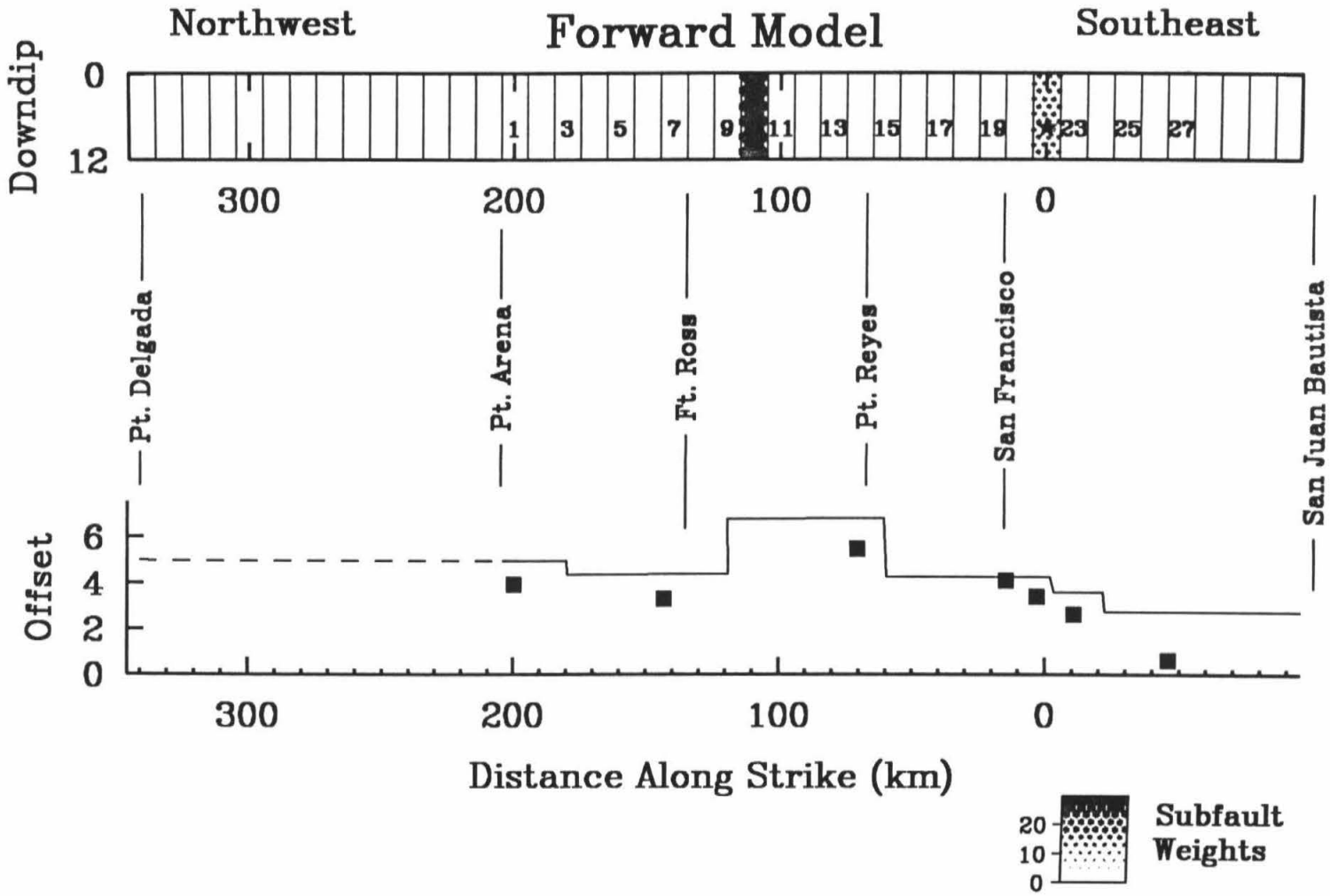
Northwest
Forward Model
Southeast
Downdip
0
12
1
3
5
7
9
11
13
15
17
19
23
25
27
300
200
100
0
Pt. Delgada
Pt. Arena
Ft. Ross
Pt. Reyes
San Francisco
San Juan Bautista
Offset
6
4
2
0
300
200
100
0
Distance Along Strike (km)
20
10
0
Subfault
Weights

Figure 5.16: Observed 1906 S waves (top) and the corresponding synthetic seismogram (middle) from the forward model. The overlay (bottom) shows both traces superimposed with the synthetic trace dashed.

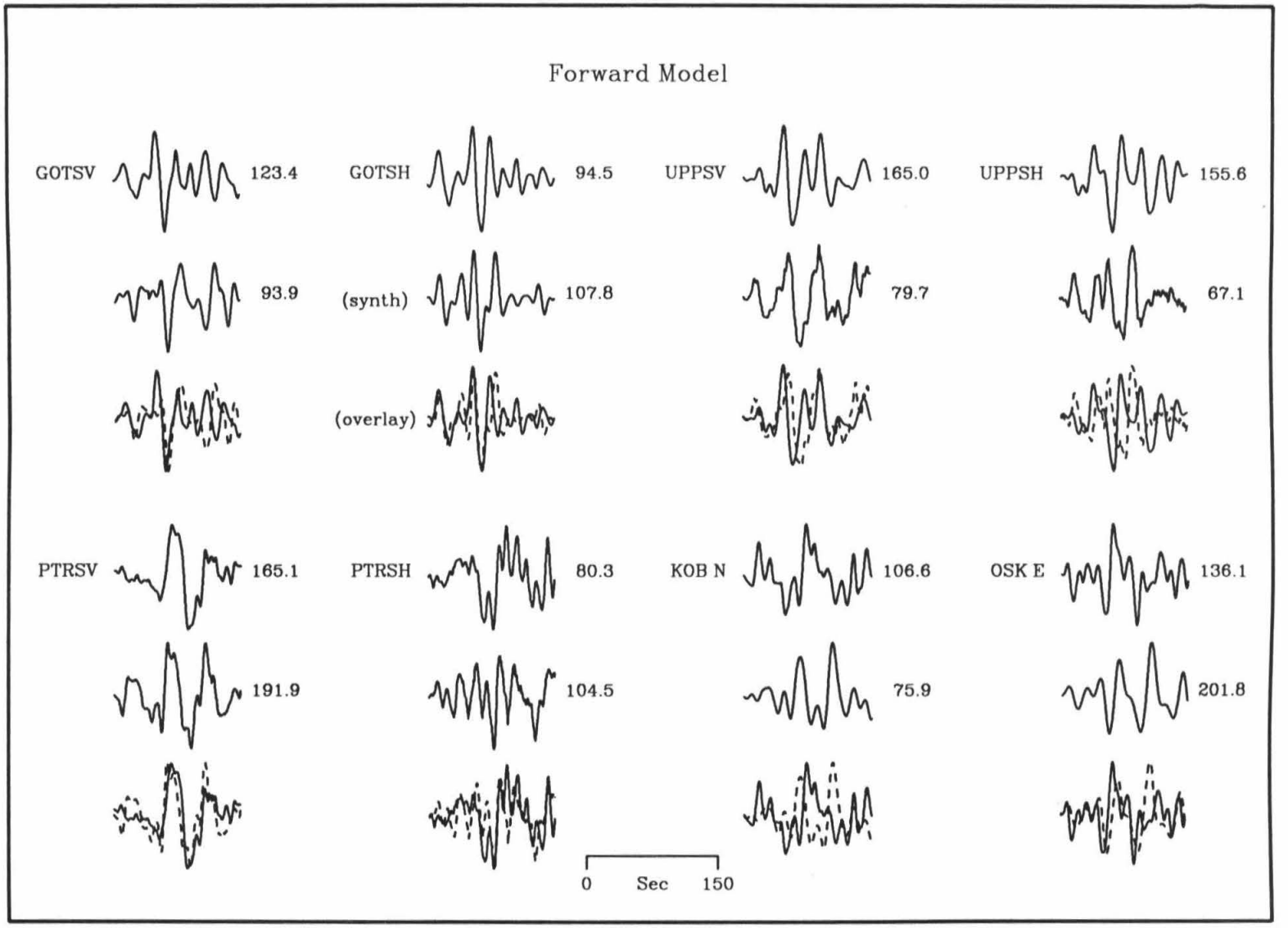
Forward Model
GOTSV
123.4
93.9
GOTSH
94.5
(synth)
107.8
(overlay)
UPPSV
165.0
79.7
UPPSH
155.6
67.1
PTRSV
165.1
191.9
PTRSH
80.3
104.5
KOB N
106.6
75.9
OSK E
136.1
201.8
0
Sec
150

Figure 5.17: Schematic of the inverse-model results. The bottom portion of the figure is the same as in Figure 5.13.

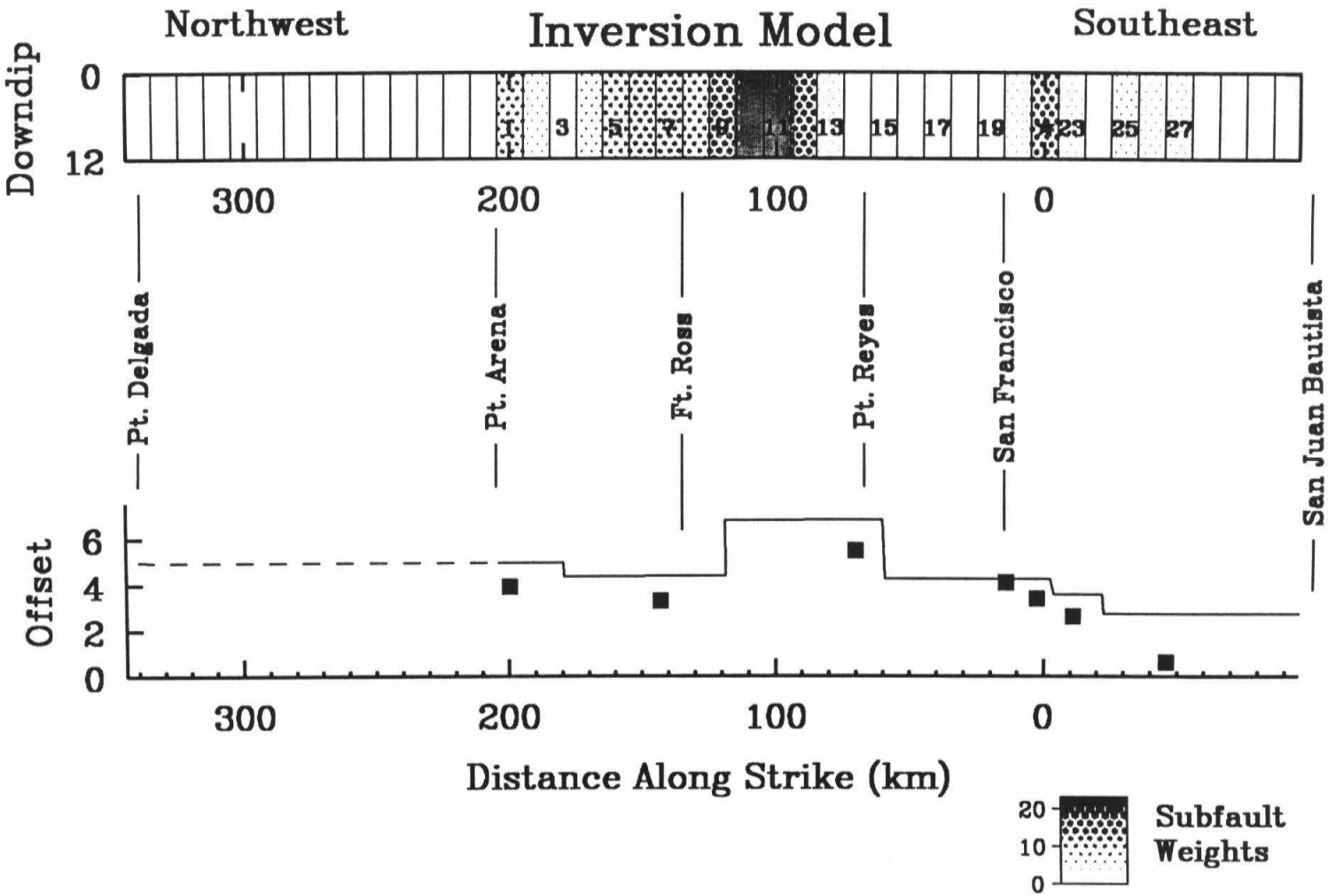
Northwest
Inversion Model
Southeast
Downdip
0
12
1
3
5
7
9
11
13
15
17
19
21
23
25
27
300
200
100
0
Pt. Delgada
Pt. Arena
Ft. Ross
Pt. Reyes
San Francisco
San Juan Bautista
Offset
6
4
2
0
300
200
100
0
Distance Along Strike (km)
20
10
0
Subfault
Weights

Figure 5.18: Observed 1906 S waves (top) and the corresponding synthetic seismogram (middle) from the inverse model. Below the synthetic for each station both traces superimposed (bottom) with the synthetic trace dashed.

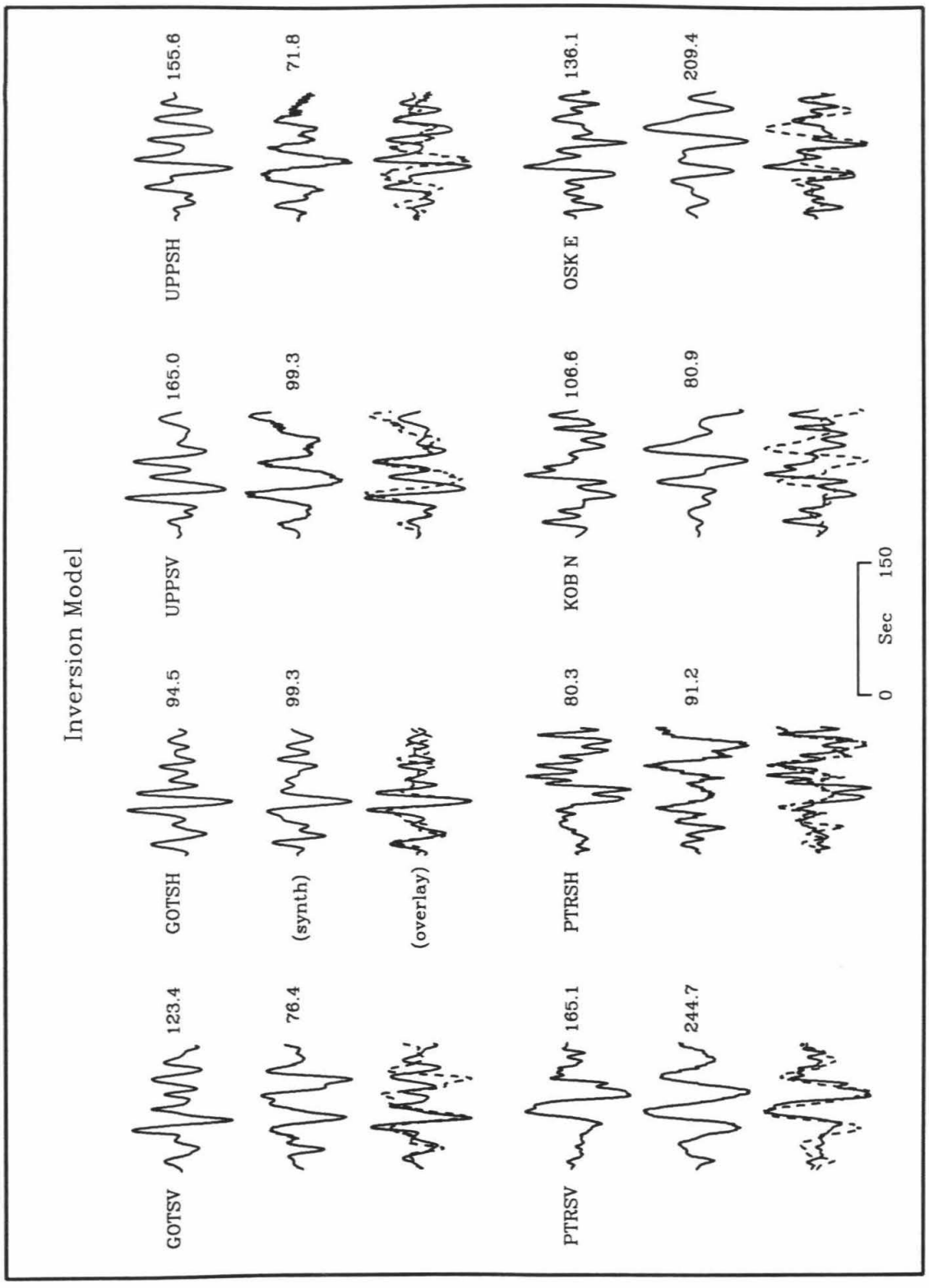
Inversion Model
GOTSV
123.4
GOTSH
94.5
UPPSV
165.0
UPPSH
155.6
76.4
(synth)
99.3
99.3
71.8
(overlay)
PTRSV
165.1
PTRSH
80.3
KOB N
106.6
OSK E
136.1
244.7
91.2
80.9
209.4
0
Sec
150

order to place constraints on the dimensions of the region of large source radiation near subfault 10, we performed a summation of empirical Green's functions lagged in space over various linear dimensions. We found that as the length along strike increases above about 40 km, the match of the details of the waveforms at the best-modeled stations is degraded (Figure 5.19). With an extended source dimension of 55 km, the higher-frequency content of the data at GOT is difficult to simulate.

5.6 Surface-Wave Analysis

Spectral ratios were computed as a function of frequency by dividing the Fourier-transformed waveforms for 1906 stations by the transform of the data from the corresponding Morgan Hill station. The advantage of computing spectral ratios in this manner rather than theoretically correcting for radiation pattern is that the site effects are best accounted for empirically. Only stations ALB, PTR and UPP had both digitizable 1906 surface waves and data recorded at the corresponding modern stations. The average spectral ratio at 50 sec was approximately 120. Assuming that the 1984 Morgan Hill earthquake had a moment of approximately $2.5x10^{25}$ dyne-cm, this requires a moment of $3.0x10^{27}$ dyne-cm for the 1906 earthquake. At a period of 100 sec, the ratio was nearly 180, yielding a moment of $4.5x10^{27}$ dyne-cm ($M_W = 7.7$). These values are quite similar to the estimates of $3.2x10^{27}$ dyne-cm at 50 sec and $4.7x10^{27}$ dyne-cm at 100 sec determined by Thatcher [1975] from Love and Rayleigh wave spectral amplitudes, though a different set of stations (UPP, GOT and ZIK) were used in that study.

5.7 Strong-Motion Estimations

In a recent study, Wald *et al.* [1992] found that the source model of the 1989 Loma Prieta earthquake determined from inversion of teleseismic data alone was sufficient

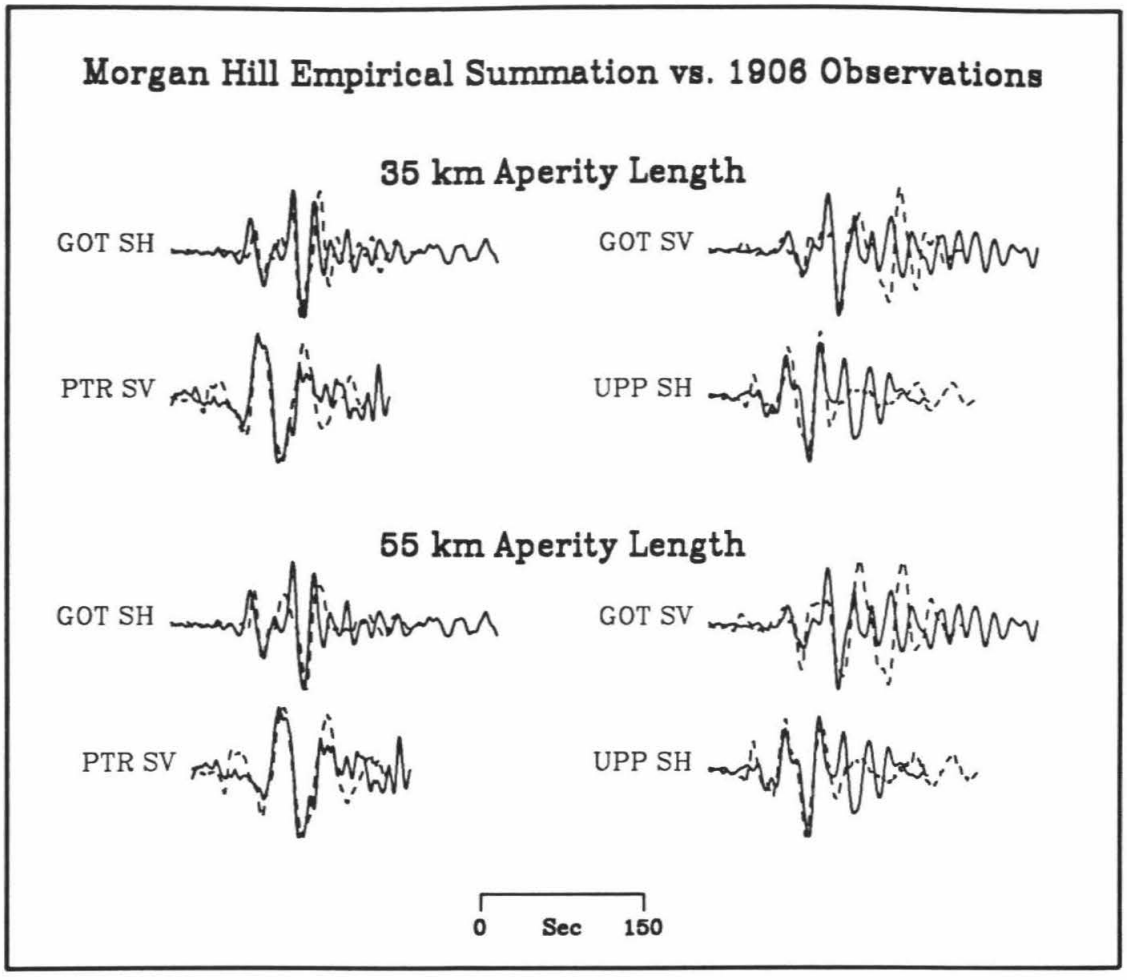

Figure 5.19: Comparison of forward-model synthetics for empirical summation of the largest asperity with source spread out over 35 km (top) and 55 km (bottom).

for predicting many of the features of observed strong motions. They determined that even with a limited overlap in the bandwidths of the two data sets, the general asperity characteristics determined at longer periods were consistent with the slip distribution needed to simulate the higher-frequency ground motions.

In the previous section, we found that the amplitudes and frequency content of the teleseismic data for 1906 allowed us to constrain the scale length of the largest asperity to be less than 40 km. Having a constraint on the largest asperity (size and magnitude) we produced synthetic ground velocities as follows. For purposes of comparison with the recent, abundant Loma Prieta strong-motion data set, we "moved" the largest 1906 asperity into the Loma Prieta region. In this way, we could compare our simulations to observations from an $M_W = 6.9$ at the same distances and station geometries. We then took the Loma Prieta slip model of Wald *et al.* [1991] and by rotating the model fault to a vertical plane and constraining the dislocation to be pure, right-lateral strike-slip, we approximated rupture along the San Andreas fault. The Loma Prieta rupture was bilateral, but we used a northwest-propagating unilateral rupture to simulate the 1906 model determined from the teleseismic data.

To be consistent with the average depth of significant slip from other strong-motion, waveform inversions of California vertical, strike-slip earthquakes [Hartzell and Heaton, 1983; Hartzell and Heaton, 1986; Beroza and Spudich, 1988; Wald *et al.*, 1990] we needed to decrease the asperity depth relative to the Loma Prieta model. This was done by bringing the top of the fault to within 0.5 km of the surface and translating the slip (shown in Figure 5.20, top) 5 km closer to the top of the fault than the Loma Prieta slip model.

To simulate the 1906 asperity, we spatially shifted and summed three Loma Prieta slip distributions (Figure 5.20, bottom) to preserve the amplitude of slip determined from the forward, empirical summation model, keeping the dimension in line with the 35 km length used to best-model the 1906 body waves. Ground-motion velocity

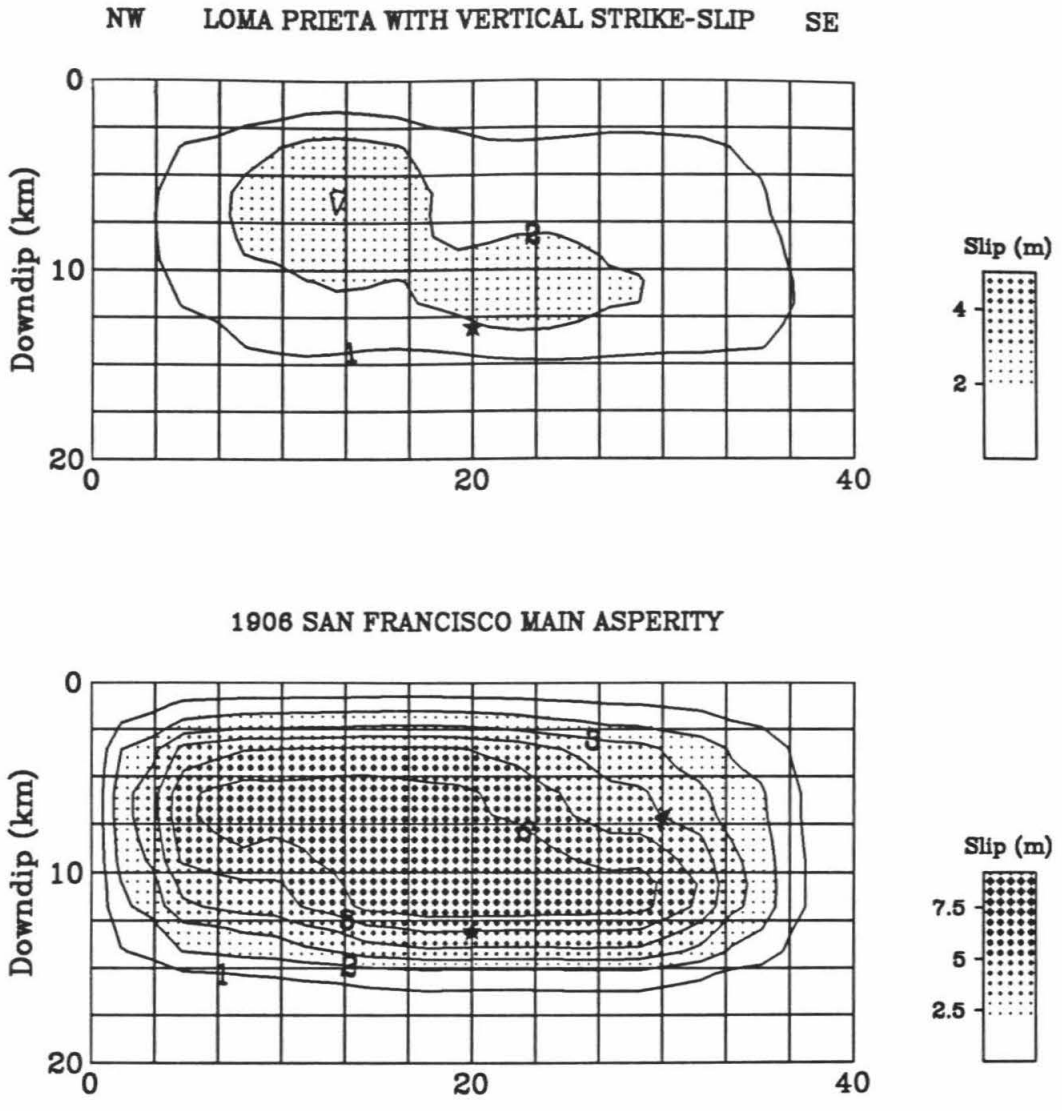

Figure 5.20: Slip distribution of Wald *et al.* [1991] for the Loma Prieta earthquake modified by shallowing the slip and rotating the dip to vertical and the rake to pure strike-slip (top). Bottom slip model is the scaled-up version of Loma Prieta used to simulate the main 1906 asperity obtained from spatial lagging.

estimates were made with the finite-fault, ground-motion techniques used in Wald *et al.* [1991], with synthetic Green's functions appropriate for the Loma Prieta region. The frequency bandwidth of the simulations is from 0.0 to 1.0 Hz.

Although many well-studied earthquakes require very short slip durations (see Heaton [1990] for a partial summary), there have been no studies of strike-slip earthquakes of this magnitude with the strong-motion recordings necessary to constrain the local slip duration. Heaton [1990] points out that the duration of slip for the 1985 Michoacan earthquake ($M_S = 8.5$) was on the order of 5 sec as indicated from near-field displacements obtained from twice-integrated accelerograms. However, the tectonic environment was that of subduction thrusting, and the fault-aspect ratio was quite different from that of the 1906 earthquake. Consider that for a rupture length of 430 km and a fault width of 10-15 km, the aspect ratio for the 1906 rupture was between about 30-45 to 1, nearly a line source. For earthquakes in the tectonic regime more similar to the northern San Andreas Fault, the slip durations are observed to be very short. For example, recent eyewitness observations of ground rupture during the 1990 Philippines earthquake ($M_S = 7.8$) suggest that the slip duration was less than about 1 sec [T. Nakata, personal communication, 1991], yet the displacement was 3-4 m. Further, Wald *et al.* [1991] found that most of the slip during the Loma Prieta earthquake occurred in less than 1 sec over most of the fault plane and less than 2 sec everywhere. From these observations, we assumed a 4-sec rise time for the 1906 slip. However, the derivative of the actual slip function is not a simple triangle, but rather is a time-expanded version of the Loma Prieta slip model determined by Wald *et al.* [1991]. The Loma Prieta slip function has 3 time windows, each 0.7-sec triangles overlapping by 0.1 sec. On average, the first window contributes half the slip, and the second and third each contain 25% of the slip, but these values change slightly as a function of position on the fault. For the 1906 ground-motion simulations, we carry through the spatial rise-time variations determined for the Loma

Prieta earthquake from the strong-motion data, but use 3 time windows each 1.4 sec long for a total duration of 4.2 sec. We also tested the dependence on rise time by computing synthetic ground motions for longer and shorter, total rise times.

Initially, we computed ground motions for the top model on Figure 5.20 to compare with the simulated ground motions [Wald *et al.*, 1991] of the Loma Prieta earthquake. This simply allows us to compare the ground motions for a deep, oblique-slip event with that of vertical strike-slip. The comparison of peak ground velocities plotted as a function of distance is shown in Figure 5.21. The distance, r_o, is defined as in Joyner and Boore [1988] as the shortest distance (km) from the recording site to the vertical projection of the fault rupture on the surface of the earth. Solid circles denote the Loma Prieta simulations, and the shaded circles represent the vertical strike-slip, modified-model results. The overall amplitudes are slightly higher for the vertical strike-slip case. Considering that the source-rupture model is identical in all other aspects, differences in the resulting ground motions can be attributed to the combined effects of change in rake and source depth.

In general, the vertical strike-slip model predicts slightly larger velocities, especially on tangential components at near-fault stations. The vertical components are slightly smaller because of the radiation pattern. Also plotted as a dashed line is the attenuation relationship of Joyner and Boore [1988] for peak ground velocity:

$$\log y = a + b(M-6) + c(M-6)^2 + d\log r + kr + s$$

$$5.0 \leq M \leq 7.7,$$

where constants a=2.17, b=0.49, c=0.0, d=-1.0, k=-0.0026, s=0.17 and

$$r = \sqrt{r_o{}^2 + h^2}.$$

Results of the simulation of the 1906 main asperity compared with the simulation of the vertical strike-slip version of Loma Prieta are shown in Figure 5.22.

Figure 5.21: Radial (top), tangential (middle) and vertical (bottom) peak ground velocities for simulations of the Loma Prieta ground motions (solid circles) compared with the modified, vertical, strike-slip Loma Prieta model (shaded circles). The attenuation relationship of Joyner and Boore [1988] is given with the dashed line for $Mw = 6.9$

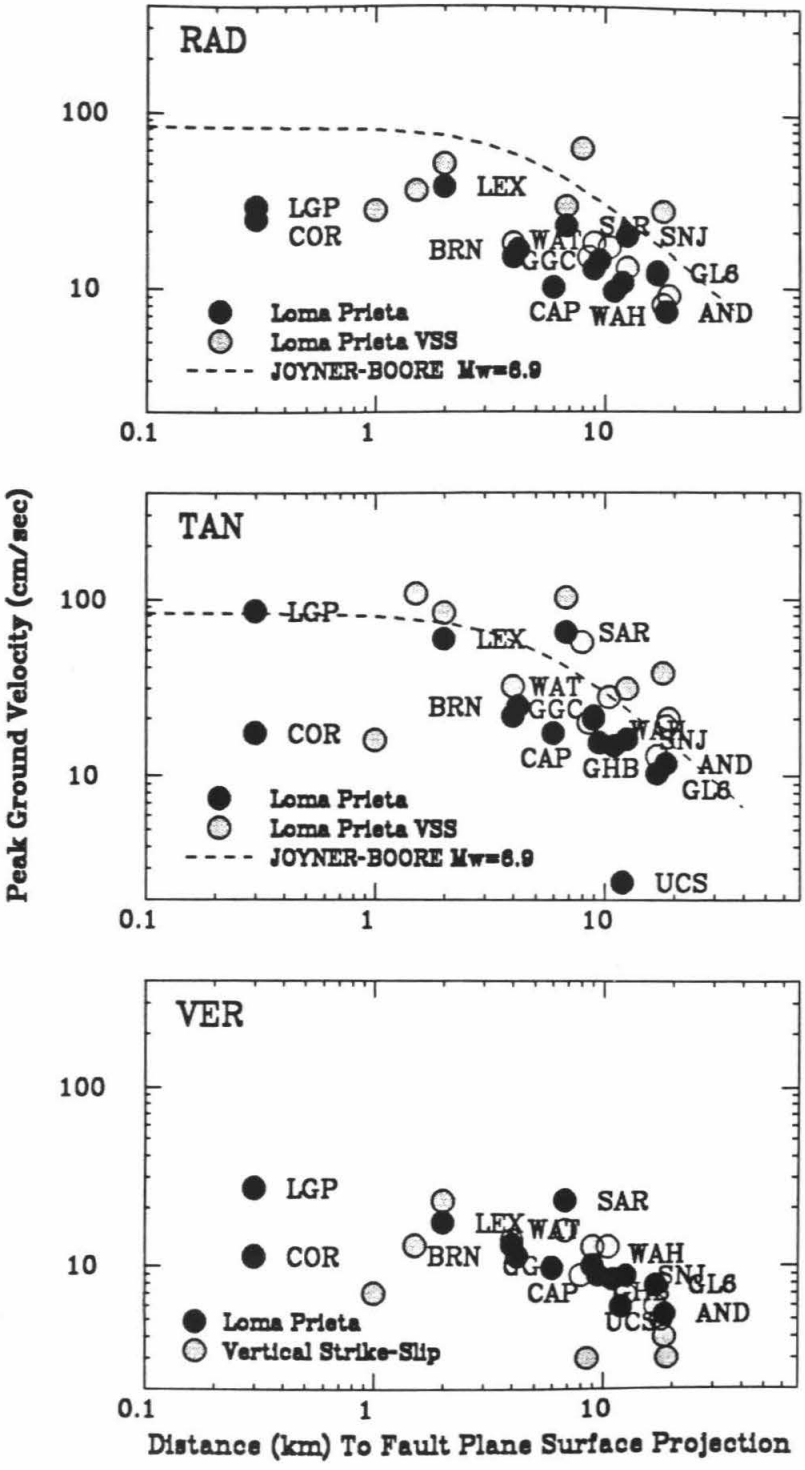
RAD
100
10
0.1
1
10
LGP
COR
LEX
BRN
WAT
SAR
SNJ
GGC
GL6
CAP
WAH
AND
Loma Prieta
Loma Prieta VSS
JOYNER-BOORE Mw=6.9
TAN
100
10
0.1
1
10
LGP
LEX
SAR
WAT
BRN
GGC
COR
SNJ
CAP
GHB
AND
GL6
Loma Prieta
Loma Prieta VSS
JOYNER-BOORE Mw=6.9
UCS
VER
100
10
0.1
1
10
LGP
SAR
LEX
WAT
COR
BRN
WAH
SNJ
GL6
CAP
AND
UCS
Loma Prieta
Vertical Strike-Slip
Peak Ground Velocity (cm/sec)
Distance (km) To Fault Plane Surface Projection

The synthetic velocity and displacement waveforms are displayed in Figure 5.23 for one station adjacent to the fault trace. The peak ground-velocity amplitudes are substantially greater than those recorded during the Loma Prieta earthquake, and are comparable to those predicted by Joyner and Boore [1988] for an $M_W = 7.7$ earthquake. Again, the tangential components are dominant because of the along strike *SH* pulse from a vertical, strike-slip rupture. Since the station distribution is fairly random, several stations are off the southeast end of the rupture and show fairly small ground motions. This is attributed to the lack of directivity at southeastern stations, and the fact that we do not add in the contributions from adjacent portions of the fault. Recall that model only a small (40 km) portion of the entire 1906 rupture and not the entire rupture length, so our durations are much shorter than would be expected. Here we are more interested in the largest-possible motions that are due to a magnitude $7\frac{3}{4}$ earthquake, rather than the average ground motions. Considering the large amount of slip known to have occurred on adjacent segments, these contributions may be important, but would not significantly alter the estimation of the greatest contribution to the ground motions.

It appears that the Joyner and Boore [1988] curve is a fairly conservative estimate considering that our data points represent the largest peak velocities expected from the greatest asperity. An overall average of stations along the length of the rupture would be considerably lower.

5.8 Discussion And Conclusions

Using Morgan Hill observations as empirical Green's functions, we found that a large part of the shear wavetrain can be modeled with pure strike-slip on two energetic regions of the fault separated by about 40 sec. Assuming a uniform rupture velocity of 2.7 km/sec, this time corresponds to a distance separation of approximately 110

Figure 5.22: Radial (top), tangential (middle) and vertical (bottom) peak ground velocities for simulations of the main 1906 asperity (solid circles) compared with the modified, vertical, strike-slip Loma Prieta model (shaded circles). The attenuation relationship of Joyner and Boore [1988] is given with the dashed line for $Mw = 7.7$

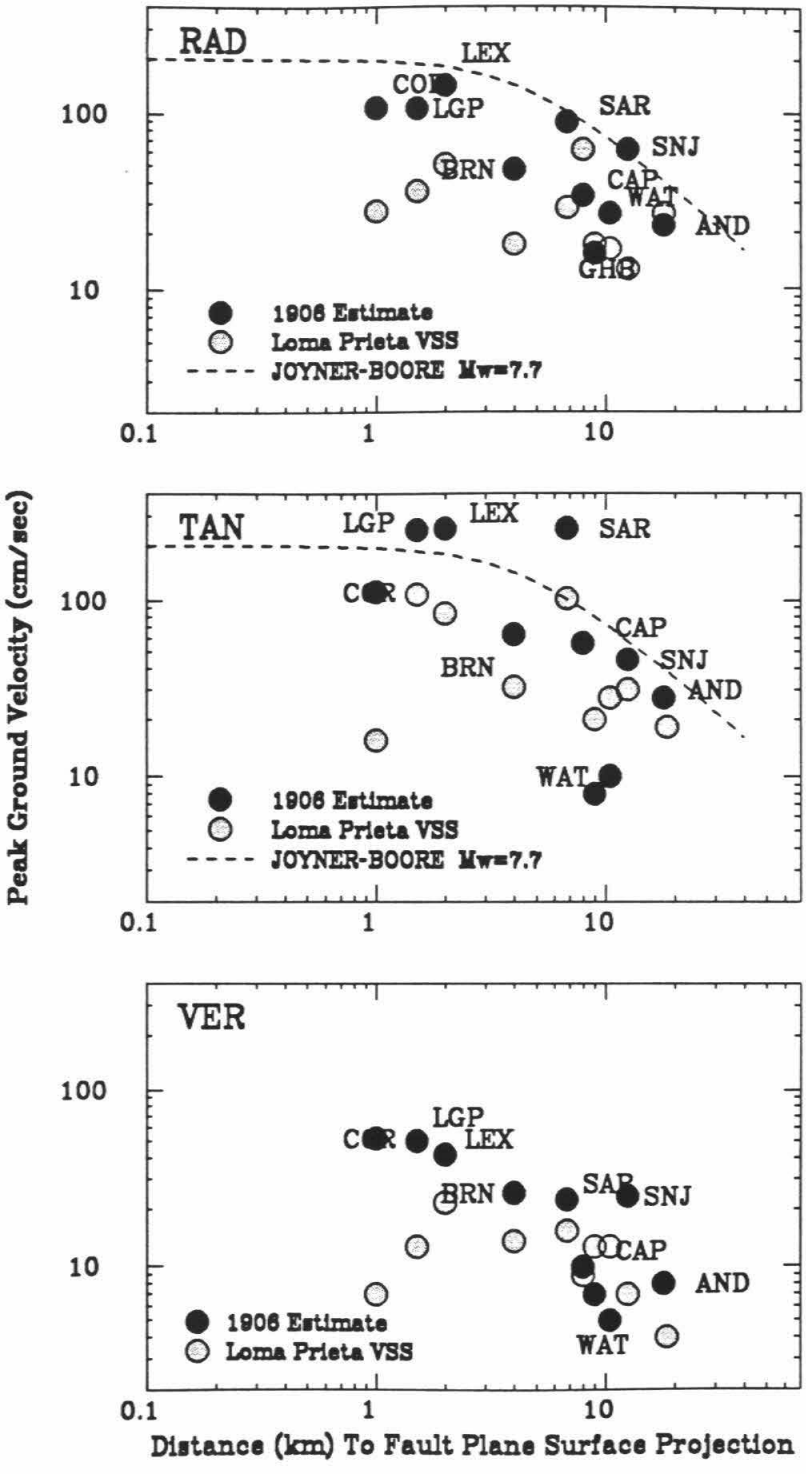
RAD
LEX
COR
LGP
SAR
SNJ
BRN
CAP
WAT
AND
GH8
100
10
1906 Estimate
Loma Prieta VSS
JOYNER-BOORE Mw=7.7
0.1
1
10
TAN
LGP
LEX
SAR
COR
CAP
SNJ
BRN
AND
WAT
100
10
1906 Estimate
Loma Prieta VSS
JOYNER-BOORE Mw=7.7
0.1
1
10
VER
LGP
COR
LEX
BRN
SAR
SNJ
CAP
AND
WAT
100
10
1906 Estimate
Loma Prieta VSS
0.1
1
10
Peak Ground Velocity (cm/sec)
Distance (km) To Fault Plane Surface Projection

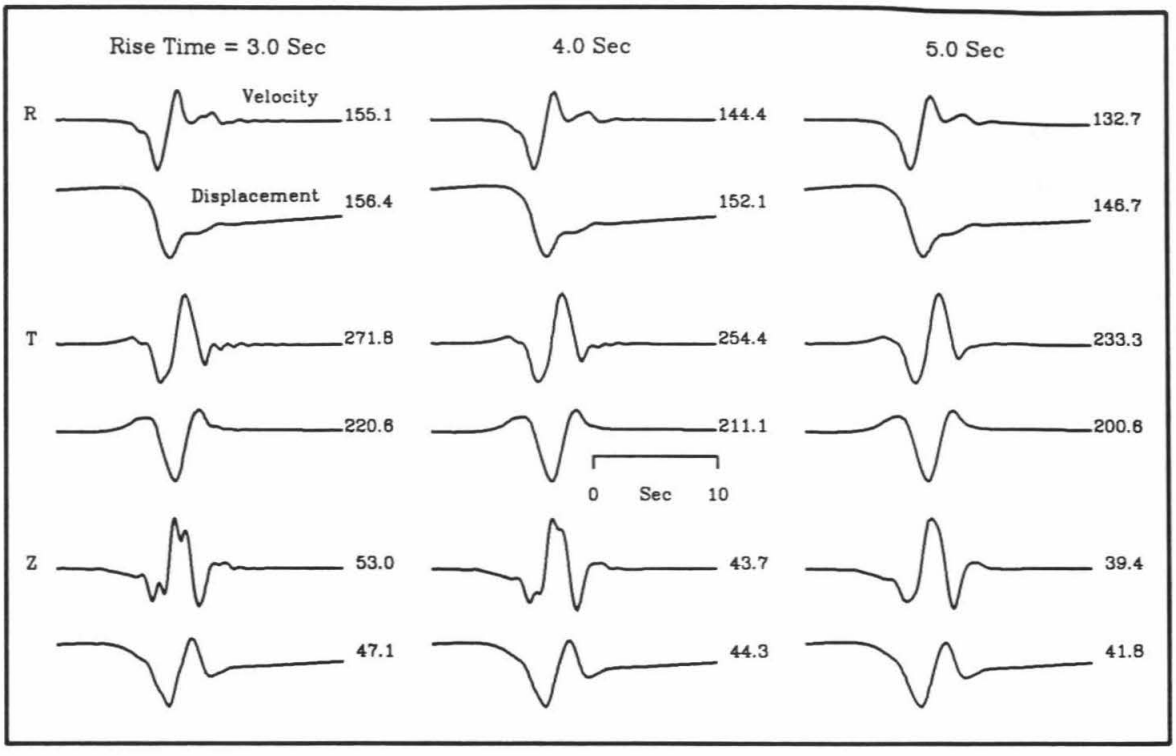

Figure 5.23: Fault parallel (R), fault perpendicular (T) and vertical (Z) estimated ground velocity and displacement at station LEX for the largest asperity during the 1906 earthquake. LEX is at a distance of 2 km from the fault trace. Waveforms are given with rise times of 3 sec (left), 4 sec (center) and 5 sec (right).

km. The rupture velocity was chosen to be 2.7 km/sec, based on the average value determined from other studies of California strike-slip earthquakes [e.g., Hartzell and Heaton, 1983, 1986; Beroza and Spudich, 1988; Wald *et al.*, 1990]. This assumption fixes the final location of the major asperity relative to the hypocenter, and reasonable perturbations from this value (2.4 - 3.0 km/sec) do not change the synthetic waveforms significantly, nor the scaling factor required to fit the data. Choosing a constant rupture velocity of 2.4 km/sec has the effect of shifting the largest source of radiation about 12 km closer to the epicenter. We also assumed that the rupture front propagates in a rather simple fashion, since a more complex rupture scenario with repeated or delayed rupture episodes cannot be resolved on the basis of the quality of the data available.

The locations of the two sources of strong 10-20 sec radiation is consistent with Boore's [1977] observation that the source of the main strong motions observed at Mt. Hamilton was at least 75 km away. This corresponds with the location of the first main asperity in our 1906 source model. The second, larger asperity certainly contributed later in the record, but was radiated from a much greater distance, nearly 200 km away.

By comparing the slip model derived from the inversion (5.17, top) with the surface offset and the modeled slip from the geodetic data (5.17, bottom), we found a general correspondence between the hypocentral asperity and a gradient in slip in the amount of slip in the region. The larger asperity between Point Reyes and Fort Ross corresponds roughly with the region of largest surface offset and geodetic slip. Note that there may really be more variation in the static slip than was suggested by the geodetic models. Thatcher [1975] assumed a constant slip with depth and a fixed depth of rupture along the fault. If the actual depth of rupture varied, or if the functional form of the slip with depth is similar to other strike-slip earthquakes in California, that is, a peak in slip at 8-9 km and tapering off both shallower and

deeper (see Chapter 6), then the solution to the geodetic displacements would be different.

Another factor that is difficult to evaluate is the effect of rupture dynamics on the teleseismic arrivals. Abrupt acceleration of the rupture front can result in starting and stopping phases on the teleseismic records. In effect, a model with uniform slip, tapered to zero at each end, can produce complex records if the rupture front is inhibited and then allowed to reaccelerate a number of times. If rupture along the central portion of the 1906 rupture zone had a complex-rupture progression, the total slip estimated in our model could be reduced. Likewise, a model with a relatively homogeneous slip and a constant rupture velocity might be difficult to recognize teleseismically because of uniformity of the radiation. It is likely that the offshore segment of the fault ruptured in this fashion.

Simulated ground velocities were produced from our estimate of the largest asperity. In doing so, we have placed a few "data" points on the attenuation curve of Joyner and Boore [1988], which has few observational constraints for these close-in distances and of this large magnitude. Unfortunately, it appears that the distribution of Modified Mercalli intensities shown in Figure 5.2 provides little information about variations in the nature of the rupture as a function of position along strike, making it difficult to relate our model to the ground motions and damage experienced in 1906. Rather, the Modified Mercali map shows a fairly uniform along strike distribution. This observation is also apparent in the full-sized isoseismal map (Rossi-Forel scale) given in the *Atlas*. As carefully noted by Lawson [1908], the most striking feature in the apparent intensity map is the correlation between the regions of strong shaking and the underlying geological conditions, particularly with river and sedimentary basins and reclaimed and tidal marsh lands. With the exception of the gradual decrease in intensity with increasing distance to the fault trace, this correlation dominates the variations in the intensities. We found no obvious in-

dependent constraints (i.e., density of topped trees or eyewitness accounts) on the variations in shaking intensity along strike.

It should be noted that there is no significant change in the nature of the surface expression of the San Andreas Fault in the region of maximum slip and radiation (between Point Reyes and Fort Ross), and in fact, the fault tends to be simpler than along other portions of the San Andreas Fault. Hence, there is no correspondence between the largest asperity (or greatest slip) and surface fault-trace complexity for the 1906 earthquake. There is, however, a substantial right-stepping (releasing) bend just north of the epicentral asperity west of the Golden Gate. This step-over is recognizable but not impressive on the scale of Figure 5.1.

We have not addressed the issue of dip-slip components in the vicinity of the Loma Prieta earthquake. From our modeling, we do not consider that the body-wave data requires a significant component of dip-slip, though it is not clear that the historic seismic data can fully resolve this issue. Recent comparison of the horizontal displacements accompanying the 1906 San Francisco and the 1989 Loma Prieta earthquakes indicate that although the Loma Prieta event exhibited nearly equal strike and dip-slip components of faulting, the 1906 data are consistent with strike-slip on a vertical plane [Segall and Lisowski, 1990]. Likewise, although rupture along the northernmost 140 km of the San Andreas (offshore) is not observed in the teleseismic body-wave arrivals, based on the historical data alone, we do have the resolving power to rule it out. Most likely, though, any slip along that portion of the fault was also relatively uniform and of low stress-drop.

5.8.1 Recent Earthquake Analogues

The results of this study allow us to make some general comparisons of the rupture style of the 1906 San Francisco earthquake with studies of other large, strike-slip events in recent years. Perhaps the best modern analogue for the 1906 earthquake

was the $M_S = 7.8$ Philippines event in 1990. Although smaller in rupture length than 1906, the degree of rupture complexity appears comparable. In fact, the 1906 teleseismic, shear-wave amplitudes were similar in amplitude and duration to those of the 1990 Philippines earthquake. Further, the rupture model of Thio *et al.* [1992] determined from the teleseismic data is relatively simple, showing two main regions of broadband radiation, the largest at the rupture initiation and a smaller one nearly 50 sec later. In contrast to the 1906 earthquake, which had the dominant source of radiation later in the rupture, the initial episode of radiation near the epicenter of the Philippines was the greatest. The seismic moment of the Philippines earthquake was estimated to be $3.6x10^{27}$ dyne-cm [Thio *et al.*, 1992] and the total rupture length along the Philippines Fault was at least 120 km [Nakata, 1990]. Perhaps the lack of rupture complexity of these two earthquakes can be attributed to the relative simplicity of the San Andreas and Philippines Fault traces over the length of their ruptures.

In contrast to the above events, other large, strike-slip earthquakes have had considerably more rupture complexity. Comparison of WWSSN shear-wave amplitudes and waveforms for the 1976 Guatemala earthquake ($M_S = 7.5$) shows that the 1906 amplitudes are nearly three times larger, yet the waveforms are clearly less complicated. Based on the long period WWSSN bodywaves, the Guatemalan event had a moment of about $2.9x10^{27}$ dyne-cm [Kikuchi and Kanamori, 1991] with a large subevent occurring about 20 sec after the origin time, in agreement with the largest subevent recognized by Young *et al.* [1989]. The location of this subevent was about 60-90 km west of the epicenter and from the model of Kikuchi and Kanamori [1991] had a moment of about $5x10^{26}$ dyne-cm, a factor of two smaller than the largest 1906 asperity. A second, comparably large subevent occurred toward the western end of the rupture with a moment of $5 - 6x10^{26}$ dyne-cm. The region of the latter subevent is used by Jennings and Kanamori [1979] to determine the distance ($\simeq$ 30 km) to a

seismoscope recording at Guatemala City from which they estimated $M_{\simeq}6.8$. This compares with the $M_L = 7.2$ estimated from the 1906 event at Carson City, Nevada.

The initiation of the Guatemala earthquake, like that of the 1906 earthquake, was not the most dramatic portion of the rupture. Both Kikuchi and Kanamori [1991] and Young *et al.* [1989] associate many other subevents during the Guatemalan earthquake with later arrivals in the teleseismic data. Ground breakage was observed along a nearly continuous trace of the Motagua Fault, extending for 230 km [Plafker, 1976]; the strike-slip displacements ranged up to 3.4 meters and averaged nearly 1.1 meters with displacements greater than 2 meters limited to region 35-50 km from the west end of the surface rupture. As for our model of the 1906 rupture, for the Guatemalan event, the region of greatest slip coincides roughly with the largest subevent of the Kikuchi and Kanamori [1991] rupture model. The surface offset was considerably lower than the average slip estimated from the body-wave data [Young *et al.*, 1989] assuming a rupture plane 15 km wide and 340 km long. Though fairly continuous with few splays, the trace follows an arcuate route with a nearly 35° change in strike over the rupture length, perhaps contributing to the relative complexity and numerous identifiable subevents. The intensity of shaking was much greater at the western end of the rupture [Espinosa *et al.*, 1976], consistent with the combined effects of directivity that were due to east-to-west rupture propagation and the locally large moment release determined by Kikuchi and Kanamori [1992].

Similar complexity was discussed in studies of the 1990 Iran earthquake ($M_S = 7.7$). Coseismic surface faulting associated with the Iran earthquake displayed three main discontinuous, complex fault segments with a total length of over 80 km [Berberian *et al.*, 1992]. They estimated the seismic moment to be $0.9x10^{27}$ dyne-cm and found three major subevents, perhaps associated with the expression of the surface segmentation of the fault. Again, the average surface offset, about one meter, is less than the 2.4-meter slip average computed from the seismic data, assuming a rupture

length of 80 km and width of 15 km [Berberian *et al.*, 1992]. Unfortunately, of the above earthquakes, only the Iran earthquake had local strong-motion recordings, and few at that. Peak accelerations at the closest station (Abbar), about 8 km from the epicenter, were 65% g.

Considering the enormous rupture length of 1906 compared with other large ruptures, more complexity in the waveforms might be expected. The above observations suggest that relatively uniform slip on lengthy portions of the northern San Andreas fault occurred during the 1906 rupture, and not 10 end-to-end "Loma Prieta"-style ruptures nor several end-to-end "Iran" or "Guatemala" events. Since we can recognize the Loma Prieta rupture clearly on the Wiechert instruments at UPP and GOT, such a complex rupture would likely be recognizable on the historical records.

We have suggested that portions of the 1906 rupture occurred such that they did not produce large signals in the teleseismic recordings in a bandwidth of 5-20 sec. This does not necessarily imply that those portions of the rupture produced only relatively moderate high-frequency ground motions. In fact, this remains a pressing issue. Can a smooth rupture, as observed at 15 sec periods, be produced by a uniform, but short-duration slip that is capable of radiating very damaging near-field motions? Alternatively, does the complexity of the 1976 Guatemala teleseismic recordings [Kikuchi and Kanamori, 1991] require that the local ground motions were comparably complex and damaging? It is important to be able to analyze independently data sets at both teleseismic and local distances for a large strike-slip earthquake in order to answer these questions fully.

Chapter 6

Comments on The Source-Rupture Processes

6.1 Comparative Asperitology

A substantial effort has been made in recent years to determine the distribution of slip on the rupture planes of important earthquakes. With the addition of the slip-distribution models described in the prior chapters to previously published models of other recent events, we now have an opportunity to comment on the systematic as well as unique rupture and asperity characteristics for a number of well-determined source models—comparative asperitology. In this chapter, we ponder and speculate on the physical phenomena that may explain such slip heterogeneity and discuss several aspects of the recently determined rupture models that pertain to issues of strong ground-motion occurrence, rupture dynamics, and earthquake recurrence.

Although there exist many rupture models for events outside the U.S.— particularly in Japan [e.g., Takeo, 1990]—the following observations and discussion are based primarily on studies of crustal earthquakes within California. Rupture models for events occurring within the State have had the advantage of the instrumentation

necessary for both sufficient frequency bandwidth sampling (several sec to several Hz) and high-density coverage of the source region. The earthquake models to be discussed below, as well as their references, are listed in Table 6.1. They are listed in order of decreasing seismic moment. The 1978 Tabas, Iran [Hartzell and Mendoza, 1991] and the 1983 Borah Peak [Mendoza and Hartzell, 1988a] earthquakes have also been included to augment the number of shallow dip-slip events available for analysis.

In order to put the rupture models presented in this thesis into a better visual perspective, the slip-distribution models from the Superstition Hills, Loma Prieta, and the Sierra Madre earthquakes have been plotted at the same scale in Figure 6.1. Only the third, largest subevent is shown for the Superstition Hills earthquake. Note that at this scale the 450-km rupture length of the 1906 San Francisco earthquake would be nearly 68 inches, or 6 times the length of the page.

At a glance, it appears that the characteristic asperity size is proportional to the overall earthquake dimensions (Figure 6.1). The term "asperity" is used here as originally defined by Lay and Kanamori [1981], referring to regions within the rupture that have relatively high-moment release. To some degree, however, the smallest asperity size reflects the highest frequency (and therefore subevent size) used in each source inversion; the high-frequency cut-offs for the Loma Prieta, Superstition Hills and Sierra Madre strong-motion data were 1, 3 and 5 Hz, respectively.

To facilitate comparison of the earthquake models derived by other researchers (listed in Table 6.1) with those presented in the previous chapters, we have displayed their results in Figures 6.2, 6.3, and 6.4. Again, the slip models are at the same scale, with the exception of the 1978 Tabas earthquake, which has a scale a factor of two smaller. On each model, the horizontal axis represents distance in km along strike, the vertical axis is distance in km downdip, and the hypocenter is represented by a solid dot.

EARTHQUAKE	M_0	L km	W km	D cm	Dmax cm	Tr sec	Vr km/s	REFERENCE
1978 Tabas	58	90	35	112	213	2.1	2.5	Harzell & Mendoza [1991]
1989 Loma Prieta	30	36	18	130	460	1.5	2.5	Wald *et al.* [1990]
1983 Borah Peak	23	40	20	82	147	0.6	2.9	Mendoza & Hartzell [1988a]
1971 San Fernando	7	12	14	120	250	0.8	2.8	Heaton [1982]
1979 Imperial Valley	5	30	10	48	180	1.0	2.6	Hartzell & Heaton [1983]
1987 Superstition Hills	4.8	20	9	56	190	0.5	2.4	Wald *et al.* [1990]
1984 Morgan Hill	2.1	20	8	38	100	0.3	2.8	Hartzell & Heaton [1986]
1986 North Palm Springs	1.8	18	10	26	45	0.4	3.0	Hartzell [1989]
1987 Whittier Narrows	0.9	10	10	29	90	0.3	2.5	Hartzell & Iida [1990]
1979 Coyote Lake	0.35	6	6	46	120	0.5	2.8	Liu & Helmberger [1983]
1991 Sierra Madre	0.28	3	3	57	120	0.2	2.7	Wald [1992]

Table 6.1: Earthquake model slip parameters. D is the average slip and M_0 is the seismic moment ($\times 10^{25}$ dyne-cm).

Figure 6.1: Slip distributions of 1987 Superstition Hills, 1989 Loma Prieta and 1991 Sierra Madre at the same horizontal and vertical scale.

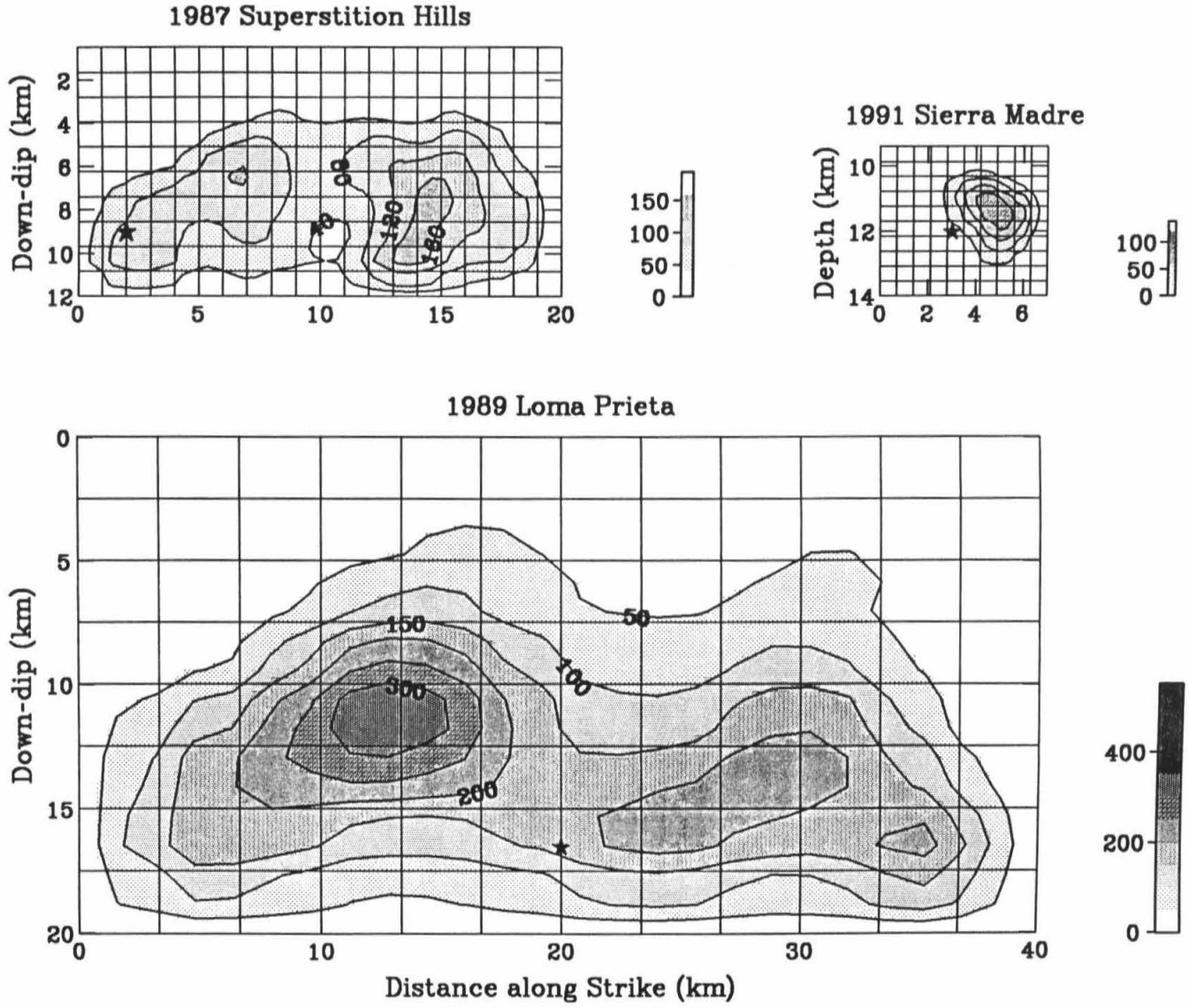
1987 Superstition Hills
Down-dip (km)
2
4
6
8
10
12
0
5
10
15
20
150
100
50
0
1991 Sierra Madre
Depth (km)
10
12
14
0
2
4
6
100
50
0
1989 Loma Prieta
Down-dip (km)
0
5
10
15
20
0
10
20
30
40
Distance along Strike (km)
150
300
200
100
50
400
200
0

Figure 6.2: Slip distribution of the 1984 Morgan Hill [Hartzell and Heaton, 1983], 1986 North Palm Springs [Hartzell, 1989], 1971 San Fernando [Heaton, 1982], 1987 Whittier Narrows [Hartzell and Iida, 1990], and the 1979 Coyote Lake [Liu and Helmberger, 1983] earthquakes. The same horizontal and vertical scales are used.

1984 Morgan Hill

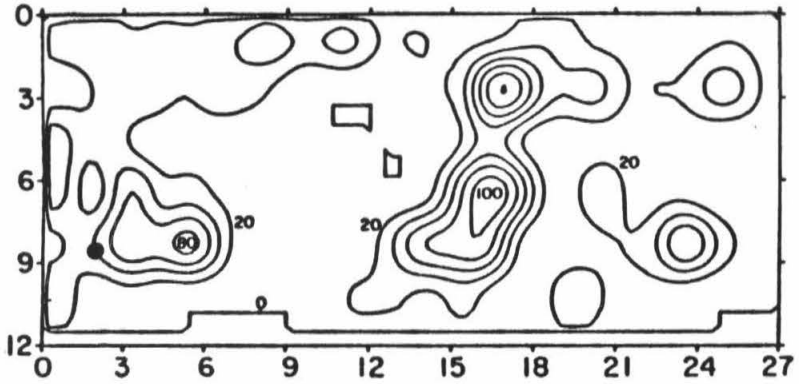

1971 San Fernando

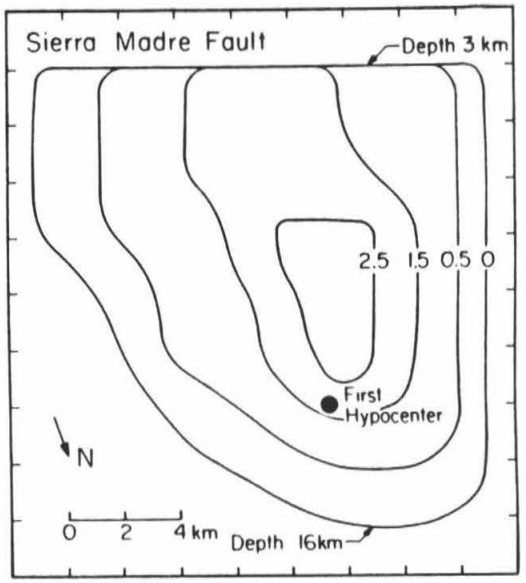

1986 North Palm Springs

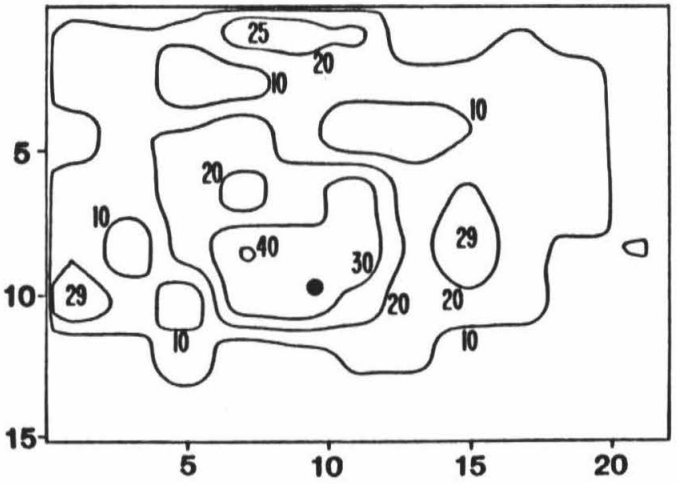

1987 Whittier Narrows

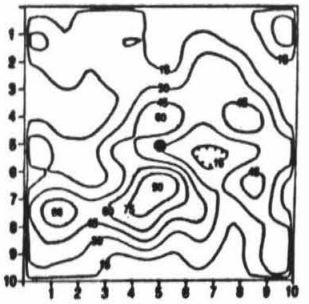

1979 Coyote Lake

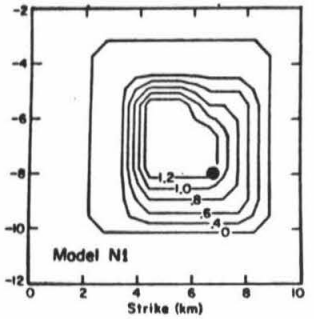

Figure 6.3: Slip distribution of 1978 Tabas, Iran [Hartzell and Mendoza, 1991] and the 1979 Imperial Valley [Hartzell and Heaton, 1983] earthquakes. The scale used for the Tabas model is a factor of two smaller than the earthquakes shown in Figures 6.1, 6.2, 6.3, and 6.4.

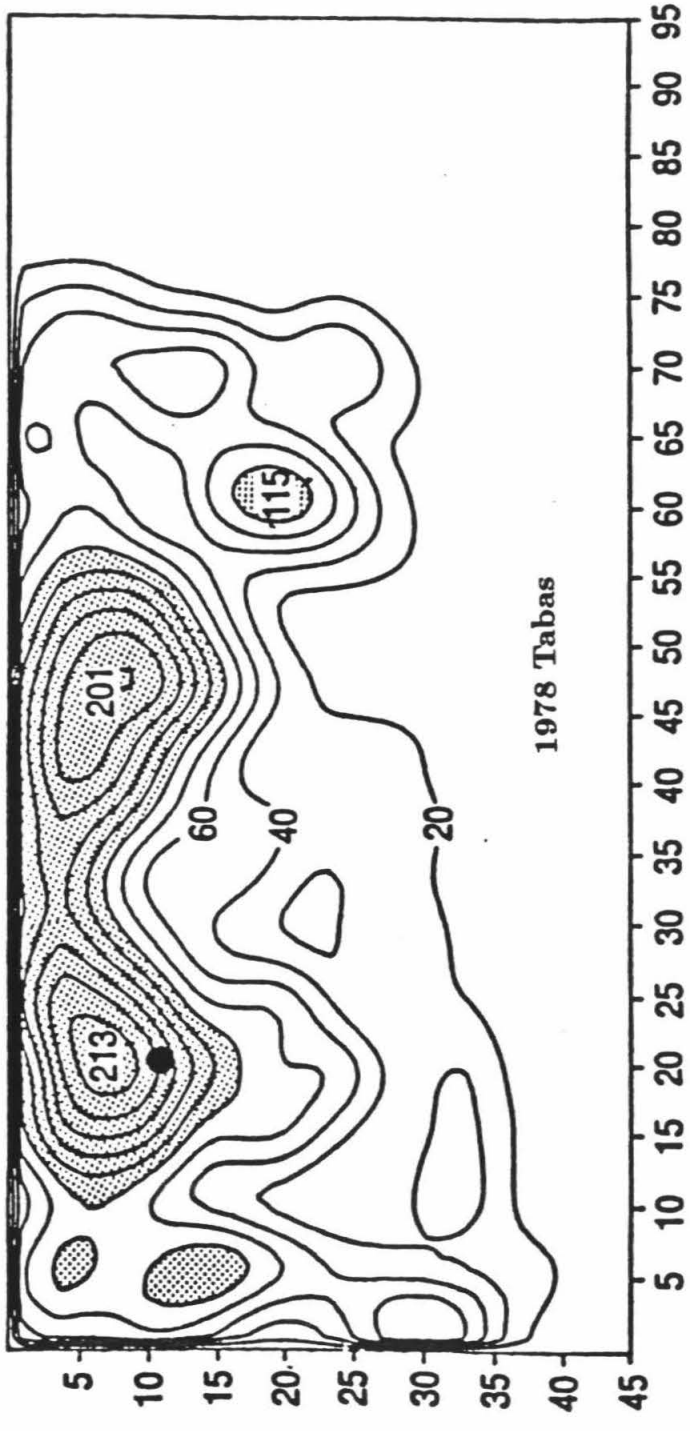
1978 Tabas
213
201
115
60
40
20
0
5 10 15 20 25 30 35 40 45
5 10 15 20 25 30 35 40 45 50 55 60 65 70 75 80 85 90 95

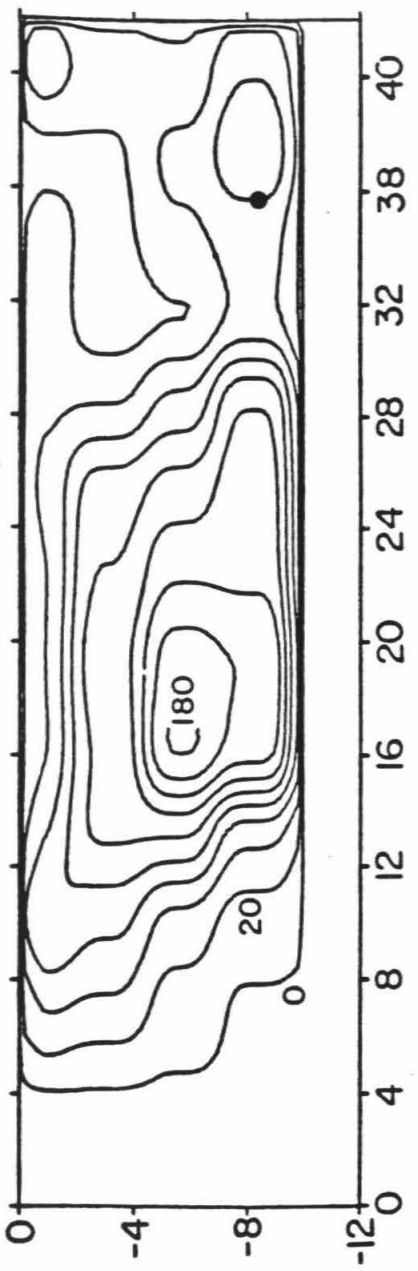
1979 Imperial Valley
180
20
0
0 -4 -8 -12
0 4 8 12 16 20 24 28 32 38 40

Figure 6.4: Slip distribution of 1983 Borah Peak earthquake [Mendoza and Hartzell, 1988a]. The same horizontal and vertical scale is used.

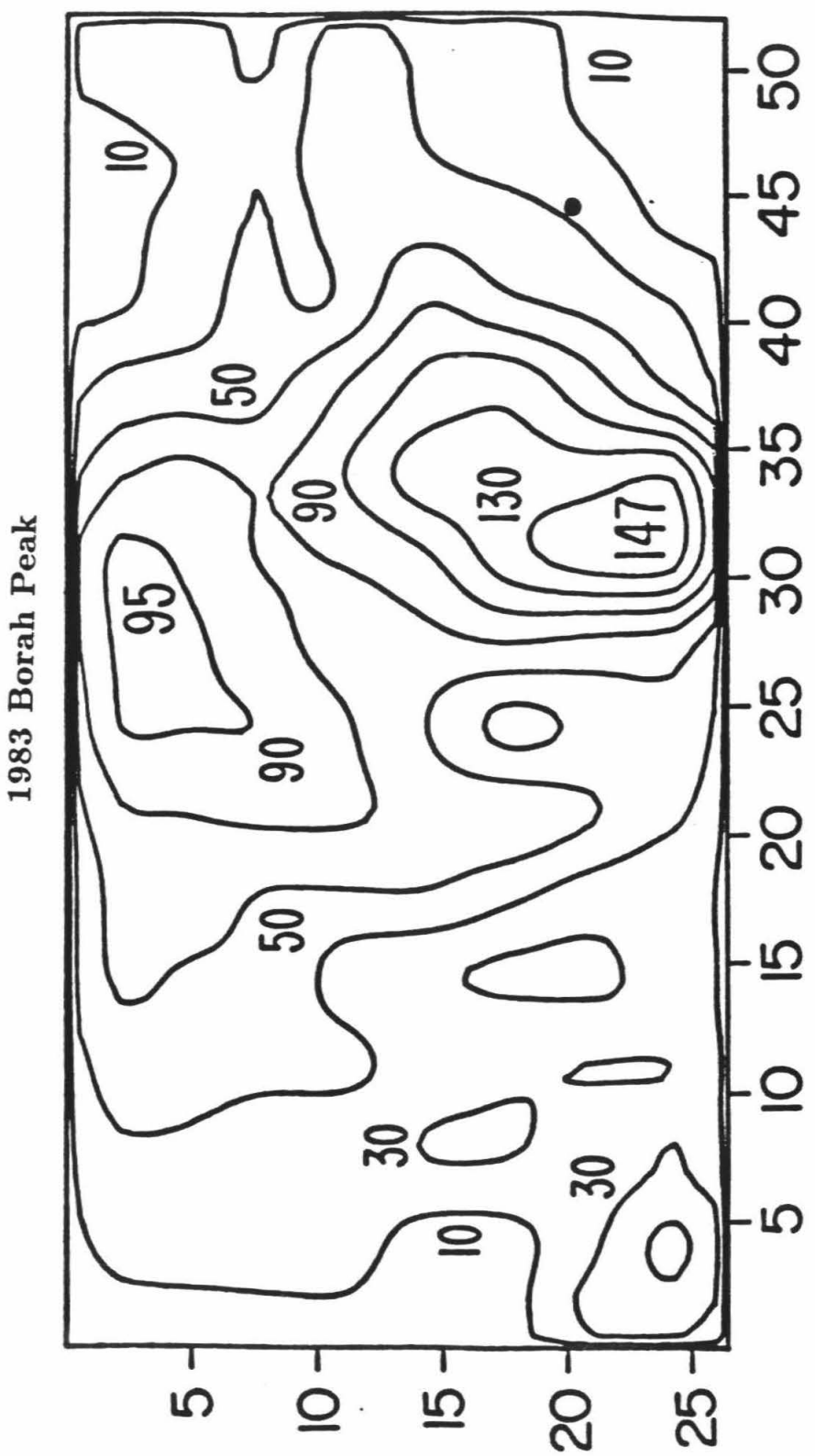
1983 Borah Peak
10
50
95
90
30
10
30
90
130
147
10
5
10
15
20
25
5
10
15
20
25
30
35
40
45
50

6.1.1 Depth Dependence of Slip

By analyzing the systematics of the slip-distribution models, we find that the slip distribution is much more systematic as a function of depth (at least for strike-slip faults) than as a function of distance along strike. In Figure 6.5 the variation of coseismic slip and moment release with depth, averaged per km over the along-strike length of the fault for the strike-slip earthquakes given in Table 6.1 is shown. There is a systematic peak or concentration of slip averaging about 8 km in depth, which tapers off gradually updip and decreases more sharply towards the base of the seismogenic zone. Nearly all the seismic-moment release occurs within the depth range of 3-12 km. Notice that both the 1979 Imperial Valley and the 1987 Superstition Hills earthquakes occurred within or near the margins of the Imperial Valley which contains a sedimentary column as thick as 5 km.

This systematic depth dependence is not a result of limited depth resolution; in fact, both teleseismic and strong-motion waveforms are strongly depth dependent. Directivity plays an important role only when the rupture front progresses at a velocity comparable to the phase of interest [Heaton, 1982, Appendix]. For this reason, the teleseismic waveforms are more sensitive to up and downdip rupture, since the vertical-phase velocity is comparable to the rupture velocity, and the horizontal-phase velocity is much higher than the phase velocity. Strong-motion Green's functions are also quite depth-dependent because the substantial free-surface multiples and surface waves develop quickly as the source shallows.

We would expect a systematic dislocation stratification as a function of depth if the dynamic rupture properties were particularly dependent on rock rheology. For example, Marone *et al.* [1991] describe shallow- and deep-velocity strengthening frictional zones that limit the vertical extent of coseismic rupture. The upper transition is controlled by the presence of sediments or well-developed fault gouge, and the lower zone represents the onset of ductility at the base of the seismogenic zone.

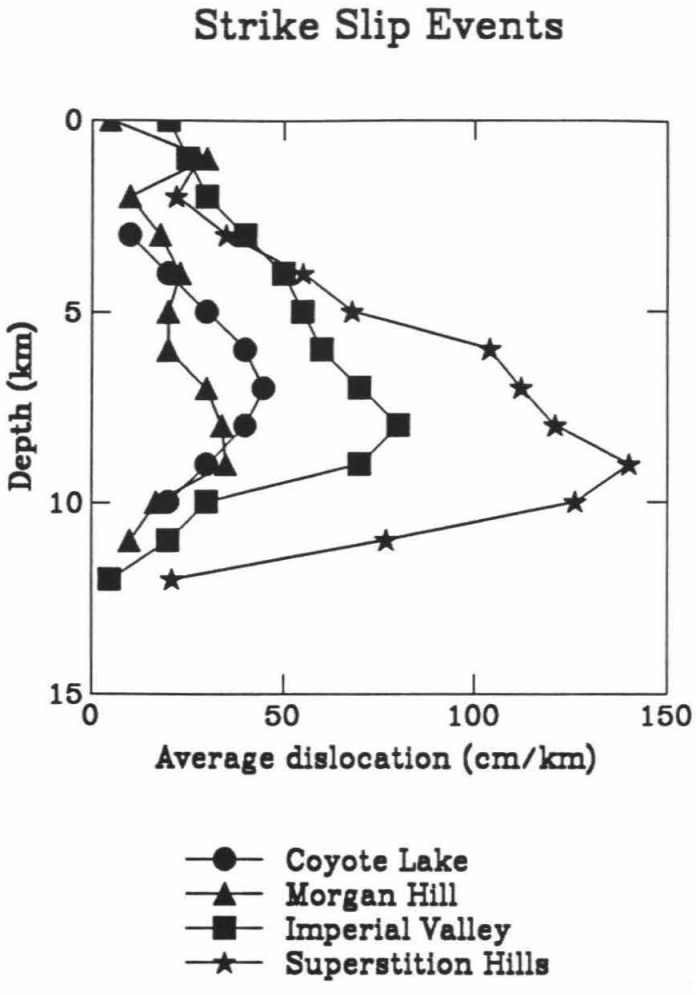

Figure 6.5: Distribution of average slip per km of rupture length as a function of depth for strike-slip earthquakes.

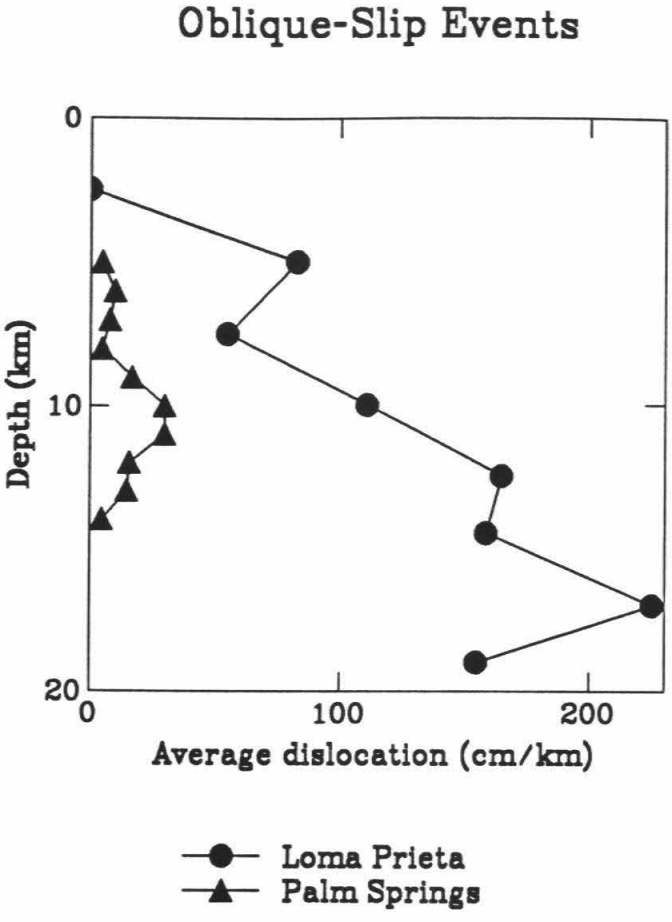

Figure 6.6: Distribution of average slip per km of rupture length as a function of depth for oblique-slip earthquakes.

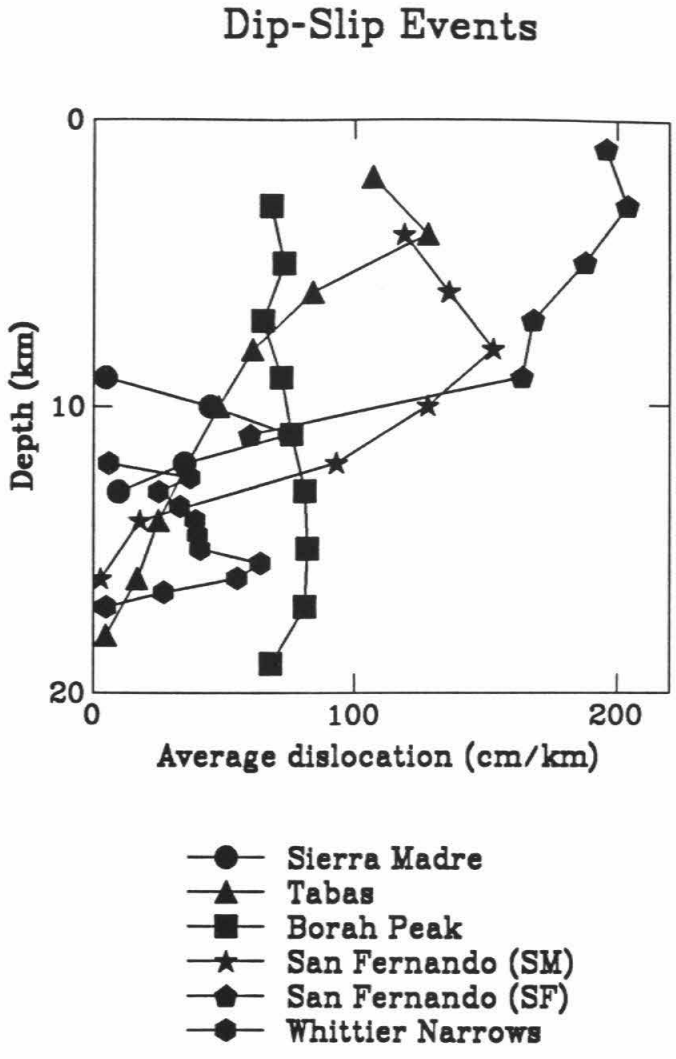

Figure 6.7: Distribution of average slip per km of rupture length as a function of depth for dip-slip earthquakes. For the 1971 San Fernando earthquake, SM refers to the Sierra Madre Fault and SF refers to the San Fernando Fault

The sediment column exhibits positive slip-rate dependence (velocity-strengthening) and is therefore inherently stable [Marone and Scholz, 1988]. Consistent with their model, for those strike-slip events described herein that resulted in surface displacement, slip at the surface manifested as coseismic slip was greatly augmented by large amounts of afterslip, especially for events situated within deep sedimentary basins (e.g., the Superstition Hills and the 1979 Imperial Valley earthquakes). Note that other moderate-sized, vertical strike-slip earthquakes, including the 1933 Long Beach ($M_L = 6.3$) and the recent 1992 Joshua Tree ($M_L = 6.1$) earthquakes, indicated no significant coseismic or postseismic surface rupture.

Although the seismogenic zone is well defined as a function of depth for pure strike-slip earthquakes, there is more variability in overall slip distributions for oblique-slip and particularly dip-slip earthquakes (Figure 6.6 and Figure 6.7). Although the two oblique events, the 1986 North Palm Springs and the 1989 Loma Prieta earthquake, hardly represent a statistical sample, they suggest potentially deeper slip than the pure strike-slip cases. These events occurred in regions of the San Andreas Fault system, which show substantial bends, and the faulting mechanisms are comprised of both thrusting and right-lateral strike-slip. The background seismicity in the Loma Prieta portion of the San Andreas fault is deeper than along straight portions of the fault, and the depth of dominant coseismic slip likely reflects a deeper seismogenic zone.

For pure-thrust or normal-slip events, the depth dependence on slip is highly variable (Figure 6.7). Unlike oblique and strike-slip events, often dip-slip earthquakes (Tabas and San Fernando) have slips that increase, on average, with decreasing depth. Other events, like the Sierra Madre and Whittier earthquakes, indicate a limited depth interval over which slip occurred, concentrated at depths greater than 10 km. Apparently, regimes of crustal extension or thickening have seismogenic zones with highly variable depth dependence. In such regimes it may be more difficult to

assess the range of likely faulting for specific earthquake-hazard scenarios.

6.1.2 Slip Heterogeneity Along Strike

A consistent feature of the slip models shown in Figures 6.1, 6.2, 6.3 and 6.4 is the pronounced variations in slip along strike. At depth, there are slip variations on the order of a meter or two over a distance of as little as 2-3 km. Coseismic slip is particularly heterogeneous as a function of position along strike. On average, the peak slip is greater than twice the average slip along the fault plane, and often regions surrounded by or adjacent to large asperities display little slip (e.g., Morgan Hill, Loma Prieta and Superstition Hills).

The importance of slip heterogeneity cannot be overstated. Our experience with ground-motion simulations [e.g., Wald et al., 1987, 1988, 1991] has shown that amplitude and roughness of large-scale slip variations greatly influence the duration and amplitude characteristics of the resulting ground motions, including ground accelerations in the frequency range of most interest in earthquake engineering (greater than 1 Hz). In short, the main asperities directly control the most damaging ground motions. In later sections of this chapter, we speculate on the physical phenomena that might explain such slip heterogeneity.

6.1.3 Repeated Rupture

Another feature consistent with the style of rupture for the three events shown in Figure 6.1 is the complexity of the rupture-time history at one point on the fault. When data are sufficient for high-resolution source inversions, repeated rupture appears to be the norm, rather than the exception. Recall from Chapter 2 that the Superstition Hills earthquake model required significant slip in the same region for three subevents or episodes of slip. The first and second subevents were separated in time by two sec, and the second and third subevents were separated by 6.5 sec.

This observation is fairly robust, being the major feature controlling the distinct, separate, shear-wave arrivals on all the strong-motion recordings. In view of the fact that a 6.5-sec delay over a small spatial area requires an effective rupture velocity of much less than 1 km/sec, it is likely that stopping and restarting of the rupture occurred. Whether or not slip actually reruptured the same portion of the fault or whether immediately adjacent areas ruptured cannot be easily resolved.

Although a two-sec delay preceded the Loma Prieta earthquake, suggesting retarded or repeated rupture, it had a much different character than the subevents at Superstition Hills. The two subevents that began the Superstitions Hills event were sharp, high-stress-drop, localized subevents rich in high-frequency radiation. In contrast, the precursor to Loma Prieta had insufficient high-frequency energy to trigger local accelerometers, and may be characteristic of a slow, smooth episode of rupture growth.

A repeated rupture was suggested from waveform modeling of the Sierra Madre earthquake, though at a finer spatial and temporal scale than the Superstition Hill and Loma Prieta models. The two-pulse nature of the strong-motion velocity data is difficult to satisfy with simple slip variations that do not include rerupturing.

Two other important, recent earthquakes, not studied here, indicate repeated ruptures with a temporal lag greater than those described above but much shorter than the expected recurrence times. One example of a multiple mainshock occurring within an overlapping source region is the 1988 Tennant Creek, Australia sequence in which three events (M_s 6.3, 6.4 and 6.7) occurred within a 12-hour period [Choy and Bowman, 1990]. Another example is the 1985 Nahanni, Northwest Territories, Canada earthquake sequence (M 6.6 on 5 October, 1985 and M 6.9 on December 23, 1985). Both the Tennant Creek events and the Nahanni events were remote in their locations, so source studies are not particularly detailed. Nonetheless, aftershock analysis of the Nahanni earthquakes [Horner *et al.*, 1990] indicated that most of the

two aftershock zones overlapped. There was also some degree of complementarity in the aftershock patterns from the first to second events—zones that showed quiescence following the first mainshock indicated heavier activity following the second mainshock. It can be inferred that some regions of the fault either reruptured after the short delay between October and December, or on the basis of the aftershock gaps, regions of maximum slip may have complemented one another.

Clearly resolving episodic or repeated rupture is an important constraint on the rupture process. Any working, dynamic model of rupture must be capable of producing the extent of spatial and temporal rupture complications deduced from the strong-motion observations discussed herein. In particular, the model of rupture for the Superstition Hills earthquake, with repeated rupture episodes occupying a localized region of the fault plane, cannot be accommodated with the existing, complete stress-drop rupture models.

6.1.4 Slip Duration

As with other earthquakes modeled with sufficiently high-frequency data sets, the Sierra Madre, Superstition Hills, and Loma Prieta events require short slip durations. From Table 6.1, we see that the rise time has been determined to be less that 1.0 sec for all but the largest events studied, the 1978 Tabas, Iran and 1989 Loma Prieta earthquakes. For each event this implies that only a portion of the fault is slipping at a particular time, as was emphasized by Heaton [1990]. These rise times are shorter than the durations required by many uniform stress-drop models (where slip near the middle of the rupture continues until "information" from the edge of the fault arrives, resulting in a long slip duration) [Brune, 1991].

Within the systematically short times for the slip-duration estimates, there appears to be a consistent but slight systematic increase of the rise time with increasing amount of slip. This observation holds true from event to event and also as a func-

tion of position on the fault for a given earthquake. For example, as depicted in Figure 4.11, the total rise time for the Loma Prieta earthquake, as reflected by the number of time windows in which slip occurs, tends to increase in regions of the fault plane that experienced the most slip.

6.1.5 Relating Long- and Short-Period Energy Release

It can be argued that the models derived from modeling strong motions exclusively miss a substantial portion of slip, and that the actual slip durations are longer than modeled. This slip might occur as either slow slip, with a duration too long to be recognized in the strong-motion data, or as immediate afterslip. If this were so, slower slip could fill in the gaps left during the high-frequency radiation, reducing the final slip irregularity.

However, we find that most strong-motion models concur with geodetic and long-period seismic moments; only the models for the Superstition Hills earthquake underestimate the total moment release (Table 6.2). On average the strong ground motions require a total moment comparable to the teleseismic models as well as long-period surface waves or long-term geodetic models. Hence, we can conclude that the strong motions do require the short slip durations and are not missing significant long-period slip. Again, we should be careful in comparing seismic moments derived from different modelers' approximations of the true velocity structure [Heaton and Heaton, 1989]. The 1987 Superstition Hills is the only obvious exception; it has a low ratio of moment release at short periods compared to long periods (.2-.5) as seen in Table 6.2.

A second reason for emphasizing the correspondence of long- and short-period rupture models, is that in general, there is much more long-period, teleseismic-waveform data available for large earthquakes than local, strong-motion recordings. For instance, the 1906 San Francisco earthquake, one of the most important earth-

EARTHQUAKE	STRONG MOTION	TELE-SEISMIC	LONG-PERIOD	REFERENCE
1971 San Fernando*	17.	10.	17.	Heaton [1982]
		9.0		Langston [1978]
1979 Imperial	5.0	4.0		Hartzell & Heaton [1983]
Valley	6.7			Archuleta [1984]
			6.0	Kanamori & Regan [1982]
			7.2	Harvard CMT
1979 Coyote Lake*	0.4	0.4		Liu & Helmberger [1983]
			0.5	Harvard CMT
1984 Morgan Hill	2.1			Hartzell & Heaton [1986]
	2.7			Beroza & Spudich [1988]
		2.0		Ekstrom [1984]
			2.7	Harvard CMT
1986 North Palm	1.8	1.7		Hartzell [1990]
Springs		1.0		Pacheco & Nabelek [1988]
			1.3	Harvard CMT
1987 Superstition	4.8			Wald et al. [1990]
Hills	1.8			Frankel & Wenner. [1989]
		10.8		Bent et al. [1989]
		8.0		Hwang et al. [1990]
		10.2		Sipkin [1989]
			7.2	Harvard CMT
			9.4	Larson [1991]
1987 Whittier	0.9			Hartzell & Iida [1990]
Narrows		1.1		Bent & Helmberger [1989]
			0.9	Harvard CMT
			1.0	Lin & Stein [1989]
1989 Loma Prieta	31.	28.		Wald et al. [1991]
	30.			Steidl et al. [1991]
	25.			Beroza [1991]
		21.		Choy & Boatwright [1990]
		30.		Hartzell et al. [1991]
		24.	33.	Wallace [1991]
		30.	28.	Kanamori & Satake [1990]
			30.	Lisowski et al. [1990]
			28.	Marshall et al. [1991]

Table 6.2: Earthquake-model seismic moments ($\times 10^{25}$ dyne-cm) from different modeling studies. "Long-Period" refers to either surface-wave determination or geodetic modeling. A star indicates forward modeling only.

quakes for assessing damage potential in northern California, was only well recorded teleseismically and at relatively long periods. It is important to know how well we can retrieve source information from long-period recordings relevant to estimating higher-frequency (damaging), strong-ground motions that occurred and that will occur in the future. An important issue for earthquake-hazard assessment is determining the extent to which long and short periods are coupled. In other words, does the rupture process as viewed from teleseismic data (3-30 sec) tell us about the radiation at higher frequencies (5 sec-10 Hz) in the near field that are responsible for most damaging ground motions?

That long- and short-period slip models often concur suggests that the asperities that control the broadband, teleseismic waveforms (3-30 sec) also dominate the higher-frequency strong motions (.3-5 sec). Wald *et al.* [1987] previously found that large-scale asperity models derived from longer-period velocity data also explained many characteristics of the higher-frequency accelerograms. Their results, in addition to the results presented in Chapter 3, indicate that the same regions of large slip that control the longer-period teleseismic waveforms and the strong-motion velocities up to 1 Hz are also responsible for higher-frequency (> 1.0 Hz) radiation.

A similar conclusion can be drawn from the work of Spudich and Cranswick [1984], involving the analysis of accelerograms recorded at the El Centro Differential Array from the 1979 Imperial Valley earthquake. Spudich and Cranswick [1984] found that the source of high-frequency acceleration came from a narrow, moving region of radiation, interpreted to be the propagating rupture front, and the largest arrivals came from the same asperity region as determined from the longer-period velocity data by Hartzell and Heaton [1983].

As a generality then, it is reasonable to make the connection from 5-15-sec teleseismic body waves to strong-motion velocities. As has been done for the 1906 earthquake (Chapter 5), we can estimate what peak ground motions might have

been experienced given the constraints from long-period data, and therefore we assess the nature of the ground motions that may be experienced in the future. This can be done for other historical events that lack strong-motion recordings. Yet, it is important to determine under what conditions and frequency bands it is appropriate to make this connection.

6.2 "Characteristic" Earthquakes

I use the term "characteristic" earthquake in reference to events that are repeated on the same fault segment with comparable slip amplitudes and distributions. The notion of "characteristic" earthquakes has played a comforting role in the arena of hazard evaluation. First, "characteristic" earthquakes by their very definition imply a temporal consistency - advantageous for long-term predictability. Second, if we have historical information and/or seismological observations concerning a particular fault segment, and if complexities in the fault zone and/or material properties control the occurrence of these asperities and the nucleation of rupture, then we might expect the same regions of the fault to represent asperities during the next earthquake. We have found that the main asperities play an important role in determining the extent of damaging ground motions (see Chapter 3); hence, if we know where rupture nucleates and how the asperities will behave, a prediction of future ground motions from that segment would be deterministically obtainable, once path and site effects can be properly addressed. For this reason, substantial effort has been expended towards identifying fault segmentation and possible structural controls on rupture nucleation and propagation. If, however, the main asperity characteristics vary greatly from event to event—and the evidence I will present suggests that they do—a wide range of faulting scenarios must be evaluated to address properly the range of possible ground motions.

For many events there is evidence that large slip gradients remain after the coseismic rupture and possibly throughout the entire seismic cycle. For example, the geodetic evidence for the 1989 Loma Prieta earthquake indicates that postseismic slip or creep has not significantly reduced the permanent slip variations that were produced at the time of the earthquake [Langbein, 1990; Lisowski, personal communication, 1992], although some slightly accelerated, postseismic deformation is taking place. Granted, the slip may eventually be equalized with long-term creep, but this must be tested over the next decade or two with repeated geodetic and leveling surveys.

Dislocation models derived from geodetic data from the the Superstition Hills earthquake [Larson, 1991] show that the coseismic slip, combined with three to four months of postseismic slip required similar distributions of static slip to the strong-motion models presented in Chapter 2. Specifically, the models showed two regions of concentrated slip (e.g., Figure 6.1), one on the northwest and one on the southwest half of the fault, with a minimum in the amount of displacement towards the fault midsection. The total seismic moments Larson [1991] determined were similar to estimates from the long-period teleseismic data [Bent *et al.*, 1989; Hwang *et al.*, 1990], suggesting that very little slip occurred at depth as afterslip. Further, only a small amount of postseismic strain ($< 10\%$ of the coseismic strain) was observed at Pinõn Flat following the Superstition Hills earthquakes [Agnew and Wyatt, 1989]. This agrees with the observation that afterslip was limited to the near surface in the shallow, low-rigidity sediments [Larson, 1991], leaving a substantial region of low slip at depth between the two regions of the fault that displayed the most coseismic slip during the mainshock.

Likewise, Crook [1984] finds that afterslip from the 1979 Imperial Valley earthquake was confined to the shallow portion of the fault in the thick (0-3 km) sediment column above the region of highest slip; there was apparently no significant read-

justment of the slip at depth in the form of afterslip. After a decade and a half, it would be interesting to resurvey the area in an effort to determine whether or not this observation holds true.

Along the fault surface of the 1984 Morgan Hill earthquake, which required two quite separate asperities (Figure 6.8), it is still not clear whether or not significant postseismic slip has occurred in the region between the two asperities. There was accelerated afterslip following the earthquake, but the line-length changes suggest that postseismic slip was shallower than the coseismic slip [Prescott *et al.*, 1984].

For the dislocation models described above, if afterslip (or creep) does not fill in slip in regions that show coseismic slip gaps, then over the seismic cycle large slip deficits must remain. Repetition of the same slip distribution along this portion of the fault would lead to a very irregular stress distribution, which could not be supported over any more than a few earthquake cycles (assuming that the slip rate along the fault is constant).

This suggests that the concept of "characteristic" earthquakes may not be applicable along the many fault-rupture segments that exhibit this heterogeneous slip behavior. Rather, if large slip deficits remain at the end of the earthquake cycle, or at the very least at the end of several earthquake cycles, then some form of complementary slip distributions must occur.

Consider the slip for the 1984 Morgan Hill earthquake displayed in the top portion of Figure 6.8. There are two asperities (along strike at 3-6 and 13-17 km), which had nearly one meter of slip, and the region between these asperities, which experienced very little slip. Note that the two quite separate asperities are robust features of the Hartzell and Heaton [1986] model required by the strong-motion data, and they are also found in the dislocation model of Beroza and Spudich [1988], although the following argument would apply equally for any fault region that displayed large gradients in slip along strike, even a single, isolated patch of slip. The solid curve

in Figure 6.8 (middle) represents the slip averaged along strike over the depth range from 5-9 km obtained from the slip model above it (Figure 6.8, top). The area between asperities, region C, as well as the segments of the fault along strike outside of A and B, represents a slip deficit relative to the adjacent asperities (A and B). What are the possible ways that the area of slip deficit (region C) can "catch up" with the surrounding regions?

The lower portion of Figure 6.8 displays several possibilities. As mentioned above, there was little indication that substantial afterslip occurred at depth immediately following this earthquake. This eliminates possibility C (long dashes) from consideration, since it represents region C recovering much of the slip deficit in the immediate postseismic period. It should be noted, though, that a substantial portion of slip was likely recovered at shallower depths. The linear curve C' (short-dashed) represents slip in the form of continuous creep within the region adjacent to and outside the two large asperities. Over a single seismic cycle, this would allow the entire fault segment to equilibrate slip. Yet, such continuous creep should produce a recognizable geodetic signature, and on many fault segments that have mapped coseismic slip distributions (e.g., Superstition Hills, Imperial Valley, Morgan Hill, and Loma Prieta), there is no evidence supporting such slippage. A notable exception is the northwestern Parkfield segment of the San Andreas Fault. At Parkfield, creep accommodating slip adjacent to and northwest of the 1934 and 1966 rupture zones allows the total slip along strike to balance, but this region marks the transition to the well-known creeping segment of the San Andreas Fault northwest of Parkfield and is not representative of other fault segments characterized by "locked" zones at depth.

Yet another possibility, depicted as dashed-curve C", represents the antithesis of the "characteristic" earthquake. This scenario involves somewhat complementary slip from one event to the next, each having extremely heterogeneous slip; the slip deficit in one earthquake becomes (to some degree) the asperity in the following

rupture.

It is curious that the Parkfield rupture zone of the San Andreas Fault, distinguished by its seemingly well-behaved "characteristic" behavior, now has a more debatable repeatability. The commonly accepted "characteristic" nature of the Parkfield segment has been well known, and is based on the similar sizes and isoseismal-intensity distributions of events repeated at fairly regular intervals in 1857, 1881, 1901, 1922, 1934 and 1966. Further, Bakin and McEvilly [1984] showed that the 25-sec surface waves recorded at De Bilt, the Netherlands, for the 1922, 1934, and 1966 events were similar, suggesting comparable locations, moments and source mechanisms.

However, the characteristic nature of ruptures on the Parkfield segment can be questioned not only on its lack of temporal repeatiblity—after all, the 1934 event was 10 years out of sequence, but also on the now often assumed similarity of the ruptures which has also been called into question. Segall and Du [1992], by inverting both line length changes and triangulation data for the 1934 and 1966 earthquakes concluded that the two events could not have been the same. Specifically, they found a slip maximum considerably farther north for the 1934 event than it was in 1966. In effect, this represents more of a complementarity of 1966 and 1934 dislocations than a repeat, which resembles scenario C" (bottom of Figure 6.8). More than likely, though, the slip balance over the entire fault plane is achieved over more than two earthquake cycles.

An alternative explanation for the geodetic variations observed from the 1934 and 1966 Parkfield events requires considerably different patterns of afterslip [Segall and Du, 1992]. In either case, the 1934 and 1966 earthquakes were substantially different in their rupture behavior and final dislocation patterns. The Segall and Du [1992] observations in no way conflict with the surface-wave similarities seen at teleseismic distances at a period of 25 sec [Bakin and McEvilly, 1984]. Since the

duration of rupture for a magnitude 6 earthquake with unilateral rupture is on the order of 7 sec, variations in the slip distribution would not be resolved at longer periods, especially considering that the events had the same basic faulting geometry, vertical strike-slip on the same section of the San Andreas Fault. It should be further noted that there must be substantial differences in the 1922 and 1934 ruptures based on the dissimilarities of the near-regional waveforms at Berkeley (BRK) [see Figure 3, Bakin and McEvilly, 1984].

Michael and Eberhart-Phillips [1991] observed that regions with large slips appear to correlate with high seismic velocities and that rupture initiation or termination is associated with lower seismic velocities. There are also clear examples of structural control on rupture nucleation and occurrence. The Superstition Hills earthquake is a familiar case in point. Rupture nucleated at depth near the intersection of the Superstition Hills and Elmore Ranch Faults and propagated unilaterally southeastward (see Chapter 2). There is little doubt that the Elmore Ranch earthquake, 12 hours earlier, triggered rupture during the Superstition Hills event, while at the same time inhibiting rupture toward the northwest along the Superstition Hills Fault. Additionally, the absence of slip along the midsection of the Superstition Hills rupture area correlates well with a step in the depth to crystalline basement rock and a marked change in the distribution of aftershocks [Magistrale *et al.*, 1989].

Fault geometry, in particular, fault segmentation, jogs and bends, have been related to rupture initiation and termination [King and Nabelek, 1985]. Recognizing however, that larger ruptures generally initiate towards the base of the seismogenic zone, rheological as well as geometrical irregularities must play a role in the nucleation process [Sibson, 1989].

Many observations support the notion of structural control on slip patterns, yet at the same time imply that repeat earthquakes, having the same static-fault properties and the same structural controls on the rupture pattern, would show characteristic

Figure 6.8: Slip distribution of 1984 Morgan Hill earthquake (Top) from Hartzell and Heaton [1986]. The middle plot shows the slip along strike averaged between 5 and 9 km in depth (solid line) from the slip model above and that for a hypothetical event (dashed line). The bottom diagram depicts possible rupture scenarios described in the text.

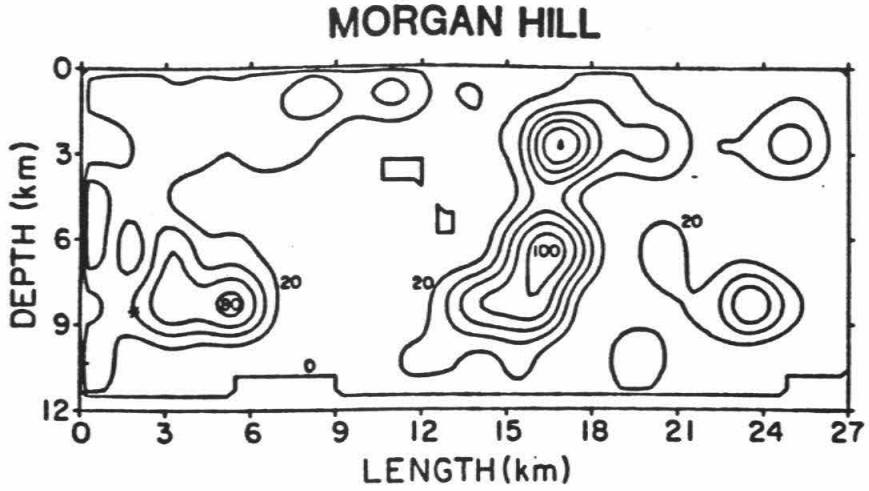
MORGAN HILL
DEPTH (km)
0
3
6
9
12
0
3
6
9
12
15
18
21
24
27
LENGTH (km)
20
100
20
20
0

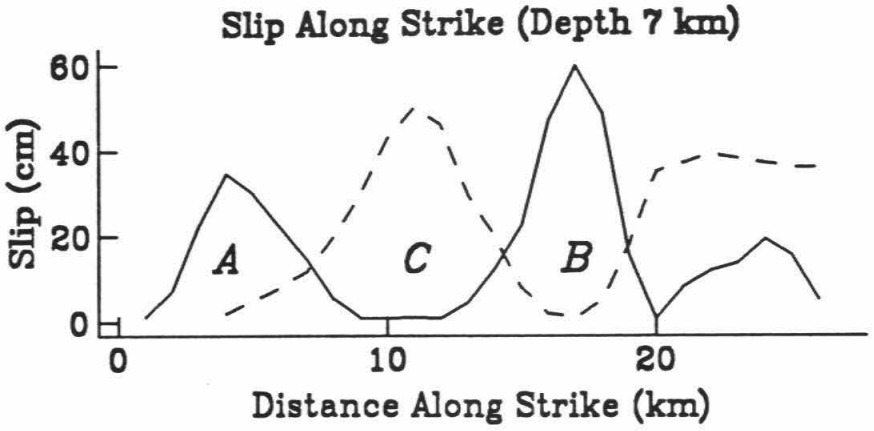
Slip Along Strike (Depth 7 km)
Slip (cm)
60
40
20
0
A
C
B
0
10
20
Distance Along Strike (km)

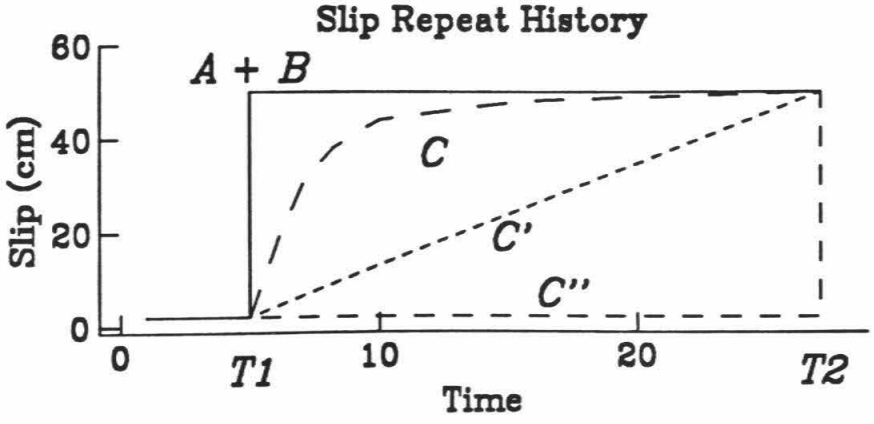
Slip Repeat History
Slip (cm)
60
40
20
0
A + B
C
C'
C''
0
T1
10
20
T2
Time

or comparable slips, with high slip in the region of high seismic velocity and low slips in the areas of low seismic velocity. Again, this inference requires "filling in" the regions of low slip with afterslip, long-term creep or smaller, gap-filling events prior to repeating a "characteristic" rupture. Yet there is little evidence for this supposition.

What then are the factors controlling the coseismic slip distribution? While there is clearly some connection between the variations of fault-material properties or structural and geometrical complexities (including fault bends and fault intersections) and the rupture nucleation and slip characteristics, the variable slip from event to event along a given fault segment suggested above requires that other factors must play an important role in determining slip heterogeniety. Perhaps the variable slip, or local variations of stress drops on the fault are not just indicative of conditions on the fault prior to the earthquake, but result from the dynamics of the rupture process itself [Brune, 1991]. Section 6.3 addresses the aspects of dynamic rupture that can be constrained by these finite-fault dislocation models, and the possible controls the dynamic rupture may have on the variable-slip distributions.

6.3 Implications For Rupture Dynamics

Though derived from kinematic-faulting models, the source information retrieved from waveform inversions contributes to the understanding of several important aspects of earthquake-rupture dynamics. Many of the above observations, including heterogeneous-slip distributions and irregular-rupture patterns, short-slip durations, and repeated ruptures along the same fault segment require certain attributes for any physical model of the dynamic-rupture process.

Extreme variations in slip along the fault require variable stress drops, ranging from perhaps near-total stress drop for concentrated asperities to a negative stress

drop in regions with small slips adjacent to the large asperities. Brune [1970] suggested that in reality, it was unlikely that slip over the entire fault would allow total stress drop. His "partial stress drop" model allows local slip velocities and stress drops to be higher than if the final static stress drop had been applied permanently [Brune, 1991].

Heaton [1990] documented evidence for an earthquake rupture model in which rupture occurs in a narrow "self-healing" pulse of slip which propagates down the fault. Among other observations, the short rise times associated with all earthquakes for which the data allowed detailed time histories to be determined, led Heaton to conclude that only a small portion of the fault is slipping at one time. Heaton [1990] also argued that the self-healing, slip-pulse model could be explained with fault friction, which is inversely related to the local slip velocity, similar to the slip-velocity-weakening suggested by workers in rock mechanics [Burridge and Knopoff, 1967; Dietrich, 1986]. Brune *et al.* [1991], using foam rubber models for earthquakes, observed that vibrations and separations normal to fault surface were capable of controlling stick-slip behavior, reducing the need for a slip-velocity weakening or displacement-weakening coefficient of friction. The particle trajectories in Brune *et al.*'s [1991] foam-rubber models were consistent with the separation waves suggested by Comninou and Dundurs [1978] and Schallamach [1971] for rubber sliding along a rigid solid.

In addition to explaining variable stress drops over the fault, the abrupt-locking, self-healing model conforms favorably to many of the other faulting characteristics determined and described in previous chapters. As mentioned above, extremely short slip durations are consistent with abrupt fault locking after the passage of the rupture front. Abrupt locking is also consistent with the minimal afterslip as observed and helps to explain the correspondence of long- and short-period slip distributions and seismic moment estimates. Further, since the propagating slip pulse cannot

travel far into a region that exhibits velocity-strengthening frictional resistance, there is a marked vertical stratification of coseismic slip along well-developed strike-slip faults; the shallow and deep gradients from large-to-small slip (Figure 6.5) mark the transition from a velocity-weakening to a velocity-strengthening frictional regime.

It is important to note that if feedback between the slipping pulse and the dynamic friction on the fault during the rupture process determine the eventual outcome of the rupture, the final distribution of slip may be quite variable and partly unrelated to the prior fault conditions. Heaton [1990] states (p. 14):

> Because the slip velocity and the dynamic friction are dependent on each other, mathematical solutions for the slip are likely to be rather unstable with respect to assumed initial conditions. It is conceivable that the static strength τ_s and the ambient stress τ_0 may both be relatively homogeneous along a rupture that has a relatively irregular slip distribution; i.e., the slip distribution may be controlled by details of the behavior of the dynamic frictional strength in the region of the slip pulse.

Apparently Ruina [1983] first associated complex earthquake recurrence with rupture dynamics as opposed to variable-material properties or initial-stress conditions. Ruina found that state-variable friction laws based on laboratory experiments, in conjunction with a simple spring-slider, produced complicated, chaotic behavior. Later work by Carlson and Langer [1989] considered a uniform chain of blocks and springs pulled slowly across a rough surface; despite the uniformity, the system exhibited complexity and gave rise to events of all sizes.

Horowitz and Ruina [1989] presented a model that predicts rupture complexity without along-strike variations in the properties or geometry. They also cautioned that repetitive events with similar spatial dimensions might be misinterpreted as strong patches on the fault, when, in fact, in their model the asperity region is not mechanically distinct from other locations. Again, their model indicates that rupture

dynamics, not simply inhomogeneous fault structure, may play an important role in rupture complexity.

Various mechanisms have been presented by which heterogeneous slip can be easily associated with relatively uniform, static fault properties. Yet, in light of the fact that examples of structural control of rupture nucleation and occurrence are convincing, it is natural to assume that both static, long-term fault properties and dynamic faulting processes to some degree are working in harmony. It will be a challenge to determine to what extent fault structural complexity and to what extent rupture dynamics control the great variations of slip along strike seen in the dislocation models presented in this thesis.

Bibliography

Abe, K, and S. Noguchi. Revision of large shallow earthquakes, 1897-1912, *Phys. Earth Planet. Int.*, **33**, 1-11, 1983.

Abrahamson, N. A., P. G. Somerville, and C. A. Cornell, Proceedings of Fourth U.S. National Conference on earthquake engineering, May 20-24, 1990, Palm Springs, California, **1**, 407-416, 1990.

Agnew, D. C., and F. K. Wyatt, The 1987 Superstition Hills earthquake sequence: strains and tilts at Pinõn Flat observatory, *Bull. Seism. Soc. Am.*, **79**, 480-492, 1989.

Aki, K., Local site effects on strong ground motion, In: *Proceedings of the Earthquake Engineering and Soil Dynamics II Conference*, American Society of Civil Engineers, Geotechnical Special Publication No. 20, 103-155, 1988.

Archuleta, R., A finite faulting model for the 1979 Imperial Valley earthquake, *J. Geophys. Res.*, **89**, 4559-4585, 1984.

Baag, C., and C. A. Langston, Shear-coupled PL, *Geophys. J. R. astr. Soc.*, **80**, 363-385, 1985.

Bakin, W., and T. V. McEvilly, Recurrence models and Parkfield, California, *J. Geophys. Res.*, **89**, 3051-3058, 1984.

Ben-Menahem, A., Source mechanism of the 1906 San Francisco earthquake, *Phys. Earth and Planet. Int.*, **17**, 163-181, 1978.

Bent, A. L., and D. V. Helmberger, Source complexity of the October 1, 1987, Whittier Narrows earthquake, *J. Geophys. Res.*, **94**, 9548-9556, 1989.

Bent, A. L., D. V. Helmberger, R.J. Stead, and P. Ho-Liu, Waveform modeling of the November 1987 Superstition Hills earthquake, *Bull. Seism. Soc. Am.*, **79**, 500-514, 1989.

Benuska, L., Loma Prieta Earthquake Reconnaissance Report, *Earthquake Spectra*, Supplement to Vol. **6**, 448 pp., 1990.

Berberian, M., M. Qorashi, J. A. Jackson, K. Priestley and T. C. Wallace, The Rudbar-Tarom earthquake of 20 June 1990 in NW Persia: preliminary field and seismological observations, and its tectonic significance, *Bull. Seism. Soc. Am.*, in press, 1992.

Beroza, G. C., Near-source modeling of the Loma Prieta earthquake: evidence for heterogeneous slip and implications for earthquake hazard, *Bull. Seism. Soc. Am.*, **81**, 1603-1621, 1991.

Beroza, G. C., and P. Spudich, Linearized inversion for fault rupture behavior: application to the 1984 Morgan Hill, California, earthquake, *Bull. Seism. Soc Am.*, **78**, 6275-6296, 1988.

Bolt, B. A., The focus of the 1906 California earthquake, *Bull. Seism. Soc. Am.*, **58**, 457-471, 1968.

Boore, D. M., Strong-motion recordings of the California earthquake of April 16, 1906, *Bull. Seism. Soc. Am.*, **67**, 561-576, 1977.

Boore, D. M., L. Seekins, and W. B. Joyner, Peak accelerations from the 17 October, 1989 Loma Prieta earthquake, *Seism. Res. Lett.*, **60**, 151-156, 1989.

Brune, J. N., Tectonic stress and the spectra of seismic shear waves from earthquakes, *J. Geophys. Res.*, **75**, 4997-5009, 1970.

Brune, J. N., Seismic Source Dynamics, Radiation and Stress, *Rev. of Geophys., Supplement*, 688-699, 1991.

Brune, J. N., S. Brown, and P. A. Johnson, Rupture mechanism and interface separation in foam-rubber models of earthquakes: a possible solution to the heat-flow paradox and the paradox of large overthrusts, submitted to the Proceedings of the International Workshop: "New horizons in strong motion: Seismic Studies and Engineering Practice," Santiago, 1991.

Burridge, R. and L. Knopoff, Model and theoretical seismicity, *Bull. Seism. Soc. Am.*, **57**, 341-371, 1967.

Carlson, J. M., and J. S. Langer, Mechanical model of an earthquake fault, *Phys. Rev. A*, **40**(11), 6470-6484, 1989.

Choy, G. L., and J. Boatwright, Source characteristics of the Loma Prieta, California, earthquake of October 18, 1989 from global, digital seismic data, *Geophys. Res. Lett.*, **17**, 1183-1186, 1990.

Choy, G. L., and J. R. Bowman, Rupture process of a multiple mainshock sequence: analysis of teleseismic, local, and field observations of the Tennant Creek, Australia, earthquakes of January 22, 1988, *J. Geophys. Res.*, **95**, 6867-6882, 1990.

Comninou, M., and J. Dundurs, Can two solids slide without slipping? *J. Solid Structures*, 251-260, 1978.

Crook, C. N., Geodetic measurement of the horizontal crustal deformation associated with the Oct. 15, 1979 Imperial Valley (California) earthquake, Ph.D. Thesis, University of London, 1984.

Dietrich, J. H., A model for the nucleation of earthquake slip, in Maurice Ewing Volume, eds. S. Das, J. Boatwright, and C. Scholz, *Am. Geophys. Union*, 37-47, 1986.

Dietz, L. D., and W. L. Ellsworth, The October, 17, 1989, Loma Prieta, California, earthquake and its aftershocks: geometry of the sequence from high- resolution locations, *Geophys. Res. Lett.*, **17**, 1417-1420, 1990.

Dreger, D. S., and D. V. Helmberger, Source parameters of the Sierra Madre earthquake from regional and local body waves, *Geophys. Res. Lett.*, **18**, 2015-2018, 1991.

Dziewonski, A. M., G. Ekström, J. H. Woodhouse, and G. Zwart , Centroid-moment tensor solutions for October-December 1987, *Phys. Earth Planet. Inter.*, **54**,10-21, 1989.

Eberhart-Phillips, D., V. F. Labson, W. D. Stanley, A. J. Michael, and B. D. Rodriguez, Preliminary velocity and resistivity model of the Loma Prieta earthquake region, *Geophys. Res. Lett.*, **17**, 1235-1238, 1990.

Ekström, G., Centroid-moment tensor solution for the April 24, 1984 Morgan Hill earthquake, in *The 1984 Morgan Hill, California Earthquake*, CDMG Special Publication 68, 1984.

Eshelby, J. D., The determination of the elastic field of ellipsoidal inclusion and related problems, *Proc. Roy. Soc. London, Series A*, **241**, 376-396, 1957.

Espinosa, A. F., R. Husid and A. Quesada, Intensity distribution and source parameters from field observations, The Guatemalan earthquake of 1976, A Preliminary report, *U.S. Geol. Surv. Prof. Pap.*, **1002**, 52-66, 1976.

Frankel, A., Comment on "Rupture process of the 1987 Superstition Hills earthquake from the inversion of strong motion data" by Wald *et al.*, *Bull. Seism. Soc. Am.*, **82**, 1992.

Frankel, A., and L. Wennerberg, Rupture process of the Ms 6.6 Superstition Hills earthquake determined from strong-motion recordings: application of tomographic source inversion, *Bull. Seism. Soc. Am.*, **79**, 515-541, 1989.

Fuis, G. S., W. D. Mooney, J.H. Healy, G.A. McMechan, and W.J. Lutter, Crustal structure of the Imperial Valley Region, in The Imperial Valley, California, earthquake of October 15, 1979,*U.S. Geol. Surv. Prof. Pap. 1254*, 25-50, 1982.

Futterman, W. I., Dispersive body waves, *J. Geophys. Res.*, **67**, 5279-5291, 1962.

Gutenberg, B., Magnitude determination for larger Kern County shocks, 1952; effects of station azimuth and calculation methods, in *Earthquakes in Kern County, California during 1952, Cal. Div. Mines. Geol. Bull.*, **171**, 171-176, 1955.

Hartzell, S. H., Comparison of seismic waveform inversion techniques for the rupture history of a finite fault: application to the 1989 North Palm Springs, California, earthquake, *J. Geophys. Res.*, **94**, 7515-7534, 1989.

Hartzell, S. H., and T. H. Heaton, Inversion of strong ground motion and teleseismic waveform data for the fault rupture history of the 1979 Imperial Valley, California earthquake, *Bull. Seism. Soc Am.*, **73**, 1553-1583, 1983.

Hartzell, S. H., and T. H. Heaton, Rupture history of the 1984 Morgan Hill, California, earthquake from the inversion of strong motion records, *Bull. Seism. Soc. Am.*, **76**, 649-674, 1986.

Hartzell, S. H., and D. V. Helmberger, Strong-motion modeling of the Imperial Valley earthquake of 1979, *Bull. Seism. Soc. Am.*, **72**, 571-596, 1982.

Hartzell, S. H., and M. Iida, Source complexity of the 1987 Whittier Narrows, California, earthquake from inversion of strong motion records, *J. Geophys. Res.*, **95**, 12,475-12,485, 1990.

Hartzell, S. H., and C. Mendoza, Application of an iterative least squares waveform inversion of strong motion and teleseismic records to the 1978 Tabas, Iran, earthquake, *Bull. Seism. Soc. Am.*, **81**, 305-331, 1991.

Hartzell, S. H., G. S. Stewart and C. Mendoza, Comparison of L1 and L2 norms in a teleseismic inversion for the slip history of the Loma Prieta, California, earthquake, *Bull. Seism. Soc. Am.*, **81**, 1518-1539, 1991.

Hauksson, E., Seismotectonics, *Rev. of Geophys., Supplement*, 721-733, 1991.

Hauksson E., and L. M. Jones, The 1987 Whittier Narrows earthquake sequence in Los Angeles, Southern California: seismological and tectonic analysis, *J. Geophys. Res.*, **94**, 9569-9589, 1989.

Hauksson, E., and L. M. Jones, The 1991 (M_L=5.8) Sierra Madre earthquake in Southern California: Seismological and Tectonic Analysis, *EOS*, **72**, 1991a.

Hauksson, E., and L. M. Jones, The 1988 and 1990 Uplands earthquakes: Left-lateral faulting adjacent to the Central Transverse Ranges, analysis, *J. Geophys. Res.*, **96**, 8143-8165, 1991b.

Heaton, T. H., The 1971 San Fernando earthquake: a double event?, *Bull. Seism. Soc. Am.*, **72**, 2037-2062, 1982.

Heaton, T. H., Evidence for and implications of self-healing pulses of slip in earthquake rupture, *Phys. Earth Planet. Inter.*, **64**, 1-20, 1990.

Heaton, T. H., and R. E. Heaton, Static deformations from point forces and force couples located in welded elastic Poissonian half-spaces: implications for seismic moment tensors, *Bull. Seism. Soc. Am.*, **79**, 813-841, 1989.

Helmberger, D. V., The location and mechanism of the Lompoc, California earthquake of November 4, 1927, *Bull. Seism. Soc Am.*, in press, 1992.

Horner, R. B., R. J. Wetmiller, M. Lamontagne, and M. Plouffe, A fault model for the Nahanni earthquakes from aftershock studies, *Bull. Seism. Soc Am.*, **80**, 1553-1570, 1990.

Horowitz, F. G., and A. Ruina, Slip patterns in a spatially homogeneous fault, *J. Geophys. Res.*, **94**, 10279-10298, 1989.

Huang, M. J., A. F. Shakal, C. Ventura, T. Cao, R. Sherburne, P. Fung, J. Wampole, M. DeLesle and C. Petersen, CSMIP strong-motion records from the Sierra Madre, California earthquakes of 28 June 1991 *Report No. OSMS 91-03, California Strong Motion Instrumentation Program*, 108 pp., 1991.

Huang, M. J., T. Q. Cao, C. E. Ventura, D. L. Parke, and A. F. Shakal, CSMIP strong motion records from the Superstition Hills, Imperial county, California, earthquakes of 23 and 24 November 1987, *Report No. OSMS 87-06, California Strong Motion Instrumentation Program*, 42 pp., 1987.

Hudnut, K. W., L. Seeber and J. Pacheco, Cross-fault triggering in the November 1987 Superstition Hills earthquake sequence, Southern California, *Geophys. Res. Lett.*, **16**, 199-202, 1989.

Hwang, L. J., H. Magistrale, and H. Kanamori, Teleseismic source parameters and rupture characteristics of the 24 November 1987, Superstition Hills earthquake, *Bull. Seism. Soc. Am.*, **80**, 23-42, 1990.

Jeffreys, H., and K. E. Bullen, *Seismological Tables*, Office of the British Association, Burlington House, London, 1958.

Jennings, C. W., Fault map of California, with locations of volcanoes, thermal springs, and thermal wells, *Geologic Data Map 1* California Division of Mines and Geology, scale 1:750,000, 1975.

Jennings, P. C. and H. Kanamori, Determination of local magnitude, M_L, from seismoscope records, *Bull. Seism. Soc. Am.*, **69**, 1267-1288, 1979.

Joyner, W. B. and D. M. Boore, Measurement, characterization, and Prediction of strong ground motion, in: *Proceedings of the Earthquake Engineering and Soil Dynamics II Conference*, American Society of Civil Engineers, Geotechnical Special Publication No. 20, 43-102, 1988.

Kanamori, H., Hauksson E. and T. H. Heaton, Experiment towards real-time seismology using TERRAscope: the 1991 Sierra Madre earthquake, *EOS*, **72**, 320, 1991.

Kanamori, H., and K. Satake, Broadband study of the 1989 Loma Prieta earthquake, *Geophys. Res. Lett.*, **17**, 1179-1182, 1990.

Kanamori, H., and J. Regan, Long-period surface waves, in The Imperial Valley, California, earthquake of October 15, 1979,*U.S. Geol. Surv. Prof. Pap. 1254*, 55-58, 1982.

Kikuchi, M., and H. Kanamori, Inversion of complex body waves - III, *Bull. Seism. Soc. Am.*, **81**, 2335-2350, 1991.

King, G. C., A. G. Lindh and D. H. Oppenheimer, Seismic slip, segmentation, and the Loma Prieta earthquake, *Geophys. Res. Lett.*, **17**, 1449-1452, 1990.

King, G. C., and J. Nabelek, The role of fault bends in faults in the initiation and termination of earthquake rupture, *Science*, **283**, 984-987, 1985.

Knopoff, L., Energy release in earthquakes, *Geophys. J.*, **1**, 44-52, 1958.

Langbein, J. O., Post-seismic slip on the San Andreas Fault at the northwestern end of the 1989 Loma Prieta rupture zone, *Geophys. Res. Lett.*, **17**, 1223-1226, 1990.

Langston, C. A. and D. V. Helmberger, A procedure for modeling shallow dislocation sources, *Geophys. J.*, **42**, 117-130, 1975.

Langston, C. A., The February 9, 1971, San Fernando earthquake: a study of source finiteness in teleseismic body waves, *Bull. Seism. Soc. Am.*, **68**, 1-29, 1978.

Larson, S. C., Geodetic measurement of deformation in Southern California, Ph.D. thesis, California Institute of Technology, Pasadena, 1991.

Lawson, A. C., chairman, The California earthquake of April 18, 1906: Rep. State Earthquake Invest. Comm. Vols. I and II; Atlas, Carnegie Inst. Washington, D. C., 1908.

Lay, T., and H. Kanamori, An asperity model of great earthquake sequences, in *Earthquake Prediction, an International Review, M. Ewing Ser. 4*, eds. D. Simpson and P. Richards. Washington, D.C.: American Geophysical Union, pp. 579-592, 1981.

Lin, J., and R. S. Stein. Coseismic folding, earthquake recurrence, and the 1987 source mechanism at Whittier Narrow, Los Angeles Basin, California, *J. Geophys. Res.*, **94**, 9614-9632, 1989.

Lisowski, M., W. H. Prescott, J. C. Savage and M. J. Johnston, Geodetic estimate of coseismic slip during the 1989 Loma Prieta, California, earthquake, *Geophys. Res. Lett.*, **17**, 1437-1440, 1990.

Liu, H. and D. V. Helmberger, The near-source ground motion of the August, 1979 Coyote Lake, California, earthquake, *Bull. Seism. Soc Am.*, **73**, 201-218, 1983.

Magistrale, H., L. Jones, H. Kanamori, The Superstition Hills, California, earthquakes of 24 November, 1987, *Bull. Seism. Soc. Am.*, **79**, 239-251, 1989.

Maley, R., A. Acosta, F. Ellis, E. Etheredge, L. Foote, D. Johnston, R. Pocella, M. Salsman and J. Switzer, U.S. Geological Survey strong-motion records from the northern California (Loma Prieta) earthquake of October 17, 1989, *U. S. Geological Survey Open-File Report. 89-568*, 1989.

Mansinha, L., and D. E. Smylie, The displacement field of inclined faults, *Bull. Seism. Soc. Am.*, **61**, 1433-1440, 1971.

Marone, C. J., C. H. Scholz, The depth of seismic faulting and the transition from stable to unstable slip regimes, *Geophys. Res. Lett.*, **15**, 621-624, 1988.

Marone, C. J., C. H. Scholz and R. Bilham, On the mechanics of earthquake afterslip, *J. Geophys. Res.*, **96**, 8441-8452, 1991.

Marshall, G. A., R. S. Stein, and W. Thatcher, Faulting geometry and slip from co-seismic elevation changes: The 18 October 1989, Loma Prieta, California, earthquake, *Bull. Seism. Soc. Am.*, **81**, 1660-1693, 1991.

McLaughlin, R. J, D. H. Sorg, J. L. Morton, J. N. Batchelder, R. A Leveque, C. Heropoulus, H. N. Ohlin, and M. B. Norman, *EOS*, **60**, 883, 1979.

Mendoza, C., and S. H. Hartzell, Inversion for slip distribution using teleseismic P waveforms: North Palm Springs, Borah Peak, and Michoacan earthquakes, *Bull. Seism. Soc. Am.*, **78**, 1092-1111, 1988a.

Mendoza, C., and S. H. Hartzell, Aftershock patterns and main shock faulting, *Bull. Seism. Soc. Am.*, **78**, 1438-1449, 1988b.

Michael, A. J, and D. Eberhart-Phillips, Relations among fault behavior, subsurface geology, and three-dimensional velocity models, *Science*, **253**, 651-654, 1991.

Miyatake, T., Reconstruction of dynamic rupture process of an earthquake with constraints of kinematic parameters, *Geophys. Res. Lett.*, **19**, 349-352, 1992.

Nakata, T., H. Tsutsumi, R. S. Punongbayan, R. E. Rimando, J. Daligdig and A. Daag, Surface faulting associated with the Philippine earthquake of 1990, unpublished manuscript, 1990.

Olson, J. A., Seismicity in the twenty years preceding the Loma Prieta, California, earthquake, *Geophys. Res. Lett.*, **17**, 1429-1432, 1990.

Olson A. H., and R. J. Apsel, Finite faults and inverse theory with applications to the 1979 Imperial Valley earthquake, *Bull. Seism. Soc. Am.*, **72**, 1969-2001, 1982.

Olson A. H., J. Orcutt, and G. Frazier, The discrete wavenumber/finite element method for synthetic seismograms, *Geophys. J. R. Astr. Soc.*, **77**, 421-460, 1984.

Oppenheimer, D. H., Aftershock slip behavior of the 1989 Loma Prieta, California, earthquake, *Geophys. Res. Lett.*, **17**, 1199-1202, 1990.

Pacheco, J. and J. Nabelek, Source mechanisms of three moderate California earthquakes of July, 1986, *Bull. Seism. Soc. Am.*, **78**, 1907-1929, 1988.

Parsons, I. D, J. F. Hall, and G. A. Lyzenga, Relationships between the average offset and the stress drop for two- and three-dimensional faults, *Bull. Seism. Soc. Am.*, **78**, 931-945, 1988.

Plafker, G., Tectonic Aspects of the Guatemala earthquake of 4 February 1976, *Science*, **193**, 1201-1208, 1976.

Ponti, D. J., and R. E. Wells, Off-fault ground ruptures in the Santa Cruz Mountains, California: Ridge-top spreading versus tectonic extension during the 1989 Loma Prieta earthquake, *Bull. Seism. Soc. Am.*, **81**, 1480-1510, 1991.

Porcella, R., E. Etheredge, R. Maley, and J. Switzer, Strong-motion data from the Superstition Hills earthquakes of 0154 and 1315 (GMT), November 24, 1987, *U. S. Geol. Surv. Open-File Rept. 87-672*, 1988.

Prentice, C. S. and D. P. Schwartz, Re-evaluation of 1906 surface faulting, geomorphic expression, and seismic hazard along the San Andreas fault in the southern Santa Cruz Mountains, *Bull. Seism. Soc Am.*, **81**, 1424-1479, 1991.

Prescott, W. H., N. E. King, and G. Guohua, Preseismic, coseismic and postseismic deformation associated with the 1985 Morgan Hill, California, earthquakes, *California Division of Mines and Geology, Special Publication 68*, 1984.

Quin, H., Dynamic stress drop and rupture dynamics of the October 15, 1979 Imperial Valley, California, earthquake, *Tectonophysics*, **175**, 83-117, 1990.

Richter, C. F., *Elementary Seismology*, W. H. Freeman and Company, San Francisco and London, 768 pp., 1958.

Ruina, A. L., Slip instability and state variable friction laws, *J. Geophys. Res.*, **88**, 10359-10370, 1983.

Rymer, M. J., Surface rupture in a fault stepover on the Superstition Hills fault, California, *U. S. Geol. Surv. Open-File Rept. 89-315*, 309-323, 1989.

Saikia, C. K., Simulated ground motions in Los Angeles due to a large hypothesized earthquake on the Elysian thrust fault zone, submitted to *Bull. Seism. Soc. Am.*, 1992.

Salsman, M., E. Etheredge, and R. Porcella, The Sierra Madre earthquake of June 28, 1991: A preliminary summary of USGS strong motion recordings, 1991.

Schallamach, A., How does rubber slide?, *Wear*, **17**, 301-312, 1971.

Schwartz, S. Y., D. L. Orange, and R. S. Anderson, Complex fault interactions in a restraining bend on the San Andreas Fault, Southern Santa Cruz Mountains, California, *Geophys. Res. Lett.*, **17**, 1207-1210, 1990.

Scholz, C. H., The mechanics of earthquake faulting, Cambridge University Press, New York, 438 pp., 1990.

Seeber, L., and J. G. Armbruster, Fault kinematics in the 1989 Loma Prieta rupture area during 20 years before that event, *Geophys. Res. Lett.*, **17**, 1425-1428, 1990.

Segall, P. and Y. Du, How similar were the 1934 and 1966 Parkfield earthquakes?, *J. Geophys. Res.*, submitted for publication, 1992.

Segall, P. and M. Lisowski, Comparison of surface displacements in the 1906 San Francisco and 1989 Loma Prieta earthquakes, *Science*, **250**, 1241-1244, 1990.

Shakal, A., M. Huang, M. Reichle, C. Ventura, T. Cao, R Sherburne, M Savage, R. Darragh, and C. Petersen, CSMIP strong-motion records from the Santa Cruz Mountains (Loma Prieta), California, earthquake of 17 October 1989, *Report No. OSMS 89-06*, California Strong-Motion Instrumentation Program, 196 pp., 1989.

Sharp, R. V., K. E. Budding, J. Boatwright, M. J. Ader, M. G. Bonilla, M. M. Clark, T. E. Fumal, K. K. Harms, J. J. Lienkaemper, D. M. Morton, B. J. O'Neill, C. L. Ostergren, D. J. Ponti, M. J. Rymer, J. L. Saxton, and J. D. Sims, Surface faulting along the Superstition Hills fault zone and nearby faults associated with the earthquakes of 24 November 1987, *Bull. Seism. Soc. Am.*, **79**, 252-281, 1989.

Sibson, R. H., Earthquake faulting as a structural process, *J. of Struct. Geol.*, **11**, 1-14, 1989.

Simila, G. W., K. C. McNally, E. Nava, M. Protti-Quesada, and J. Yellin, Evidence of very early aftershock activity along the northwest portion of the 18 October 1989 earthquake rupture zone, *Geophys. Res. Lett.*, **17**, 1785-1788, 1990.

Sipkin, S. A., Moment-tensor solutions for the 24 November 1987 Superstition Hills, California earthquake, *Bull. Seism. Soc. Am.*, **79**, 493-499, 1989.

Spudich, P. K. P., On the inference of absolute stress levels from seismic radiation, *Tectonophysics*, accepted for publication, 1992.

Spudich, P., and E. Cranswick, Direct observation of rupture propagation during the 1979 Imperial Valley earthquake using a short baseline accelerometer array, *Bull. Seism. Soc. Am.*, **79**, 2083-2114, 1984.

Steidl, J. H., R. J. Archuleta, and S. Hartzell, Rupture history of the 1989 Loma Prieta, California, earthquake, *Bull. Seism. Soc. Am.*, **81**, 1573-1602, 1991.

Stover, C. W., and B. G. Reagor, Preliminary isoseismal map for the Sierra Madre, California, earthquake of June 28, 1991 UTC, *U. S. Geol. Surv. Open-File Rept. 91-388*, 1991.

Stover, C. W., B. G. Reagor, F. W., Baldwin, and L. R. Brewer, Preliminary isoseismal map for the Santa Cruz (Loma Prieta), California, earthquake of October 18, 1989 UTC, *U. S. Geol. Surv. Open-File Rept, 90-18*, 1990.

Thatcher, W., Strain accumulation and release mechanism of the 1906 San Francisco earthquake, *J. Geophys. Res.*, **80**, 4862-4872, 1975.

Thatcher, W., Strain accumulation on the northern San Andreas fault zone since 1906, *J. Geophys. Res.*, **80**, 4873-4880, 1975.

Thatcher, W. and M. Lisowski, 1906 earthquake slip on the San Andreas fault in offshore northwestern California, *EOS*, **68**, 1507, 1987a.

Thatcher, W. and M. Lisowski, Long-term seismic potential of the San Andreas fault southeast of San Francisco, California, *J. Geophys. Res.*, **92**, 4771-4784, 1987b.

Thio, H. K., K. Satake, M. Kikuchi, and H. Kanamori, The 1990 Philippines earthquake, submitted for publication, 1992.

Toppozada, T. R. and D. L. Parke, Areas damaged by California earthquakes, 1900-1949, *California Division of Mines and Geology, Open-File Rept. 82-17 SAC*, 1982.

U.S. Geological Survey Staff, The Loma Prieta, California, earthquake: an anticipated event, *Science*, **247**, 286-293, 1990.

Wald, D. J., Strong motion and broadband teleseismic analysis of the 1991 Sierra Madre, California, earthquake, *J. Geophys. Res.*, , 1992

Wald, D. J., S. H. Hartzell and D. V. Helmberger, Reply to Arthur Frankel's "Comments on 'Rupture Process of the 1987 Superstition Hills earthquake from the inversion of strong motion data,' " *Bull. Seism. Soc. Am.*, **82**, 1992.

Wald, D. J., T. H. Heaton and D. V. Helmberger, Rupture model of the 1989 Loma Prieta from the inversion of strong motion and broadband teleseismic data, *Bull. Seism. Soc. Am.*, **81**, 1540-1572, 1991.

Wald, D. J., T. H. Heaton and D. V. Helmberger, Strong-motion and broadband teleseismic analysis of the 1989 Loma Prieta earthquake for rupture process and hazards assessment, accepted for publication in *U.S.G.S. Professional Paper*, 1992.

Wald, D. J., D. V. Helmberger, and S. H. Hartzell, Rupture process of the 1987 Superstitions Hills earthquake from the inversion of strong-motion data, *Bull. Seism. Soc. Am.*, **80**, 1079-1098, 1990.

Wald, D. J., D. V. Helmberger, and T. H. Heaton, The rupture initiation process of a large earthquake: Loma Prieta, *Seism. Res. Lett.*, **62**, p. 29, 1991.

Wald, D. J., and P. G. Somerville, Simulation of accelerograms of the 1987 Superstition Hills earthquake sequence, paper presented at Seismol. Soc. Am. meeting, Honolulu, 24-27 May 1988, 1988.

Wald, D. J., P. Somerville, and L. J. Burdick, Simulation of recorded accelerograms of the Whittier Narrows earthquake, *Earthquake Spectra*, **4**, 139-156, 1988.

Wald, D. J., P. G. Somerville, and D. V. Helmberger, Compatibility of accelerograms of the 1979 Imperial Valley, California, earthquake with slip-distribution asperity models, *Seism. Res. Lett.*, **58**, 59, 1987.

Wallace T. C., A broadband seismological investigation of the Loma Prieta, California earthquake: evidence for deep slow slip?, *Bull. Seism. Soc. Am.*, **81**, 1622-1646, 1991.

Williams, P. L., and H. W. Magistrale, Slip along the Superstition Hills fault associated with the 24 November 1987 Superstition Hills, California, earthquake, *Bull. Seism. Soc. Am.*, **79**, 390-410, 1989.

Working Group on California Earthquake probabilities, Probabilities of large earthquakes occurring in California on the San Andreas Fault, *U. S. Geol. Surv. Open-File Rept., 88-398*, 1988.

Young, C. J., T. Lay and C. S. Lynnes, Rupture of the 4 February 1976 Guatemalan earthquake, *Bull. Seism. Soc. Am.*, **79**, 670-689, 1989.